61 /3/2023

JOURNAL OF THEORETICAL AND APPLIED MECHANICS

WARSAW 2023, QUARTERLY, VOLUME 61, INDEX 365238, ISSN 1429-2955

POLISH SOCIETY OF THEORETICAL AND APPLIED MECHANICS

POLISH SOCIETY OF THEORETICAL AND APPLIED MECHANICS

JOURNAL OF THEORETICAL AND APPLIED MECHANICS

No. 3 • Vol. 61

Quarterly

WARSAW, JULY 2023

JOURNAL OF THEORETICAL AND APPLIED MECHANICS
(until 1997 Mechanika Teoretyczna i Stosowana, ISSN 0079-3701)

Beginning with Vol. 45, No. 1, 2007, *Journal of Theoretical and Applied Mechanics* (JTAM) has been selected for coverage in Thomson Reuters products and custom information services. Now it is indexed and abstracted in the following:

- **Science Citation Index Expanded** (also known as SciSearch®)
- **Journal Citation Reports/Science Edition**

* * * * *

Editorial Office

Al. Armii Ludowej 16, room 650; 00-637 Warsaw, Poland
phone (+48) 664 099 345, e-mail: biuro@ptmts.org.pl

www.jtam.pl

* * * * *

Ministerstwo Edukacji i Nauki
Publication supported by Ministry of Science and Higher Education of Poland

Rozwój kwartalnika naukowego *Journal of Theoretical and Applied Mechanics*, ISSN 1429-2955, jest dofinansowany ze środków Ministra Edukacji i Nauki przyznanych z pomocy *de minimis* w ramach programu „Rozwój czasopism naukowych", umowa RCN/SN/0056/2021/1.

JOURNAL OF THEORETICAL AND APPLIED MECHANICS
61, 3, pp. 419-426, Warsaw 2023
https://doi.org/10.15632/jtam-pl/165938

AN INVESTIGATION OF SPHERICAL MICRO/NANOPARTICLE MELTING USING ASYMPTOTIC MATCHINGS IN A WEAK FORMULATION

Yue Chan

Institute for Advanced Study, Shenzhen University, Nanshan District Shenzhen, Guangdong, China
e-mail: unimelbat@hotmail.com

In this paper, we investigate the speed of moving boundaries for melting micro/nanoparticles in the initial and final stages using asymptotic matchings in a weak formulation of the problem. We find that such a speed is initially proportional to the flux across the moving boundary, however a blowup occurs in a finite time when the surface tension is considered, both numerically and theoretically, by assuming linear relations between thermal conductivities and diffusivities, which paves the way to tackle the related two and higher phase change problems. Last but not least, we verify our theoretical outcomes using a quasi-stationary approximation approach.

Keywords: micro/nanoparticle, Stefan problem, blowup, weak formulation, asymptotic analysis

1. Introduction

Phase changes are ubiquitous in nature and technologies. Usually, bulk melting temperature is independent on its size. However, micro/nanoparticle melting temperature depends on its size owing to the higher value of surface by the volume ratio. Such an effect will lower the melting temperature (Buffat and Borel, 1976), which can be described by the Gibbs-Thomson equation (Langer, 1980) (see Eq. (2.3)). The lowering of the melting temperature will promote the molten speed, especially towards the final stage of the melting process resulting in blowing up the melting speed in a finite time (Herrero and Velázquez, 1996; McCue *et al.*, 2009) (see Fig. 2).

It is found that the prescribed Gibbs-Thomson condition at the solid-molten interface leads to mathematical complexity of solving the Stefan problems analytically (Carslaw and Jaeger, 1959; Crank, 1984) so that asymptotic techniques, for example using the large Stefan number (Davis and Hill, 1982; Herrero and Velázquez, 1997; Kucera and Hill, 1986; McCue *et al.*, 2008, 2009) and numerical methods (Crank, 1984; Meyer, 1973; Voller and Cross, 1981), are sought. The existence and uniqueness of certain functions related to phase-change problems are also studied (Ceretani *et al.*, 2020). Moreover, the Gibbs-Thomson condition imposed on the moving boundary poses difficulty on using the Baiocchi transform so that one can not employ the enthalpy method (Meyer, 1973; Voller and Cross, 1981) to tackle the governing equations numerically (McCue *et al.*, 2009). Due to the abundant aforementioned theoretical and numerical methods on solving the two-phase Stefan problems taking into account the surface tension, here, we extend our investigation by observing that such a condition can be naturally absorbed in the weak formulation (Evans, 2010; Roubiček, 2013) of the problem. Therefore, upon using asymptotic matchings, the retreating speed of the moving boundary at the initial and final stages can be estimated without directly solving the governing equations. We find that the initial speed depends linearly on the incoming heat flux at the boundary while the final speed will experience a finite time blowup, which is consistent with the existing literature (Herrero and Velázquez, 1996; McCue *et al.*, 2009).

In order to verify our outcomes, for simplicity, we assume that the solid temperature is constant. As the system is tiny, the molten temperature can reach quasi-stationary states after Δt so that a more complicated diffusion equation can be approximated by solving the Laplace equation at a certain time t (Howison, 2005; Yi, 2005). The molten temperature can then be solved using Eq. (3.1), from which the frontier of the moving boundary can be predicted iteratively by taking into account both the curvature and the surface tension, i.e. Eq. (3.2) by minimizing Eq. (3.3). The present author has successfully employed such methodology to scrutinize the effects of curvature and surface tension on the solidification of micro/nanoparticles, and designs certain smart materials (Gao *et al.*, 2023).

The structure of the present paper is organized as follows: governing equations for the present problem are given in Section 2, followed by a quasi-stationary approximation solution in Section 3. While weak formulations and a brief discussion of the existence of weak solutions are shown in Section 4, asymptotic analysis based on the weak formulations is ultimately made in the final Section.

2. Governing equations

Governing equations for both the molten and solid regimes by assuming axisymmetric micro/nano particles, are given below

$$\begin{aligned} \frac{\partial T_\ell(r,t)}{\partial t} &= \kappa_\ell\Big[\frac{\partial^2 T_\ell(r,t)}{\partial r^2}+\frac{2}{r}\frac{\partial T_\ell(r,t)}{\partial r}\Big] && R<r<a \\ \frac{\partial T_s(r,t)}{\partial t} &= \kappa_s\Big[\frac{\partial^2 T_s(r,t)}{\partial r^2}+\frac{2}{r}\frac{\partial T_s(r,t)}{\partial r}\Big] && 0<r<R \end{aligned} \tag{2.1}$$

where $T_\ell(r,t)$, $T_s(r,t)$, κ_ℓ, κ_s denote the molten temperature, solid temperature, molten thermal diffusivity and solid thermal diffusivity, respectively. For simplicity, we drop (r,t) for $T_\ell(r,t)$ and $T_s(r,t)$. We comment that we investigate the simplest possible model in which no convective and source effects are imposed on the system. The schematic of the present problem is shown in Fig. 1.

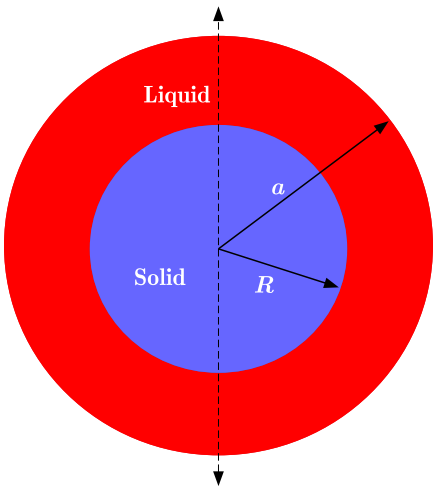

Fig. 1. Schematic diagram of the present melting process where the micro/nano particle is axisymmetric about the double arrow line

To obtain unique solutions of T_ℓ and T_s, both initial and boundary conditions including the Gibbs-Thomson moving boundary condition (Langer, 1980) are applied to give

$$\begin{aligned}
&\text{IC} \quad T_s = T_\ell \quad \text{on} \quad R(t=0) = a \\
&\text{BC} \quad T_\ell = T_a \quad \text{on} \quad r = a \qquad \frac{\partial T_s}{\partial r} = 0 \quad \text{on} \quad r = 0 \\
&\qquad T_\ell = T_s = T_f(R) \quad \text{on} \quad r = R(t) \\
&\text{MBC} \quad k_\ell \frac{\partial T_\ell}{\partial r} - k_s \frac{\partial T_s}{\partial r} = -\rho_\ell \frac{dR(t)}{dt}[(c_\ell - c_s)(T_f(R) - T_m) + L] \quad \text{on} \quad r = R(t)
\end{aligned} \tag{2.2}$$

where k_ℓ, k_s, ρ_ℓ, c_ℓ, c_s, T_f, T_m and L denote the thermal conductivity of the liquid, thermal conductivity of the solid, density of the material, specific heat capacity of the liquid, specific heat capacity of the solid, curvature dependent temperature of the melting point, melting temperature and latent heat, respectively. For simplicity, we drop (t) for $R(t)$. We also note that $T_s \leqslant T_\ell \leqslant T_a$.

In addition, the curvature-dependent melting point, known as the Gibbs-Thomson effect, which basically implies a modification (decrease) of the melting temperature by surface tension, is defined below

$$T_f(R) = T_m\Big(1 - \frac{\omega}{R}\Big) \qquad \omega = \frac{2\sigma}{\rho_s L} \tag{2.3}$$

where σ and ρ_s further denote the interfacial tension coefficient and mass density of the solid, respectively. In addition, capillary pressure is radially dependent due to the term ω/R.

3. Quasi-stationary approximation simulation

To simulate the melting process, instead of solving more complicated diffusion equations, i.e. Eq. (2.1), we adopt a quasi-approximation approach, where we assume that the system and the Peclet number are tiny that it can reach a quasi-stationary state (Howison, 2005) for each time step so that the time evolution of the moving boundary can be updated by simulations (3.4). We assume T_s is constant for all times, which is valid due to the tiny size of particles as well as the satisfaction of Eq. (2.1) as well as the boundary conditions. The aforementioned assumptions will be relaxed in the later Sections. Using separation of variables, we obtain a general solution of T_ℓ, which is given by

$$T_\ell = \mathrm{e}^{\lambda t}\left[\frac{A\sinh\Big(\sqrt{\frac{\lambda}{\kappa_\ell}}r\Big) + B\cosh\Big(\sqrt{\frac{\lambda}{\kappa_\ell}}r\Big)}{r}\right] \tag{3.1}$$

where λ is the separation constant yet to be determined by the boundary conditions. Moreover, λ, A and B are to be obtained from the initial and boundary conditions excluding the moving boundary, which are given below

$$\begin{aligned}
&\frac{A\sinh\Big(\sqrt{\frac{\lambda}{\kappa_\ell}}a\Big) + B\cosh\Big(\sqrt{\frac{\lambda}{\kappa_\ell}}a\Big)}{a} = T_s \\
&\mathrm{e}^{\lambda t}\left[\frac{A\sinh\Big(\sqrt{\frac{\lambda}{\kappa_\ell}}a\Big) + B\cosh\Big(\sqrt{\frac{\lambda}{\kappa_\ell}}a\Big)}{a}\right] = T_a \\
&\mathrm{e}^{\lambda t}\left[\frac{A\sinh\Big(\sqrt{\frac{\lambda}{\kappa_\ell}}R\Big) + B\cosh\Big(\sqrt{\frac{\lambda}{\kappa_\ell}}R\Big)}{R}\right] = T_f(R)
\end{aligned} \tag{3.2}$$

To maintain the compatibility of the first and second equations of Eq. (3.2), we can estimate λ as $\lambda = (1/a)\log(T_a/T_s)$, which makes sense when a temporal change in the molten temperature depends on temperature differences between the embedding environment and solid temperature.

It also depends on how big a micro/nanoparticle is. Therefore, the conditions of Eq. (3.2) reduce from three to two. R is still unresolved, however the moving boundary condition provides an extra condition to save us

$$\min_{0\leqslant R\leqslant a}\left\{\left|k_\ell\frac{\partial T_\ell}{\partial r}+\rho_\ell\frac{a-R}{\Delta t}[(c_\ell-c_s)(T_f(R)-T_m)+L]\right|\right\} \tag{3.3}$$

Now, Eqs. (3.2) and (3.3) can be used to obtain A, B and R. Since multiple solutions are possible, we only select A and B, when R is close to a when a tiny time is chosen. Given that the trace of the moving boundary can be estimated using the modified Euler method taking both the speed and curvature into account

$$R_{n+1}=R_n+\Delta t\frac{dR_n}{dt}+\frac{\Delta t^2}{2!}\frac{d^2R_n}{dt^2} \tag{3.4}$$

where n denotes the number of iterations to trace the moving boundary. We firstly use Eq. (3.4) to simulate the moving boundary of gold microparticles of the size 1 nm using the parameters given in Table 1. In addition, we let $T_s=300\,\mathrm{K}$ and $T_a=2000\,\mathrm{K}$. Using Eqs. (3.2) and (3.3), the coefficients A and B for gold are estimated to be -0.58822 and 0.00124, respectively. From which, we can first estimate $\lambda=0.1897\cdot10^7$. Parameters for Sn and Pb can be found in Table 1. Now, we adopt Eq. (3.4) to simulate the location of the moving boundaries for the proposed metals, where the numerical results are shown in Fig. 2.

Table 1. Parameters for Au, Sn and Pb (McCue *et al.*, 2009)

Parameters	Gold	Sn	Pb
ρ_s	$19.3\cdot10^3\,\mathrm{kg/m^3}$	$7.27\cdot10^3\,\mathrm{kg/m^3}$	$11.34\cdot10^3\,\mathrm{kg/m^3}$
ρ_ℓ	$17.31\cdot10^3\,\mathrm{kg/m^3}$	$6.99\cdot10^3\,\mathrm{kg/m^3}$	$10.66\cdot10^3\,\mathrm{kg/m^3}$
L	63718 J/kg	59225 J/kg	23020 J/kg
T_m	1337.3 K	505.8 K	600.6 K
ω	0.2396 nm	0.4447 nm	0.6847 nm
$\kappa_\ell=k_\ell/(\rho_\ell c_\ell)$	$1.47\cdot10^{-3}\,\mathrm{m^2/s}$	$1.36\cdot10^{-3}\,\mathrm{m^2/s}$	$0.684\cdot10^{-3}\,\mathrm{m^2/s}$
k_ℓ	320 W/(m·K)	67 W/(m·K)	35 W/(m·K)
c_s	0.128 J/gK	0.226 J/gK	0.13 J/gK
c_ℓ	12.55 J/gK	7.029 J/gK	4.799 J/gK

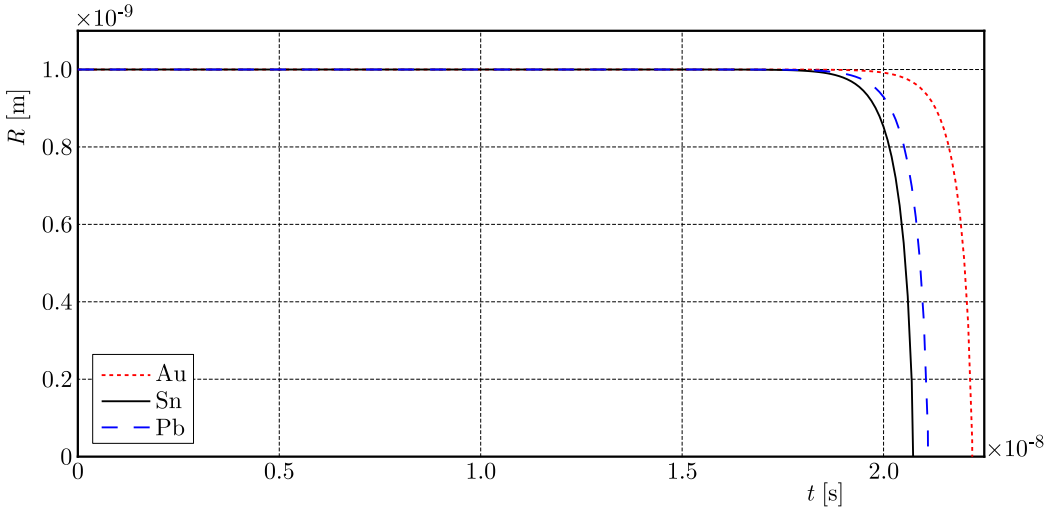

Fig. 2. Melting process for Au, Sn and Pb

We can observe from Fig. 2 that the moving boundaries retreat steadily or initially linearly but accelerate rapidly, even with a blowup after $2\cdot 10^{-8}$ s. Such behavior will be fully scrutinized in Section 5.

4. Weak formulation

A weak formulation forms a basis for seeking weak solutions and the finite element method. In this Section, we determine the weak formulation of Eq. (2.1). Upon multiplying both sides of Eq. (2.1) by $v \in C^{\infty}(I, V)$, where I and V denote the usual temporal and spatial domains, respectively, and upon integrating by parts and applying appropriate boundary conditions at R and a, we obtain

$$\int_R^a \frac{\partial T_\ell}{\partial t} v \, dr = -\kappa_\ell \left(v \frac{\partial T_\ell}{\partial r}\Big|_R + \int_R^a \frac{\partial T_\ell}{\partial r}\frac{\partial v}{\partial r} \, dr - 2\int_R^a \frac{v}{r}\frac{\partial T_\ell}{\partial r} d\, r \right) \tag{4.1}$$

Similarly, we obtain the weak formulation for T_s

$$\int_0^R \frac{\partial T_s}{\partial t} v \, dr = \kappa_s \left(v \frac{\partial T_s}{\partial r}\Big|_R - \int_0^R \frac{\partial T_s}{\partial r}\frac{\partial v}{\partial r} \, dr + 2\int_0^R \frac{v}{r}\frac{\partial T_s}{\partial r} \, dr \right) \tag{4.2}$$

where the weak solutions for Eqs. (4.1) and (4.2) have been thoroughly studied using the coercivity of T_ℓ and T_s, the first temporal derivatives, proper growth conditions and pseudomonotonic or weakly continuous approaches for the nonlinearity (Roubiček, 2013).

5. Asymptotic analysis

Now we relax that T_s is a constant and illustrate the asymptotic behavior of the moving boundary using an energy method as given in the previous Section. Replacing v in Eqs. (4.1) and (4.2) by T_ℓ and T_s, respectively, we obtain

$$\begin{aligned} \frac{1}{2}\frac{\partial}{\partial t}\|T_\ell\|^2_{L^2(R)} &= -\kappa_\ell \left(T_f(R)\frac{\partial T_\ell}{\partial r}\Big|_R + \|T_\ell\|^2_{H^1(R)} - 2\int_R^a \frac{T_\ell}{r}\frac{\partial T_\ell}{\partial r} \, dr \right) \\ \frac{1}{2}\frac{\partial}{\partial t}\|T_s\|^2_{L^2(R)} &= \kappa_s \left(T_f(R)\frac{\partial T_s}{\partial r}\Big|_R - \|T_s\|^2_{H^1(R)} + 2\int_0^R \frac{T_s}{r}\frac{\partial T_s}{\partial r} \, dr \right) \end{aligned} \tag{5.1}$$

where we have used the boundary conditions that $T_\ell = T_s = T_f(R)$ on $r = R(t)$ to obtain Eq. (5.1). For simplicity, we have dropped the notation of temporal and spatial domains. The values in $H(\cdot)$ denote the integration limit for integrals in Eqs. (4.1) and (4.2), where $R \in [0, a]$.

— In the **initial stage**, since the molten state is completely absent, we have

$$\frac{1}{2}\frac{\partial}{\partial t}\|T_s\|^2_{L^2(a)} = \kappa_s \left(T_f(a)\frac{\partial T_s}{\partial r}\Big|_a - \|T_s\|^2_{H^1(a)} + 2\int_0^a \frac{T_s}{r}\frac{\partial T_s}{\partial r} \, dr \right) \tag{5.2}$$

— In the **final stage**, since the condensed state is completely absent, we have

$$\frac{1}{2}\frac{\partial}{\partial t}\|T_\ell\|^2_{L^2(0)} = -\kappa_\ell \left(T_f(0)\frac{\partial T_\ell}{\partial r}\Big|_0 + \|T_\ell\|^2_{H^1(0)} - 2\int_0^a \frac{T_\ell}{r}\frac{\partial T_\ell}{\partial r} \, dr \right) \tag{5.3}$$

— In the **intermediate stage**, both the solid and molten stages coexist so that by using Eq. (5.1) the change in total kinetic energies for both the solid and molten regimes is obtained

$$\begin{aligned}
&\frac{1}{2}\frac{\partial}{\partial t}\Big(\|T_\ell\|^2_{L^2(R)}+\|T_s\|^2_{L^2(R)}\Big)=-T_f(R)\bigg[\kappa_\ell\frac{\partial T_\ell}{\partial r}\Big|_R-\kappa_s\frac{\partial T_s}{\partial r}\Big|_R\bigg]\\
&\quad-\kappa_\ell\|T_\ell\|^2_{H^1(R)}-\kappa_s\|T_s\|^2_{H^1(R)}+2\bigg(\kappa_s\int_0^R\frac{T_s}{r}\frac{\partial T_s}{\partial r}\,dr+\kappa_\ell\int_R^a\frac{T_\ell}{r}\frac{\partial T_\ell}{\partial r}\,dr\bigg)\\
&\quad\approx-T_f(R)\rho_\ell\frac{dR}{dt}\Big[(c_\ell-c_s)\Big(\frac{T_m\omega}{R}\Big)-L\Big]-\kappa_\ell\|T_\ell\|^2_{H^1(R)}-\kappa_s\|T_s\|^2_{H^1(R)}\\
&\quad+2\bigg(\kappa_s\int_0^R\frac{T_s}{r}\frac{\partial T_s}{\partial r}\,dr+\kappa_\ell\int_R^a\frac{T_\ell}{r}\frac{\partial T_\ell}{\partial r}\,dr\bigg)
\end{aligned}\tag{5.4}$$

where we have assumed $\kappa_\ell\approx k_\ell$ and $\kappa_s\approx k_s$ (or else if there are linear relations between thermal diffusivities and conductivities). We comment that there is a common relation between them for simple metals, i.e. $\kappa_i=k_i/(\rho_i c_i)$, where $i=s,\ell$ (McCue *et al.*, 2009), and the moving boundary condition is imposed in the second equation of Eq. (5.4). We might make rather restrictive assumptions here for mathematical convenience as we can yield dR/dt and make certain simplifications using the moving boundary condition as given in Eq. (2.2). Now, the asymptotic speed of the moving boundary condition can be matched with the melting speeds of the initial and final stages.

— In the **nearly initial stage**, upon ignoring T_ℓ, Eq. (5.4) becomes

$$\begin{aligned}
&\frac{1}{2}\frac{\partial}{\partial t}\|T_s\|^2_{L^2(a)}=-T_f(a)\rho_\ell\frac{dR}{dt}\Big[(c_\ell-c_s)\Big(\frac{T_m\omega}{a-\varepsilon}\Big)-L\Big]-\kappa_s\|T_s\|^2_{H^1(a)}+2\kappa_s\int_0^{a-\varepsilon}\frac{T_s}{r}\frac{\partial T_s}{\partial r}\,dr\\
&\quad\approx-T_f(a)\rho_\ell\frac{dR}{dt}\Big[\frac{(c_\ell-c_s)T_m\omega}{a}\Big(1+\frac{\varepsilon}{a}\Big)-L\Big]-\kappa_s\|T_s\|^2_{H^1(a)}\\
&\quad+2\kappa_s\int_0^a\frac{T_s}{r}\frac{\partial T_s}{\partial r}\,dr+O(\varepsilon^2)
\end{aligned}\tag{5.5}$$

where ε denotes an infinitesimal positive number. Now comparing Eq. (5.5) with Eq. (5.2), we obtain

$$\frac{dR}{dt}=-\frac{\kappa_s a}{\rho_\ell}\Big[\frac{1}{(c_\ell-c_s)T_m\omega-aL}\Big]\frac{\partial T_s}{\partial r}\Big|_a+O(\varepsilon)\tag{5.6}$$

Hence, the melting speed is linearly proportional to the heat flux across the boundary. We comment that in this formulation, whether the initial temperature is fusion or not, (Kucera and Hill, 1986) it is not crucial.

— In the **nearly melting stage**, upon ignoring T_s and matching Eq. (5.4) with Eq. (5.3), we obtain

$$\frac{dR}{dt}=\frac{\kappa_\ell}{\rho_\ell}\Big[(c_\ell-c_s)\frac{T_m\omega}{\varepsilon}-L\Big]^{-1}\frac{\partial T_\ell}{\partial r}|_\varepsilon\tag{5.7}$$

where the melting speed blows up when

$$\varepsilon^*=\frac{(c_\ell-c_s)T_m\omega}{L}\tag{5.8}$$

Hence, we can observe from Eq. (5.8) that no blowup is observed when the surface tension is zero happening in the macroscopic melting problems. Figure 2 confirms the linear correlation with the temperature flux and the blowup in the initial and final stages, respectively. ε^* is $0.62466 \cdot 10^{-10}$ m, $0.25837 \cdot 10^{-10}$ m and $0.83407 \cdot 10^{-10}$ m for Au, Sn and Pb, respectively, which partially agrees with Fig. 2, where Sn supposes to melt the slowest but it melts the fastest simply due to the fact that we neglect the heat transfer in the sold regime when we conduct the quasi-stationary approach.

6. Conclusion

Using the weak formulation of the Stefan problem and asymptotic matchings, we find that the retreating speed of the moving boundary of spherical micro/nanoparticles depends initially linearly on the incoming heat flux but blows up in the finite time at the latter stage without solving the original equations. No boundary problem occurs as the boundary conditions are absorbed naturally in the weak formulation. Such techniques can be employed to two and multi-phase change problems. A quasi-stationary approximation has also been employed to verify the claims of our theoretical results.

Acknowledgements

This research was financially supported by Shenzhen Basic Research Program under Grant No. JCYJ20190808144813101, Shenzhen High-end Talent Scheme under Grant No. 827/000567, Shenzhen University Starting Up Fund Grant No. 860/000002110377 and Shenzhen University Key Project Grant No. 860-000002081303.

References

1. Buffat P.A., Borel J.P., 1976, Size effect on the melting temperature of gold particles, *Physical Review A*, **13**, 2287-2298
2. Carslaw H.S., Jaeger J.C., 1959, *Conduction of Heat in Solids*, Clarendon, Oxford
3. Ceretani A.N., Salva N.N., Tarzia D.A., 2020, Auxiliary functions in the study of Stefan-like problems with variable thermal properties, *Applied Mathematics Letters*, **104**, 106204
4. Crank J., 1984, *Free and Moving Boundary Problems*, Clarendon, Oxford
5. Davis G.B., Hill J.M., 1982, A moving boundary problem for the sphere, *IMA Journal of Applied Mathematics*, **29**, 99-111
6. Evans L.C., 2010, *Nonlinear Partial Differential Equations*, American Mathematical Society, Berkeley
7. Gao J., Chan Y., Hou T., Ren Y., 2023, Quasi-equilibrium approximation of the solidification process for micro phase change materials taking into account curvature and surface tension, *International Journal of Thermal Sciences*, **184**, 107916
8. Herrero M.A., Velázquez J.J.L., 1996, Singularity formation in the one-dimensional supercooled Stefan problem, *European Journal of Applied Mathematics*, **7**, 119-150
9. Herrero M.A., Velázquez J.J.L., 1997, On the melting of ice balls, *SIAM Journal on Mathematical Analysis*, **28**, 1-32
10. Howison S., 2005, *Practical Applied Mathematics*, Cambridge University Press
11. Kucera A., Hill J.M., 1986, On inward solidifying cylinders and spheres initially not at their fusion temperature, *International Journal of Non-Linear Mechanics*, **21**, 73-82

12. Langer J.S., 1980, Instabilities and pattern formation in crystal growth, *Reviews of Modern Physics*, **52**, 81-94

13. McCue S.W., Wu B., Hill J.M., 2008, Classical two-phase Stefan problem for spheres, *Proceedings of the Royal Society A*, **464**, 2055-2076

14. McCue S.W., Wu B., Hill J.M., 2009, Micro/nanoparticle melting with spherical symmetry and surface tension, *IMA Journal of Applied Mathematics*, **74**, 439-457

15. Meyer G.H., 1973, Multidimensional Stefan problems, *SIAM Journal on Numerical Analysis*, **10**, 522-538

16. Roubiček T., 2013, *Nonlinear Partial Differential Equations with Applications*, Birkhauser, Basel

17. Voller V., Cross M., 1981, Accurate solutions of moving boundary problems using the enthalpy method, *International Journal of Heat and Mass Transfer*, **24**, 545-556

18. Yi F., 2005, Global classical solution of quasi-stationary Stefan free boundary problem, *Applied Mathematics and Computation*, **160**, 797-817

Manuscript received February 15, 2023; accepted for print March 29, 2023

JOURNAL OF THEORETICAL AND APPLIED MECHANICS
61, 3, pp. 427-439, Warsaw 2023
https://doi.org/10.15632/jtam-pl/165949

STUDY ON THE ISOLATION EFFECT OF A COMPOSITE MULTILAYER WAVE IMPEDING BLOCK ON THE *S*-WAVE IN AN UNSATURATED FOUNDATION

Ye Jiang
School of Civil Engineering, Qinghai University, Xining, China
Qiang Ma, Yan-Hong Bao
School of Civil Engineering, Qinghai University, Xining, China, and
Qinghai Provincial Key Laboratory of Energy-Saving Building Materials and Engineering Safety, Xining, China
corresponding author Qiang Ma, e-mail: maqiang0104@163.com

The traditional wave impeding block (WIB) is improved to a composite multilayer WIB with the same thickness (tri-layer as an example). Firstly, a physical model of the composite multilayer WIB installed in an unsaturated foundation is established, and the isolation effect on the *S*-wave is studied based on the wave theory in unsaturated porous and elastic media. The purpose of this study is to enhance the isolation frequency of WIB and to show the best isolation effect achieved by selecting the appropriate wave impedance ratio. The influence of saturation on its vibration isolation effect is also analyzed.

Keywords: unsaturated foundation, composite multilayer WIB, environmental vibration isolation

1. Introduction

With the rapidly developing industry and transportation, while improving people's living quality, artificial vibration problems caused by various industrial activities and traffic operations seriously impact structures, precision instruments, and people's normal lives. Therefore, it is of great practical significance to study vibration damping and isolation measures for unsaturated foundations under environmental vibration.

There is no wave propagation in soil when the excitation frequency is lower than the cut-off frequency. In this principle, Chouw *et al.* (1991a,b) was first to propose that a hard interlayer installed in the foundation forms a finite size artificial bedrock for vibration isolation, which is named the wave impeding block (WIB). Yang and Hung (1997) compared the vibration isolation effect of an open trench and WIB under a moving load in an elastic foundation. The results showed that WIB has a better vibration isolation effect. Takemiya and Jiang (1993) established a numerical model of WIB vibration isolation and found that WIB had a better vibration isolation effect at a low frequency below 15.3 Hz. Li *et al.* (2011) compared the vibration isolation effect of the entity wave impeding block (EWIB) and the honeycomb wave impeding block (HWIB) in the elastic foundation and concluded that HWIB had a better vibration isolation effect. But EWIB was more effective for low-frequency vibration at 0-10 Hz. Zhou *et al.* (2016) and Ma *et al.* (2019) investigated the ground vibration control with a fluid-saturated porous WIB and graded WIB, and the results showed that the two types of WIB were superior than a single-phase traditional WIB. Tian *et al.* (2019) and Gao *et al.* (2021) investigated the vibration isolation effect of Duxseal materials in 2D homogeneous elastic foundations and proposed the method of combined vibration isolation by filling Duxseal in the WIB. The results showed that DXWIB could improve the frequency bandwidth of vibration damping, and the vibration isolation effect

was better in the range of 5-70 Hz. However, although the above-mentioned studies show that a non-homogeneous WIB can improve the vibration isolation efficiency and performance compared with the conventional WIB, these studies treat the foundation as an elastic or saturated two--phase medium to simplify the complex dynamic problem, which is far from actual engineering.

In the actual engineering, most of foundations are unsaturated soils, and the variation of saturation has a significant influence on vibration wave propagation characteristics. Vibration control measures for unsaturated foundations need to be further studied. Therefore, Shu and Ma (2022) and Shu *et al.* (2022) investigated propagation characteristics of the P_1-wave passing through a single-layer and multilayer WIB in unsaturated foundations, respectively, and the results showed that the wave impedance ratio, shear modulus and density of the WIB material had a significant influence on the transmission and reflection amplitude ratio. Jiang and Ma (2022) investigated the vibration isolation performance of a single-layer WIB in an unsaturated foundation under S-wave incidence. The findings showed that the vibration isolation effect of WIB increased with an increase in saturation, and the single-layer WIB failed to isolate the middle and high frequencies. To enhance the frequency range for vibration isolation of WIB in the unsaturated foundation, according to the literature (Sun and Li, 2011), it is known that the more significant the difference between the interfaces of multilayer and thin-layer, the more significant the vibration wave transmission and reflection effect. Hence, this paper proposes an innovative vibration isolation system with a composite multilayer WIB as a barrier. Based on the wave propagation theory in an unsaturated porous medium and a single-phase elastic medium, and Snell's theorem, the vibration isolation performance of the composite multilayer WIB in the unsaturated foundation under the S-wave incidence is investigated. The analytical solution of the surface vertical displacement after the S-wave incident from the bedrock to the unsaturated soil through the composite multilayer WIB is derived. According to numerical calculations, the influence of the wave impedance ratio at the interface between the unsaturated soil and WIB and that between the layers of composite multilayer WIB on its vibration isolation effect were analyzed, and the isolation effect of single-layer and composite multilayer WIB installed in the unsaturated foundation were compared. The influence laws of various parameters such as the incidence angle, incidence frequency and saturation on the vibration isolation effect of the composite multilayer WIB in the unsaturated foundation were analyzed, thereby providing a guideline for the application of the composite multilayer WIB vibration isolation in unsaturated foundations.

2. Wave equation in unsaturated porous media

This paper is based on the mixture theory of unsaturated porous media (Borja, 2006; Chen *et al.*, 2011). The wave equation of a triphase solid-liquid-gas is expressed as follows. The solid, liquid and gas phases in unsaturated soil layers are indicated by subscripts: S, L and G, respectively

$$\begin{aligned}
&n^S\rho^S\ddot{\varphi}^S = (\gamma_{SS}+n^S\lambda_S+2n^S\mu_S)\nabla^2\varphi_S+\gamma_{SL}\nabla^2\varphi_L+\gamma_{SG}\nabla^2\varphi_G\\
&\quad +\xi_L(\dot{\varphi}_L-\dot{\varphi}_S)+\xi_G(\dot{\varphi}_G-\dot{\varphi}_S)\\
&n^L\rho^L\ddot{\varphi}^L = \gamma_{SL}\nabla^2\varphi_S+\gamma_{LL}\nabla^2\varphi_L+\gamma_{LG}\nabla^2\varphi_G-\xi_L(\dot{\varphi}_L-\dot{\varphi}_S)\\
&n^G\rho^G\ddot{\varphi}^G = \gamma_{SG}\nabla^2\varphi_S+\gamma_{LG}\nabla^2\varphi_L+\gamma_{GG}\nabla^2\varphi_G-\xi_G(\dot{\varphi}_G-\dot{\varphi}_S)\\
&n^S\rho^S\ddot{\psi}_S = n^S\mu_S\nabla^2\psi_S+\xi_L(\dot{\psi}_L-\dot{\psi}_S)+\xi_G(\dot{\psi}_G-\dot{\psi}_S)\\
&n^L\rho^L\ddot{\psi}_L = -\xi_L(\dot{\psi}_L-\dot{\psi}_S)+\xi_G(\dot{\psi}_G-\dot{\psi}_S)\\
&n^G\rho^G\ddot{\psi}_G = -\xi_G(\dot{\psi}_G-\dot{\psi}_S)
\end{aligned} \tag{2.1}$$

where n^α (throughout this paper, the character $\alpha = S, L, G$) indicates the initial volume occupied by the α phase. ρ^α denotes the actual mass density of the α phase. ∇^2 represents the Laplace

operator in the Cartesian coordinate. The expressions of γ_{SS}, γ_{LL}, γ_{GG}, γ_{SL}, γ_{SG} and γ_{LG} are given in the literature (Chen *et al.*, 2011). ξ_L and ξ_G are the drag force parameters representing the viscous dissipation between the fluids (liquid and gas) and the solid skeleton, respectively.

The general solutions to Eqs. (2.1) are assumed to be

$$\varphi_\alpha = A_\alpha \exp[\mathrm{i}k_p(lx + nz - c_p t)] \qquad \psi_\alpha = B_\alpha \exp[\mathrm{i}k_s(lx + nz - c_s t)] \tag{2.2}$$

where $\mathrm{i} = \sqrt{-1}$. l and n denote the direction vectors of the respective waves. k_p and k_s are the wave numbers of the P-waves and the SV-wave. c_p and c_s are the phase velocities of the P-waves and the SV-wave, respectively.

Substituting Eqs. (2.2) into Eqs. (2.1), the P_1-, P_2-, P_3- and SV-wave velocities in an unsaturated foundation can be obtained.

3. Physical model

The horizontal semi-infinite bedrock is covered by an unsaturated soil layer whose thickness is H. A composite multilayer WIB whose thickness is $H_{w1} + H_{w2} + H_{w3}$ and burial depth H_2 is embedded in the unsaturated foundation. Assuming that the S-wave with frequency ω is incident at any angle φ to the WIB in the unsaturated foundation, the transmission and reflection are shown in Fig. 1.

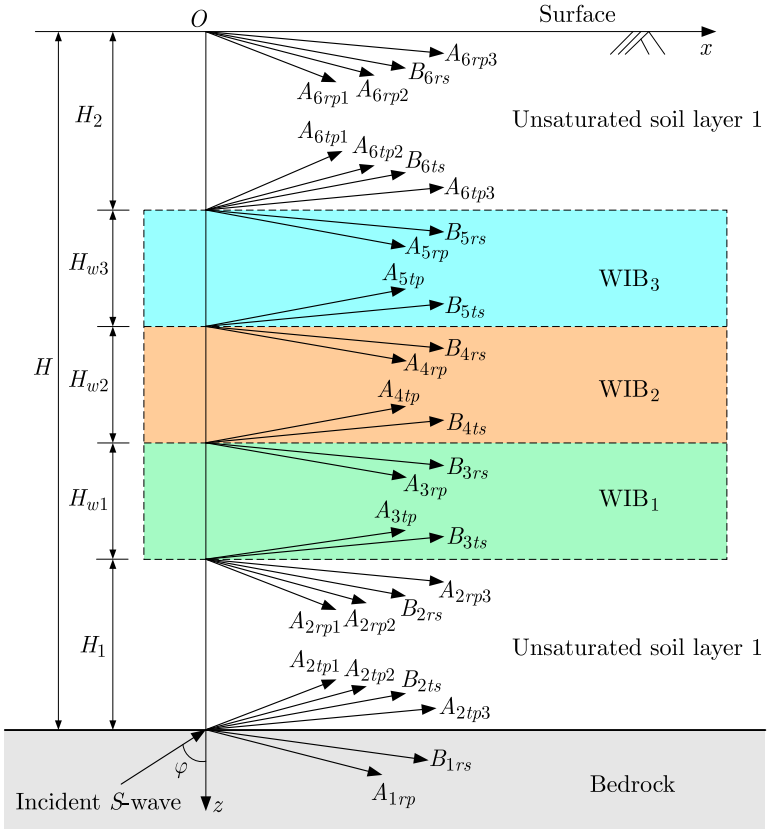

Fig. 1. Propagation of the S-wave when setting the composite multilayer WIB in an unsaturated foundation

4. Analysis of the total wavefield

The bedrock and composite multilayer WIB are simulated with a single-phase elastic medium, and the unsaturated foundation is simulated with an unsaturated porous medium. The wave field in the two-dimensional xz-plane is obtained as we can obtain one compressional wave: P-wave and one shear wave: SV-wave in the single-phase medium, and three compressional: P_1-, P_2- and P_3-waves as well as one shear: SV-wave in the unsaturated porous medium.

4.1. Wave potential functions

The displacement potential functions of the up-going and down-going waves can be indicated as below.

(1) In the bedrock

$$\begin{aligned}\varphi_1^e &= A_{1rp}\exp[\mathrm{i}(\omega t - k_{1rpx}x - k_{1rpz}z)]\\ \psi_1^e &= B_{1is}\exp[\mathrm{i}(\omega t - k_{1isx}x + k_{1isz}z)] + B_{1rs}\exp[\mathrm{i}(\omega t - k_{1rsx}x - k_{1rsz}z)]\end{aligned} \tag{4.1}$$

(2) In unsaturated soil layers I and II

The solid phase can be indicated as

$$\begin{aligned}\mathrm{I}:&\begin{cases}\varphi_2^S = \sum\limits_{i=1}^{3}\Big\{A_{2tpi}\exp[\mathrm{i}(\omega t - k_{2tpix}x + k_{2tpiz}z)] + A_{2rpi}\exp[\mathrm{i}(\omega t - k_{2rpix}x - k_{2rpiz}z)]\Big\}\\ \psi_2^S = B_{2ts}\exp[\mathrm{i}(\omega t - k_{2tsx}x + k_{2tsz}z)] + B_{2rs}\exp[\mathrm{i}(\omega t - k_{2rsx}x - k_{2rsz}z)]\end{cases}\\ \mathrm{II}:&\begin{cases}\varphi_6^S = \sum\limits_{i=1}^{3}\Big\{A_{6tpi}\exp[\mathrm{i}(\omega t - k_{6tpix}x + k_{6tpiz}z)] + A_{6rpi}\exp[\mathrm{i}(\omega t - k_{6rpix}x - k_{6rpiz}z)]\Big\}\\ \psi_6^S = B_{6ts}\exp[\mathrm{i}(\omega t - k_{6tsx}x + k_{6tsz}z)] + B_{6rs}\exp[\mathrm{i}(\omega t - k_{6rsx}x - k_{6rsz}z)]\end{cases}\end{aligned} \tag{4.2}$$

The liquid and gas phases can be indicated as

$$\begin{aligned}\mathrm{I}:&\begin{cases}\varphi_2^F = \sum\limits_{i=1}^{3}\delta_{Fi}^{\mathrm{I}}\Big\{A_{2tpi}\exp[\mathrm{i}(\omega t - k_{2tpix}x + k_{2tpiz}z)] + A_{2rpi}\exp[\mathrm{i}(\omega t - k_{2rpix}x - k_{2rpiz}z)]\Big\}\\ \psi_2^F = \delta_{FS}^{\mathrm{I}}\Big\{B_{2ts}\exp[\mathrm{i}(\omega t - k_{2tsx}x + k_{2tsz}z)] + B_{2rs}\exp[\mathrm{i}(\omega t - k_{2rsx}x - k_{2rsz}z)]\Big\}\end{cases}\\ \mathrm{II}:&\begin{cases}\varphi_6^F = \sum\limits_{i=1}^{3}\delta_{Fi}^{\mathrm{II}}\Big\{A_{6tpi}\exp[\mathrm{i}(\omega t - k_{6tpix}x + k_{6tpiz}z)] + A_{6rpi}\exp[\mathrm{i}(\omega t - k_{6rpix}x - k_{6rpiz}z)]\Big\}\\ \psi_6^F = \delta_{FS}^{\mathrm{II}}\Big\{B_{6ts}\exp[\mathrm{i}(\omega t - k_{6tsx}x + k_{6tsz}z)] + B_{6rs}\exp[\mathrm{i}(\omega t - k_{6rsx}x - k_{6rsz}z)]\Big\}\end{cases}\end{aligned} \tag{4.3}$$

(3) In the WIB_1, WIB_2 and WIB_3

$$\begin{aligned}\mathrm{WIB}_1:&\begin{cases}\varphi_3^{w1} = A_{3tp}\exp[\mathrm{i}(\omega t - k_{3tpx}x + k_{3tpz}z)] + A_{3rp}\exp[\mathrm{i}(\omega t - k_{3rpx}x - k_{3rpz}z)]\\ \psi_3^{w1} = B_{3ts}\exp[\mathrm{i}(\omega t - k_{3tsx}x + k_{3tsz}z)] + B_{3rs}\exp[\mathrm{i}(\omega t - k_{3rsx}x - k_{3rsz}z)]\end{cases}\\ \mathrm{WIB}_2:&\begin{cases}\varphi_4^{w2} = A_{4tp}\exp[\mathrm{i}(\omega t - k_{4tpx}x + k_{4tpz}z)] + A_{4rp}\exp[\mathrm{i}(\omega t - k_{4rpx}x - k_{4rpz}z)]\\ \psi_4^{w2} = B_{4ts}\exp[\mathrm{i}(\omega t - k_{4tsx}x + k_{4tsz}z)] + B_{4rs}\exp[\mathrm{i}(\omega t - k_{4rsx}x - k_{4rsz}z)]\end{cases}\\ \mathrm{WIB}_3:&\begin{cases}\varphi_5^{w3} = A_{5tp}\exp[\mathrm{i}(\omega t - k_{5tpx}x + k_{5tpz}z)] + A_{5rp}\exp[\mathrm{i}(\omega t - k_{5rpx}x - k_{5rpz}z)]\\ \psi_5^{w3} = B_{5ts}\exp[\mathrm{i}(\omega t - k_{5tsx}x + k_{5tsz}z)] + B_{5rs}\exp[\mathrm{i}(\omega t - k_{5rsx}x - k_{5rsz}z)]\end{cases}\end{aligned} \tag{4.4}$$

where the superscript e indicates the bedrock, $\delta_{Fi}^{\mathrm{I,II}}$ $(i = 1, 2, 3)$ are the three compression wave participation parameters of the F phase. $\delta_{FS}^{\mathrm{I,II}}$ is the shear wave participation parameters of the

F phase. The subscripts i, t and r refer to quantities corresponding to the incidence, transmission and reflection, respectively. k_{1ipx}, k_{1rpx}, k_{2tpix}, k_{2rpix}, k_{2tsx}, k_{2rsx}, k_{3tpx}, k_{3rpx}, k_{3tsx}, k_{3rsx}, k_{4tpx}, k_{4rpx}, k_{4tsx}, k_{4rsx}, k_{5tpx}, k_{5rpx}, k_{5tsx}, k_{5rsx}, k_{6tpix}, k_{6rpix}, k_{6tsx}, k_{6rsx} are the waves mentioned above that must have equal wave numbers in the x-direction, respectively. The Snell law describing the relations between the angles of incidence, reflection and transmission are given by

$$\begin{aligned} k_{1isx} &= k_{1rpx} = k_{1rsz} = k_{2tpix} = k_{2rpix} = k_{2tsx} = k_{2rsx} = k_{6tpix} = k_{6rpix} \\ &= k_{6tsx} = k_{6rsx} = k_x = k_s \sin\varphi \end{aligned} \tag{4.5}$$

4.2. Boundary conditions

The amplitudes A_{1rp}, B_{1rs}, A_{2tpi}, A_{2rpi}, B_{2ts}, B_{2rs}, A_{3tp}, A_{3rp}, B_{3ts}, B_{3rs}, A_{4tp}, A_{4rp}, B_{4ts}, B_{4rs}, A_{5tp}, A_{5rp}, B_{5ts}, B_{5rs}, A_{6tpi}, A_{6rpi}, B_{6ts}, B_{6rs} can be determined by boundary conditions at the interfaces. The boundary conditions of interfaces are: continuities of normal stresses, tangential stress, normal displacements and tangential displacement.

— At the interface between the bedrock and unsaturated soil layer I

$$\begin{aligned} &\sigma^e_{zz}\Big|_{z=H} = \sigma^S_{zz\mathrm{I}}\Big|_{z=H} + \sigma^L_{zz\mathrm{I}}\Big|_{z=H} + \sigma^G_{zz\mathrm{I}}\Big|_{z=H} \qquad \sigma^e_{xz}\Big|_{z=H} = \sigma^S_{xz\mathrm{I}}\Big|_{z=H} \\ &u^e_z\Big|_{z=H} = u^S_{z\mathrm{I}}\Big|_{z=H} = u^L_{z\mathrm{I}}\Big|_{z=H} = u^G_{z\mathrm{I}}\Big|_{z=H} \qquad u^e_x\Big|_{z=H} = u^S_{x\mathrm{I}}\Big|_{z=H} \end{aligned} \tag{4.6}$$

— At the interface between WIB_1 and unsaturated soil layer I

$$\begin{aligned} &\sigma^{w1}_{zz}\Big|_{z=H-H_1} = \sigma^S_{zz\mathrm{I}}\Big|_{z=H-H_1} + \sigma^L_{zz\mathrm{I}}\Big|_{z=H-H_1} + \sigma^G_{zz\mathrm{I}}\Big|_{z=H-H_1} \qquad \sigma^{w1}_{xz}\Big|_{z=H-H_1} = \sigma^S_{xz\mathrm{I}}\Big|_{z=H-H_1} \\ &u^{w1}_z\Big|_{z=H-H_1} = u^S_{z\mathrm{I}}\Big|_{z=H-H_1} = u^L_{z\mathrm{I}}\Big|_{z=H-H_1} = u^G_{z\mathrm{I}}\Big|_{z=H-H_1} \qquad u^{w1}_x\Big|_{z=H-H_1} = u^S_{x\mathrm{I}}\Big|_{z=H-H_1} \end{aligned} \tag{4.7}$$

— At the interface between WIB_1 and WIB_2

$$\begin{aligned} &\sigma^{w2}_{zz}\Big|_{z=H_2+H_{w2}+H_{w3}} = \sigma^{w1}_{zz}\Big|_{z=H_2+H_{w2}+H_{w3}} \qquad \sigma^{w2}_{xz}\Big|_{z=H_2+H_{w2}+H_{w3}} = \sigma^{w1}_{xz}\Big|_{z=H_2+H_{w2}+H_{w3}} \\ &u^{w2}_z\Big|_{z=H_2+H_{w2}+H_{w3}} = u^{w1}_z\Big|_{z=H_2+H_{w2}+H_{w3}} \qquad u^{w2}_x\Big|_{z=H_2+H_{w2}+H_{w3}} = u^{w1}_x\Big|_{z=H_2+H_{w2}+H_{w3}} \end{aligned} \tag{4.8}$$

— At the interface between WIB_2 and WIB_3

$$\begin{aligned} &\sigma^{w3}_{zz}\Big|_{z=H_2+H_{w3}} = \sigma^{w2}_{zz}\Big|_{z=H_+H_{w3}} \qquad \sigma^{w3}_{xz}\Big|_{z=H_2+H_{w2}+H_{w3}} = \sigma^{w2}_{xz}\Big|_{z=H_2+H_{w3}} \\ &u^{w3}_z\Big|_{z=H_2+H_{w3}} = u^{w2}_z\Big|_{z=H_2+H_{w3}} \qquad u^{w3}_x\Big|_{z=H_2+H_{w3}} = u^{w2}_x\Big|_{z=H_2+H_{w3}} \end{aligned} \tag{4.9}$$

— At the interface between WIB_3 and unsaturated soil layer II

$$\begin{aligned} &\sigma^{w3}_{zz}\Big|_{z=H_2} = \sigma^S_{zz\mathrm{II}}\Big|_{z=H_2} + \sigma^L_{zz\mathrm{II}}\Big|_{z=H_2} + \sigma^G_{zz\mathrm{II}}\Big|_{z=H_2} \qquad \sigma^{w3}_{xz}\Big|_{z=H_2} = \sigma^S_{xz\mathrm{II}}\Big|_{z=H_2} \\ &u^{w3}_z\Big|_{z=H_2} = u^S_{z\mathrm{II}}\Big|_{z=H_2} = u^L_{z\mathrm{II}}\Big|_{z=H_2} = u^G_{z\mathrm{II}}\Big|_{z=H_2} \qquad u^{w3}_x\Big|_{z=H_2} = u^S_{x\mathrm{II}}\Big|_{z=H_2} \end{aligned} \tag{4.10}$$

— At the free surface ($z = 0$)

$$\sigma^S_{zz\mathrm{II}}\Big|_{z=0} = \sigma^L_{zz\mathrm{II}}\Big|_{z=0} = \sigma^G_{zz\mathrm{II}}\Big|_{z=0} = \sigma^S_{xz\mathrm{II}}\Big|_{z=0} = 0 \tag{4.11}$$

With the introduction of a potential function, where the expressions of the potential function are detailed in the literature (Jiang and Ma, 2022), the linear systems can be obtained by substituting Eqs. (4.1)-(4.4) into Eqs. (4.6)-(4.11) and Snell law (4.5) as follows

$$\mathbf{MN} = B_{1is}\mathbf{Q} \tag{4.12}$$

where $\mathbf{M}$ is the coefficient matrix of wave amplitudes in $\mathbf{N}$, $\mathbf{Q}$ is the coefficient matrix of wave amplitude of the incident S-wave, and

$$\mathbf{N} = \left[A_{1rp}, B_{1rs}, A_{2tpi}, B_{2ts}, A_{2rpi}, B_{2rs}, A_{3tp}, B_{3ts}, A_{3rp}, B_{3rs}, A_{4tp}, B_{4ts}, A_{4rp}, B_{4rs}, A_{5tp}, B_{5ts}, A_{5rp}, B_{5rs}, A_{6tpi}, B_{6ts}, A_{6rpi}, B_{6rs}\right]^{\mathrm{T}}$$

Supposing $B_{1is} = 1$, the values of the elements in the matrix $\mathbf{N}$ can be derived, thereby the displacements and stresses at each point in the wavefield can be calculated. This work mainly considers the vertical displacement at the surface, which can be obtained by substituting Eqs. (4.2) into the potential function

$$u_z = \left| \sum_{j=1}^{3} (k_{6tpjz} A_{6tpj} - k_{6rpjz} A_{6rpj}) - k_{6tsx} B_{6ts} - k_{6rsx} B_{6rs} \right| \tag{4.13}$$

5. Numerical analysis

5.1. Model verification

The ground motion of the unsaturated soil layer-bedrock system excited by the S-wave, as investigated by Li *et al.* (2018), is chosen to verify the accuracy of this work. Taking the parameters consistent with the literature (Li *et al.*, 2018), variation curves of the surface vertical displacement amplification coefficient with the S-wave angle of incidence for $n = 0.3$, $Sr = 0.8$ and $\omega/\omega_1 = 1.0$ are plotted in Fig. 2. It is shown in Fig. 2 that the present solution is in good consistency with the literature solution, which verifies the validity of the present method.

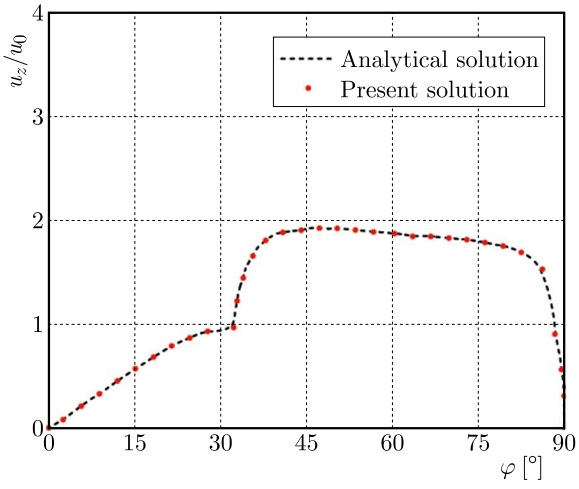

Fig. 2. Comparison between the solution of this paper and the solution from literature

5.2. Effect of the wave impedance ratio on the isolation capacity of a composite multilayer WIB

In this Section, MATLAB is used to analyze the effect of interlayers wave impedance ratio between WIB_1 and unsaturated soil, WIB_1 and WIB_2, and WIB_2 and WIB_3 on the surface

displacement. The physical parameters were selected from the literature (Chen *et al.*, 2011), the parameters of the unsaturated foundation are shown in Table 1 and the parameters of the bedrock and composite multilayer WIB are shown in Table 2.

Table 1. Physical and mechanical parameters of the unsaturated porous medium

Material parameters	Porosity	Density of			Bulk modulus of		
		soil particle	liquid	gas	soil particle	liquid	gas
Symbol [unit]	n [–]	ρ_S [kg/m^3]	ρ_L [kg/m^3]	ρ_G [kg/m^3]	K_S [GPa]	K_L [GPa]	K_G [MPa]
Magnitude	0.3	2700	1000	1.2	35	2.2	0.1

Material parameters	Intrinsic permeabil. of the soil	Viscosity coefficient of liquid	Viscosity coefficient of gas	Lamé constant	Lamé constant	Van Genuchten parameter	Van Genuchten parameter
Symbol [unit]	k [m^2]	η^L [Pa·s]	η^G [Pa·s]	λ_S [GPa]	μ_S [GPa]	m_{vg} [–]	α_{vg} [Pa^{-1}]
Magnitude	$3.0 \cdot 10^{-13}$	0.001	$1.8 \cdot 10^{-5}$	9.0	4.0	0.5	0.0001

Table 2. Physical and mechanical parameters of the WIB and bedrock

Material parameters	Lamé constants in GPa							
Symbol	μ_{w1}	λ_{w1}	μ_{w2}	λ_{w2}	μ_{w3}	λ_{w3}	μ_e	λ_e
Magnitude	8.0	12.0	8.0	12.0	8.0	12.0	8.0	12.0

When the S-wave incides from the single-phase bedrock medium to the unsaturated porous medium, there exists a critical angle of incidence φ_{cr}, and the wave velocities of P- and S-waves can be obtained from the formula in elastic mechanics: $v_{is} = \sqrt{\mu_e/\rho_e} = 1721\,\mathrm{m/s}$, $v_{rp} = \sqrt{(\lambda_e + 2\mu_e)/\rho_e} = 3220\,\mathrm{m/s}$. In which $\varphi_{cr} = \sin^{-1}(v_{is}/v_{rp}) \approx 32.3°$. The transmission and reflection of the wave will disappear when the incident angle of the S-wave exceeds the critical angle, so the variation range of the incident angle is taken as 0°-30° in the later discussion.

According to the literature (Sun and Li, 2011), it is known that the definition of wave impedance is the multiplication of velocity v and density ρ. The ratio between the first medium wave impedance $\rho_1 v_1$ and the second medium wave impedance $\rho_2 v_2$ is the wave impedance ratio, which can be expressed as: $\gamma = \rho_1 v_1/\rho_2 v_2$. The wave impedance of the unsaturated soil is Z_0, the wave impedance of WIB$_1$ is Z_1, the wave impedance of WIB$_2$ is Z_2 and the wave impedance of WIB$_3$ is Z_3. Then the wave impedance ratio at the interface between the WIB$_1$ and unsaturated soil layer would be

$$\gamma_1 = \frac{Z_1}{Z_0} = \frac{\sqrt{(\lambda_{w1} + 2\mu_{w1})\rho_{w1}}}{\rho_s v_{p1}}$$

the wave impedance ratio at the interface between WIB$_2$ and WIB$_1$ would be

$$\gamma_2 = \frac{Z_2}{Z_1} = \sqrt{\frac{(\lambda_{w2} + 2\mu_{w2})\rho_{w2}}{(\lambda_{w1} + 2\mu_{w1})\rho_{w1}}}$$

the wave impedance ratio at the interface between WIB$_3$ and WIB$_2$ would be

$$\gamma_3 = \frac{Z_3}{Z_2} = \sqrt{\frac{(\lambda_{w3} + 2\mu_{w3})\rho_{w3}}{(\lambda_{w2} + 2\mu_{w2})\rho_{w2}}}$$

According to the formula of wave impedance ratio, the material parameters which affect the wave impedance ratio are mainly the density and Lamé constant. The surface vertical displacement under simultaneous variation of the wave impedance ratio between material layers in the range of 0.5-20 is calculated by MATLAB. The wave impedance ratio corresponding to the minimum surface vertical displacement will be selected to determine the material parameters for vibration isolation design: density and shear modulus of the composite multilayer WIB. Six cases of density of WIB are discussed as follows:

Case 1: $\rho_{w1} < \rho_{w2} < \rho_{w3}$ which $\rho_{w1} = 2000\,\mathrm{kg/m^3}$, $\rho_{w2} = 2400\,\mathrm{kg/m^3}$, $\rho_{w3} = 2700\,\mathrm{kg/m^3}$
Case 2: $\rho_{w1} < \rho_{w2} > \rho_{w3}$ which $\rho_{w1} = 2000\,\mathrm{kg/m^3}$, $\rho_{w2} = 2700\,\mathrm{kg/m^3}$, $\rho_{w3} = 2400\,\mathrm{kg/m^3}$
Case 3: $\rho_{w1} > \rho_{w2} < \rho_{w3}$ which $\rho_{w1} = 2400\,\mathrm{kg/m^3}$, $\rho_{w2} = 2000\,\mathrm{kg/m^3}$, $\rho_{w3} = 2700\,\mathrm{kg/m^3}$
Case 4: $\rho_{w1} < \rho_{w2} > \rho_{w3}$ which $\rho_{w1} = 2400\,\mathrm{kg/m^3}$, $\rho_{w2} = 2700\,\mathrm{kg/m^3}$, $\rho_{w3} = 2000\,\mathrm{kg/m^3}$
Case 5: $\rho_{w1} > \rho_{w2} > \rho_{w3}$ which $\rho_{w1} = 2700\,\mathrm{kg/m^3}$, $\rho_{w2} = 2400\,\mathrm{kg/m^3}$, $\rho_{w3} = 2000\,\mathrm{kg/m^3}$
Case 6: $\rho_{w1} > \rho_{w2} < \rho_{w3}$ which $\rho_{w1} = 2700\,\mathrm{kg/m^3}$, $\rho_{w2} = 2000\,\mathrm{kg/m^3}$, $\rho_{w3} = 2400\,\mathrm{kg/m^3}$

Considering the saturation $Sr = 0.8$, incidence frequency $\omega = 10\,\mathrm{Hz}$, angle of incidence $\varphi = 30^\circ$, thickness of the composite multilayer WIB $H_{w1} = H_{w2} = H_{w3} = 0.3\,\mathrm{m}$, and burial depth $H_2 = 1.0\,\mathrm{m}$, 3D curves of the surface vertical displacement with simultaneous variation of the wave impedance ratio γ_1, γ_2 and γ_3 under six cases are plotted in Fig. 3, respectively. As shown in Fig. 3, the surface vertical displacement decreases with an increase in the wave impedance ratio, and the amplitude of the surface vertical displacement reaches the minimum when the wave impedance ratio increases to a certain degree. In addition, it can also be seen from the values of the axes in the right side of Fig. 3 that the range of the vertical displacement amplitude at the surface in Case 3 is the minimum. The minimum value of the surface vertical displacement and the corresponding wave impedance for six cases are calculated as follows:

(1) when $\rho_{w1} < \rho_{w2} < \rho_{w3}$, $\gamma_1 = 2.0$, $\gamma_2 = 11.5$, $\gamma_3 = 19.5$, $u_{z\,min} = 9.35 \cdot 10^{-12}$,m
(2) when $\rho_{w1} < \rho_{w2} > \rho_{w3}$, $\gamma_1 = 16.0$, $\gamma_2 = 2.5$, $\gamma_3 = 10.5$, $u_{z\,min} = 5.14 \cdot 10^{-10}\,\mathrm{m}$
(3) when $\rho_{w1} > \rho_{w2} < \rho_{w3}$, $\gamma_1 = 16.0$, $\gamma_2 = 2.5$, $\gamma_3 = 10.5$, $u_{z\,min} = 8.68 \cdot 10^{-12}\,\mathrm{m}$
(4) when $\rho_{w1} < \rho_{w2} > \rho_{w3}$, $\gamma_1 = 14.5$, $\gamma_2 = 11.5$, $\gamma_3 = 13.0$, $u_{z\,min} = 2.33 \cdot 10^{-10}\,\mathrm{m}$
(5) when $\rho_{w1} > \rho_{w2} > \rho_{w3}$, $\gamma_1 = 13.5$, $\gamma_2 = 3.0$, $\gamma_3 = 9.5$, $u_{z\,min} = 8.71 \cdot 10^{-11}\,\mathrm{m}$
(6) when $\rho_{w1} > \rho_{w2} < \rho_{w3}$, $\gamma_1 = 6.5$, $\gamma_2 = 16.5$, $\gamma_3 = 4.0$, $u_{z\,min} = 4.39 \cdot 10^{-8}\,\mathrm{m}$

The above six density cases show that the surface vertical displacement obtained in Case 3 is the minimum value. At this time, the composite multilayer WIB achieves the most effective isolation effect. And the shear modulus of the composite multilayer WIB, in this case, can be back-calculated from the wave impedance ratio: $\mu_{w1} = 3.53 \cdot 10^{11}\,\mathrm{Pa}$ for WIB_1, $\mu_{w2} = 1.17 \cdot 10^{14}\,\mathrm{Pa}$ for WIB_2, and $\mu_{w3} = 1.39 \cdot 10^{15}\,\mathrm{Pa}$ for WIB_3. In summary, the calculation can find the wave impedance ratio corresponding to the optimal vibration isolation effect of the composite multilayer WIB to determine the material parameters of the composite multilayer WIB and derive design guidelines for multilayer vibration barriers. In the design of a multilayer vibration barrier, physical material parameters with greater density on both sides, smaller density in the center and the shear modulus increasing gradually from the bottom to the top can be selected to achieve the optimal vibration isolation effect.

5.3. Analysis of vibration isolation law for the composite multilayer WIB

In this Section, the material parameters are taken from Case 3, which is discussed in Section 5.2 when the optimal isolation effect of the composite multilayer WIB is achieved, and the vibration isolation performance is analyzed. For the evaluation of the vibration isolation effect of the composite multilayer WIB, this paper adopts the amplitude attenuation ratio A_R proposed by Woods *et al.* (1974) to evaluate its vibration isolation effect. The formula is expressed as: $A_R = u_z/u_z^*$, where u_z is the surface vertical displacement after installing the WIB in the

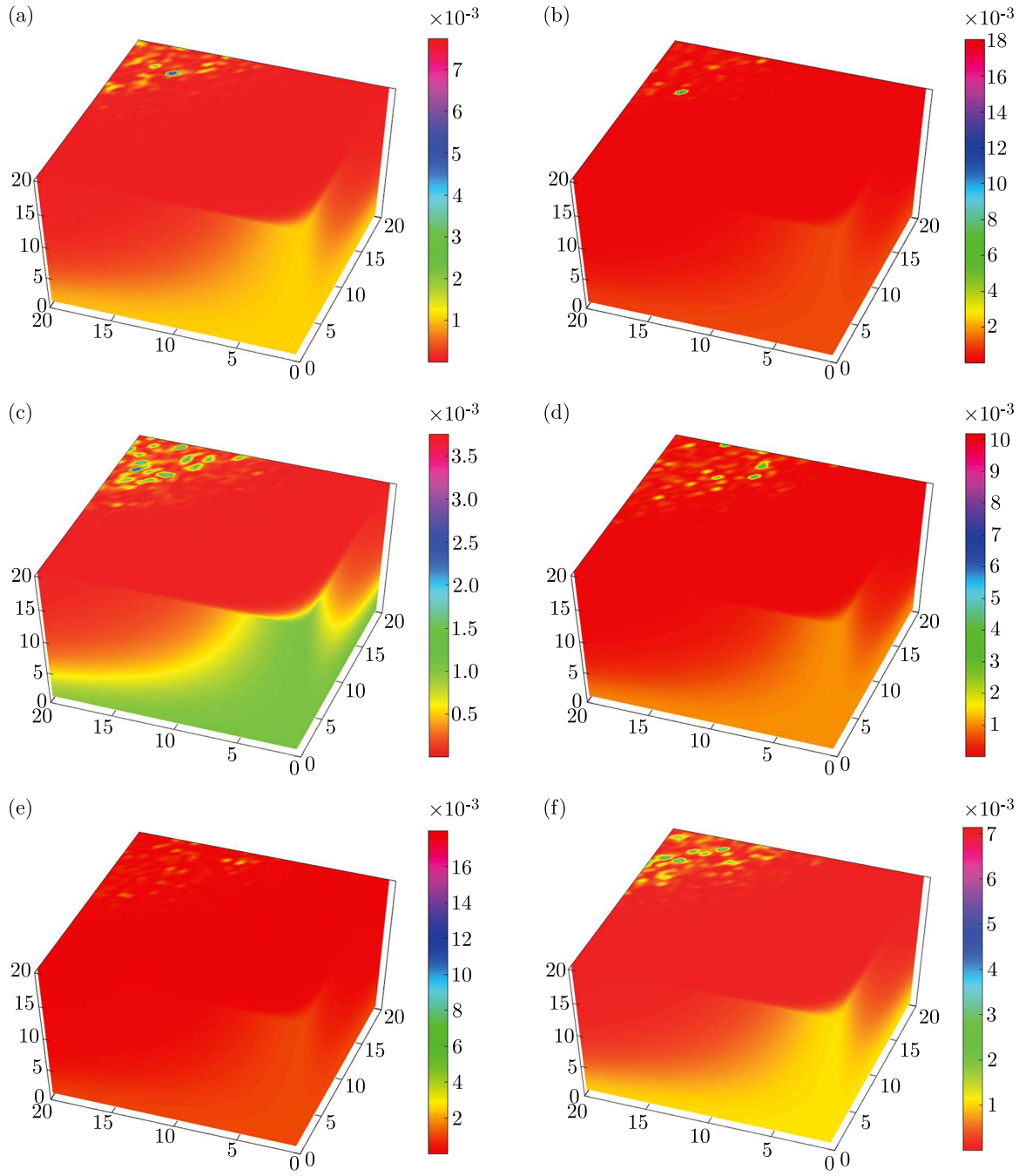

Fig. 3. 3D curves of the vertical surface displacement with simultaneous variation of the wave impedance ratio: (a) Case 1, (b) Case 2, (c) Case 3, (d) Case 4, (e) Case 5, (f) Case 6

unsaturated foundation, u_z^* is the surface vertical displacement without installation of WIB in the unsaturated foundation.

Figure 4 plots the comparison of the isolation effect of a single-layer WIB and the composite multilayer WIB for burial depth $H_2 = 1.0\,\mathrm{m}$, saturation $Sr = 0.8$, incidence frequency $\omega = 10\,\mathrm{Hz}$, total thickness of the soil layer $H = 20\,\mathrm{m}$ and other parameters taken from Table 1. The material parameters of the composite multilayer WIB are taken from Case 3. The material parameters of the single-layer WIB are taken as corresponding to those of each layer in the composite multilayer WIB. Accordingly, thickness of the single-layer WIB is 0.9 m, and density and shear modulus are as follows: (1) $\rho_w = 2000\,\mathrm{kg/m^3}$, $\mu_w = 1.17 \cdot 10^{14}\,\mathrm{Pa}$; (2) $\rho_w = 2400\,\mathrm{kg/m^3}$, $\mu_w = 3.53 \cdot 10^{11}\,\mathrm{Pa}$;

(3) $\rho_w = 2700\,\mathrm{kg/m^3}$, $\mu_w = 1.39 \cdot 10^{15}\,\mathrm{Pa}$. It can be seen from Fig. 4 that the isolation effect of the single-layer homogeneous WIB with three kinds of materials is not as good as the composite multilayer WIB. For the calculation in this paper, the effective isolation angle range of the single-layer WIB is 12°-28° when $\rho_w = 2000\,\mathrm{kg/m^3}$, and the average amplitude attenuation ratio is $A_R = 0.678$ in this range. When $\rho_w = 2400\,\mathrm{kg/m^3}$, the effective isolation angle range of the single-layer WIB is 10°-29°, and the average amplitude attenuation ratio in this range $A_R = 0.509$. When $\rho_w = 2700\,\mathrm{kg/m^3}$, the effective isolation angle range of the single-layer WIB is 4°-28°, and the average amplitude attenuation coefficient in this range is $A_R = 0.36$. The composite multilayer WIB has effective vibration isolation in the critical angle range and its average amplitude attenuation ratio is $A_R = 0.093$. In summary, the vibration isolation efficiency of the composite multilayer WIB is enhanced by 86.28% over the single-layer WIB for $\rho_w = 2000\,\mathrm{kg/m^3}$, 81.73% over the single-layer WIB for $\rho_w = 2400\,\mathrm{kg/m^3}$, and 74.17% over the single-layer WIB for $\rho_w = 2700\,\mathrm{kg/m^3}$. Therefore, with the same thickness of vibration isolation system, the isolation effect of the composite multilayer WIB is significantly better than that of the single-layer homogeneous WIB.

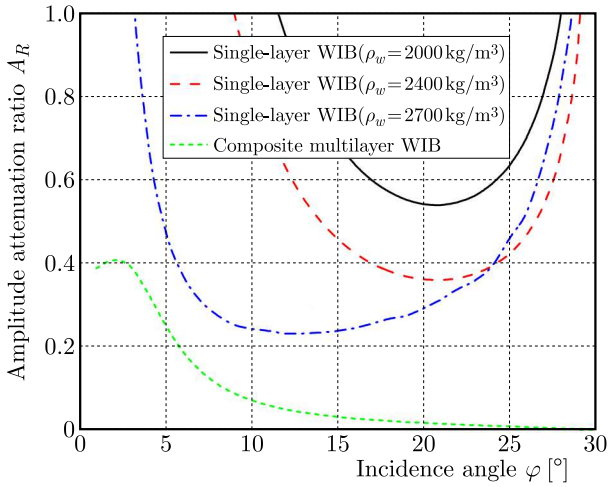

Fig. 4. Comparison of A_R with the angle of incidence for the single-layer and composite multilayer WIB

The effects of the same incidence frequency on the vibration isolation effect of the single--layer and composite multilayer WIB in the unsaturated foundation will be analyzed next. In the analysis, the saturation is 0.8, thickness of the unsaturated soil layer $H = 20\,\mathrm{m}$, burial depth $H_2 = 1.0\,\mathrm{m}$, thickness of single-layer and composite multilayer WIB 0.9 m, and other parameters are taken from Table 1. Three cases of the incidence frequency, $\omega = 10\,\mathrm{Hz}$, 50 Hz and 100 Hz are considered, respectively. As shown in Fig. 5, the average amplitude attenuation ratio is $A_R = 0.91$ for the single-layer WIB and $A_R = 0.066$ for the composite multilayer WIB when $\omega = 50\,\mathrm{Hz}$, in which case the isolation efficiency is 92.75% higher than for the single-layer WIB. When $\omega = 100\,\mathrm{Hz}$, the single-layer WIB vibration isolation fails, its average amplitude attenuation ratio is $A_R = 4.43$ and $A_R = 0.036$ for the composite multilayer WIB, whose isolation efficiency is 99.18% higher than that of the single-layer WIB. Consistently, it is evident that the composite multilayer WIB can improve the defect that the single-layer WIB has only good vibration isolation effect at a low frequency. The composite multilayer WIB can isolate the incidence frequencies at low, medium and high frequencies effectively, and the isolation efficiency gradually increases with an increase in the incidence frequency. Among the common types of environmental vibration in cities, the main vibration frequency caused by tamping is concentrated in 10-20 Hz, the main vibration frequency caused by elevators is within 20-25 Hz, and the main vibration frequency caused by subway is higher, between 50-80 Hz. On the whole, the frequency of environmental vibration will not exceed 100 Hz in general. Thus, the composite

multilayer WIB is suitable for isolating common city environmental vibrations, especially those caused by traffic.

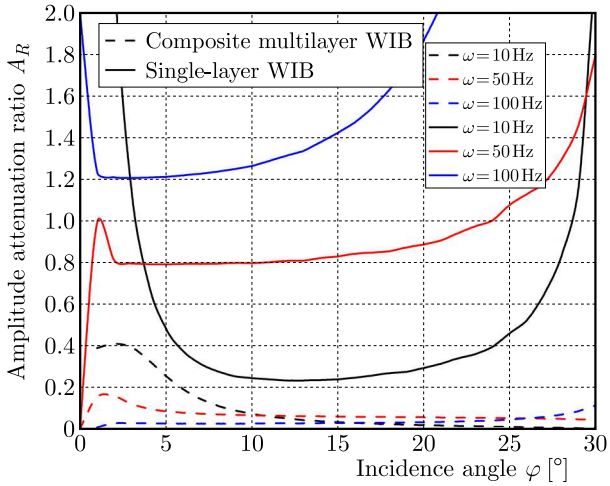

Fig. 5. Variations of the vertical displacement amplitude attenuation ratio at the surface along with ω

The following Section investigates the effect of saturation on the vibration isolation effect of the composite multilayer WIB in the unsaturated foundation for thickness of the soil layer $H = 20\,\text{m}$, burial depth $H_2 = 1.0\,\text{m}$, thickness of the composite multilayer WIB $H_{w1} = H_{w2} = H_{w3} = 0.3\,\text{m}$, incidence frequency $\omega = 10\,\text{Hz}$, and other parameters taken from Table 1. The saturation is $Sr = 0.2$, 0.4, 0.6 and 0.8, respectively. The variation curves of the surface vertical displacement amplitude attenuation ratio with the angle of incidence for different saturations when the composite multilayer WIB is set up in the unsaturated foundation are given in Fig. 6. Firstly, it can be seen from Fig. 6 that the surface vertical displacement amplitude attenuation

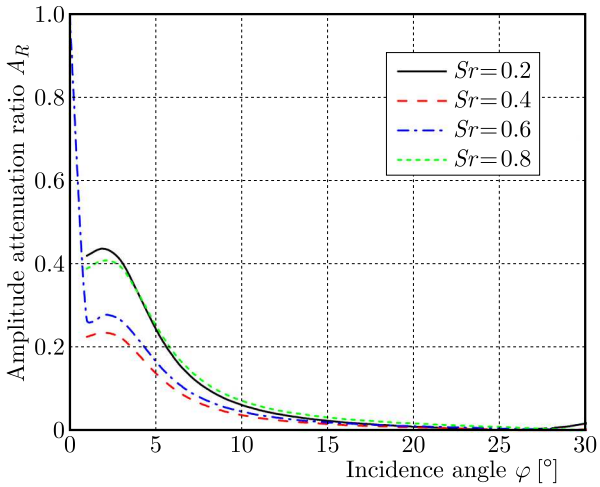

Fig. 6. Variations of the vertical displacement amplitude attenuation ratio at the surface along with Sr

ratio exhibits irregularity with the variation of saturation. When $Sr = 0.2$, the average amplitude attenuation ratio is $A_R = 0.0899$, $A_R = 0.0508$ when $Sr = 0.4$. The vibration isolation effect is 43.49% higher than that for $Sr = 0.2$. The average amplitude attenuation ratio $A_R = 0.0916$ at $Sr = 0.6$ and its vibration isolation effect is 44.54% lower than that for $Sr = 0.4$, whereas the vibration isolation effect at $Sr = 0.8$ is 1.51% lower than that for $Sr = 0.6$. It means that the vibration isolation effect of the composite multilayer WIB in the unsaturated foundation increases and then decreases with an increase of saturation. To sum up, the saturation has a significant effect on the isolation effect of the composite multilayer WIB. It is difficult to

simulate the actual situation by simplifying the foundation into a single-phase elastic and two--phase saturated foundation.

6. Conclusion

Combining the wave propagation theory and Snell's theorem, the vibration isolation performance of a composite multilayer WIB in an unsaturated foundation, which is more consistent with reality, is investigated. The vibration isolation performance of the composite multilayer WIB and a single-layer WIB under the same thickness have been compared and analyzed. The influence laws of saturation and incidence frequency on the isolation effect of the composite multilayer WIB in the unsaturated foundation have been investigated. Conclusions can be drawn as follows.

- Physical parameters of large density on both sides and small density in the center and a gradually increasing shear modulus from bottom to top can achieve the optimal isolation effect when designing a composite multilayer vibration barrier.
- Vibration multilayer barriers can isolate common environmental vibration sources in cities, especially, medium and high frequency vibrations caused by traffic. For the same thickness of the vibration isolation system, the isolation effect of the composite multilayer WIB is better than thaf of a single-layer WIB. At a low incidence frequency ($\omega = 10\,\mathrm{Hz}$), the vibration isolation efficiency of the composite multilayer WIB is 86.28% higher than that of the single-layer WIB. At a medium incidence frequency ($\omega = 50\,\mathrm{Hz}$), the vibration isolation efficiency of the composite multilayer WIB is 92.75% higher than that of the single-layer WIB. At a high incidence frequency ($\omega = 100\,\mathrm{Hz}$), the vibration isolation efficiency of the composite multilayer WIB is 99.18% higher than that of the single-layer WIB.
- The isolation effect of the composite multilayer WIB increases and then decreases with an increase of saturation, and gradually increases with an increase of the angle of incidence.

References

1. Borja R.I., 2006, On the mechanical energy and effective stress in saturated and unsaturated porous continua, *International Journal of Solids and Structures*, **43**, 1764-1786
2. Chen W., Xia T., Hu W., 2011, A mixture theory analysis for the surface-wave propagation in an unsaturated porous medium, *International Journal of Solids and Structures*, **48**, 2402-2412
3. Chouw N., Le R., Schmid G., 1991a, An approach to reduce foundation vibrations and soil waves using dynamic transmitting behavior of a soil layer, *Bauingenieur*, **66**, 215-221
4. Chouw N., Le R., Schmid G., 1991b, Propagation of vibration in a soil layer over bedrock, *Engineering Analysis with Boundary Elements*, **8**, 125-131
5. Gao M., Zhang Z.S., Wang C.G., Tian S.P., 2021, Field test on vibration isolation performance by WIB-Duxseal under vertical excitation (in Chinese), *Rock and Soil Mechanics*, **42**, 537-546
6. Jiang Y., Ma Q., 2022, Study on vibration isolation effect of wave impeding block in unsaturated soil under *S*-wave incidence, *Acta Mechanica*, **233**, 4119-4139
7. Li Z.J., He Z., Tan Y., Xiao J.H., 2011, HWIB isolation analysis of low-frequency vibration from high speed railways by using HWIB (in Chinese), *Journal of Huazhong University of Science and Technology (Natural Science Edition)*, **39**, 34-38
8. Li W., Zheng J., Trifunac M.D., 2018, Saturation effects on ground motion of unsaturated soil layer-bedrock system excited by plane *P* and *SV* waves, *Soil Dynamics and Earthquake Engineering*, **110**, 159-172

9. Ma Q., Zhou F., Zhang W., 2019, Vibration isolation of saturated foundations by functionally graded wave impeding block under a moving load, *Journal of the Brazilian Society of Mechanical Sciences and Engineering*, **41**, 1-10

10. Shu J., Ma Q., 2022, Study the propagation characteristics of P_1-wave passing through composite multilayer wave impeding block in unsaturated soil, *The European Physical Journal Plus*, **137**, 1-16

11. Shu J.H, Ma Q., Zhou F.X., Li Q., 2022, Study on the propagation characteristics of P_1 wave passing through wave impeding block in unsaturated soil (in Chinese), *Rock and Mechanics*, **43**, 1135-1146

12. Sun C.Y., Li Z.C., 2011, *The Fundamentals of Seismic Wave Dynamics*, Petroleum Industry Press, Beijing

13. Takemiya H., Jiang J., 1993, Wave impeding effect by buried rigid block and response reduction of dynamically excited pile foundation, *Doboku Gakkai Ronbunshu*, **1993**, 45-52

14. Tian S.P., Gao M., Wang Y., Chen Q.S., 2019, Two dimensional analysis of Duxseal material as active vibration isolation in homogeneous elastic foundation (in Chinese), *Journal of Vibration Engineering*, **32**, 701-711

15. Woods R.D., Barnett N.E., Sagesser R., 1974, Holography – A new tool for soil dynamics, *Journal of the Geotechnical Engineering Division*, **100**, 1231-1247

16. Yang Y.B., Hung H.H., 1997, A parametric study of wave barriers for reduction of train-induced vibrations, *International Journal for Numerical Methods in Engineering*, **40**, 3729-3747

17. Zhou F.X., Ma Q., Lai Y.M., 2016, Ground vibration control with fluid-saturated porous wave impeding blocks (in Chinese), *Journal of Vibration and Shock*, **35**, 96-105

Manuscript received January 9, 2023; accepted for print March 26, 2023

JOURNAL OF THEORETICAL AND APPLIED MECHANICS
61, 3, pp. 441-452, Warsaw 2023
https://doi.org/10.15632/jtam-pl/165937

ANALYSIS OF DYNAMIC CHARACTERISTICS OF A SEALED ENDS SQUEEZE FILM DAMPER CONSIDERING THE FLUID INERTIA FORCE

Hai Lun Zhou, Yang Guang Cang, Yu Qi Zhang, Chao Guo

School of Aero-engine, Shenyang Aerospace University, Shenyang, China, and Liaoning Key Laboratory of Advanced Measurement and Test Technology for Aircraft Propulsion System, School of Economics and Management, Tongji University, ShangHai, China

Corresponding author Chao Guo, e-mail: gcdzq@163.com

In order to effectively calculate dynamic characteristics of a sealed ends squeeze film damper (SFD) under the influence of the inertial force, a computational fluid dynamics model of the sealed ends SFD is established. The fluid inertia coefficient of SFD is investigated by using an energy approximation method. Both the theoretical calculation and numerical simulation are conducted to analyze the effects of eccentricity ratio and whirling frequency on stiffness and damping. In this research, the oil film inertia force of the sealed ends SFD is solved by using long bearing approximation (LBA) theory, which provides guidance for the design and application of the sealed ends SFD.

Keywords: squeeze film damper, fluid inertia, computational fluid dynamics, damping, stiffness

1. Introduction

Squeeze film dampers (SFDs) suppress vibration and enhance stability of rotating machines (Miyachi *et al.*, 1979). In the LBA to Reynolds equation, which is justified if a damper is long in the axial direction, the flow in the damper is circumferential, and thus the circumferential pressure gradient is much larger than the axial pressure gradient. In practice, if the damper is tightly sealed, the flow is circumferential even if the dampers are physically short. In this case, the LBA would describe the conditions better than the short bearing approximation (SBA) (El-Shafei and Crandall, 1991). SFDs with sealed ends absorb more vibration than open ends SFDs when passing critical speeds under the same operation condition as sealed SFDs produce more damping (San Andrés and Seshagiri, 2013). But current and related investigations are not sufficient in that matter.

Establishing accurate mathematical functions is difficult as fluid motion inside the oil film clearance is complicated, so logical simplifications and assumptions are compulsive. In classical lubrication theory, fluid inertia is neglected and the Reynolds equation governing SFDs is obtained (Szeri, 1980). However, past examinations have revealed that film forces calculated by theoretical functions do not correspond with the results obtained from experiments due to neglection of fluid inertia, and the error could even go up to 60%. The fluid inertia should be taken into consideration when the Reynolds number is larger than 1.

Researchers paid attention to the effects of fluid inertia many years ago. Kuzma (1968) demonstrated that the fluid inertia produced a significant squeeze film effect, and the theoretical model considering the fluid inertia corresponded with experimental results well. Chen *et al.* (2021) investigated dynamics of a rotor system supported on SFD considering the fluid inertia. Numerical integration was employed to calculate the pressure and oil film force. The results showed that oil film pressure was sensitive to fluid inertia when the journal eccentricity ratio

was large. The radial force decreased while the tangential force increased. The fluid inertia suppressed the resonance amplitude under high rotating speed and large eccentricity. San Andrés investigated the effect of fluid inertia on rotor dynamics supported on an SFD and found that increasing fluid inertia reduced the occurrence of bistable operation and jump phenomena (San Andrés and Vance, 1988). Hamzehlouia and Behdinan (Hamzehlouia and Behdinan, 2016) did numerical analysis towards a finite length SFD considering the unstable state inertia term, and compared the results with the existing SFD model. The comparison showed that the fluid inertia produced a significant effect on the oil film pressure and force even at small Reynolds numbers.

With the development of computers, computational fluid dynamics (CFD) software has been employed to do simulations on SFDs. The CFD software make complex geometric model flow analysis available (Guo *et al.*, 2005). Lee *et al.* (2017) investigated the effect of oil supply groove and sealed piston ring on the oil film at a small clearance using CFD software. The results showed that the oil film pressure decreased as oil supply depth, piston ring radial clearance and axial clearance increased, and the radial and tangential forces decreased accordingly. Dousti *et al.* (2016) addressed the oil film pressure distribution and oil film force changing under different groove depths and rotating speeds through CFX software. The results indicated that considerable pressure was generated in a sealed groove, and the pressure changed along the circumferential direction rather than the axial one. Zhou *et al.* (2020a,b) calculated SFD dynamic characteristics with SBA, which provide more ideas for the open ends SFD design.

Szeri *et al.* (1982) added an acceleration term and pointed out that oil film reaction forces were generated by both viscous and inertial forces. El-Shafei (1991) used momentum and energy approximation to analyze the inertial term independently of the viscous term. The inertial term was determined by the Lagrange equation and Reynolds transport law.

Through the above research, it is found that the effect of oil film fluid inertia on SFD dynamic characteristic is mostly based on a short open ends SFD, but there are few theoretical studies on the LBA considering the oil film inertia force and numerical simulation of dynamic characteristics of the sealed ends SFD. This paper investigates the fluid inertia effect using the energy approximation method (Crandall and El-Shafei, 1993) and derives stiffness and damping coefficients with the LBA. The numerical simulation is conducted on CFX to verify the derived functions. Based on the functions and simulations, the effects of frequency and eccentricity ratio on SFD dynamic characteristics are analyzed.

2. Long bearing approximation theoretical analysis

2.1. Analysis of the long bearing approximation SFD viscosity term

The LBA theory assumes that if the axial length is long enough or there are seals at both ends, the oil film pressure gradient along circumferential direction is much larger than that along the axial one, and the changes in the circumferential direction are much larger than in the axial direction. In order to study dynamic characteristics of the sealed ends SFD, the LBA theoretical analysis was carried out.

The structure of an SFD is usually simplified for deducing dynamic characteristics formula of the SFD and the corresponding coordinate system is established, as shown in Fig. 1a. Taking the middle line of the central groove as the reference line, the left or right part of the structure is extracted, which is shown in Fig. 1b, where O_b is the origin of the SFD coordinate system in the center of the SFD housing, O_j is the center of the journal, h is thickness of the oil film, θ measured from the positive r-axis of the rotating coordinate system (r, t, z), ϕ is the static coordinate system (x, y, z) and from the positive x axis. The measured angle is $\theta = \phi - \psi$. For stable circular precession $\psi = \omega t$, where ω is the journal rotation speed, e is the dynamic

eccentricity of the SFD journal, X is the circumferential direction, Y is the normal direction, z is the axis direction of the journal, R is radius of the SFD journal, L is the SFD axial length.

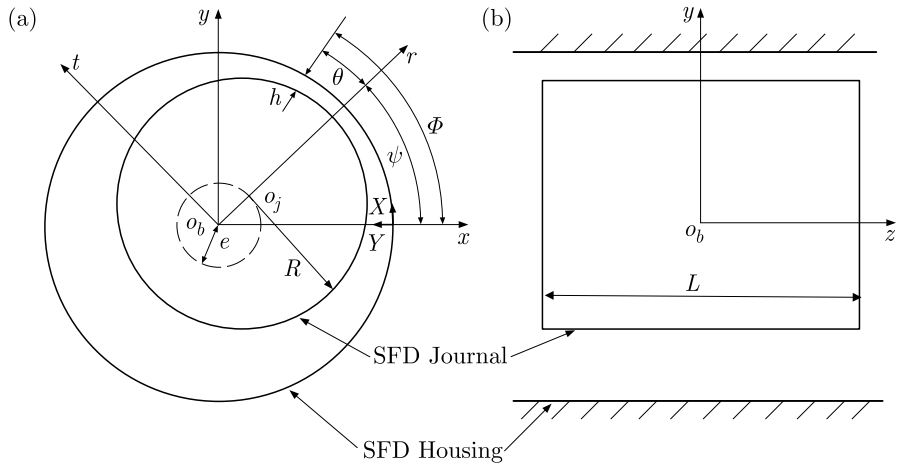

Fig. 1. SFD coordinate system

Since the NS equation is a nonlinear partial differential equation, it cannot be directly used to solve the SFD oil film pressure. The Reynolds equation is simplified from the NS equation with several assumptions in the case of low viscosity flow. The pressure distribution and oil film force of the SFD can be obtained with appropriate boundary conditions. The Reynolds equation is as follows

$$\frac{1}{R^2}\frac{\partial}{\partial\theta}\Big(\frac{h^3}{\mu}\frac{\partial P}{\partial\theta}\Big)+\frac{\partial}{\partial z}\Big(\frac{h^3}{\mu}\frac{\partial P}{\partial z}\Big)=6(\omega_j-2\dot{\psi})\frac{\partial h}{\partial\theta}+12\frac{de}{dt}\cos\theta \tag{2.1}$$

Since the journal of the damper does not rotate and the housing is fixed, precession will only occur due to an unbalanced excitation, so the journal rotation speed ω_j is 0.

According to the geometric relationship shown in Fig. 1, the film thickness h at any given location is given by

$$h=c(1-\varepsilon\cos\theta) \tag{2.2}$$

where c is the clearance, ε is the eccentricity ratio of the journal, $\varepsilon=e/c$.

In a simplified analysis, it is considered that the oil film pressure does not change along the thickness of the oil film, and the damper journal only performs stable circular motion. Neither the damper housing nor the journal rotates, the SFD Reynolds equation is obtained as

$$\frac{1}{R^2}\frac{\partial}{\partial\theta}\Big(h^3\frac{\partial P}{\partial\theta}\Big)+\frac{\partial}{\partial z}\Big(h^3\frac{\partial P}{\partial z}\Big)=-12\dot{\psi}\mu\frac{\partial h}{\partial\theta} \tag{2.3}$$

In LBA theory, the pressure gradient along axial direction is negligible comparing with the circumferential direction, so $\partial P/\partial z$ term is omitted and the following equation is obtained

$$\frac{1}{R^2}\frac{\partial}{\partial\theta}\Big(h^3\frac{\partial P}{\partial\theta}\Big)=-12\dot{\psi}\mu\frac{\partial h}{\partial\theta} \tag{2.4}$$

where μ is viscosity of the oil, R is radius of the journal, P is pressure, $\dot{e}$ and $e\dot{\psi}$ are the radial and tangential velocity of the journal, respectively.

Integrating twice with π-film boundary conditions (Booker, 1965), the oil film pressure is

$$P=\frac{6\mu R^2}{c^3}\Big\{\Big[\frac{1}{\varepsilon(1-\varepsilon\cos\theta)^2}-\frac{1}{\varepsilon(1+\varepsilon)^2}\Big]\dot{e}+\Big[\frac{2\sin\theta(2-\varepsilon\cos\theta)}{(2+\varepsilon^2)(1-\varepsilon\cos\theta)^2}\Big]e\dot{\psi}\Big\} \tag{2.5}$$

Area-integrating the pressure and decomposing it tangentially and radially

$$\begin{aligned} F_{rc} &= -\frac{\mu R^3 L}{c^3}\frac{6\pi}{(1-\varepsilon^2)^{\frac{3}{2}}}\dot{e} - \frac{\mu R^3 L}{c^3}\frac{24\varepsilon}{(2+\varepsilon^2)(1-\varepsilon^2)}e\dot{\psi} \\ F_{tc} &= -\frac{\mu R^3 L}{c^3}\frac{24}{(1+\varepsilon^2)(1-\varepsilon^2)}\dot{e} - \frac{\mu R^3 L}{c^3}\frac{12\pi}{(2+\varepsilon^2)(1-\varepsilon^2)^{\frac{1}{2}}}e\dot{\psi} \end{aligned} \tag{2.6}$$

The radial and tangential viscosity damping forces acting on the journal F_{rc} and F_{tc} are determined, respectively.

2.2. Analysis of the SFD inertia term of long bearing approximation

Based on the assumption that the velocity distribution with inertia is the same as that of inertialess fluids, the fluid inertial forces in the long damper are obtained by using the energy approximation method (El-Shafei and Crandall, 1991). For a long damper, the circumferential velocity is solved based on the Reynolds equation as

$$u = \frac{6R}{h}\Big(\frac{Y}{h} - \frac{Y^2}{h^2}\Big)\Big[\dot{e}\sin\theta - e\dot{\psi}\cos\theta + \frac{3\varepsilon}{2+\varepsilon^2}e\dot{\psi}\Big] \tag{2.7}$$

At a particular time t, it is convenient to establish a control volume consistent with the fluid mass boundary. Over some time, the control volume remains fixed in space, while the fixed unit of fluid mass changes its shape: the extrusion film becomes thinner and the suction film thickens. Some fixed characteristic fluid near the end of the extrusion film is expelled from the control volume, and some new fluid not belonging to the fixed characteristic mass is sucked into the control volume at the end of the extrusion film. The dynamic coefficient of the fluid inside the damper is

$$T^* = \frac{1}{2}\int_{\theta_2}^{\theta_1}\int_{0}^{h}\int_{-L/2}^{L/2}\rho u^2 R d\theta\, dY\, dZ \tag{2.8}$$

When the damper journal is in the steady state circular precession, $\ddot{\psi} = \ddot{e} = \dot{e} = 0$. The dynamic coefficient of the fluid inside the damper can be calculated

$$T^* = \frac{1}{2}\frac{12\rho R^3 L}{10c}\left[\Big(\frac{3\varepsilon}{2+\varepsilon^2}\Big)^2\frac{\pi}{(1-\varepsilon^2)^{\frac{1}{2}}} - \frac{6}{2+\varepsilon^2}\Big(\frac{\pi}{(1-\varepsilon^2)^{\frac{1}{2}}} - \pi\Big) + \frac{1}{\varepsilon^2}\Big(\frac{\pi}{(1-\varepsilon^2)^{\frac{1}{2}}} - \pi\Big)\right](e\dot{\psi})^2 \tag{2.9}$$

The inertia forces in the damper can be obtained by Lagrange's equations. The radial and tangential inertial forces obtained by combining the Reynolds transport theorem with the Lagrange equation are

$$F_{ir} = F_{ri} + R_{ri} \qquad F_{it} = F_{ti} + R_{ti} \tag{2.10}$$

where F_{ir} is the radial inertial force, F_{it} is the tangential inertial force, R_{ri} and R_{ti} are inertial forces due to the flux of fluid particles across the control surface along the radial and tangential directions, respectively. F_{ri} and F_{ti} obtained by the Lagrange equation are given as follows

$$F_{ri} = -\frac{d}{dt}\Big(\frac{\partial T^*}{\partial \dot{e}}\Big) + \frac{\partial T^*}{\partial e} \qquad F_{ti} = -\frac{1}{e}\frac{d}{dt}\Big(\frac{\partial T^*}{\partial \dot{\psi}}\Big) + \frac{1}{e}\frac{\partial T^*}{\partial \psi} \tag{2.11}$$

Substituting (2.9) into (2.11), we get

$$\begin{aligned} F_{ri} &= \frac{\partial T^*}{\partial e} = \frac{\partial T^*}{c\partial\varepsilon} = \frac{12\rho R^3 L\pi}{10c(\varepsilon^2+2)^2}\left[12 - 2\frac{(10-\varepsilon^2)(1-\varepsilon^2)^{\frac{1}{2}}}{\varepsilon^2+2}\right]e(\dot{\psi})^2 \\ F_{ti} &= \frac{1}{e}\frac{\partial T^*}{\partial\psi} = -\frac{1}{e}\frac{12\rho R^3 L}{10c}\left[\frac{\varepsilon(8+\varepsilon^2)}{(\varepsilon^2+2)^2}\right](e\dot{\psi})^2 \end{aligned} \tag{2.12}$$

Since the π-film theory and motion of the SFD journal are mainly studied, the flux terms R_{ri} and R_{ti} are simplified and integrated

$$R_{ri} = 0 \tag{2.13}$$

and

$$\begin{aligned} R_{ti} = e(\dot{\psi})^2\frac{\rho R^3 L}{c}\Bigg\{ &\underbrace{\left[-\frac{27}{35}\varepsilon\frac{\left(\frac{3\varepsilon}{2+\varepsilon^2}+1\right)^3}{(1+\varepsilon)^2} + \frac{3}{5}\frac{\left(\frac{3\varepsilon}{2+\varepsilon^2}+1\right)^2}{1+\varepsilon}\right]}_{\mathcal{A}_1} \\ &+ \underbrace{\left[\frac{27}{35}\varepsilon\frac{\left(\frac{3\varepsilon}{2+\varepsilon^2}-1\right)^3}{(1-\varepsilon)^2} - \frac{3}{5}\frac{\left(\frac{3\varepsilon}{2+\varepsilon^2}-1\right)^2}{1-\varepsilon}\right]}_{\mathcal{A}_2}\Bigg\} \end{aligned} \tag{2.14}$$

Substituting (2.14) and $(2.12)_2$ into $(2.10)_2$, the tangential inertial force becomes

$$F_{it} = e(\dot{\psi})^2\frac{\rho R^3 L}{c}\Big[\mathcal{A}_1 + \mathcal{A}_2 - \frac{12}{10}\frac{\varepsilon(8+\varepsilon^2)}{(2+\varepsilon^2)^2}\Big] \tag{2.15}$$

Substituting (2.13) and $(2.12)_1$ into $(2.10)_1$, the radial inertia force becomes

$$F_{ir} = \frac{12\rho R^3 L\pi}{10c(\varepsilon^2+2)^2}\left[12 - 2\frac{(10-\varepsilon^2)(1-\varepsilon^2)^{\frac{1}{2}}}{\varepsilon^2+2}\right]e(\dot{\psi})^2 \tag{2.16}$$

The oil film tangential force formula is obtained by adding tangential viscous force formula $(2.6)_2$ and tangential inertial force formula (2.15). The tangential force becomes

$$F_t = F_{it} + F_{tc} = e(\dot{\psi})^2\frac{\rho R^3 L}{c}\left[\mathcal{A}_1 + \mathcal{A}_2 - \frac{12}{10}\frac{\varepsilon(8+\varepsilon^2)}{(2+\varepsilon^2)^2}\right] - \frac{\mu R^3 L}{c^3}\frac{12\pi}{(2+\varepsilon^2)(1-\varepsilon^2)^{\frac{1}{2}}}e\dot{\psi} \tag{2.17}$$

The equivalent oil film damping is

$$C = -\frac{F_t}{e(\dot{\psi})} = -\dot{\psi}\frac{\rho R^3 L}{c}\left[\mathcal{A}_1 - \mathcal{A}_2 + \frac{12}{10}\frac{\varepsilon(8+\varepsilon^2)}{(2+\varepsilon^2)^2}\right] + \frac{\mu R^3 L}{c^3}\frac{12\pi}{(2+\varepsilon^2)(1-\varepsilon^2)^{\frac{1}{2}}} \tag{2.18}$$

The oil film radial force formula is obtained by adding radial viscous force formula $(2.6)_1$ and radial inertial force formula (2.16). Then the radial force becomes

$$F_r = F_{ir} + F_{rc} = \frac{12\rho R^3 L\pi}{10c(\varepsilon^2+2)^2}\left[12 - 2\frac{(10-\varepsilon^2)(1-\varepsilon^2)^{\frac{1}{2}}}{\varepsilon^2+2}\right]e(\dot{\psi})^2 - \frac{\mu R^3 L}{c^3}\frac{24\varepsilon}{(2+\varepsilon^2)(1-\varepsilon^2)}e\dot{\psi} \tag{2.19}$$

The equivalent oil film stiffness is

$$K = -\frac{F_r}{e} = -\frac{12\rho R^3 L\pi}{10c(\varepsilon^2+2)^2}\left[12 - 2\frac{(10-\varepsilon^2)(1-\varepsilon^2)^{\frac{1}{2}}}{\varepsilon^2+2}\right](\dot{\psi})^2 + \frac{\mu R^3 L}{c^3}\frac{24\varepsilon}{(2+\varepsilon^2)(1-\varepsilon^2)}\dot{\psi} \tag{2.20}$$

From the solution analysis of the above equation, it can be seen that the inertia force of the oil film fluid has a great influence on the oil film damping. When the journal speed is large, the influence of oil film inertia force should be considered in the analysis of the squeeze oil film force.

3. Nunerical simulation verification and analysis

3.1. SFD solution model and numerical simulation verification

According to the geometry of SFD shown in Fig. 2, the fluid domain model can be established according to the parameters of SFD, as shown in Fig. 2a. It is considered a computational domain. The hexahedral mesh has been generated by the Multizone mesh generation method. The fluid domain model grid is shown in Fig. 2b. The model local mesh of the fluid domain is shown in Fig. 2c. According to the assumption of the Reynolds equation, the flow condition is usually regarded as laminar flow, which conforms to Newton's viscosity law (Crandall and El-Shafei, 1993). In the numerical simulation, the lubricating oil used in model 1 is ISO VG2 reference (Zhou *et al.*, 2020b), and the room temperature is 23°C. The dynamic viscosity of the oil is $\mu = 0.0031$ Pa·s and density $\rho = 785\,\mathrm{kg/m^3}$. The lubricating oil used in model 2 is the mixture of ISO VG2 and Aviation No. 8 lubricating oil. Its dynamic viscosity is $\mu = 0.0035$ Pa·s, density $\rho = 850\,\mathrm{kg/m^3}$. In order to verify the derived models, CFD software simulation is conducted on two different SFDs. Geometric parameters and lubricant properties are listed in Table 1 and 2.

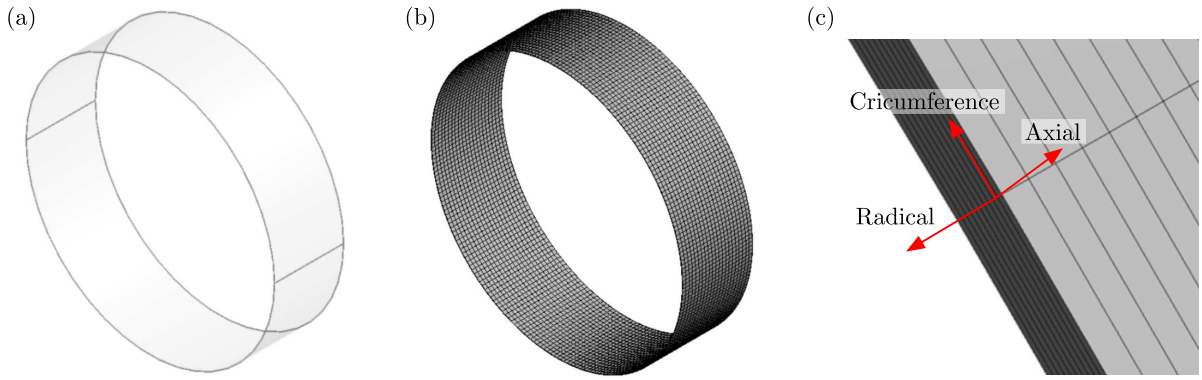

Fig. 2. 3D SFD model: (a) SFD model, (b) SFD meshing, (c) local mesh of fluid domain

Table 1. Theoretical model 1 geometric dimensions and lubricating oil parameters

Journal diameter D [mm]	Oil film clearance c [mm]	Axial length L [mm]	Density ρ [kg/m^3]	Dynamic viscosity μ [Pa·s]
73.8	0.14	20.6	785	0.0031

Table 2. Theoretical model 2 geometric dimensions and lubricating oil parameters

Journal diameter D [mm]	Oil film clearance c [mm]	Axial length L [mm]	Density ρ [kg/m^3]	Dynamic viscosity μ [Pa·s]
74.92	0.15	18.2	850	0.0035

According to reference (Zhou *et al.*, 2020a,b), the simulation is conducted on CFX. The grid division adopts the oil film axial grid of 0.06 mm, the oil film circumferential grid of 1 mm and the oil film radial grid of 10 layers. On the premise of considering both CFD simulation analysis accuracy and calculation time, this paper adopts the number of calculation cycles as 3 cycles, and the time step of each cycle takes 200 steps to obtain the convergent solution of the SFD oil film damping and stiffness.

Since the SFD Reynolds number is small, the flow state is set to a laminar flow. The boundary conditions are shown in Fig. 3. According to the LBA, the axial end of the "end land" is modeled as a wall to ambient pressure. The housing and journal of SFD is set to the "wall". The housing is stationary, while the journal moves as circular centered-orbit motion in the steady state as follows (Zhou *et al.*, 2020a,b)

$$X = e\cos(\Omega t) \qquad Y = e\sin(\Omega t) \tag{3.1}$$

where e is the eccentricity and Ω the precession speed. By changing e and Ω, different precession amplitudes and precession frequencies are simulated, and the conversion relationship between the precession speed and frequency is $\Omega = 2\pi f$.

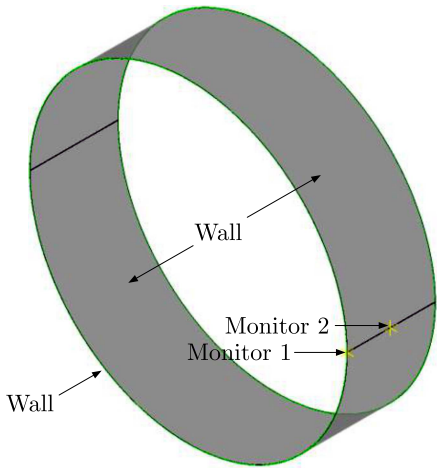

Fig. 3. SFD boundary conditions

In order to better observe the movement of the oil film, the monitoring point 1 and point 2 are added to observe the pressure change. The monitoring point 1 is located at the axial edge of the SFD, and the monitoring point 2 is located in the middle of the oil film, as shown in Fig. 3.

The tangential F_t and radial force F_r were obtained by integrating the oil film pressure obtained by numerical simulation, and then the corresponding oil film damping C and oil film stiffness K coefficients were obtained. The corresponding integral formula is shown in Eq. (3.2), where θ_1 and θ_2 represent the boundary of the oil film pressure zone

$$F_r = -\int_{L/2}^{L/2}\int_{\theta_1}^{\theta_2} P\cos(\theta)Rd\theta\, dz \qquad F_t = -\int_{L/2}^{L/2}\int_{\theta_1}^{\theta_2} P\sin(\theta)Rd\theta\, dz \tag{3.2}$$

3.2. Analysis of the effect of eccentricity ratio on vibration reduction characteristics of the sealed ends SFD

In order to analyze the effect of journal eccentricity ratio on dynamic characteristics of the oil film, the oil film damping and stiffness are calculated by the theoretical formula and CFX simulation at a different eccentricity ratio of 100 Hz. The comparison results are shown in Figs. 4 and 5.

Through comparative analysis, it can be seen that the damping and stiffness of SFD with end seals roughly increase with an increase of the eccentricity ratio, but the increase range is small. Therefore, considering the oil film inertia is conducive to reduce the amplitude and improve the stability.

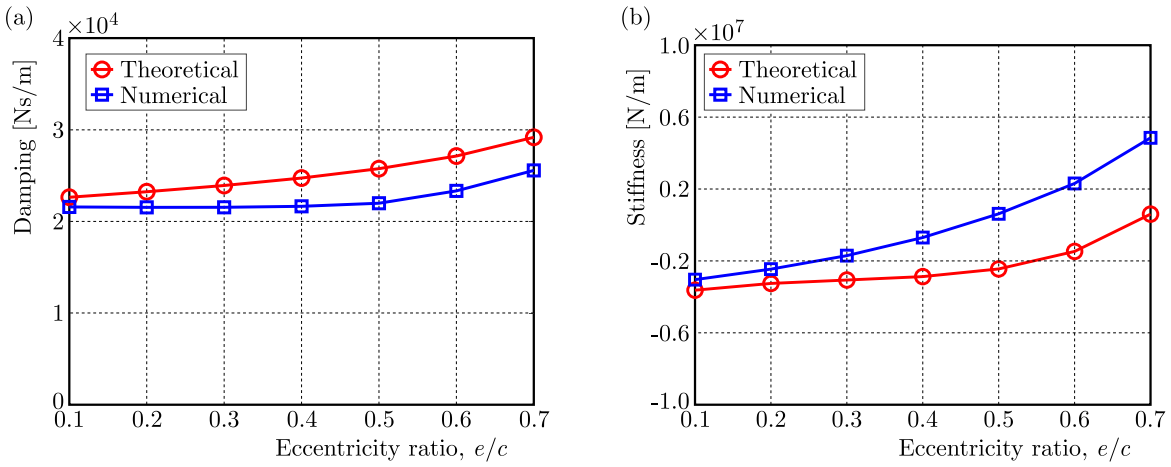

Fig. 4. Model 1 curve of (a) damping and (b) stiffness with eccentricity ratio

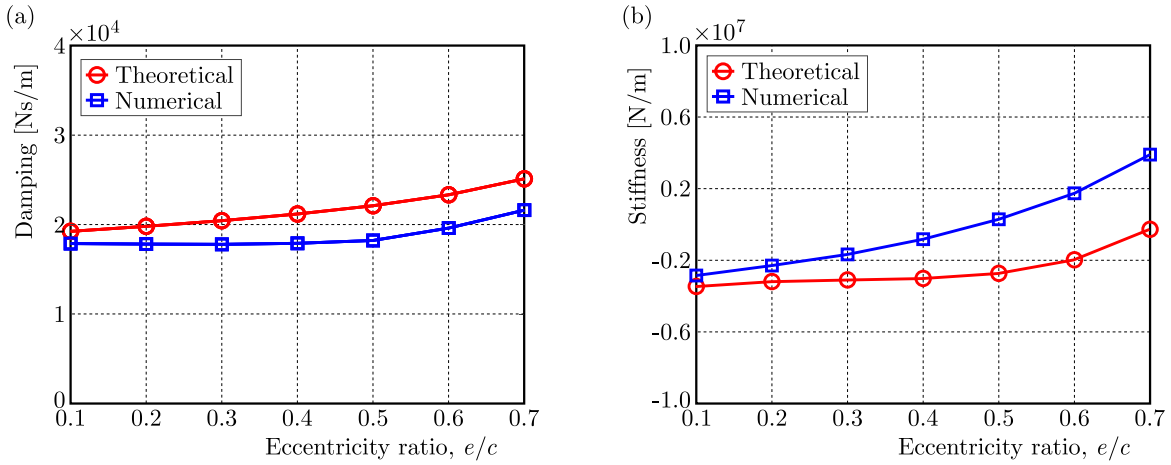

Fig. 5. Model 2 (a) damping and (b) stiffness curve with eccentricity ratio

4. Comparative analysis of sealed ends and open ends SFD

4.1. Numerical solution of short bearing SFD simulation

Referring to derivation of the theoretical formula of the short bearing SFD considering the inertia of the oil film, the oil film stiffness and equivalent oil film damping formula of the short bearing SFD containing the inertia term during stable circular precession are obtained (Zhou *et al.*, 2020a,b)

$$\begin{aligned} K &= \frac{\mu R L^3}{c^3}\left[\frac{2\varepsilon}{(1-\varepsilon^2)^2}\right]\omega - \frac{\pi\rho R L^3}{70c\varepsilon^2}\left[27 - \frac{27-17\varepsilon^2}{(1-\varepsilon^2)^{\frac{1}{2}}}\right]\omega^2 \\ C &= \frac{\mu R L^3 \pi}{2c^3(1-\varepsilon^2)^{\frac{3}{2}}} - \frac{27\rho R L^3}{70c\varepsilon}\left(2 + \frac{1}{\varepsilon}\ln\frac{1-\varepsilon}{1+\varepsilon}\right)\omega \end{aligned} \tag{4.1}$$

In order to study the vibration reduction performance of the short open ends SFD, a numerical modeling of the short open ends SFD is firstly carried out. In order to compare the dynamic characteristics of the the sealed ends SFD and the the open ends SFD, the same geometric parameters and meshing are used to reduce the effect of the corresponding factors. Figure 6 shows the local oil film absolute pressure gradient distribution of the open ends SFD and the

sealed ends SFD when the eccentricity ratio is $\varepsilon = 0.1$ and the precession frequency $f = 50\,\text{Hz}$, respectively.

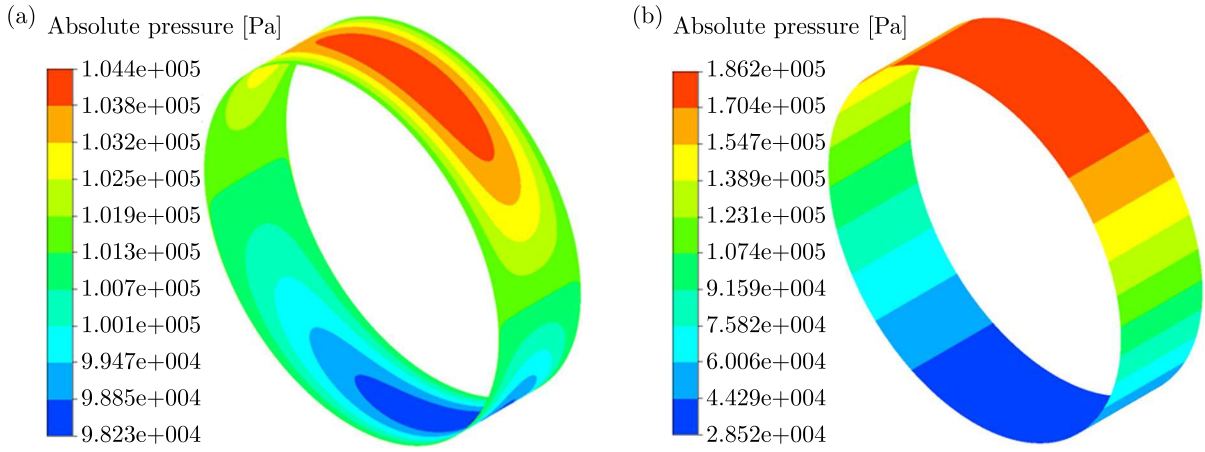

Fig. 6. SFD oil film pressure distribution: (a) open ends SFD oil film, (b) sealed ends SFD oil film

It can be seen from the pressure cloud diagram that because the short open ends SFD is open at both ends in the axial direction, and the oil film pressure change is mainly concentrated in the middle of the oil film, a certain gradient change from the middle to the two ends is observed, whereas the short sealed ends SFD is sealed at both ends in the axial direction. In the entire oil film area, there is a certain pressure gradient change. The oil film damping which plays an important role in vibration reduction is obtained by integrating the oil film pressure along the axial and circumferential directions to determine the tangential component of the oil film force. So it can be seen from the cloud diagram that the actual working oil film area of the short sealed ends SFD is larger than that of the short open ends SFD with the same structural size. Since the reference pressure at the axial ends of the short open ends SFD is the ambient pressure (0.1 MPa), the peak value of the oil film pressure under the same working conditions is also smaller than the short sealed ends SFD.

4.2. Comparative analysis of vibration reduction characteristics of the sealed and open ends SFD

The oil film tangential and radial forces are obtained by integrating the oil film pressure, and then the corresponding oil film damping and oil film stiffness are obtained. Taking the eccentricity ratio of $\varepsilon = 0.1$ and precession frequency f of 50 Hz, 75 Hz, 100 Hz, 125 Hz and 150 Hz as an example to compare damping and stiffness of the sealed and open ends SFD under the same structural parameters and working conditions, the theoretical results of model 1 are shown in Figs. 7 and 8, and the results of model 2 are shown in Figs. 9 and 10. Theoretical formula 1 is the LBA damping and stiffness formula with the inertia term, and numerical simulation 1 corresponds to the sealed ends SFD. Theoretical formula 2 is the SBA damping and stiffness formula with the inertia term, and numerical simulation 2 is made for the open ends SFD.

From the comparison curves Figs. 7-10, it can be seen that for both models 1 and 2, the variation laws of oil film damping and oil film stiffness obtained by CFD simulation with the precession frequency are in good agreement with the corresponding results obtained by the theoretical formula. With an increase of the precession frequency, the corresponding oil film damping of both sealed and open ends SFD shows an increasing trend, whereas the oil film stiffness shows a decreasing trend. Both the LBA and SBA damping and stiffness formula with the inertia term are obtained by logical simplification and assumption of oil film pressure and velocity, so there is a small deviation from the simulation results. Under the same working

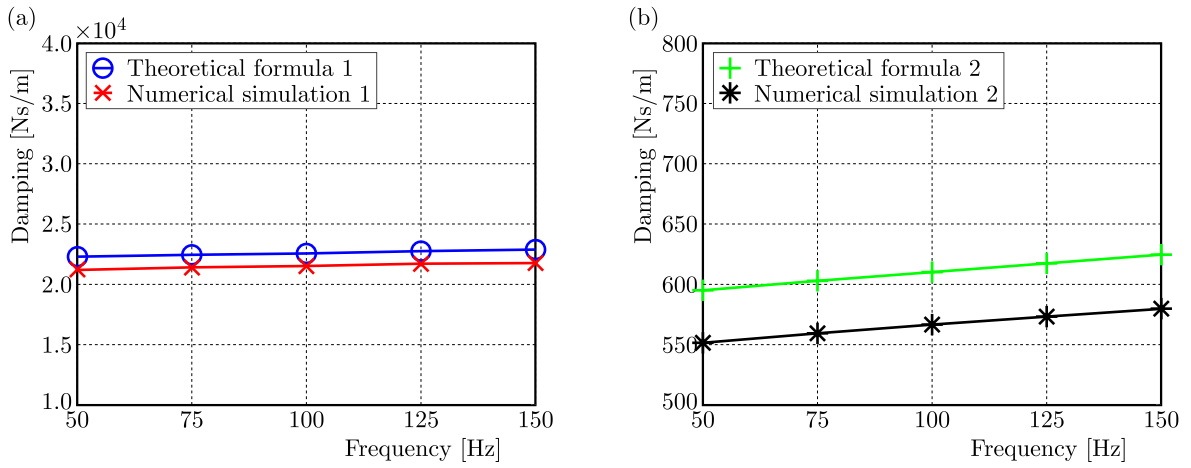

Fig. 7. Model 1 oil film damping comparison verification curve: (a) the sealed ends SFD damping versus frequency, (b) the open ends SFD damping versus frequency

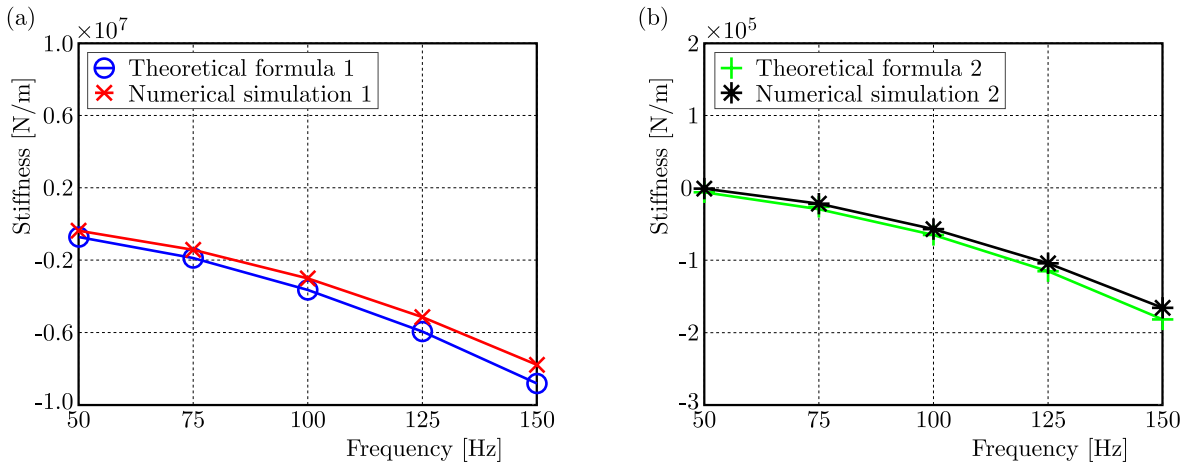

Fig. 8. Model 1 oil film stiffness comparison verification curve: (a) the sealed ends SFD damping versus frequency, (b) the open ends SFD damping versus frequency

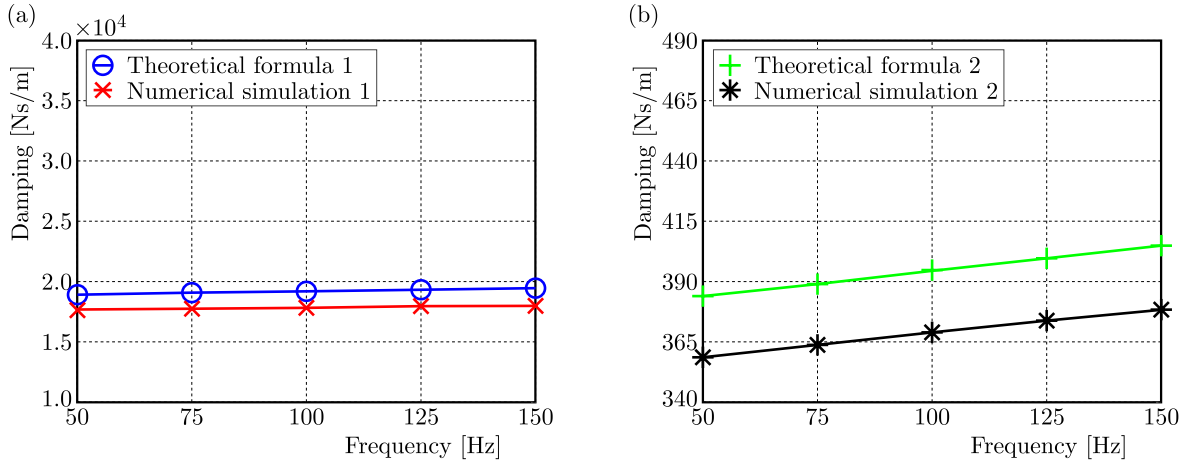

Fig. 9. Model 2 oil film damping comparison verification curve: (a) the sealed ends SFD damping versus frequency, (b) the open ends SFD damping versus frequency

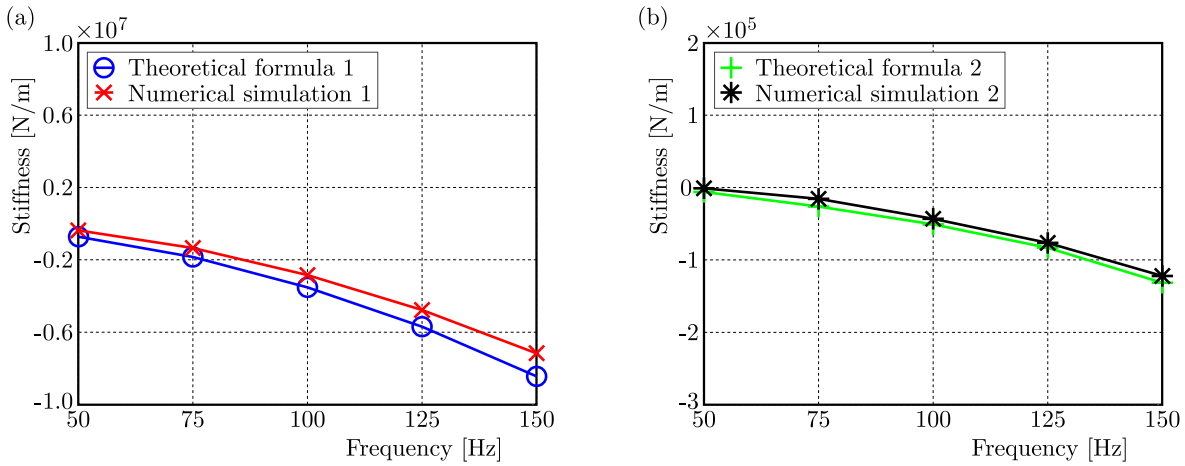

Fig. 10. Model 2 oil film stiffness comparison verification curve: (a) the sealed ends SFD damping versus frequency, (b) the open ends SFD damping versus frequency

conditions, the sealed ends SFD reveals characteristics of larger oil film damping and smaller oil film stiffness.

5. Conclusions

In this paper, an energy approximation method is used to deduce oil film damping and stiffness formulas of SFD under the assumption of long bearings. A numerical model of SFD under the LBA is established. The derived theoretical formulas are in good agreement with the numerical simulation results. The following conclusions are obtained through theoretical analysis and numerical simulation:

- The oil film damping and oil film stiffness of the sealed ends SFD generally tend to increase with a growth of the eccentricity ratio. The range of the increase of stiffness is small, which shows that the SFD with sealed ends SFD considering the effect of inertial force is conducive to reduce the amplitude and improve the stability.
- With an increase of the precession frequency of the sealed and open ends SFD, the oil film damping generally shows an increasing trend, and the oil film stiffness decreases.
- The variation laws of sealed and open ends SFD damping and stiffness obtained by CFD simulation with the precession frequency are in good agreement with the corresponding results obtained by the LBA and SBA theoretical formulas.
- Under the same working conditions and structural dimensions, the sealed ends SFD has greater oil film damping.

Acknowledgement

This research was supported by the National Natural Science Foundation of China (52175106); Plan for Young and Middle-aged Innovators of Shenyang (No: RC220326). The authors are grateful to the reviewers for their insightful and constructive comments.

References

1. Booker J., 1965, A table of the journal-bearing integral, *Journal of Basic Engineering*, **87**, 2, 533-535

2. Chen X., Ren G.M., Gan X.H., 2021. Dynamic behavior of a flexible rotor system with squeeze film damper considering oil-film inertia under base motions, *Nonlinear Dynamics*, **106**, 4, 3117-3145

3. Crandall S.H., El-Shafei A., 1993, Momentum and energy approximations for elementary squeeze-film damper flows, *Journal of Applied Mechanics*, **60**, 3, 728-736

4. Dousti S., Gerami A., Dousti M., 2016, A numerical CFD analysis on supply groove effects in high pressure, open end squeeze film dampers, *International Journal of Engineering Innovation and Research*, **5**, 1, 80-89

5. El-Shafei A., 1991, Unbalance response of a Jeffcott rotor incorporating long squeeze film dampers, *Journal of Vibration and Acoustics*, **113**, 85-94

6. El-Shafei A., 1995, Modeling fluid inertia forces of short journal bearings for rotor dynamic applications, *Journal of Vibration and Acoustics*, **117**, 462-469

7. El-Shafei A., Crandall S., 1991, Fluid inertia forces in squeeze film dampers, *Proceedings of the ASME 1991 Design Technical Conferences. 13th Biennial Conference on Mechanical Vibration and Noise: Rotating Machinery and Vehicle Dynamics*, **35**, 219-228

8. Guo Z., Hirano T., Kirk R.G., 2005, Application of CFD analysis for rotating machinery – Part I: Hydrodynamic, hydrostatic bearings and squeeze film damper, *Journal of Engineering for Gas Turbines and Power*, **127**, 2, 445-451

9. Hamzehlouia S., Behdinan K., 2016, Squeeze film dampers executing small amplitude circular--centered orbits in high-speed turbomachinery, *International Journal of Aerospace Engineering*, **1**, 1-16

10. Kuzma D.C., 1968, Fluid inertia effects in squeeze films, *Applied Scientific Research*, **18**, 1, 15-20

11. Lee G.J., Kim J., Steen T., 2017, Application of computational fluid dynamics simulation to squeeze film damper analysis, *Journal of Engineering for Gas Turbines and Power*, **139**, 10, 1-11

12. Miyachi T., Hoshiya S., Sofue Y., Matsuki M., Torisaki T., 1979, Oil squeeze film dampers for reducing vibration of aircraft gas turbine engines, *Proceedings of the ASME 1979 International Gas Turbine Conference and Exhibit and Solar Energy Conference. Volume 1B: Gas Turbines*, American Society of Mechanical Engineers, 1-11

13. San Andrés L., Seshagiri S., 2013, Damping and inertia coefficients for two end sealed squeeze film dampers with a central groove: measurements and predictions, *Journal of Engineering for Gas Turbines and Power*, **135**, 11, 1-9

14. San Andrés L., Vance J.M., 1988, Effect of fluid inertia on the performance of squeeze film damper supported rotors, *Journal of Engineering for Gas Turbines and Power*, **110**, 1, 51-57

15. Szeri A.Z., 1980, *Fluid Film Lubrication*, Cambridge University Press, New York, USA

16. Szeri A.Z., Raimondi A.A., Giron-Duarte A., 1982, Linear force coefficients for squeeze film dampers, *Journal of Lubrication Technology*, **105**, 326-334

17. Zhou H.L., Chen X., Zhang C.S., 2020a, Numerical simulation and influence factors analysis for dynamic characteristics of squeeze film damper, *Journal of Vibroengineering*, **22**, 7, 1593-1605

18. Zhou H.L., Chen X., Zhang Y.Q., Ai Y.T., Sun D., 2020b, An analysis on the influence of air ingestion on vibration damping properties of squeeze film dampers, *Tribology International*, **145**, 106168

Manuscript received October 13, 2022; accepted for print March 10, 2023

JOURNAL OF THEORETICAL AND APPLIED MECHANICS
61, 3, pp. 453-463, Warsaw 2023
https://doi.org/10.15632/jtam-pl/165954

ROBUST GENERATION METHOD OF A SIGNED DISTANCE FUNCTION FOR PREPROCESSING OF CARTESIAN-GRID-BASED CFD

Yuki Takeda, Kazuyuki Ueno, Yuta Takahashi, Karin Matsubara
Faculty of Science and Engineering, Iwate University, Japan
correspondin author Yuki Takeda, e-mail: takeday@iwate-u.ac.jp

In practical computational fluid dynamics simulations around industrial products with complex surface shapes, the robustness of preprocessing to "dirty" geometry is an important issue. The dirty STL (Standard Triangle Language) data contains errors such as gaps between facets, overlapping of facets, and flipping of normal vectors. These errors in the STL data are difficult to avoid in 3D modeling of complex geometry. Using a Cartesian grid is advantageous to the boundary-fitted grid in the aspect of preprocessing for dirty STL files. In this study, a robust and automatic generation method of a signed distance function for the preprocessing of Cartesian grid solvers is proposed. To ensure robustness to the complex and dirty STL data, the proposed method uses information of all STL facets to determine each grid point. The proposed preprocessing method is verified by numerical simulation of the flow around the NASA common research model.

Keywords: Cartesian grid dolvers, computational fluid dynamics, signed distance function, preprocessing

1. Introduction

The Cartesian grid system enables easy and automatic generation of computational grids. A favorable aspect of the Cartesian grid is that it does not require the grid system to fit the shape of the object. The voxel method (Ishida *et al.*, 2008), immersed boundary method (Peskin, 1977; Iaccarino and Verzicco, 2003) and Cartesian cut-cell method (Hu *et al.*, 2006; Takeda *et al.*, 2020a,b) are typical Cartesian grid solvers in computational fluid dynamics (CFD).

Cartesian grid solvers require an algorithm to detect the object surface to predict the flow along the surface in body-unfitted grid systems. A scalar field function that defines the object shape is commonly used in the surface detection algorithm. A signed distance function is a widely used indicator to define the object shape in Cartesian grid solvers. In the case of a flow around a rigid and static body, the signed distance function is generated in the preprocessing, and it is not updated during the main process. The level-set function in the level-set method (Sussman *et al.*, 1994; Estellers *et al.*, 2012) is a famous application of the signed distance function in CFD.

The absolute value of the signed distance function is equivalent to the distance function from the object surface. The signed distance function has a positive value when the point is outside the object and a negative value when the point is within the object. This function around a simple object shape is easily generated by a combination of piecewise elementary scalar field functions. However, object shapes associated with the computer-aided design (CAD) in practical numerical simulations cannot be described by elementary functions.

The STL file format (Szilvási-Nagy and Mátyási, 2003) in CAD software is often used to generate the signed distance function around complex geometry. In STL files, the object shape is reproduced by triangular facets, and large curvature is represented by refinement of these facets (Szilvási-Nagy and Mátyási, 2003). The STL file comprises vertices of triangular facets and unit

normal vectors of the facets. The unit normal vector defines the front or back side of each facet. Usually, the facet normal vector is defined in the outward direction of the object. However, some so-called "dirty" STL files (Lahur *et al.*, 2012) contain errors such as gaps between facets, overlapping of facets, and flipping of normal vectors. These errors are caused by the treatment of the 3D object shape in CAD software.

In 3D-CAD software, it is difficult to avoid generating of this dirty STL data. The robustness of generation of the signed distance function to dirty geometry is effective in reducing the lead time of CFD. In this study, a robust and automatic generation method of the signed distance function for Cartesian grid-based CFD is proposed. The quality of the generated signed distance function is verified by the benchmark problem in CFD.

2. Numerical method for calculating the signed distance field

2.1. Calculation of the distance from a triangular facet

An arbitrary triangular facet that constitutes STL data of an object surface is defined as a triangle ABC, as shown in Fig. 1, and this section determines the distance to an arbitrary grid point D in a 3D space. The volume V of tetrahedron $ABCD$ is expressed using vectors $\overrightarrow{AB} = \mathbf{b}$, $\overrightarrow{AC} = \mathbf{c}$, and $\overrightarrow{AD} = \mathbf{d}$ as follows

$$V = \frac{1}{6}(\mathbf{b} \times \mathbf{c}) \cdot \mathbf{d} \tag{2.1}$$

The volume V is also expressed as

$$V = \frac{1}{3} S_{ABC} |\overrightarrow{ED}| \tag{2.2}$$

where $S_{ABC} = |\mathbf{b} \times \mathbf{c}|/2$ is the area of triangle ABC and $|\overrightarrow{ED}|$ is height of tetrahedron $ABCD$. From Eqs. (2.1) and (2.2), distance d_E is expressed as follows

$$d_E = |\overrightarrow{ED}| = \frac{(\mathbf{b} \times \mathbf{c}) \cdot \mathbf{d}}{|\mathbf{b} \times \mathbf{c}|} \tag{2.3}$$

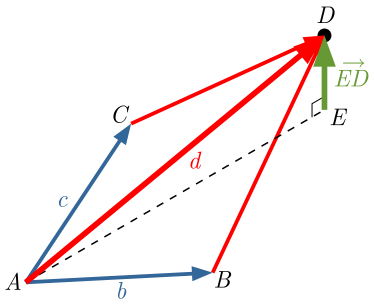

Fig. 1. Geometry of tetrahedron $ABCD$ and foot E

Let us introduce d_{ABC} as the distance between point D and the triangular facet. This distance is calculated according to the positional relationship between triangle ABC and foot E perpendicular to plane D, including triangle ABC. Expressing the vector $\overrightarrow{AE} = k_1\mathbf{b} + k_2\mathbf{c}$, the vector $\overrightarrow{AE}$ is

$$\overrightarrow{ED} = \mathbf{d} - (k_1\mathbf{b} + k_2\mathbf{c}) \tag{2.4}$$

The vector $\overrightarrow{ED}$ is orthogonal to the vectors $\mathbf{b}$ and $\mathbf{c}$

$$\mathbf{b}\cdot[\mathbf{d}-(k_1\mathbf{b}+k_2\mathbf{c})]=0 \qquad \mathbf{c}\cdot[\mathbf{d}-(k_1\mathbf{b}+k_2\mathbf{c})]=0 \tag{2.5}$$

Coefficients k_1 and k_2 are obtained by solving simultaneous Eq. (2.5)

$$\begin{bmatrix}k_1\\k_2\end{bmatrix}=\frac{1}{Det}\begin{bmatrix}\mathbf{c}\cdot\mathbf{c} & -\mathbf{b}\cdot\mathbf{c}\\ -\mathbf{b}\cdot\mathbf{c} & \mathbf{b}\cdot\mathbf{b}\end{bmatrix}\begin{bmatrix}\mathbf{b}\cdot\mathbf{d}\\ \mathbf{c}\cdot\mathbf{d}\end{bmatrix} \tag{2.6}$$
$$Det=(\mathbf{b}\cdot\mathbf{b})(\mathbf{c}\cdot\mathbf{c})-(\mathbf{b}\cdot\mathbf{c})^2$$

The positional relationships between triangle ABC and point E expressed by k_1 and k_2 are shown in Fig. 2. The distance d_{ABC} is determined via different formulas according to the values of k_1 and k_2. In the case of point E inside the triangle, the distance d_{ABC} coincides with d_E

$$d_{ABC}=\frac{(\mathbf{b}\times\mathbf{c})\cdot\mathbf{d}}{|\mathbf{b}\times\mathbf{c}|} \tag{2.7}$$

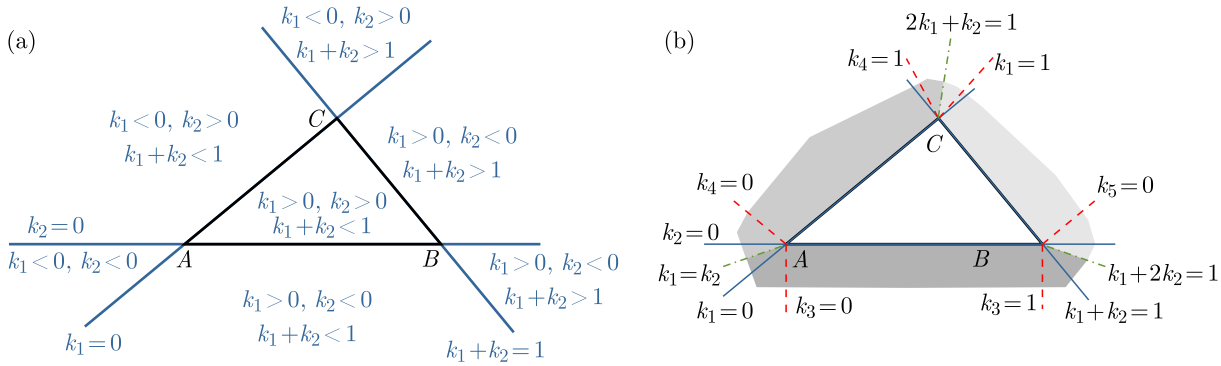

Fig. 2. Distribution of the functions k_1, k_2, k_3 and k_4 around triangle ABC: (a) distribution of the solutions k_1 and k_2, (b) relation between (k_1, k_2) and the position of foot E in the perpendicular direction

If point E is outside the triangle, d_{ABC} is determined by Table 1 using the area division in Fig. 2b. The coefficients k_3, k_4 and k_5 are as follows

$$k_3=\frac{\mathbf{b}\cdot\mathbf{d}}{\mathbf{b}\cdot\mathbf{b}} \qquad k_4=\frac{\mathbf{c}\cdot\mathbf{d}}{\mathbf{c}\cdot\mathbf{c}} \qquad k_5=\frac{(\mathbf{c}-\mathbf{b})\cdot(\mathbf{d}-\mathbf{b})}{(\mathbf{c}-\mathbf{b})\cdot(\mathbf{c}-\mathbf{b})} \tag{2.8}$$

Table 1. Area division of point E placed outside the triangle ABC

Position of point E (range of k_1 and k_2)	Range of coefficients k_i and value of d_{ABC}		
Vicinity of side AB ($k_1 > k_2$ and $k_1 + 2k_2 < 1$)	$k_3 \leqslant 0$ $\lvert\mathbf{d}\rvert$	$0 < k_3 < 1$ $\lvert\mathbf{b}\times\mathbf{d}\rvert/\lvert\mathbf{b}\rvert$	$k_3 \geqslant 1$ $\lvert\mathbf{d}-\mathbf{b}\rvert$
Vicinity of side AC ($k_1 < k_2$ and $2k_1 + k_2 < 1$)	$k_4 \leqslant 0$ $\lvert\mathbf{d}\rvert$	$0 < k_4 < 1$ $\lvert\mathbf{c}\times\mathbf{d}\rvert/\lvert\mathbf{c}\rvert$	$k_4 \geqslant 1$ $\lvert\mathbf{d}-\mathbf{c}\rvert$
Vicinity of side BC ($k_1 + 2k_2 > 1$ and $2k_1 + k_2 > 1$)	$k_5 \leqslant 0$ $\lvert\mathbf{d}-\mathbf{b}\rvert$	$0 < k_5 < 1$ $\lvert(\mathbf{c}-\mathbf{b})\times(\mathbf{d}-\mathbf{b})\rvert/\lvert\mathbf{c}-\mathbf{b}\rvert$	$k_5 \geqslant 1$ $\lvert\mathbf{d}-\mathbf{c}\rvert$

The distance from the object surface is obtained by sweeping all triangular facets. The minimum value of d_{ABC} is the absolute value $|\phi|$ of the signed distance function ϕ. To determine $|\phi|$, only the values of the nearest facet for point D are selected, and other facets have no effect after the selection.

2.2. Sign evaluation of the signed distance function ϕ

The sign of the signed distance function is determined by considering the positional relationship with the object. This inside/outside evaluation regarding the object (represented by a polyhedron) is called the point-in-polyhedron test (Carvalho and Cavalcanti, 1995; Baerentzen and Aanaes, 2005; Li and Wang, 2017). The ray casting method (Roth, 1982) and the method using the sign of the inner product are well-known and simple implementations of the point-in--polyhedron testing. However, these implementations are non-robust against errors in the STL data file because they refer to limited number of facets to detect the sign of a grid point. This study implements a point-in-polyhedron testing method using summation of the solid angle. In contrast to the conventional method, this method uses the information of all STL facets to determine the sign of each grid point. This method refers to the point-in-polyhedron testing method originally proposed by Carvalho and Cavalcanti (1995) in the context of computer graphics.

The solid angle ω is defined as shown in Fig. 3 as the area of a spherical triangle on a unit sphere centered at grid point D. The absolute value $|\omega|$ of the solid angle ω is given by

$$|\omega| = \alpha + \beta + \gamma - \pi \tag{2.9}$$

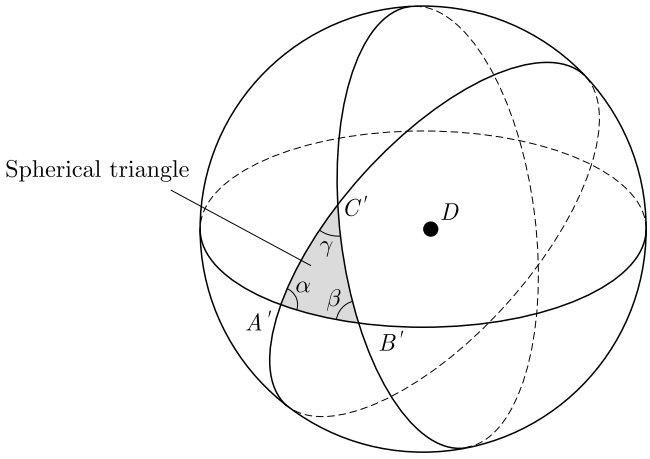

Fig. 3. Definition of the spherical triangle $A'B'C'$ on a unit sphere

We consider the interior angles α, β and γ. The intersection of the straight line DA and the unit sphere centered at D is defined as point A'. Points B' and C' are defined in the same way

$$\mathbf{a}' = \overrightarrow{DA'} = -\frac{\mathbf{d}}{|\mathbf{d}|} \qquad \mathbf{b}' = \overrightarrow{DB'} = \frac{\mathbf{b}-\mathbf{d}}{|\mathbf{b}-\mathbf{d}|} \qquad \mathbf{c}' = \overrightarrow{DC'} = \frac{\mathbf{c}-\mathbf{d}}{|\mathbf{c}-\mathbf{d}|} \tag{2.10}$$

The normal vector of the plane that includes the great circle $A'B'$ shown in Fig. 3 is expressed by $\overrightarrow{DA'} \times \overrightarrow{DB'}$, while the normal vector of the plane that includes the great circle $A'C'$ is $\overrightarrow{DA'} \times \overrightarrow{DC'}$. The angle between these two planes is equivalent to the interior angle α

$$\alpha = \arccos \frac{(\mathbf{a}' \times \mathbf{b}') \cdot (\mathbf{a}' \times \mathbf{c}')}{|\mathbf{a}' \times \mathbf{b}'|\,|\mathbf{a}' \times \mathbf{c}'|} \tag{2.11}$$

Similarly, β and γ are expressed as follows

$$\beta = \arccos \frac{(\mathbf{b}' \times \mathbf{c}') \cdot (\mathbf{b}' \times \mathbf{a}')}{|\mathbf{b}' \times \mathbf{c}'|\,|\mathbf{b}' \times \mathbf{a}'|} \qquad \gamma = \arccos \frac{(\mathbf{c}' \times \mathbf{a}') \cdot (\mathbf{c}' \times \mathbf{b}')}{|\mathbf{c}' \times \mathbf{a}'|\,|\mathbf{c}' \times \mathbf{b}'|} \tag{2.12}$$

The sign of the signed solid angle ω is determined by considering the positional relationship from grid point D to triangular facet ABC: front side or back side. An arbitrary point F on triangle ABC is introduced as follows

$$\overrightarrow{DF} = \mathbf{f} = -\mathbf{d} + s_1\mathbf{b} + s_2\mathbf{c} \qquad s_1 \geqslant 0 \qquad s_2 \geqslant 0 \qquad s_1 + s_2 \leqslant 1 \tag{2.13}$$

We take the inner product of $\mathbf{f}$ and the unit normal vector $\mathbf{n}$ that is directed to the front of the triangle facet ABC

$$\mathbf{f} \cdot \mathbf{n} = (-\mathbf{d}) \cdot \mathbf{n} + s_1\mathbf{b} \cdot \mathbf{n} + s_2\mathbf{c} \cdot \mathbf{n} = (-\mathbf{d}) \cdot \mathbf{n} \tag{2.14}$$

where $\mathbf{f} \cdot \mathbf{n}$ is equal to $(-\mathbf{d}) \cdot \mathbf{n}$ and independent of the position of point F on triangle ABC. Thus, the sign of the solid angle ω is determined as follows

$$\begin{cases} \omega > 0 & \text{if} \quad (-\mathbf{d}) \cdot \mathbf{n} > 0 \quad (D \text{ locates in the back-side of triangle } ABC) \\ \omega < 0 & \text{if} \quad (-\mathbf{d}) \cdot \mathbf{n} < 0 \quad (D \text{ locates in the front-side of triangle } ABC) \end{cases} \tag{2.15}$$

The positional relationship of grid point D and the object surface is estimated by integrating the signed solid angle ω as follows

$$\sum_{\text{all facet}} \omega = \begin{cases} 0 & \text{if} \quad D \text{ locates outside of the object} \\ 4\pi & \text{if} \quad D \text{ locates inside of the object} \end{cases} \tag{2.16}$$

Considering the dirty STL data, the detection threshold is implemented as follows

$$\begin{cases} \phi > 0: & \text{outside} & \text{if} & \displaystyle\sum_{\text{all facet}} \omega \leqslant 2\pi \\ \phi < 0: & \text{inside} & \text{if} & \displaystyle\sum_{\text{all facet}} \omega > 2\pi \end{cases} \tag{2.17}$$

The estimation of the signed distance function ϕ is summarized as follows: 1. Calculate the distance by Eq. (2.7) and Table 1 and 2 determine the sign by Eq. (2.17). In contrast to the estimation of $|\phi|$, the information of all facets is reflected for the estimation of the sign of the signed distance function ϕ.

3. Numerical results of the signed distance function around complex and dirty geometry

The signed distance function around the NASA Common Research Model (NASA-CRM) (Uchiyama *et al.*, 2019), a wind tunnel model of an airplane, is calculated to test the performance of the present method for complex and dirty geometry. The NASA-CRM consists of a body, main wing and tail wing, as shown in Fig. 4a. In this test, robustness to dirty STL data, including gaps, overlaps or inversion of the normal vector of the facets, is evaluated.

Figure 4b shows an example of overlapping facets. Orange, blue and green triangles overlap each other. On the other hand, triangle facets in Fig. 4c are colored by the direction of the normal vector of the facet. Although the main wing consists of one convex surface, some facets are colored red. This suggests an inversion normal vector.

A conventional simple point-in-polyhedron testing method is introduced for comparison. The vector from grid point D to arbitrary point F on the nearest triangle facet is defined as $\mathbf{f}$. Considering the unit normal vector $\mathbf{n}$ is directed outside the object, the sign of the distance function is estimated by the inner product $\mathbf{f} \cdot \mathbf{n}$

$$\begin{cases} \phi > 0: & \text{outside} & \text{if} & \mathbf{f} \cdot \mathbf{n} < 0 \\ \phi < 0: & \text{inside} & \text{if} & \mathbf{f} \cdot \mathbf{n} > 0 \end{cases} \tag{3.1}$$

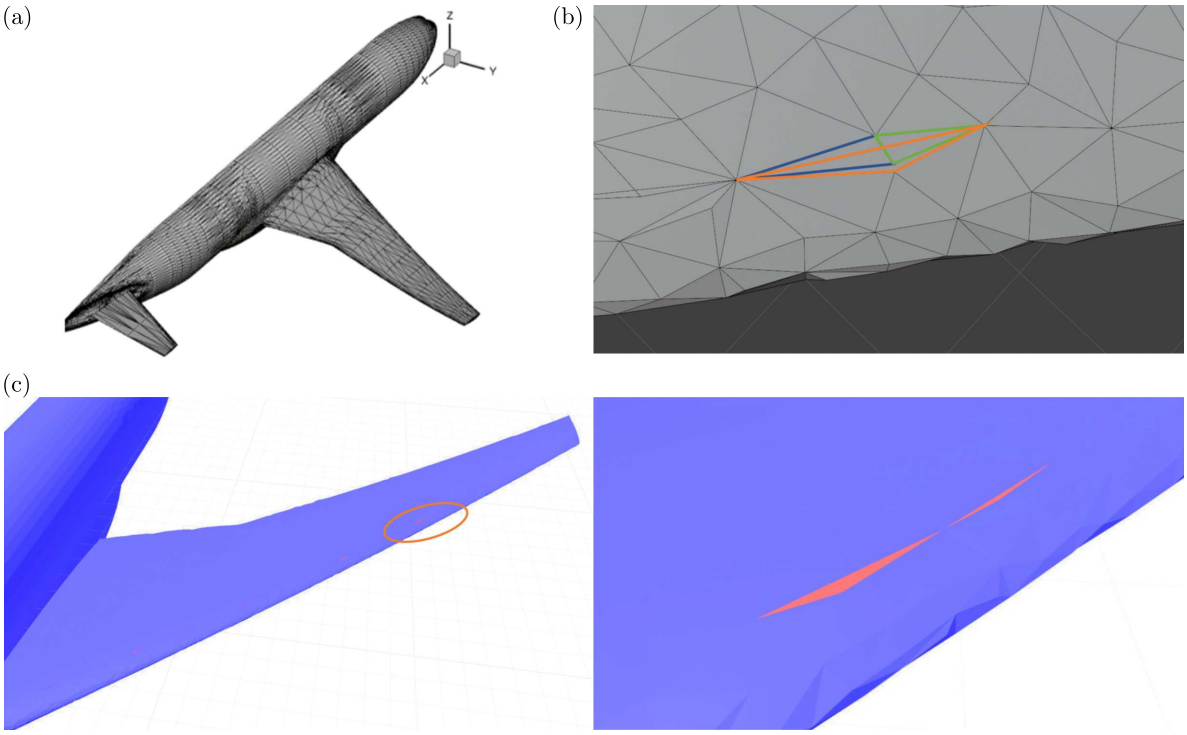

Fig. 4. Goemetry of NASA-CRM and typical errors in the STL data: (a) geometry of NASA-CRM, (b) overlapped triangle facets, (c) triangle facets with the inversion normal vector (red facet), (d) vicinity of the orange circle of the figure (c)

This inner product is independent of the position on the facet, similar to that shown in Eqs. (2.13) and (2.14). Thus, the implementation is as follows

$$\begin{cases} \phi \geqslant 0: & \text{outside} & \text{if} & (-\mathbf{d}) \cdot \mathbf{n} < 0 \\ \phi < 0: & \text{inside} & \text{if} & (-\mathbf{d}) \cdot \mathbf{n} > 0 \end{cases} \tag{3.2}$$

Figure 5 shows the isosurface $\phi = 0$ of the signed distance function for NASA-CRM. In the technique using the summation of solid angles, the sign is correctly determined. However, the trailing edge of the main wing and the tail wing have a saw-like shape. This arises from the grid resolution and has been confirmed to exhibit grid convergence.

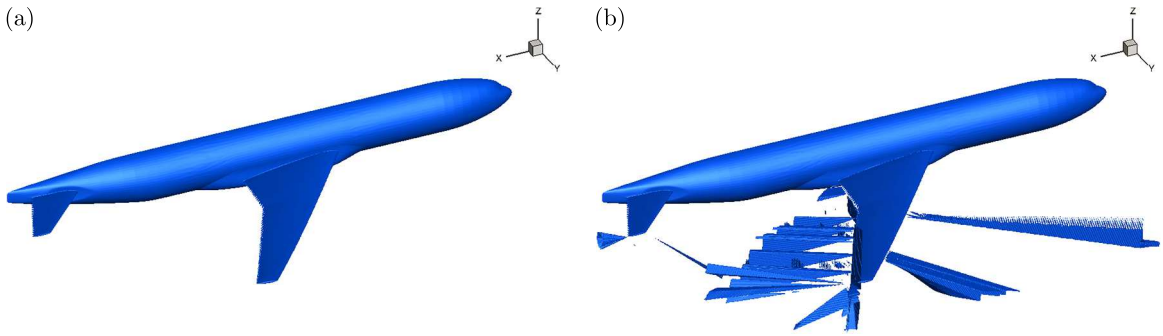

Fig. 5. Distribution of the zero-level isosurface of the signed distance function ϕ: (a) estimation (2.17) based on spherical trigonometry, (b) conventional estimation (3.2) based on the facet normal

In the result of the technique using the unit normal vector of the nearest facet, there are many grid points where the sign of ϕ is misevaluated. When a facet includes inversion of the unit normal vector, the misevaluation of the sign is radially distributed.

Figure 6 shows the errors of volume estimation, and the error is defined as follows

$$\text{Error} = \frac{|V_{\text{Estimated}} - V_{\text{STL}}|}{V_{\text{STL}}} \tag{3.3}$$

Here, $V_{\text{Estimated}}$ is the volume of the NASA-CRM estimated by voxel estimation and cut-cell estimation. The voxel volume estimation is applied to the signed distance function evaluated by the unit normal vector of nearest facet (3.2) and the summation of solid angles (2.17). The cut-cell volume estimation is applied to the signed distance function by the summation of the solid angle. The error of volume estimation of the signed distance function using the summation of the solid angles is converged with a grid refinement. However, the error of the method using the unit normal vector of the nearest facet is independent of the grid resolution.

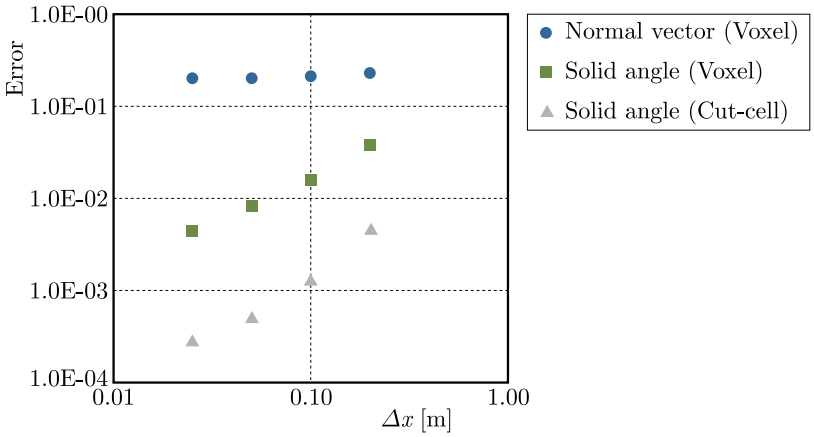

Fig. 6. Errors of volume estimation by two point-in-polyhedron methods: blue circle plots indicate method (3.2) using the unit normal vector of the nearest facet (voxel estimation); green square plots and gray triangle plots indicate method (2.17) using the summation of the solid angles (voxel estimation and cut-cell estimation)

In order to confirm the influence of a facet on the solid angle at an arbitrary grid point, we now calculate the solid angle for a single facet of an equilateral triangle with a side length of 1, and the facet normal vector is $\mathbf{n} = [1, 0, 0]$. It is assumed that the facet is in the y-z plane and that the position of the center of gravity coincides with the origin. The maximum solid angle for the facet is obtained in the surface. Figure 7 shows the distribution of the solid angle ω in the x-y cross-section of $z = 0$. The absolute value of the solid angle is $x \to 0$, and the maximum value is 2π. As $|x|$ increases, the value of $|\omega|$ decreases rapidly. Therefore, when the direction of the normal vector of a facet is reversed, its influence on the neighbor grid point is larger, and grid points far from the facet are only minimally influenced.

The value of ω is negligible at the point shifted from the facet normal direction. Therefore, even when the direction of the normal vector of two or more adjacent facets is reversed, the effects are minimal.

When using the summation of solid angles, the evaluation inversion of the sign occurs if and only if the grid point is extremely close to the facet which exhibits inversion of the normal vector. Even in such a case, the inversion is limited to only one grid point. This indicates the robustness of sign determination (2.17) using the summation of the solid angle when this approach is applied to the data, including the inversion of the facet normal vector.

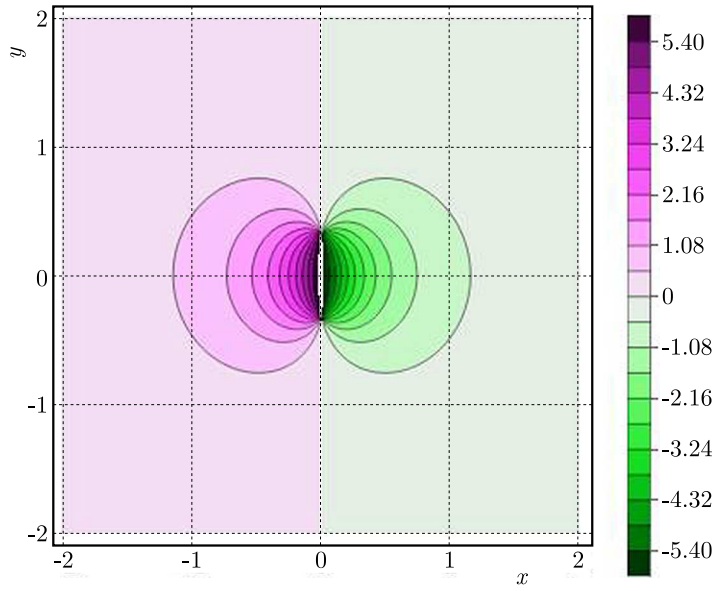

Fig. 7. Distribution of ω along the facet normal coordinate x and the parallel coordinate y

4. Numerical example for application to computational fluid dynamics

4.1. Calculation conditions

In this study, the calculation condition refers to the experimental study by Uchiyama *et al.* (2019). The object is a half-cut shape of the NASA-CRM composed of the main wing, body, and tail wing. The average aerodynamic chord length c of the main wing is 7.00532 m, and the span length b is 29.38145 m. The angle of attack α has two values: 11.05° and 13.08°. The Mach number of the far uniform flow is set at 0.168. The Reynolds number based on the average aerodynamic chord length is $1.06 \cdot 10^6$. For details of the experimental settings, see Uchiyama *et al.* (2019).

The CFD analysis is performed by the Cartesian cut-cell simulation code developed by Takeda *et al.* (2020a). The Cartesian cut-cell method gives a better volume estimation than the voxel method, as shown in Fig. 6. The calculation area is set to exceed 300 m in both the x and y directions and to exceed 900 m in the z direction. The uniform grid is applied to $2\,\mathrm{m} \leqslant x \leqslant 70\,\mathrm{m}$, $0\,\mathrm{m} \leqslant y \leqslant 32\,\mathrm{m}$, and $2\,\mathrm{m} \leqslant z \leqslant 15\,\mathrm{m}$. The nose of the NASA-CRM places at $x = 2.36$ m. The grid width of the uniform grid normalized by chord length $\Delta x/c$ is $7.14 \cdot 10^{-3}$. The implicit large eddy simulation (ILES) is employed in this study, and the wall-stress model by Kawai and Larsson (2012) is used to estimate the wall shear stress.

The inflow boundary condition at the x and z boundaries corresponds to a uniform flow, and the outflow boundary condition is a zero gradient. A symmetric boundary condition is applied at $y = 0$, and the boundary condition at $y = y_{max}$ corresponds to the uniform flow.

4.2. Flow around the NASA-CRM

Figure 8 shows the instantaneous distribution of the contour map of the Mach number in an isosurface of the second invariant of the velocity gradient tensor (Q-criterion) around the NASA-CRM. A leading-edge separation is observed on the suction side of the main wing along the wide range of the wing span.

Figure 9 shows an oilflow visualization of the experiment (Uchiyama *et al.*, 2019) and the time-averaged surface streamlines in the present study. The blue arrow indicates the origin of the leading edge separation in the spanwise direction. The starting point of the leading edge

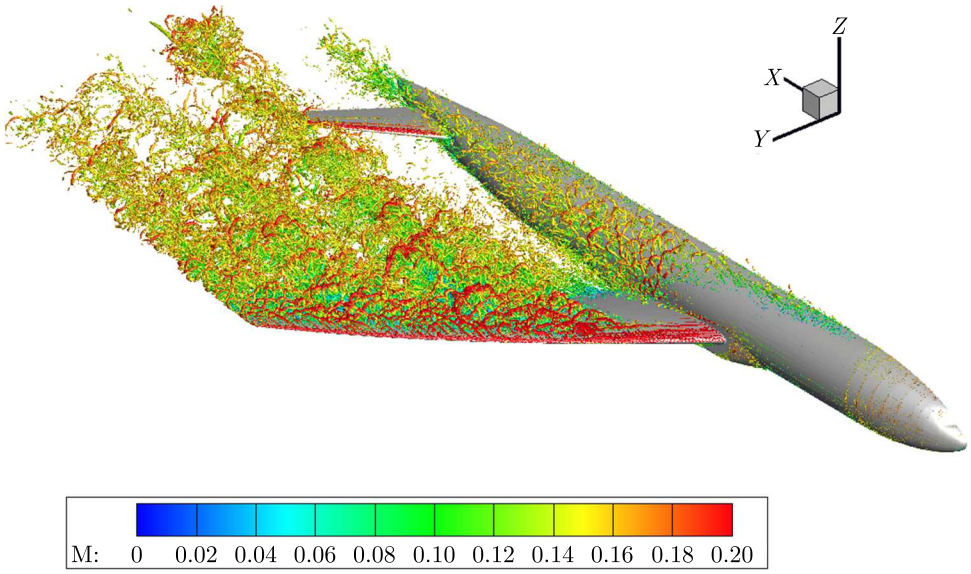

Fig. 8. Instantaneous distribution of the contour map of the Mach number in an isosurface of the second invariant of the velocity gradient tensor at $\alpha = 11.05°$

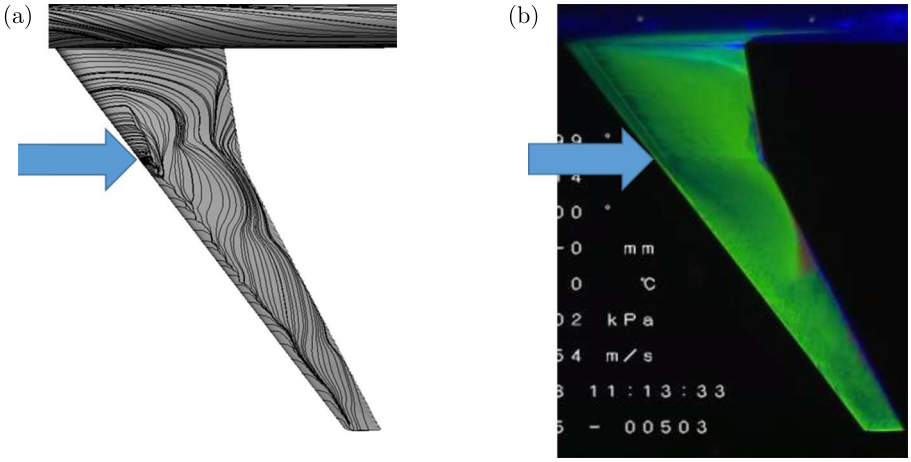

Fig. 9. (a) Surface streamline from the present CFD analysis, (b) oilflow visualization of the experiment (Uchiyama *et al.*, 2019) at $\alpha = 11.05°$

separation agrees with the experimental results. Furthermore, the separation area around the wingtip is also consistent with these results.

4.3. Aerodynamic coefficients

The lift coefficient C_L, drag coefficient C_D, and pitching moment coefficient C_M are calculated using the following expressions

$$C_L = \frac{L}{\frac{1}{2}\rho_\infty U_\infty^2 S} \qquad C_D = \frac{D}{\frac{1}{2}\rho_\infty U_\infty^2 S} \qquad C_M = \frac{M}{\frac{1}{2}\rho_\infty U_\infty^2 Sc} \tag{4.1}$$

Here, $S = 383.6895552\,\mathrm{m}^2$ is the reference area. The constants ρ_∞ and U_∞ indicate the free-stream density and velocity, respectively.

Figures 10a, 10b and 10c show the C_L-α, C_D-α and C_M-α diagrams, respectively. The angle-of-attack dependency of the present CFD is consistent with the experimental results, and the error of C_L in the experiment at $\alpha = 11.05°$ is 6.4%. The underestimation of C_D and C_M at $\alpha = 13.08°$ is caused by the underestimation of contribution of the underresolved tail wing.

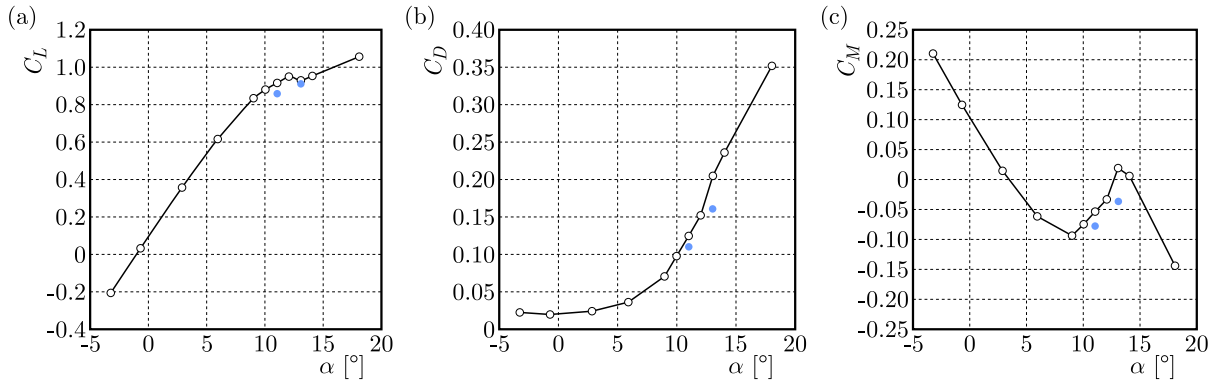

Fig. 10. Aerodynamic coefficients: blue filled circles indicate the present CFD analysis; open circles indicate the experimental results (Uchiyama *et al.*, 2019): (a) C_L-α diagram, (b) C_D-α diagram, (c) C_M-α diagram

5. Conclusion

A robust and automatic generation method of the signed distance function for the preprocessing of CFD is proposed. The proposed method uses summation of the solid angle of all facets of the object to ensure robustness for complex and dirty STL data. This generation method of the signed distance function is compared with the conventional method using the facet normal vector of the nearest facet.

In order to test the robustness, the signed distance function is generated from the STL data of the NASA-CRM that contains errors. The summation of the solid angle gives an appropriate signed distance function. However, the conventional method using a facet normal vector of the nearest facet misrecognizes external points of the NASA-CRM as inside points of the object. This misevaluation occurs at the grid point associated with facets with a flipped normal vector.

Computational fluid dynamics simulations of the external flow around the NASA-CRM are conducted to verify the signed distance function generated using the solid angle. This CFD analysis appropriately predicts the starting point of the leading edge separation. The angle-of-attack dependency of the aerodynamic coefficients (C_L, C_D and C_M) agrees with the experimental results.

Acknowledgments

The authors express their profound gratitude to the Cyber Science Center of Tohoku University and Earth Simulator Center of Japan Agency for Marine-Earth Science and Technology (JAMSTEC) for providing computational resources for this research.

References

1. Baerentzen J.A., Aanaes H., 2005, Signed distance computation using the angle weighted pseudonormal, *IEEE Transactions on Visualization and Computer Graphics*, **11**, 3, 243-253

2. Carvalho P.C.P., Cavalcanti P.R., 1995, *Point in Polyhedron Testing Using Spherical Polygons, Graphics Gems V*, Academic Press, Inc., 42-49

3. Estellers V., Zosso D., Lai R., Osher S., Thiran J.P., Bresson X., 2012, Efficient algorithm for level set method preserving distance function, *IEEE Transactions on Image Processing*, **21**, 12, 4722-4734

4. Hu X.Y., Khoo B.C., Adams N.A., Huang F.L., 2006, A conservative interface method for compressible flows, *Journal of Computational Physics*, **219**, 2, 553-578

5. Iaccarino G., Verzicco R., 2003, Immersed boundary technique for turbulent flow simulations, *Applied Mechanics Reviews*, **56**, 3, 331-347

6. Ishida T., Takahashi S., Nakahashi K., 2008, Efficient and robust Cartesian mesh generation for building-cube method, *Journal of Computational Science and Technology*, **2**, 4, 435-446

7. Kawai S., Larsson J., 2012, Wall-modeling in large eddy simulation: Length scales, grid resolution, and accuracy, *Physics of Fluids*, **24**, 1, 1-10

8. Lahur P.R., Hashimoto A., Murakami K., 2012, Automatic grid generation for dirty STL data using approximate concave feature, *50th AIAA Aerospace Sciences Meeting Including the New Horizons Forum and Aerospace Exposition*, January, 1-10

9. Li J., Wang W., 2017, Fast and robust GPU-based point-in-polyhedron determination, *CAD Computer Aided Design*, **87**, 20-28

10. Peskin C.S., 1977, Numerical analysis of blood flow in the heart, *Journal of Computational Physics*, **25**, 3, 220-252

11. Roth S.D., 1982, Ray casting for modeling solids, *Computer Graphics and Image Processing*, **18**, 2, 109-144

12. Sussman M., Smereka P., Osher S., 1994, A level set approach for computing solutions to incompressible two-phase flow, *Journal of Computational Physics*, **114**, 1, 146-159

13. Szilvási-Nagy M., Mátyási G., 2003, Analysis of STL files, *Mathematical and Computer Modelling*, **38**, 7-9, 945-960

14. Takeda Y., Ueno K., Ishikawa T., Takahashi Y., 2020a, Prediction capability of Cartesian cut-cell method with a wall-stress model applied to high Reynolds number flows, *Applied Sciences* (Switzerland), **10**, 15

15. Takeda Y., Ueno K., Matsuyama S., Tanno H., 2020b, Coupled numerical analysis of three--dimensional unsteady flow with pitching motion of reentry capsule – investigation of the third harmonics of the aerodynamic force, *Transactions of the Japan Society for Aeronautical and Space Sciences*, **63**, 6, 249-256

16. Uchiyama T., Kohzai M., Miki H., Hirotani T., Sudani N., Shutoku H., 2019, Experimental investigation of a 160% scaled NASA common research model at low speed conditions, *AIAA Scitech 2019 Forum*, January, 1-21

Manuscript received January 24, 2023; accepted for print April 18, 2023

JOURNAL OF THEORETICAL AND APPLIED MECHANICS
61, 3, pp. 465-480, Warsaw 2023
https://doi.org/10.15632/jtam-pl/166276

INSTABILITY MECHANISM AND ANCHORING CONTROL TECHNOLOGY OF EXPANSIVE WEAKLY CEMENTED SOFT ROCK ROADWAY

Wei Zhang

School of Architecture and Civil Engineering, Liaocheng University, Liaocheng, China
e-mail: 1125671372@qq.com

A long-term discontinuous development of the plastic zone and broken zone of weakly cemented surrounding rock is the main reason for instability of the surrounding rock of a roadway. The load-bearing support concept of "allowable deformation + releasable pressure + limited deformation" for a weakly cemented soft rock roadway is proposed, and an "allow-release-limit" support structure mechanical model with U-shaped steel as the main body is established. Anchoring control measures of "U-shaped steel + flexible material wall backfill + key parts strengthening" can solve problems of large deformation and long deformation duration of weakly cemented roadways.

Keywords: weakly cemented soft rock, roadway support, deformation control, expansion, support concept

1. Introduction

Hongqingliang mine is a modern large-scale mine at the background of China's in-depth implementation of the western development strategy and acceleration of construction of key mining areas and coal power as well as coal chemical bases in the Inner Mongolia Autonomous Region (Zhao *et al.*, 2020; Zhang *et al.*, 2022a, 2023). The coal-bearing strata of Hongqingliang coal mine are widely distributed in a special kind of soft rock, namely weakly cemented soft rock. Fang *et al.* (2019) found through triaxial testing that the ultimate strength of wet rock blocks is 60%-85% of the ultimate strength of dry rock blocks. Theocharis *et al.* (2020) determined that the softening coefficient of weakly cemented sandstone ranges from 0.22 to 0.92. Sharma *et al.* (2010) confirmed that the failure mode of weakly cemented sandstone during water softening is mainly due to detachment of cementitious materials. Weakly cemented soft rock has properties of low strength, poor cementation, and easy mudding in contact with water (Wang *et al.*, 2020; Zhang *et al.*, 2022b; Li *et al.*, 2018). The RQD (Rock Quality Designation) and uniaxial compressive strength of weakly cemented soft rock are smaller than the common soft rock indicators in the eastern mines in the past (Zhang *et al.*, 2022c). According to the past domestic and engineering experience, weakly cemented soft rock roadways have characteristics of short self-stabilization time and large deformation, which often leads to traditional construction and support methods that cannot effectively maintain long-term stability of the roadway, which seriously threatens safety of mine production (Mineo and Pappalardo, 2019; Aguilera *et al.*, 2019; Showkati *et al.*, 2015).

In the recent years, many scholars have studied the engineering support method of soft rock roadways from different aspects, among which the most representative theories are the Fenner and Kastner formula, new Austrian method and energy support theory. Yang *et al.* (2019) proposed a support method that used a rigid truss with sufficient strength to limit deformation of soft rock. Luo *et al.* (2018) proposed a comprehensive reinforcement support method using high prestressed and high-strength anchor rods. Kang *et al.* (2015) proposed a design concept of

the step-by-step joint support. Bhuiyan *et al.* (2018) proposed a strong anchoring and grouting support technology. The research on the instability mechanism of expansive cemented soft rock roadways is not thorough, and there are few ideas for roadway supports, and a set of research techniques suitable for weakly cemented soft rock roadways that are prone to disintegration has not been formed. In the present application process, the support structure and roadway deformation are often not coupled, or the support structure is wasted, or the support structure cannot reach the strength. Therefore, studying deformation characteristics and stress patterns of weakly cemented soft rock to solve the problems encountered in support design and construction can provide experience and reference for similar research.

During the excavation process of Hongqingliang mine, there are notable features such as poor roadway formation, large deformation of surrounding rock and long duration of a large deformation rate. Yang and Jing (2011) found that the surface of the roadway is broken, and the roadway tray is plunged into the anchor net by using the anchor net spray. Tu *et al.* (2022) found that the anchor net became a pocket under the action of broken surrounding rock, the roof and floor were seriously deformed. Zhang *et al.* (2020) found that the maximum value exceeds 800 mm, and the volume of the bottom drum reached more than 600 mm, which seriously affected formation and safety of the roadway. Therefore, it is necessary to carry out research on the instability mechanism and control technology of expansive weakly cemented soft rock roadways to provide a guarantee for safe production of coal mines.

While the intensity of coal resource extraction has significantly increased, in order to meet the requirements of coal mine intelligence and intensification, more large cross-section chambers need to be arranged underground. The cavern group is generally characterized by a large cross section, dense layout, long service life, etc., and the surrounding roadways are complex. Affected by unpredictable geological conditions such as high ground stress, faults, folds, etc., it is difficult to maintain the cavern group, the surrounding rock deformation is serious, and the surrounding rock instability is easily induced, which is a major problem to be solved in the geotechnical engineering field. At present, research on large cross-section chambers in high stress concentration areas near the intersection of complex rock strata is relatively rare, and the design and support methods are not yet mature. The research results have important significance in improving the current situation of mine safety production, maintaining stable and sustainable development of mining areas, and improving enterprise economic benefits. They have important practical significance and certain reference value for achieving safe and efficient mining in mines with such geological conditions. At the same time, they can further enrich the relevant theories of weak cemented soft rock roadway surrounding rock control.

2. Analysis of instability mechanism and influencing factors of roadways

2.1. Instability form of a soft rock roadway

The coal-measure stratum in Hongqingliang mine is a weakly cemented soft rock, and the surrounding rock of the roadway has characteristics of easy expansion, low strength, weak cementation, developed fissures, softening in contact with water, easy disintegration and rheological properties.

At present, deformation and failure forms of the surrounding rock of the anchor-net-spray--cable support structure adopted in Hongqingliang mine are manifested in the following aspects:

- The surrounding rock on the roof is broken, and there are pockets, tearing of the mesh and damage to the overlap of the mesh.
- The anchor rod and anchor cable are pulled or sheared, resulting in a reduction in the support strength,

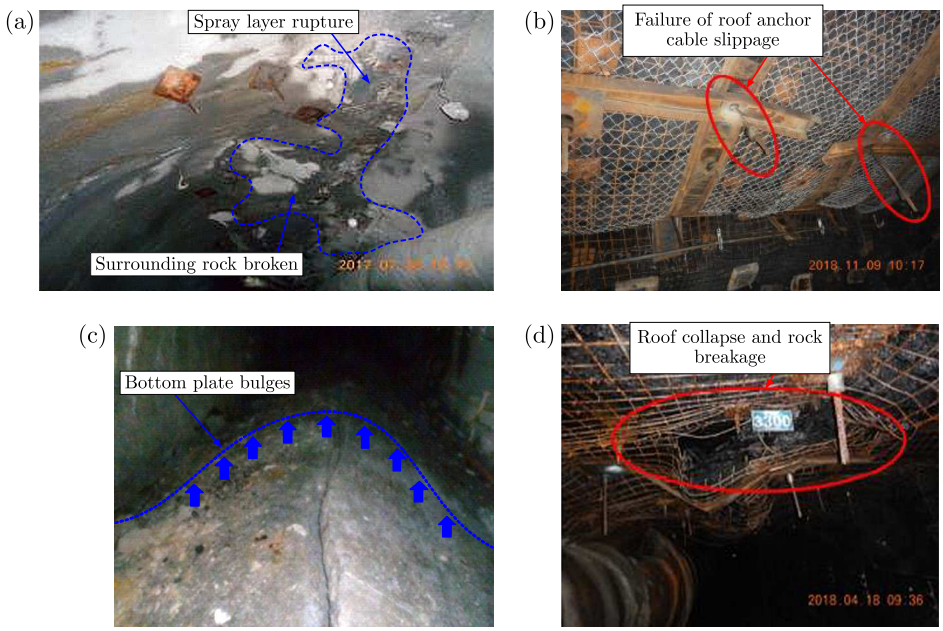

Fig. 1. The failure mode of a weakly cemented soft rock roadway: (a) spray layer rupture, (b) roof anchor cable slippage, (c) deformation of the bottom plate, (d) failure of the roof

- The lap joint of the mesh is cracked, the surface spray layer is cracked, and the spray layer falls off.
- The rock around the pallet is crushed and sheared, and the bolt pallet falls into the anchor net.

The anchor net becomes pocket-shaped under the action of broken surrounding rock, and the support resistance is reduced.

2.2. Deformation characteristics of the weakly cemented soft rock roadway

The deformation characteristics of the surrounding rock in weakly cemented soft rock roadways are mainly manifested in a short self-stabilization time, large initial deformation rate, long deformation duration, easy to be disturbed, and easy to become muddy when encountering water. The deformation of the weakly cemented soft rock roadway is obvious after excavation, which is embodied in:

- The self-stabilization time is short and the stress release is obvious. Within a few hours of excavation or excavation of the roadway, the surface surrounding rock of the roof and the two sides begins to break or even peel off.
- The initial deformation rate is fast and the deformation lasts for a long time. The maximum deformation rate of the roadway after one-time support is 50 mm/d, the average deformation rate of the roadway is 8-15 mm/d, and the deformation rate of the roadway gradually slows down into a stable state at about 60 d and keeps deforming at a low rate.
- The surrounding rock of the roadway is easily disturbed. Due to development of cracks, low strength and disintegration in water, the stability of the roadway can easily be changed and leads to deformation and damage when the stress of the rock mass changes under the influence of dynamic pressure.

2.3. Analysis of the instability mechanism of the weakly cemented soft rock roadway

The excavation of the roadway destroys the original stress balance state of the surrounding rock, resulting in redistribution of the surrounding rock stress and occurrence of stress con-

centration in the surrounding rock of the roadway. The surrounding rock mass of the roadway changes from the original three-way stress state to a two-way or even one-way stress state, and the bearing capacity of the surrounding rock is greatly reduced, resulting in deformation or even rupture of the surrounding rock, and a certain range of damage areas is formed. The factors affecting roadway stability of Hongqingliang mine are divided into two categories: mining condition factors and construction quality factors.

- The mining condition factors are mainly affected by inherent characteristics of the coal strata and coal-forming environment, which are embodied in:
  - The roof and floor rocks are weakly cemented, soft and broken, easily disturbed, and have low integrity.
  - The rock strength is low. The average uniaxial compressive strength of mudstone is 3-7 MPa, and the average uniaxial compressive strength of fine sandstone is 5-11 MPa, and the uniaxial compressive strength of coal generally does not exceed 6 MPa.
  - The initial in-situ stress field has a great influence. The maximum principal stress of Hongqingliang mine is mainly horizontal stress, and it is easy to cause large deformation of the bottom drum and the two sides.
- Construction quality factors are mainly determined by the level of design and construction management, which are embodied in:
  - The size and shape of the roadway section. There is a close relationship between the size of the roadway section and the deformation of the surrounding rock.
  - Design support strength is not reached. The flexibility or stiffness of the support body is not up to the standard, and some surrounding rock is not coupled with the deformation of the support structure, resulting in deformation and damage of the roadway, or even instability.

3. Thinking and principle of the soft rock roadway support

3.1. Supporting ideas for the weakly cemented soft rock roadway

The key measures for the roadway support should be placed on making a full use of and exerting the self-supporting capacity of the surrounding rock, so that the surrounding rock pressure can be fully released while supporting in time. Combined with the present situation of Hongqingliang mine, the support idea of "timely closure, combination of long and short supports, secondary control, reinforcement of key parts, and long-term monitoring" and the load-bearing support concept of "allowable deformation + releasable pressure + limited deformation" for weakly cemented soft rock roadway are proposed as shown in Fig. 2.

3.1.1. Timely closure

The surrounding rock on the roadway surface of Hongqingliang mine is generally broken after excavation. If it is not closed in time, the surrounding rock will be easily broken and extended to depth under the condition of one-way or two-way force and weathering, resulting in formation of fins or roofs rock falls. Therefore, after excavation, the surrounding rock should be sealed by the initial injection in time, and a support should be carried out immediately after the initial injection to ensure integrity of the surrounding rock on the roadway surface.

3.1.2. Combination of long and short supports

Because the plastic loosening area formed by the soft rock is generally large, the supporting pressure is also relatively large, and the bearing ring formed by the anchor net spraying to

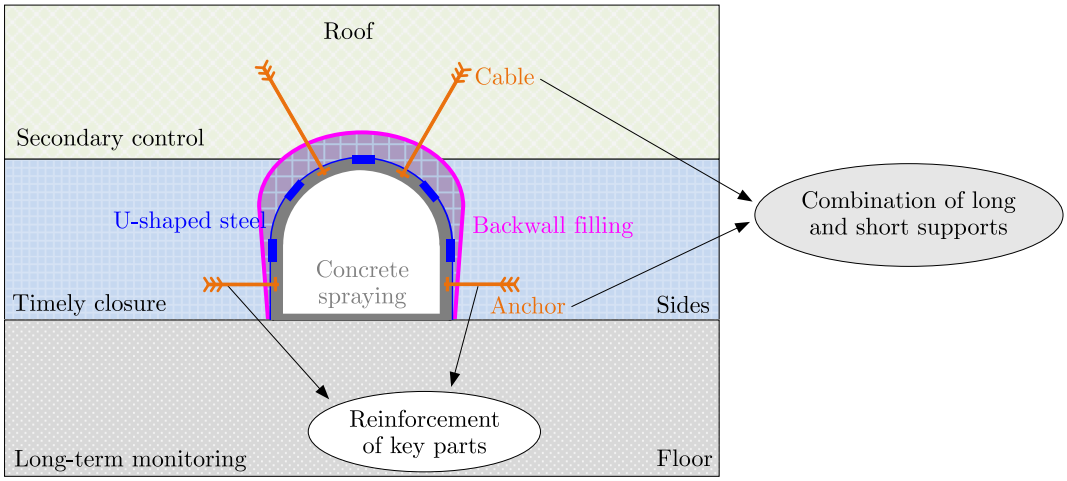

Fig. 2. Support concept of the weak cementation roadway

stabilize the shallow surrounding rock often cannot achieve an effective supporting effect. It is necessary to use an anchor cable to mobilize strength of deep surrounding rock and realize combination of long and short structures, so that the entire support body and the surrounding rock within the largest range can achieve the best supporting mechanical state.

3.1.3. Secondary control

In order to ensure that the deformation of the surrounding rock is controlled within a reasonable range and realize safety and normal use of the roadway, the "allowable deformation" should be fully considered when restoring the support, and the support body should leave a certain deformation space for the surrounding rock of the roadway. The "releasable pressure" allows the surrounding rock to release a certain amount of pressure. The "limited deformation" keeps the surrounding rock deformation within a controllable range to ensure the shape of the roadway section.

3.1.4. Reinforcement of key parts

The key point of the reinforcement is to determine the key parts, which can be judged according to stress field distribution characteristics in numerical simulation results. The U-shaped steel bracket has a certain shrinkability, which can realize full-section support of the roadway, evenly bear the surrounding rock stress, and fully guarantee the cross-sectional shape of the roadway. The concept of restoration and support requires a U-shaped steel shed as the main support method. On the basis of the support of the retractable U-shaped steel bracket, the cobblestone wall is backfilled, which has functions of flexible energy release and deformation and conforms to the support and bearing concept of "allowable deformation" and releasable pressure.

3.1.5. Long-term monitoring

The deformation of the surrounding rock is the most direct manifestation of the mechanical shape change of the surrounding rock. By performing on-site deformation measurements, the active state and time effect of surrounding rock deformation can be grasped, and the supporting structure and parameters can be determined. The deformation of weakly cemented strata has characteristics of a long time effect, so insisting on long-term monitoring is of great signifi-

cance for timely understanding the stability information of the surrounding rock and taking the corresponding reinforcement measures.

3.2. Principles for maintaining residual strength of surrounding rock

The strength of weakly cemented soft rock will generally decrease after being affected by water or weathering. Therefore, after excavation of the roadway, concrete should be shot in time to seal the rock surface to prevent weathering and deliquescence of the surrounding rock, reduce the loss of surrounding rock strength, and help maintain the surrounding rock strength. There are four technical ways to improve the residual strength of the surrounding rock.

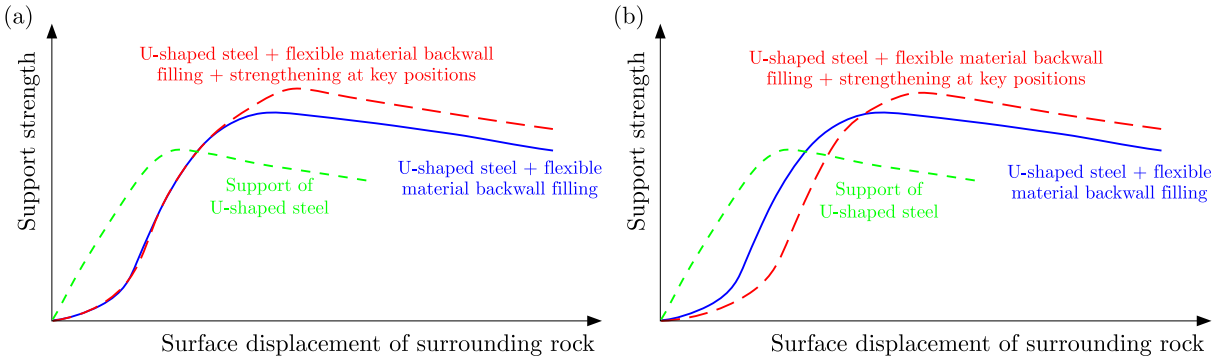

Fig. 3. Support concept of the weak cementation roadway: (a) effect of roadway roof repair, (b) effect of roadway sides repair

- Enhance support resistance and improve surrounding rock stress state. After the roadway is excavated, the support should be carried out as soon as possible to make the surrounding rock change from a one-way or two-way stress state to a three-way stress state, so as to improve the residual strength of the surrounding rock. The support body must not only have a certain support strength, but also a considerable amount of deformation, and the deformation of the support body should always occur under a higher support resistance.
- Give full play to the bearing capacity of the surrounding rock. Considering factors such as the existence of voids and the broken surrounding rock after U-shaped steel repairs the support wall, problems such as a poor contact state between the support and surrounding rock and uneven stress on the support are caused. The surrounding rock is easy to damage the U-shaped steel support to different degrees under the action of a concentrated load, or even lose its function, resulting in a poor overall support effect and unnecessary economic losses. Therefore, on the basis of the support of the retractable U-shaped steel bracket, the backfilling of the cobblestone (flexible material) wall is performed. At the same time, the shed anchors are added to the shed legs at the key parts of the surrounding rock support, and the steel mesh + concrete is laid on the bottom plate.
- Focus on the secondary support. It is generally difficult to use a rigid support with a strong resistance in soft rock roadways, because it is not suitable for characteristics of large initial deformation and fast deformation speed of soft rock roadways. In order to adapt to the deformation characteristics of soft rock, the method of the secondary support and repair should be adopted. The primary support is mainly to strengthen the surrounding rock and improve its residual strength. Under the condition of no excessive expansion and shear deformation, the active support is used to control deformation of the surrounding rock and relieve the pressure. The secondary repair and support should be completed in a timely manner after the surrounding rock is deformed and stabilized, so as to provide the final support strength and stiffness to the surrounding rock of the roadway and maintain stability and safety reserves of the roadway for a long time.

4. Engineering practice of soft rock roadway control

The auxiliary transportation roadway of Hongqingliang mine is arranged in 2 coal seams. The lithology of the roof and floor is mainly muddy and sandy rocks, the uniaxial compressive strength is 3-11 MPa, and the cohesion is 1.8-3.4 MPa. The surrounding rock is determined to be expansive soft rock by physical component analysis, and its mineral composition is made of quartz, albite, illite and chlorite, which belongs to the category of geological soft rock. During construction of an auxiliary transportation roadway, the following problems occurred: after the roadway was excavated, the roof of the newly excavated roadway sinked, and the shotcrete layer was cracked and damaged. Secondly, the bottom plate bulged and the concrete floor was damaged. Finally, the gangway was damaged. Roadway damage was mainly due to roof sinking and bottom bulging. In view of the failure of the auxiliary transportation inclined roadway, the supplementary anchor cable is used for support, but the effect is limited, and the roadway deformation continues to increase. Finally, the support method of U-shaped steel + flexible material wall backfill + reinforcement of key parts was used.

4.1. Engineering practice of the U-shaped steel support and backfilling

Combined with the original section size of the roadway, the parameters of the U-shaped steel restoration support section are designed, and the spacing between the U-shaped steel restoration and support sheds is determined by numerical simulation.

4.1.1. Determination of section size

As shown in Fig. 4, the section size of the roadway failure zone is 5.3 (5.0) m×4.35 (4.1) m in width and height. The arch radius of the net section is 2.3 m and the height of the right--angle side is 1.8 m. In order to maintain the original shape of the roadway section and consider installation of U-shaped steel into the roadway, the arch radius of the U-shaped steel support section is 2.4 m, and the installation space of the roof and the two gangs is 0.1 m.

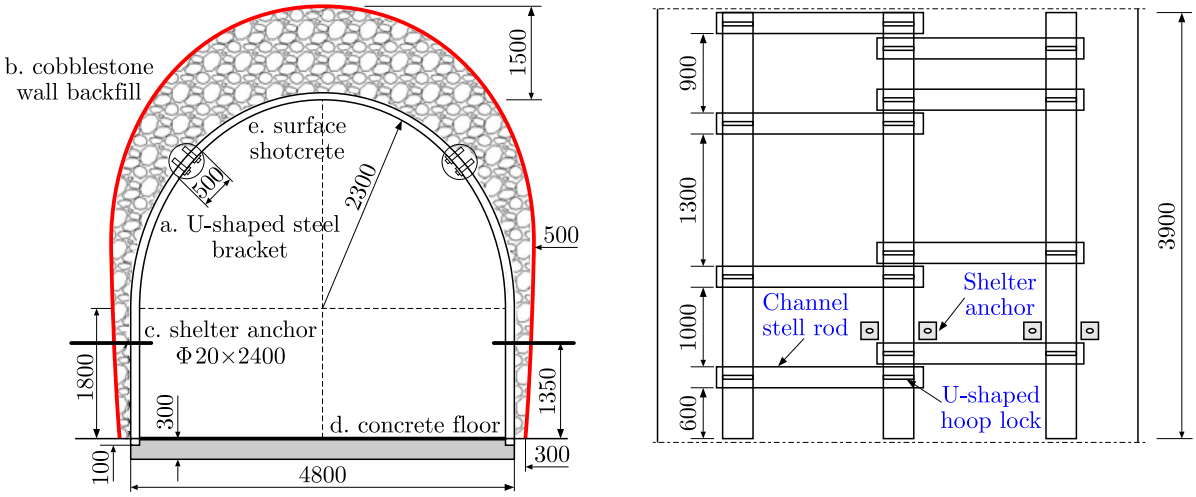

Fig. 4. Schematic diagram of the support section (unit: mm)

The maximum axial force of U-shaped steel is located at the spandrel position, where depth of the brush and cobblestone filling needs to be increased. Considering the arch radius of the U-shaped steel section with a radius of 2.4 m and height of the right-angle edge of the U-shaped steel of 1.9 m, the filling thickness of the cobblestone is 0.5 m. At the height of 3/4 of the straight leg of the scaffolding (1.35 m above the scaffolding foot), the bending moment is the

largest, where it is easy to bend and deform, and the scaffolding anchor rod of Ø20 mm×2400 mm is added to restrain the scaffolding deformation. The axial force at the lap joint of the roof and shed is close to the maximum axial force of the U-shaped steel, which is easily subjected to concentrated stress. By installing the U-shaped hoop, U-shaped steel expansion and relative slippage are prevented. The foot of the U-shaped steel frame has a large force, and it needs to be reinforced by shotcrete. The bottom plate reserves a shotcrete thickness of 0.3 m to prevent the bottom plate from extruding and deforming the U-shaped steel.

4.1.2. Determination of the U-shaped steel spacing

In order to fully compare the influence of U-shaped steel support parameters on the control effect of roadway surrounding rock, three support schemes with U-shaped steel spacing of 0.8 m, 1 m and 1.2 m were studied by numerical simulation. The numerical calculation model was established by FLAC3D. The size of the model is 50 m×50 m×30 m, 50 m in the x direction, 50 m in the y direction, and 30 m in the z direction, as shown in Fig. 5. The Mohr-Coulomb model is selected for the constitutive relationship, and the beam unit is used for U-shaped steel. The top, left and right boundaries of the model are stress boundaries. The uniformly distributed forces of 10 MPa and 25 MPa are applied to represent the ground stress, and the front, back and bottom boundaries are displacement boundaries. The mechanical parameters of the rock stratum are listed in Table 1. The U-shaped steel spacing is set to 0.8 m, 1.0 m and 1.2 m, and the stress and plastic zone corresponding to the three shed spacing schemes are calculated respectively.

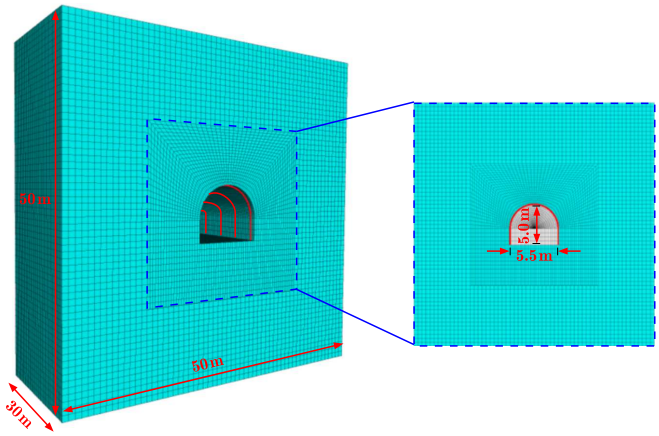

Fig. 5. Schematic diagram of the support section

Table 1. Rock layer physical and mechanical parameters

Name of rock stratum	Density [kg/m^3]	Bulk modulus [GPa]	Shear modulus [GPa]	Tensile strength [MPa]	Cohesion [MPa]	Internal friction angle [°]
Siltstone	2450	0.70	0.49	0.96	4.84	40
Coal	1300	0.41	0.23	0.20	0.34	29
Mudstone	2620	0.39	0.24	0.25	2.42	40

According to Fig. 6, under the condition of different spacing support schemes, the vertical and horizontal stress distribution are similar, and stress concentration occurs at the top and bottom of the roadway. The difference is that the stress distribution range increases with an increase of spacing. Compared with 1 m and 1.2 m spacing, the vertical stress distribution range is reduced by 15% and 60%, and the horizontal stress distribution range is reduced by 20%

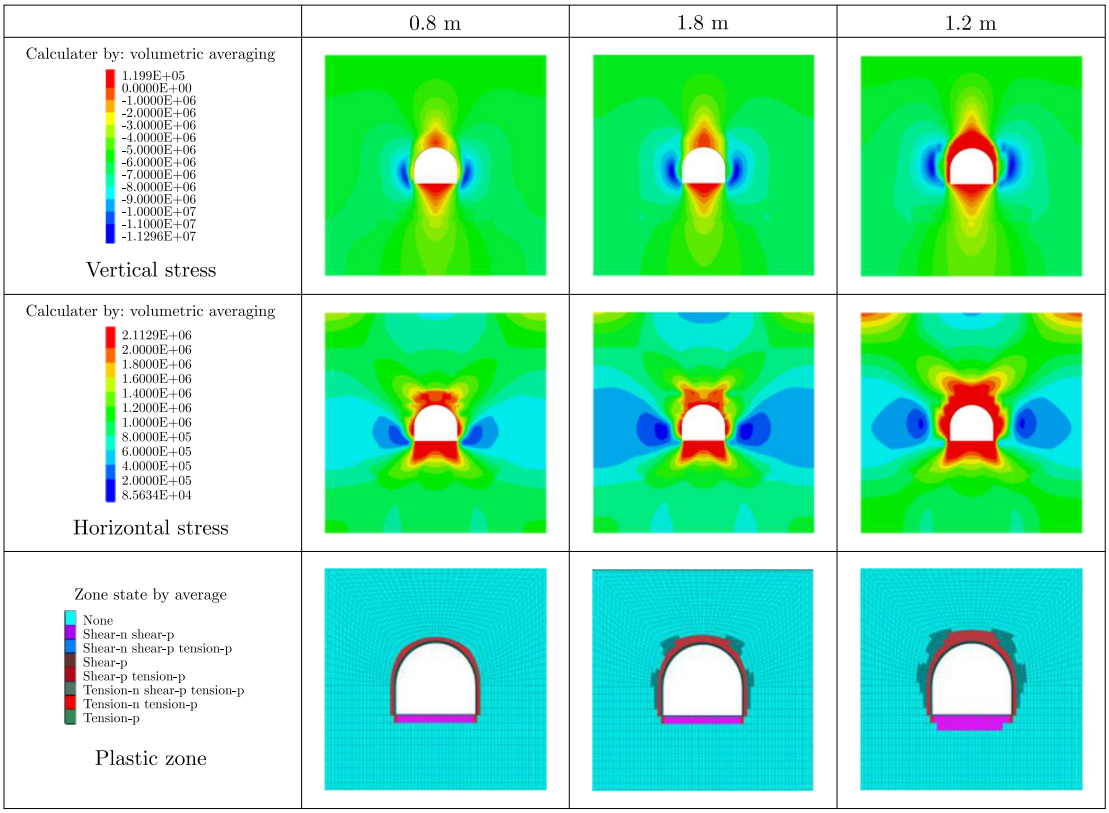

Fig. 6. Calculation results of the stress and plastic zone

and 90% respectively when the spacing is 0.8 m. It shows that shortening the spacing can fully improve the bearing capacity of U-shaped steel, and the difference between 0.8 m and 1 m in reducing the stress range is within 20%.

After the U-shaped steel support is adopted, the overall distribution range of the plastic zone in the failure zone of the roadway is reduced. When the U-shaped steel spacing is 0.8 m, the plastic deformation is concentrated on the edge of the U-shaped steel. When the spacing is 1 m, the plastic zone is concentrated on the roof of the roadway, and the range of the plastic zone is 0.2 m. When the spacing is 1.2 m, the plastic zone expands more obviously on the roof and floor of the roadway, and the scope of the plastic zone is increased to 0.5 m, which is significantly larger than that of the 0.8 m and 1 m spacing. It shows that shortening the spacing can reduce the area of the plastic zone around the U-shaped steel, and the spacing of 0.8 m and 1 m is similar in reducing the area of the plastic zone.

According to the deformation amount, the stress value and plastic zone distribution of the surrounding rock, it is comprehensively analyzed that the spacing of 0.8 m can effectively control the deformation of the surrounding rock of the roadway compared with the spacing of 1 m and 1.2 m. The gap between the support effect of 0.8 m and 1 m spacing is small, but the 1 m spacing can save large economic cost compared with the 0.8 m spacing.

4.2. Application practice of the support parameter optimization

The construction process of the U-shaped steel support on the roadway site mainly includes: brush the roof and sides, brush the floor, reinforce the mesh on the floor, install I-beams and shed legs, install the ceiling, backfill, lay the floor, repair shed anchor and shotcrete.

4.2.1. Brush the roof and sides

As shown in Fig. 7, the brushing is performed by a rock drill. In the case of uneven rock, it is necessary to use the air pick to further complete the brushing to ensure that the two bottoms are brushed out on average 300 mm each, and the waist is brushed out on average 500 mm.

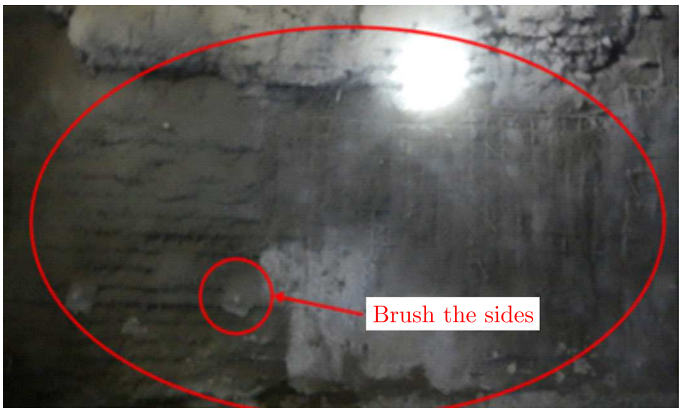

Fig. 7. Clear the roadway anchor

4.2.2. Brush the floor

After the top of the roadway is supplemented with anchor cables and the nets are laid on the side to supplement the bolts, the fully mechanized excavator is used to sweep the bottom, and then the forklift is used for leveling. Finally, manual leveling is performed to ensure that depth of the roadway is about 300 mm. The scope of sweeping the bottom is within 10 m in front of the U-shaped steel, and the gangue generated by the supplementary anchor cable, brushing and bottom pulling is transported out through the belt.

4.2.3. Reinforcing mesh on the floor

After sweeping the floor of the roadway, use the explosion-proof vehicle to transport the steel mesh to the floor of the roadway where the mesh is laid, and start laying the steel mesh at the floor as shown in Fig. 8. The size of the steel mesh is Ø6.5 mm, the mesh size is 100×100 mm, and the size of the steel mesh is 1200×2000 mm. The roadway floor is completely covered by the steel mesh, and the two steel meshes are tightened with steel wires.

Fig. 8. Laying reinforced mesh

4.2.4. Install I-beams and shed legs

As shown in Fig. 9, after the net laying is over, the explosion-proof truck transports the 12# I-beam to the net laying place, and manually arranges the I-beam at a spacing of 1 m.

Fig. 9. Field installation of U-shaped steel shed legs

The laying length of the I-beam is within 10 m in front of the U-shaped steel. The U-shaped steel shed legs are erected from the side of the lane, and the base of the shed legs is placed on the I-beam. There are four sets of screw holes on the base of the shed leg, and 2 U-shaped steels are inserted into the screw holes from the bottom of the I-beam, and the screws are tightened with a pneumatic wrench. At this time, it is necessary to prevent the shed leg from being sideways.

4.2.5. Install the ceiling

After the two sets of U-shaped steel are erected, the ceiling is erected from the initial erection legs firstly, and the second channel steel tie rod of the lane is erected. The ceiling is lifted by a forklift, and the ceiling is pulled by ropes and hung on the top of the roadway finally. Then a 40 mm U-shaped steel is installed in the groove with the upper end of the U-shaped steel scaffolding down 500 mm as a limit device to prevent the upper beam from sliding down and expanding. Two 40 mm U-shaped hoops are installed on both sides of the overlapping section between the ceiling and the shed legs, as shown in Fig. 10.

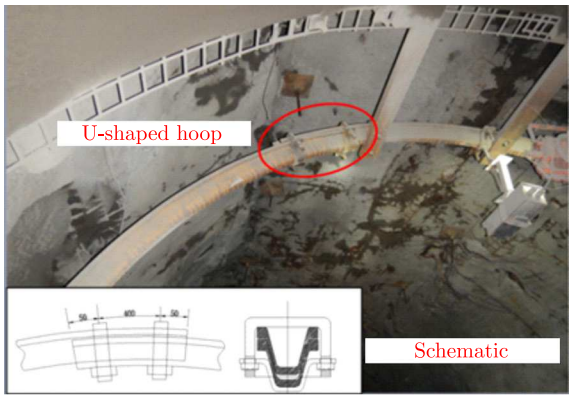

Fig. 10. Erecting the ceiling in the roadway

4.2.6. Backfill

As shown in Fig. 11, the order of filling behind the wall is to fill the gap between the roadway and the U-shaped shed firstly. Then the cobblestone is lifted with a forklift, and the worker stands above the bare netting shed and fills the gap between the top and the U-shaped shed. The cobblestone filling of the roof and lanes is gradually advanced at a speed of 1 m.

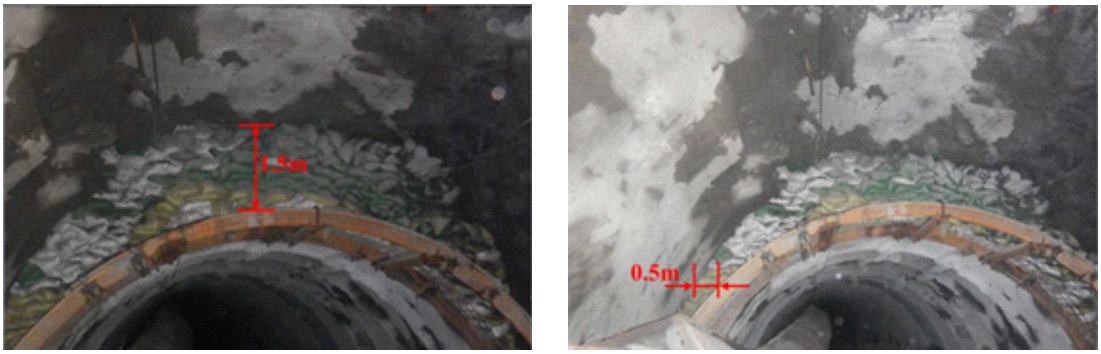

Fig. 11. Backfill with pebbles

4.2.7. Laying the floor

After the roof and sides of the roadway are filled with cobblestones, the floor will be laid. The thickness of concrete laid on the floor is about 300 mm, and the concrete burial depth of the base of scaffolding is about 100 mm (the floor is laid as shown in Fig. 12). The laying length of the floor is within 10 m in front of the shed, and the uneven area needs to be leveled manually.

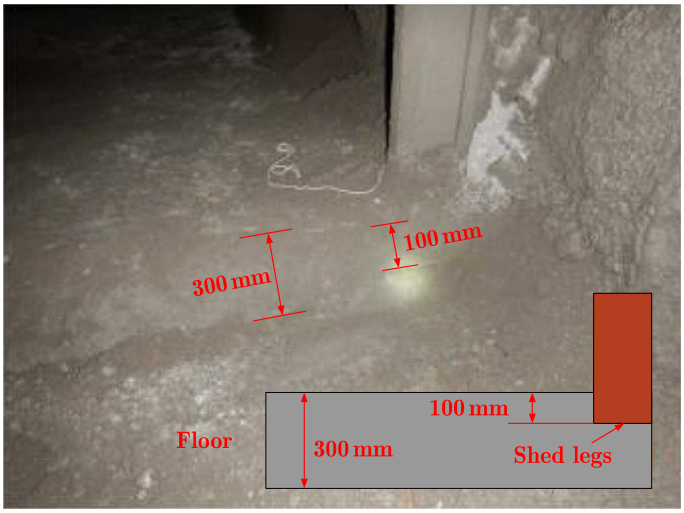

Fig. 12. Laying concrete in the roadway floor

4.2.8. Repair shed anchor

After the roadway floor is laid with concrete, two shed anchors are installed at each of the shed legs. The specification of the anchors is $\emptyset 20 \times 2400$ mm. The specific arrangement is shown in Fig. 13.

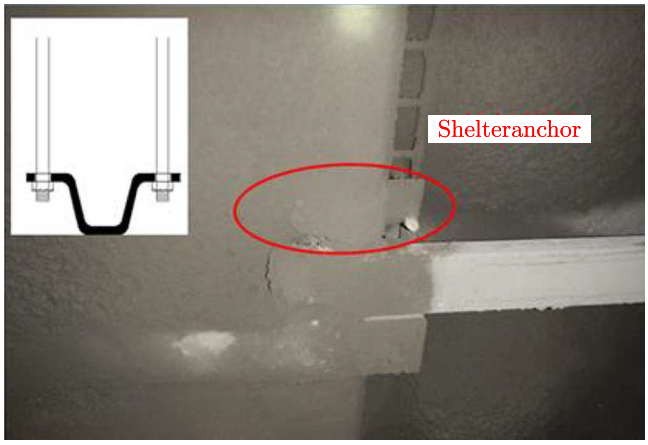

Fig. 13. Repair shed anchor

4.2.9. Shotcrete

After the shed guard bolts of the two gangs of the roadway are finished, the shotcrete work will be carried out. According to the construction requirements, the thickness of the shotcrete layer is not less than 70 mm, and the actual thickness of the shotcrete layer is about 100 mm. The on-site effect of the U-shaped steel shed is shown in Fig 14.

Fig. 14. Application diagram of the U-shaped steel support

4.3. On-site monitoring

After the roadway damage area is supported by the U-shaped steel, in order to detect the support effect, two groups of monitoring stations 1# and 2# are arranged in the roadway. The displacement of the roadway surface is observed by the cross point method, and the bolt force is monitored by a bolt dynamometer. As shown in Fig. 15, the surface displacement of the roadway 1# and 2# measurement points are both 0 during the monitoring time. The minimum value of the force monitoring of the 1# bolt is 19 kN, the maximum value is 23 kN, and the overall force value fluctuates around 21 kN. The minimum value of the force monitoring of the 2# bolt is 19 kN, the maximum value is 24 kN, and the overall force value fluctuates around 22 kN. The monitoring data of the bolt stress gauge fluctuates around a certain value and is relatively stable, indicating that the U-shaped steel-rod support plays an important role in the support of the surrounding rock of the roadway. After the roadway in the damaged area is supported by the U-shaped steel, the section is complete and the deformation of the surrounding rock is effectively controlled.

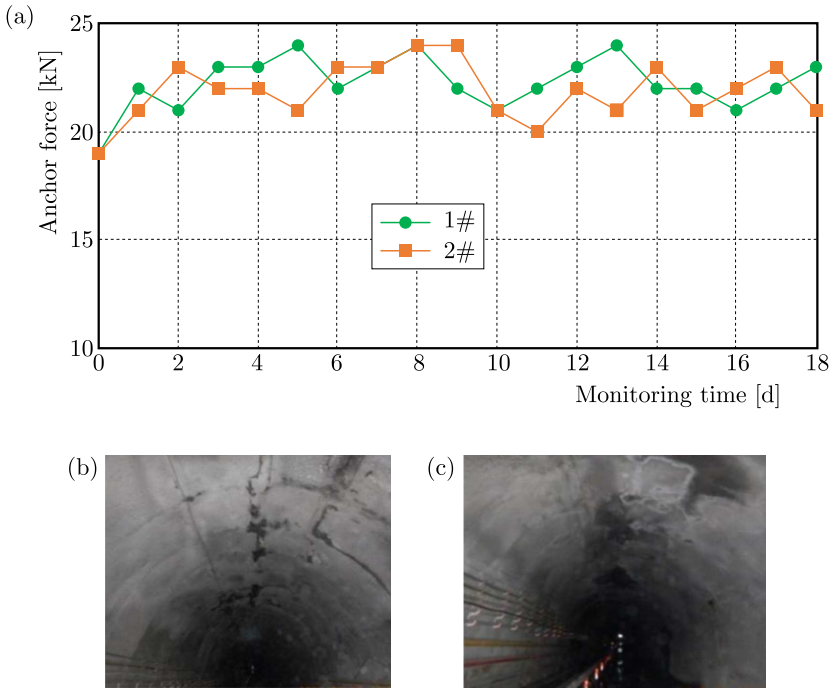

Fig. 15. Supporting effect monitoring method and equipment: (a) anchor dynamometer, (b) deformation of 1#, (c) deformation of 2#

5. Conclusion

- The main reasons for deformation and failure of weakly cemented caverns and surrounding tunnels are the large cross-section of the cavern, complex geological and mechanical conditions of the surrounding rock, low strength of the surrounding rock, and abundant easily expandable clay minerals. The roof and floor of the tunnel are the key points for reinforcement and support.
- The support idea of "timely closure, combination of long and short supports, secondary control, reinforcement of key parts, and long-term monitoring" and the load-bearing support concept of "allowable deformation + releasable pressure + limited deformation" for weakly cemented soft rock roadways are proposed, which effectively solves the problem of excessive excavation deformation of the roadways and plays a key role in maintaining the integrity of surrounding rock of the roadways.
- The location of adjacent weakly cemented chambers should be conducive to stability of the surrounding rock, efficient production, convenient transportation and construction safety while avoiding mutual interference between the chambers and other tunnels in the mine. On this basis, a mechanical model of the cave group under complex geological conditions is constructed to explore the mechanism of rock failure and instability in the cave group. This can provide a theoretical basis for the layout design of large cross-section cave groups and control of rock stability.

Acknowledgements

The authors would like to thank the editors and anonymous referees for detailed and valuable suggestions that helped to improve the original manuscript to its present form.

Funding

The research described in this paper was financially supported by Natural Science Foundation of Shandong Province (No. ZR2022ME060 and ZR2022ME165), National Natural Science Foundation of China (No. 52204093) and Scientific Research Fund of Liaocheng University (318052263).

References

1. Aguilera M.A., Arias R.M., Manzur T., 2019, Mapping microhabitat thermal patterns in artificial breakwaters: Alteration of intertidal biodiversity by higher rock temperature, *Ecology and Evolution*, **9**, 22, 12915-12927
2. Bhuiyan M.Y., Lin B., Giurgiutiu V., 2018, Acoustic emission sensor effect and waveform evolution during fatigue crack growth in thin metallic plate, *Journal of Intelligent Material Systems and Structures*, **29**, 7, 1275-1284
3. Fang K., Zhao T.B., Zhang Y.B., Qiu Y., Zhou J.H., 2019, Rock cone penetration test under lateral confining pressure, *International Journal of Rock Mechanics and Mining Sciences*, **119**, 149-155
4. Kang H.P., Lin J., Fan M.J., 2015, Investigation on support pattern of a coal mine roadway within soft rocks – a case study, *International Journal of Coal Geology*, **140**, 1, 31-40
5. Li J., Tang S.H., Zhang S.H., Li L., Wei J.G., Xi Z.D., Sun K., 2018, Characterization of unconventional reservoirs and continuous accumulations of natural gas in the Carboniferous-Permian strata, mid-eastern Qinshui basin, China, *Journal of Natural Gas Science and Engineering*, **49**, 298-316
6. Luo Z.S., Li J.L., Jiang Q., Zhang Y.C., Huang Y.S., Assefa E., Deng H.F., 2018, Effect of the water-rock interaction on the creep mechanical properties of the sandstone rock, *Periodica Polytechnica-Civil Engineering*, **62**, 2, 451-461
7. Mineo S., Pappalardo G., 2019, InfraRed Thermography presented as an innovative and non-destructive solution to quantify rock porosity in laboratory, *International Journal of Rock Mechanics and Mining Sciences*, **115**, 99-110
8. Sharma M.S.R., O'Regan M., Baxter C.D.P., Moran K., Vaziri H., Narayanasamy R., 2010, Empirical relationship between strength and geophysical properties for weakly cemented formations, *Journal of Petroleum Science and Engineering*, **72**, 1, 134-142
9. Showkati A., Maarefvand P., Hassani, H., 2015, Stresses induced by post-tensioned anchor in jointed rock mass, *Journal of Central South University*, **22**, 4, 1463-1476
10. Theocharis A., Roux J., Langlois V., 2020, Elasticity of model weakly cemented granular materials: A numerical study, *International Journal of Solids and Structures*, **193**, 13-27
11. Tu W.F., Li L.P., Zhou Z.Q., Shang C.S., 2022, Thickness calculation of accumulative damaged zone by rock mass blasting based on Hoek-Brown failure criterion, *International Journal of Geomechanics*, **22**, 2, Paper ID: 04021273
12. Wang S., Han L.J., Meng Q.B, Jin Y.H., Zhao W.S., 2020, Water absorption/dehydration by NMR and mechanical response for weakly cemented mudstones subjected to different humidity conditions, *Bulletin of Engineering Geology and the Environment*, **79**, 1, 1275-1288
13. Yang S.Q., Jing H.W., 2011, Strength failure and crack coalescence behavior of brittle sandstone samples containing a single fissure under uniaxial compression, *International Journal of Fracture*, **168**, 2, 227-250
14. Yang S.Q., Yin P.F., Zhang Y.C., Chen M., Zhou X.P., Jing H.W., Zhang Q.Y., 2019, Failure behavior and crack evolution mechanism of a non-persistent jointed rock mass containing a circular hole, *International Journal of Rock Mechanics and Mining Sciences*, **114**, 101-121
15. Zhang C.W., Jin Z.X., Feng G.R., Song X.M., Rui G., Zhang Y.J., 2020, Double peaked stress-strain behavior and progressive failure mechanism of encased coal pillars under uniaxial compression, *Rock Mechanics and Rock Engineering*, **53**, 7, 3253-3266
16. Zhang W., Guo W.Y., Wang Z.Q., 2022a, Influence of lateral pressure on mechanical behavior of different rock types under biaxial compression, *Journal of Central South University*, **29**, 11, 3695-3705

17. Zhang W., Zhao T.B., Guo W.Y., Xing M.L., 2022b, Study on mechanical characteristics of rock type I fracture and anchorage strengthening mechanism, *Journal of Theoretical and Applied Mechanics*, **60**, 3, 423-434

18. Zhang W., Zhao T.B., Yin Y.C., 2022c, Prefabricated fractured rock under stepwise loading and unloading, *Journal of Theoretical and Applied Mechanics*, **60**, 1, 167-179

19. Zhang W., Zhang B.L., Zhao T.B., 2023, Study on the law of failure acoustic-thermal signal of weakly cemented fractured rock with different dip angles, *Rock Mechanics and Rock Engineering*, DOI: 10.1007/s00603-023-03296-1

20. Zhao T. B., Zhang W., Gu S.T., Lv Y.W., Li Z.H., 2020, Study on fracture mechanics of granite based on digital speckle correlation method, *International Journal of Solids and Structures*, **193**, 192-199

Manuscript received October 22, 2022; accepted for print April 27, 2023

JOURNAL OF THEORETICAL AND APPLIED MECHANICS
61, 3, pp. 481-494, Warsaw 2023
https://doi.org/10.15632/jtam-pl/166369

THE DEVELOPMENT OF TWO MULTIAXIAL DUCTILITY FACTOR PREDICTING MODELS BASED ON CREEP CAVITY GROWTH THEORY

Dongquan Wu, Yupeng Li, Zixiang Liu, Dinghe Li

Sino-European Institute of Aviation Engineering, Civil Aviation University of China, Tianjin, China

corresponding author Dongquan Wu, e-mail: dqwu@cauc.edu.cn

In this study, the multiaxial ductility factor was analyzed based on the power-law creep grain-boundary cavities growth theory under multiaxial stress states. Based on this theory, the theoretical cavities growth rates under a multiaxial stress state were discussed and the predicting model of a stress-state parameter α was revised by using an empirical fitting expression denoted as α_{Wu}, which exhibited a good agreement to analytical results of the stress-state parameter α and multiaxial cavities growth rates. Then, according to the relationship between uniaxial and multiaxial creep failure strain, a new empirical predicting model of multiaxial ductility factor MDF_{Wu} was established which involved the multiaxial parameter α_{Wu} and uniaxial parameter α_0. Besides, the theoretical model of multiaxial ductility factor MDF could also be established. By fitting the theoretical values of MDF, another predicting model MDF_{WM} was proposed. The development of two multiaxial ductility factor predicting models could be achieved. Finally, predictions of these two novel multiaxial ductility factor models and the Cocks-Ashby as well as Wen-Tu model were compared with experimental data, and the prediction accuracy of MDF_{Wu} and MDF_{WM} models was significantly improved, especially for the latter one.

Keywords: multiaxial ductility factor, cavities growth theory, power-law creep, multiaxial stress state

1. Introduction

Metallic components in modern industrial core equipment (such as aero engines, ultra supercritical generator sets, nuclear motor sets, etc.) are subjected to higher temperature in order to realize the continuous improvement of energy conversion efficiency. Thus, creep cracking is one of the most important failure mechanisms of these components, especially when containing precracks, which will cause failures before their design life (Yatomi *et al.*, 2004). A large number of theories and experiments have proved that creep crack initiation and propagation are the main causes of structural failure in service (Holdsworth, 1992).

For safety reasons, the structural integrity assessment of components operating in the creep regime is imperative (Wen and Tu, 2014). The analysis of creep cracking and failure based upon continuum damage mechanics has made a remarkable development in recent years, which makes up for deficiency of fracture mechanics (Wen and Tu, 2014). Within this approach, the creep cracking process will be directly correlated to the creep damage described by a damage variable around the crack tip. Once the damage variable of one material point reaches the critical value, it is thought to be failed, and the crack growth length can be measured by the whole damaged area. To effectively describe the complex stress state around the crack tip, for example, the stress state around the crack tip of a compact tension specimen should be a multiaxial distribution. A multiaxial ductility factor (MDF) is usually used to build the relationship between the multiaxial ductility ε_f^* and uniaxial ductility ε_f

$$\varepsilon_f^* = MDF\varepsilon_f \tag{1.1}$$

To effectively characterize the relationship between them, various multiaxial ductility factor (*MDF*) models were proposed, which can be roughly divided into the following bases: empirical formula; semi-empirical formula; physical mechanisms.

For empirical formula, Manjoine (1975) proposed an *MDF* model which was inversely proportional to triaxiality according to mechanical performance of annealed 304 stainless steel

$$MDF = \frac{\varepsilon_f^*}{\varepsilon_f} = \frac{\sigma_{eq}}{3\sigma_m} \tag{1.2}$$

where σ_m and σ_{eq} are the hydrostatic stress and von Mises equivalent stress, respectively.

For a semi-empirical formula, Spindler (2004) modified the Rice-Tracey *MDF* model (Rice and Tracey, 1969) and developed a semi-empirical *MDF* model considering the nucleation and growth of creep voids

$$MDF = \frac{\varepsilon_f^*}{\varepsilon_f} = \exp\Big[p\Big(1 - \frac{\sigma_1}{\sigma_e}\Big) + q\Big(0.5 - 1.5\frac{\sigma_m}{\sigma_{eq}}\Big)\Big] \tag{1.3}$$

where σ_1 is the principal stress, and p and q are material coefficients.

For the *MDF* model based on physical mechanisms, different mechanisms such as cavity growth (Rice and Tracey, 1969; McClintock, 1968; Cocks and Ashby, 1980) and cavity nucleation (Spindler, 2004a,b) have been discussed. Typically, Cocks and Ashby (1980) proposed a creep model based on micromechanical consideration of the void growth and coalescence and extended it to multiaxial stress states as well as the most notable Cocks-Ashby *MDF* models

$$MDF = \frac{\varepsilon_f^*}{\varepsilon_f} = \sinh\Big(\frac{2}{3}\frac{n-0.5}{n+0.5)}\Big) \Big/ \sinh\Big(2\frac{n-0.5}{n+0.5}\frac{\sigma_m}{\sigma_{eq}}\Big) \tag{1.4}$$

where n is the steady-state creep exponent. Alang and Nikbin (2018) and Spindler *et al.* (2001) also proposed other (semi) empirical models, which may be also suitable for different conditions. Due to perfect establishment and application at the grain size level, the Cocks-Ashby *MDF* has been widely used to estimate the multiaxial creep ductility during simulation or estimation of creep damage (Wen and Tu, 2014; Yatomi and Tabuchi, 2010; Wu *et al.*, 2018b,c,d) and creep cracking life (Davies, 2006; Wu *et al.*, 2018a,e, 2019, 2020). Nevertheless, the Cocks-Ashby *MDF* may conservatively predict multiaxial creep ductility under some conditions. Thus, Wen *et al.* (2014) developed another purely empirical Wen-Tu *MDF* based on the Cocks-Ashby *MDF*, which could more effectively estimate the experimental results

$$MDF = \frac{\varepsilon_f^*}{\varepsilon_f} = \exp\Big(\frac{2}{3}\frac{n-0.5}{n+0.5)}\Big) \Big/ \exp\Big(2\frac{n-0.5}{n+0.5}\frac{\sigma_m}{\sigma_{eq}}\Big) \tag{1.5}$$

However, the above models are approximate solutions of the theoretical model based on the power-law creep growth of grain-boundary cavities theory, which will be explained in detail in Section 2, and there is a large conservation under some conditions, so it is necessary to establish a more accurate multiaxial ductility factor based on the creep cavity growth model. Therefore, the critical task of the present study is to develop a more accurate *MDF* based on the grain boundary void growth model.

2. Power-law creep regime based on growth of grain-boundary cavities

Experimental morphology from different steels of creep crack growth has indicated that creep voids or cavities mainly nucleate and grow on grain boundary facets (especially when a tensile stress is perpendicular to the facets), then the cavities may be coalescing to form a grain-size

microcrack, and finally the coalescence of microcracks leads to creep crack propagation (Tan *et al.*, 2013; Wen and Tu, 2014; Wen *et al.*, 2016; You and Lee, 1996; Al-Rifaie and Sumelka, 2019; Al-Rifaie *et al.*, 2021).

Cocks and Ashby (1980) proposed an approximate method to calculate the growth of grain-boundary cavities by a power-law creep under multiaxial stress states. In this theory, the cavity growth was estimated by a volume change of the cylinder containing a void, and some strict assumptions should be met, such as grain-boundary cavities grow by a power-law creep. The creep rate is independent of hydrostatic pressure, the grain boundaries and take a relative rigid-body displacement, width of the cylinder is larger than its thickness, and it is constrained by the surrounding material to contract laterally, the voids stay spherical during the creep process, the material is incompressible and its total volume does not change.

The problem then arises with calculation of the volume change in the cylinder containing voids, since they cause the cavities to grow.

A detailed view of a cylinder containing a void is shown in Fig. 1, in which d is the grain size, r_h is the void radius, $2l$ is the voids distance, $2w$ is a calculation bound, σ_a is the axial stress in the cylinder and T is the superimposed triaxial stress.

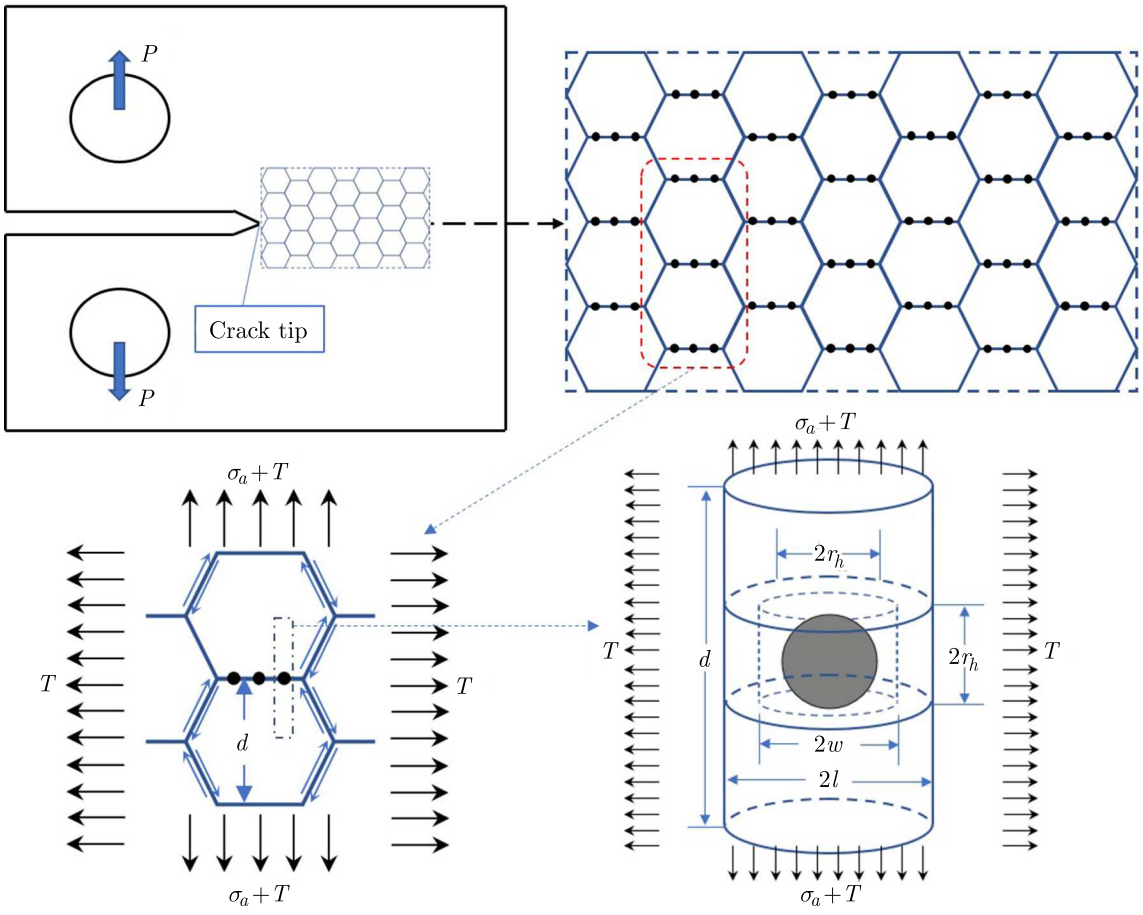

Fig. 1. Grain-boundary cavities growth by a power-law creep under multiaxial stress states

Cocks and Ashby (1980) established the upper bound for the axial strain rate $\dot{\varepsilon}_{ss}$ for uniaxial stress by using the energy principles

$$\frac{1}{1-f_n}\frac{df_h}{dt} = \dot{\varepsilon}_{ss}\left[\frac{1}{(1-f_h)^{n+1}} - 1\right] \tag{2.1}$$

where f_h is the area fraction of holes on the grain boundary, $f_w = r_h^2/l^2$, $\dot{\varepsilon}_{ss}$ is the steady creep rate in the absence of voids. And for a multiaxial stress condition, the axial strain rate is described as

$$\frac{df_h}{dt} = \dot{\varepsilon}_{ss}\frac{f_h}{f_w}\left[\frac{\sqrt{(1+G)^{n+1}}}{(1-f_w)^n} - (1-f_w)\right] \tag{2.2}$$

where f_w is an area fraction entering the bound calculation, $f_w = r_h^2/w^2$, and G is a stress-state parameter defined by

$$G = 3\Big(\frac{n}{n+1}\frac{1-f_w}{\ln f_w}\frac{T}{\sigma_a}\Big)^2 \tag{2.3}$$

The optimum value of f_w was found by minimizing df_h/dt with respect to f_w, with the constraint that f_w cannot be less than f_h. The unconstrained optimum value was found using the Newton-Raphson method.

Be aware of that it is difficult to directly obtain the relationship between the void growth rate and stress triaxiality, and to make the predicting results more practical. Cocks and Ashby (1980) fitted a semi-empirical equation to the curves of Fig. 2. It was fitted by a result which closely resembled that for a imple uniaxial tension condition, Eq. (2.1), namely

$$\frac{df_h}{dt} = \frac{\dot{\varepsilon}_{ss}}{\alpha}\Big[\frac{1}{(1-f_h)^n} - (1-f_h)\Big] \tag{2.4}$$

where α is a stress-state parameter defined by

$$\alpha = \sinh^{-1}\Big[\frac{2(n-0.5)}{n+0.5}\frac{\sigma_m}{\sigma_{eq}}\Big] \tag{2.5}$$

As expected, cavity growth rates are increasing with the increasing stress triaxiality. It is also observed from Fig. 5 that the results are not well fitted when the triaxiality $\sigma_m/\sigma_{eq} < 0.8$ or creep exponent $n < 3$. This is mainly because the most weight is artificially given to the predicting results at high stress triaxiality in the Cocks and Ashby fitting process. To resolve this conflict, Wen and Tu (2014) proposed another approximate model formulated as

$$\alpha = \Big[2 - 0.5\Big(\frac{1}{5n}\Big)^{n-1}\Big]\Big/\Big[\frac{2(n-0.5)}{n+0.5}\frac{\sigma_m}{\sigma_{eq}}\Big] \tag{2.6}$$

In the case of simple tension, substituting $\sigma_m/\sigma_{eq} = 1/3$ into Eq. (2.5) or Eq. (2.6) yields the void growth rate under the uniaxial condition with α_0.

Here, we try to propose a new formula for describing the relationship between the parameter α and triaxiality σ_m/σ_{eq}, which is built by fitting the theoretical results.

First, the variations of α_{true} against triaxiality σ_m/σ_{eq} for different n values are obtained from Eq. (2.4) and Eq. (2.2)

$$\alpha_{true} = \Big[\frac{1}{(1-f_h)^2} - (1-f_h)\Big]\Big/\left\{\frac{f_h}{f_w}\left[\frac{\sqrt{(1+G)^{n+1}}}{(1-f_w)^n} - (1-f_w)\right]\right\} \tag{2.7}$$

Moreover, the theoretical data of α_{true} could be obtained by re-arranging the results from Fig. 3, then the curves of $\ln\alpha_{true}$ against σ_m/σ_{eq} with different n can be described in Fig. 2.

It can be found that α_{true} decreases as n is increasing, and the difference between the curves is unobvious when n is larger than 6. Besides, it is concluded that with the increasing stress triaxiality σ_m/σ_{eq}, the curves of $\ln\alpha_{true}$ against σ_m/σ_{eq} are rapidly decreasing when σ_m/σ_{eq} is smaller than 1.5, while it becomes smooth when σ_m/σ_{eq} is larger than 1.5. By fitting

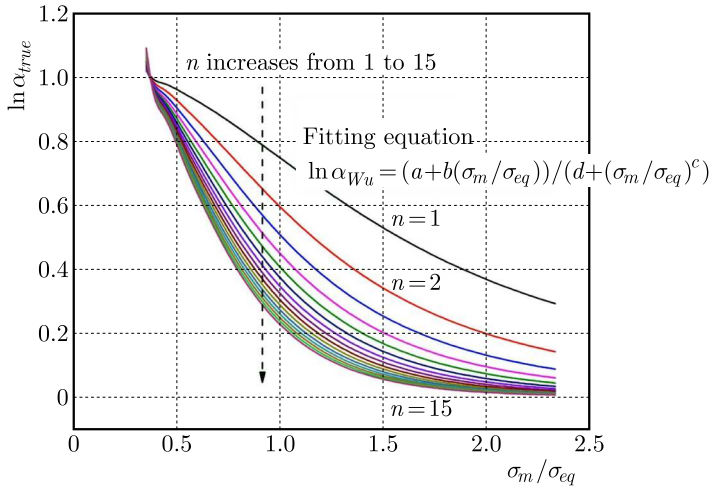

Fig. 2. Variation of the stress-state parameter α_{true} against σ_m/σ_{eq} under different n values

the relationship between the parameter α_{true} and stress triaxiality for different n values, it is indicated that all of the curves could be expressed by a similar type of mathematical expression, and the fitting equation is expressed as follows using the parameter α_{Wu}

$$\ln \alpha_{Wu} = \left[a + b\left(\frac{\sigma_m}{\sigma_{eq}}\right)^c\right] \Big/ \left[d + \left(\frac{\sigma_m}{\sigma_{eq}}\right)^c\right] \tag{2.8}$$

or expressed by

$$\alpha_{Wu} = \exp\left\{\left[a + b\left(\frac{\sigma_m}{\sigma_{eq}}\right)^c\right] \Big/ \left[d + \left(\frac{\sigma_m}{\sigma_{eq}}\right)^c\right]\right\} \tag{2.9}$$

where a, b, c, d are all parameters related to n, which can be also correlated by the following formula by using coefficients a_i, b_i, c_i, d_i. Perfect fitting performance is also found here, and the coefficient of determination R-square is larger than 0.999. These parameters could be obtained directly from Table 1

$$\begin{aligned} &a, c = \frac{a_i + b_i n}{1 + c_i n + d_i n^2} && i \text{ is represented by } a \text{ or } c \\ &b, d = a_i b_i^{\frac{1}{n}} n^{c_i} && i \text{ is represented by } b \text{ or } d \end{aligned} \tag{2.10}$$

Table 1. The details of fitting coefficients (a, b, c, d) between above coefficients against n values

Coef. 1	Coefficient 2			
	a_i	b_i	c_i	d_i
a	0.020863	−0.51239	0.215807	−0.00294
b	0.090558	0.557567	0.57484	–
c	−2.15624	−0.36378	0.227893	0.000304
d	0.30566	0.382147	−0.19855	–

Then the parameter α_{Wu} can be characterized by combining Eqs. (2.9) and (2.10), which is related to the stress triaxiality σ_m/σ_{eq} and n values

$$\alpha_{Wu} = \exp\left\{\left[\frac{a_a + b_a n}{1 + c_a n + d_a n^2} + a_b b_b^{\frac{1}{n}} n^{c_b}\left(\frac{\sigma_m}{\sigma_{eq}}\right)^{\frac{a_c + b_c n}{1 + c_c n + d_c n^2}}\right] \Bigg/ \left[a_d b_d^{\frac{1}{n}} n^{c_d} + \left(\frac{\sigma_m}{\sigma_{eq}}\right)^{\frac{a_c + b_c n}{1 + c_c n + d_c n^2}}\right]\right\} \tag{2.11}$$

Figure 3 compares the predictions and true values of α for $n = 18$ and $n = 20$, where these two conditions are not considered in the above fitting process, so the comparison between these two conditions and predictions can effectively verify the accuracy of α_{Wu} model in predicting the parameter α.

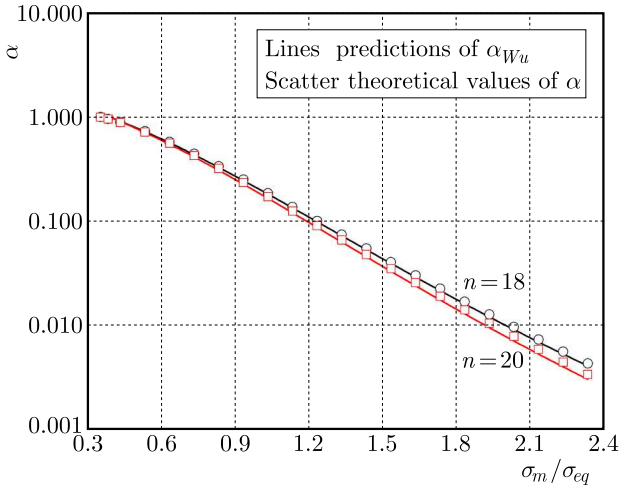

Fig. 3. Comparison between predictions of α_{Wu} and true values of α with $n = 18$ and $n = 20$

Finally, the normalized hole growth rate, $\ln[(df_h/dt)/(1/\dot{\varepsilon}_{ss} f_h)]$ for different n is compared by using different α models (i.e. Cocks-Ashby model in Eq. (2.5), Wen-Tu model in Eq. (2.6) and Wu model in Eq. (2.11)), as shown in Fig. 4. The Cocks-Ashby approximate model shows large conservativeness when $n = 1$, σ_m/σ_{eq} is smaller than 0.5 and n is larger than 5. The Wen-Tu model is relatively more accurate than the Cocks-Ashby approximate model at $n = 1$ and small values of σ_m/σ_{eq}, but its prediction is still much too conservative when n is larger than 5. Apparently, compared with the Cocks-Ashby approximate model and Wen-Tu model, the proposed model (Wu model) is perfectly suitable to predict theoretical data of the hole growth rate no matter how the stress triaxiality σ_m/σ_{eq} or creep exponent n varies. The predictions of Wu model (solid line) nearly coincide with the theoretical data (dash line). Especially, there is a significant improvement for the predicting accuracy when $\sigma_m/\sigma_{eq} < 0.5$ and creep exponent $n > 5$ compared with other models.

The time to fracture at a constant stress is generally obtained by integrating the creep voids growth rate between the limits, and the creep failure strain could be simply assumed by the ratio of the time to fracture and the steady creep rate in absence of voids. And then there are two conditions for assuming the time to failure: one is using theoretical differential equations, the other is using approximate or fitting equations.

The first is using the theoretical differential equations.

To get the creep failure strain under the uniaxial loading condition, differential Eq. (2.1) can be integrated between the limits

$$\begin{aligned} f_h &= f_i \qquad \text{at} \qquad t = 0 \\ f_h &= f_{c0} \qquad \text{at} \qquad t = t_{c0} \end{aligned} \tag{2.12}$$

where f_i is the initial area fraction of the cavities, which is thought to be $f_i \ll 1$, f_{c0} is the area fraction of the cavities at which the linkage occurs, which is taken to be $f_{c0} = 0.25$ (Wen and

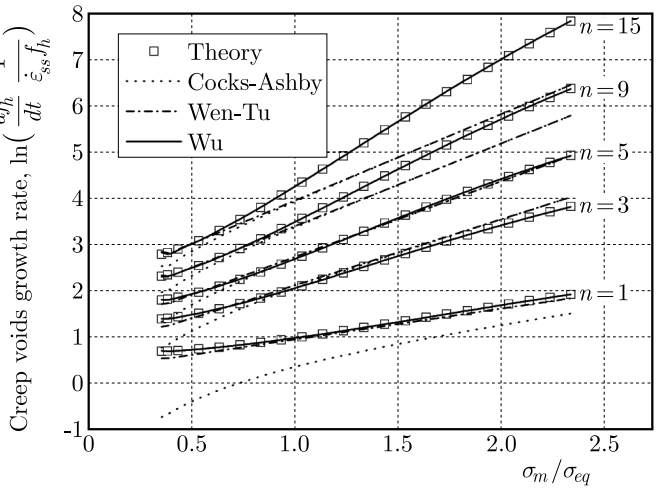

Fig. 4. Comparison of predictions and theoretical results of the creep voids growth rate

Tu, 2014). And t_{c0} is the time to coalescence. The result for a constant stress is an equation for the failure time

$$t_{c0} = \frac{1}{\dot{\varepsilon}_{ss}(n+1)} \ln \frac{1-(1-f_c)^{n+1}}{1-(1-f_i)^{n+1}} \tag{2.13}$$

Then the creep failure strain under a uniaxial loading condition is

$$\varepsilon_f = \dot{\varepsilon}_{ss} t_{c0} = \frac{1}{n+1} \ln \frac{1-(1-f_c)^{n+1}}{1-(1-f_i)^{n+1}} \tag{2.14}$$

To get the creep failure strain under multiaxial loading conditions, differential Eq. (2.2) can be integrated between the limits

$$\begin{aligned} f_h &= f_i \qquad \text{at} \qquad t = 0 \\ f_h &= f_c \qquad \text{at} \qquad t = t_c \end{aligned} \tag{2.15}$$

where t_c is the time to coalescence.

For theoretical differential Eq. (2.2) integrated between the above limits, the time to failure could be expressed by

$$t_c = \frac{f_w}{\dot{\varepsilon}_{ss}} \ln \frac{f_c}{f_i} \Big/ \left[\frac{\sqrt{(1+G)^{n+1}}}{(1-f_w)^n} - (1-f_w) \right] \tag{2.16}$$

Then, the creep failure strain under multiaxial loading conditions is calculated as

$$\varepsilon_f^* = \dot{\varepsilon}_{ss} t_c = f_w \ln \frac{f_c}{f_i} \Big/ \left[\frac{\sqrt{(1+G)^{n+1}}}{(1-f_w)^n} - (1-f_w) \right] \tag{2.17}$$

Finally, the multiaxial ductility factor (MDF) can be defined as

$$MDF = \frac{\varepsilon_f^*}{\varepsilon_f} = \frac{f_w \ln \frac{f_c}{f_i}}{\ln \frac{1-(1-f_c)^{n+1}}{1-(1-f_i)^{n+1}}} \Big/ \left[\frac{\sqrt{(1+G)^{n+1}}}{(1-f_w)^n} - (1-f_w) \right] \tag{2.18}$$

In this formula, it is found that except for stress triaxiality σ_m/σ_{eq}, the initial area fraction of the cavities f_i also affects MDF, which will be studied in the following Section.

The other condition for assuming the time to failure is using simplified differential equations. For the multiaxial loading condition, differential Eq. (2.5) can be integrated between the limits, the time to failure could be expressed by

$$t_c = \frac{\alpha}{\dot{\varepsilon}_{ss}(n+1)} \ln \frac{1-(1-f_c)^{n+1}}{1-(1-f_i)^{n+1}} \tag{2.19}$$

The creep failure strain under multiaxial loading conditions is described as

$$\varepsilon_f^* = \dot{\varepsilon}_{ss} t_c = \frac{\alpha}{n+1} \ln \frac{1-(1-f_c)^{n+1}}{1-(1-f_i)^{n+1}} \tag{2.20}$$

For the uniaxial condition, the void growth rate is described as α_0 by substituting $\sigma_m/\sigma_{eq} = 1/3$ into Eq. (2.6). Hence, similarly, the time to failure under this condition is characterized by

$$t_{c0} = \frac{\alpha}{\dot{\varepsilon}_{ss}(n+1)} \ln \frac{1-(1-f_c)^{n+1}}{1-(1-f_i)^{n+1}} \tag{2.21}$$

The creep failure strain under uniaxial loading conditions is calculated by

$$\varepsilon_f = \dot{\varepsilon}_{ss} t_{c0} = \frac{\alpha}{n+1} \ln \frac{1-(1-f_c)^{n+1}}{1-(1-f_i)^{n+1}} \tag{2.22}$$

Finally, the *MDF* can be re-defined as

$$MDF = \frac{\varepsilon_f^*}{\varepsilon_f} = \frac{\alpha}{\alpha_0} \tag{2.23}$$

In our study, according to the new α_{Wu} proposed in Eq. (2.12), the modified *MDF* is described as

$$MDF_{Wu} = \frac{\varepsilon_f^*}{\varepsilon_f} = \frac{\alpha_{Wu}}{\alpha_{Wu0}} = \frac{\exp\left\{\left[a + b\left(\frac{\sigma_m}{\sigma_{eq}}\right)^c\right] \Big/ \left[d + \left(\frac{\sigma_m}{\sigma_{eq}}\right)^c\right]\right\}}{\exp\left\{\left[a + b\left(\frac{1}{3}\right)^c\right] \Big/ \left[d + \left(\frac{1}{3}\right)^c\right]\right\}} \tag{2.24}$$

where a, b, c, d are all parameters related to n, which are described above.

Figure 5 compares *MDF* results for different predicting models and theoretical data with varied values of f_i. With an increase of f_i, the curves of *MDF* are descended, and these curves are almost coincident when $f_i < 10^{-4}$. The Wu model shows a perfect coincidence with the theoretical results when n is small, while both the Cocks-Ashby and Wen-Tu models are conservative. As the creep power law exponent n increases, the difference between Wu model and theoretical results becomes obvious, especially when the stress triaxiality is smaller than 1. This is mainly caused by simplification using the creep void growth rate with α_0 under the uniaxial tension condition. Compared to the theoretical uniaxial creep void growth rate in Eq. (2.3), α_0 is not equal to 1 in the simplified creep void growth rate Eq. (2.7), and this difference will be enlarged at high n values. Besides, for large n, the difference between Wu and Wen-Tu models is decreased, and the predictions of Wen-Tu model at large n may be overestimated when $\sigma_m/\sigma_{eq} > 1$. Due to relatively poor predictions of these models at large n, a new model for predicting *MDF* should be proposed.

Therefore, a fitting formula for *MDF* is obtained by fitting the theoretical results of *MDF* with $f_i = 10^{-4}$, because the curves of *MDF* are almost coincident when $f_i < 10^{-4}$.

The theoretical results of $\ln MDF$ against σ_m/σ_{eq} with $f_i = 10^{-4}$ for different n are compared. All of the curves could be well fitted by the following equation (WM means modified Wu model)

$$\ln MDF_{WM} = \frac{a + b\left(\frac{\sigma_m}{\sigma_{eq}}\right)^c}{d + \left(\frac{\sigma_m}{\sigma_{eq}}\right)^c} \qquad MDF_{WM} = \exp\left[\frac{a + b\left(\frac{\sigma_m}{\sigma_{eq}}\right)^c}{d + \left(\frac{\sigma_m}{\sigma_{eq}}\right)^c}\right] \tag{2.25}$$

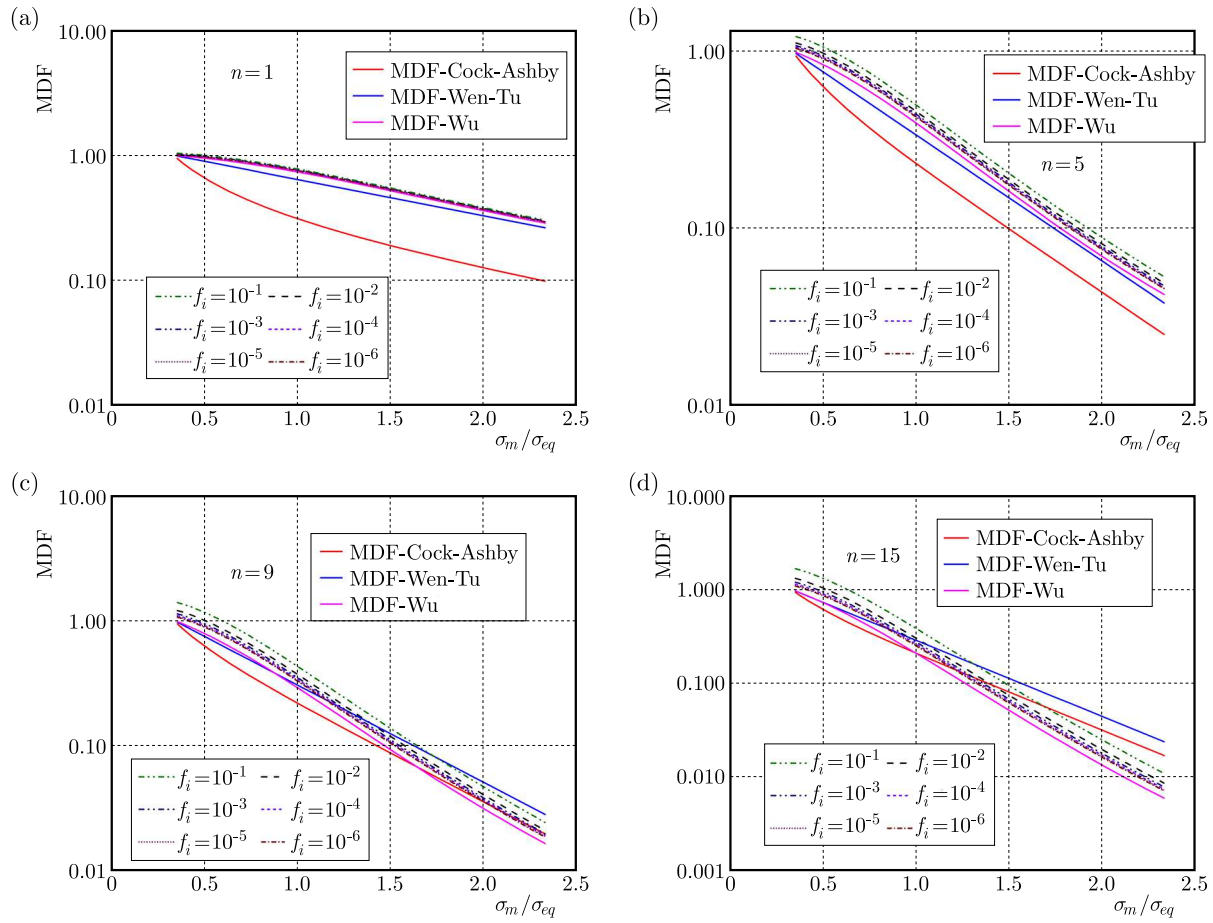

Fig. 5. Comparison of predictions and theoretical results of *MDF*

where a, b, c, d are parameters related to the creep power exponent n, and the following expression could be established

$$\begin{aligned} a, b, c &= \frac{a_i + b_i n}{1 + c_i n + d_i n^2} \qquad i \text{ is represented by } a,\ b,\ c \\ d &= a_i + b_i + c_i^n + d_i n \qquad i \text{ is represented by } d \end{aligned} \tag{2.26}$$

The related parameters are summarized in Table 2.

Table 2. Fitting parameters of above parameters against n values

Coef. 1	Coefficient 2			
	a_i	b_i	c_i	d_i
a	0.037707	−0.51284	0.228236	−0.00278
b	−0.00624	0.071408	0.085232	−8.17E-04
c	−2.25401	−0.49529	0.29565	−3.88E-04
d	0.194207	−0.17086	0.375464	−0.00112

To further validate the suitability of the modified Wu (WM) model, the *MDF* for $n = 8$, $n = 15$, $n = 18$ and 20 are also compared between different models in Fig. 6. The predictions from the WM model (black solid line) are quite accurate compared to the theoretical data (scatters data), while the other predictions are far below the theoretical data when $\sigma_m/\sigma_{eq} < 0.5$. Note

that $n = 18$ and 20 conditions are not considered in the above fitting process, so the comparison could effectively support the conclusion that the WM model could be the most competitive theory in assessing the *MDF*.

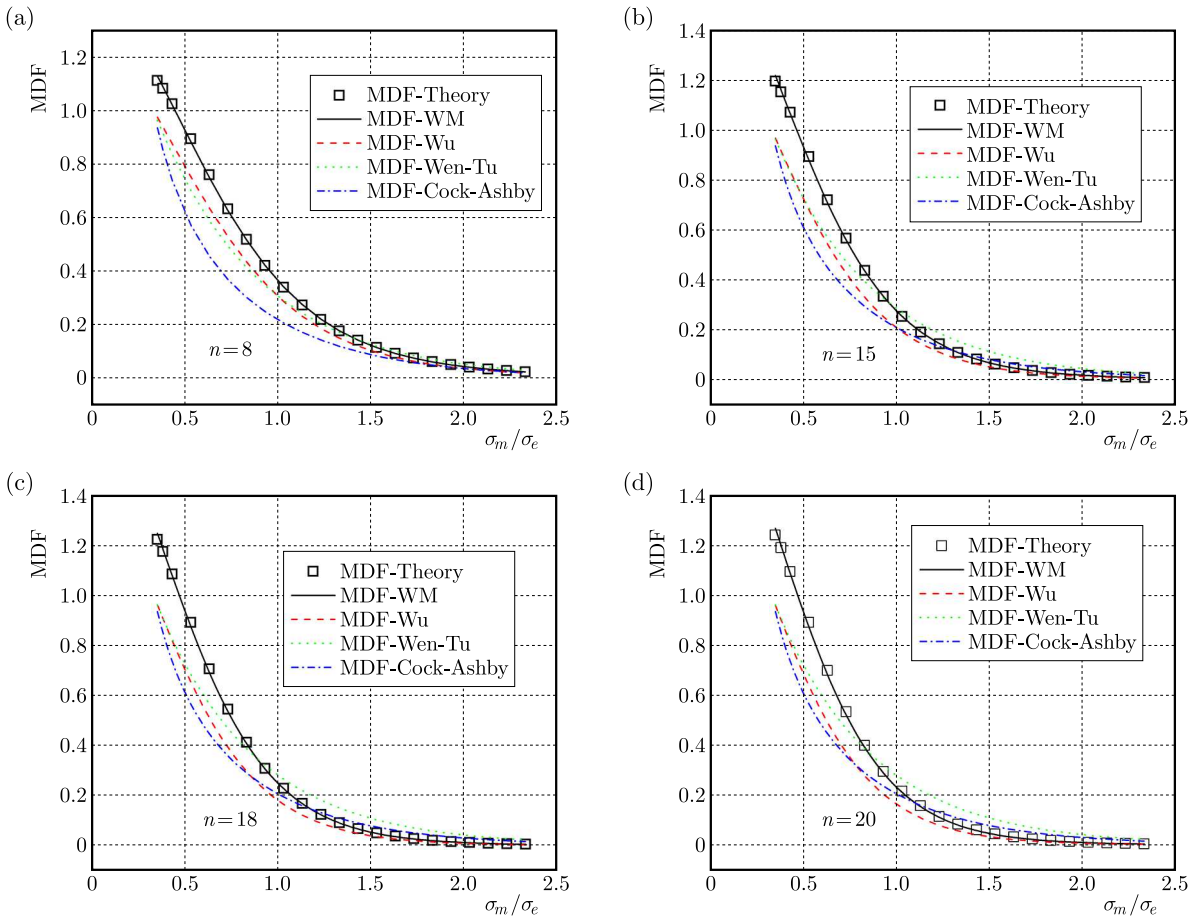

Fig. 6. Comparison of predictions and theoretical results of *MDF*

Figure 7 shows the influence of stress triaxiality on the multiaxial ductility factor. The data for steels of the pipe and rotor are collected from Wichtmann (2002), and the data for C-Mn steel at 360°C from Yatomi *et al.* (2004), 316H at 550°C (Wen and Tu, 2014) and for 316 type steel at 600°C (Spindler, 2004b). As presented in Fig. 7, the Cocks-Ashby model may underestimate the multiaxial creep ductility at high stress triaxiality, while the Wen-Tu and Wu models give more closer results to the experimental data and may become close to the average results of tested data. The WM model gives more improved solutions at small stress triaxiality while more conservative predictions at higher stress state. This is due to theoretical solutions of the WM model, which indeed have these variation laws as observed in Fig. 7, and which may be larger than the predictions of the other three models at low stress triaxiality but may be less than these predictions at high stress triaxiality. In general, it could be said that the new Wu and WM models could give better predictions for the multiaxial ductility factor compared to the previous models. The WM model may give a more precise upper bound of *MDF* for pipe and rotors steel as well as for 316 steel at 600°C, while WM predictions are also effectively consistent with the average experimental results for C-Mn steel at 360°C and 316H at 550°C.

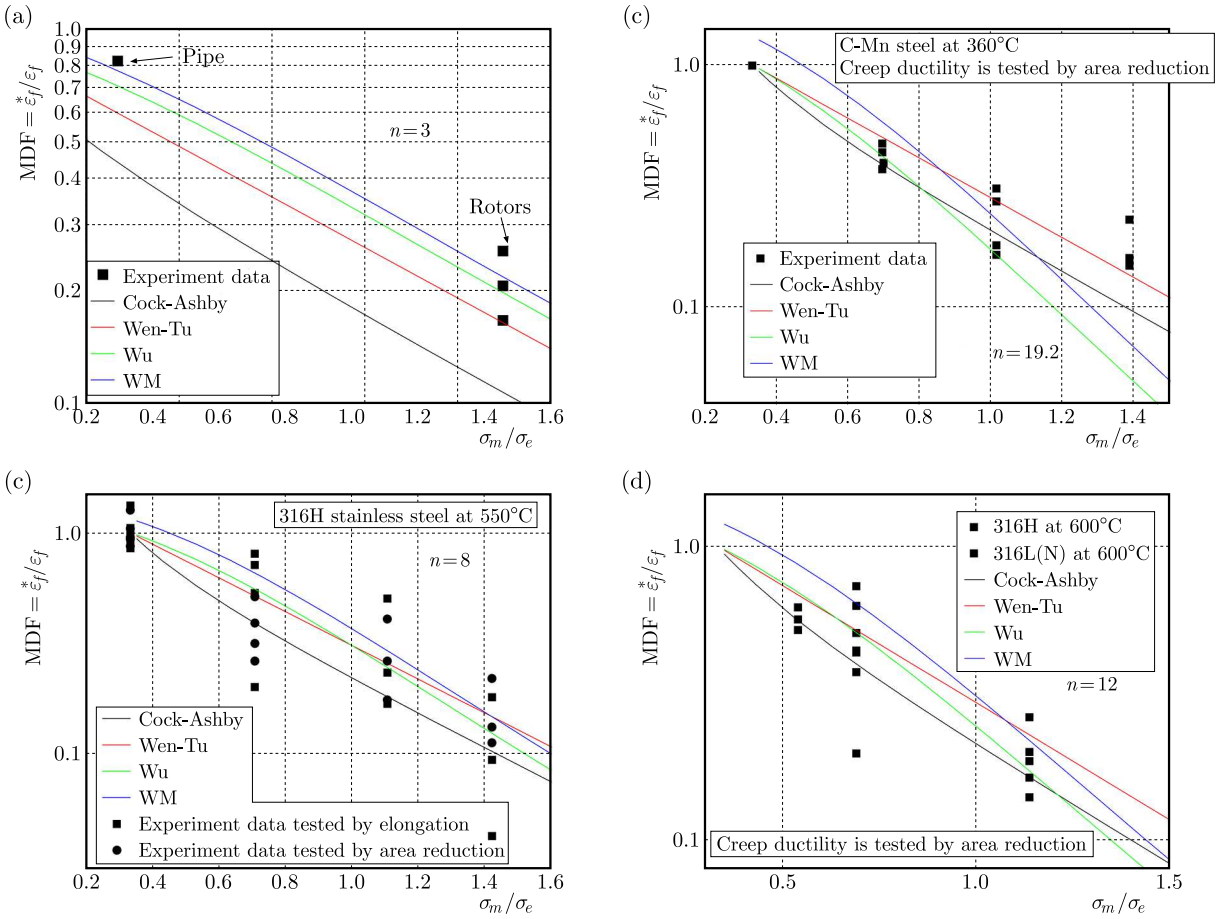

Fig. 7. Comparison of predictions and experimental data of *MDF*: (a) for pipe and rotors, (b) for C-Mn steel at 360°C, (c) for 316H at 550°C, (d) for 316H(L) at 600°C

Figure 8 compares the predictions by using different models and experimental data of the multiaxial ductility factor. The experimental data under the same stress triaxiality are simplified by calculating the geometric mean values. It could be found for these limited data for different materials and conditions, all predictions of the Cocks-Ashby model could be located within the range with a scatter factor of 2, and for the Wen-Tu and Wu models, this error band is with a scatter factor of 1.8 and 1.6, respectively. For the WM model, the predictions are located within the range with a scatter factor of 1.4. This demonstrates the accuracy of the WM model in predicting *MDF* based on growth of grain-boundary cavities by a power-law creep.

3. Conclusion

In this study, the multiaxial ductility factor was analyzed and two novel predicting models were developed based on the power-law creep grain-boundary cavities growth theory under multiaxial stress states proposed by Cocks and Ashby. The details are summarized as follows.

- The predicting model of stress-state parameter α was revised by using an empirical equation denoted as α_{Wu}, and the relationship between uniaxial and multiaxial creep failure strain could be obtained, then an empirical multiaxial ductility factor MDF_{Wu} was built by using α_{Wu}.

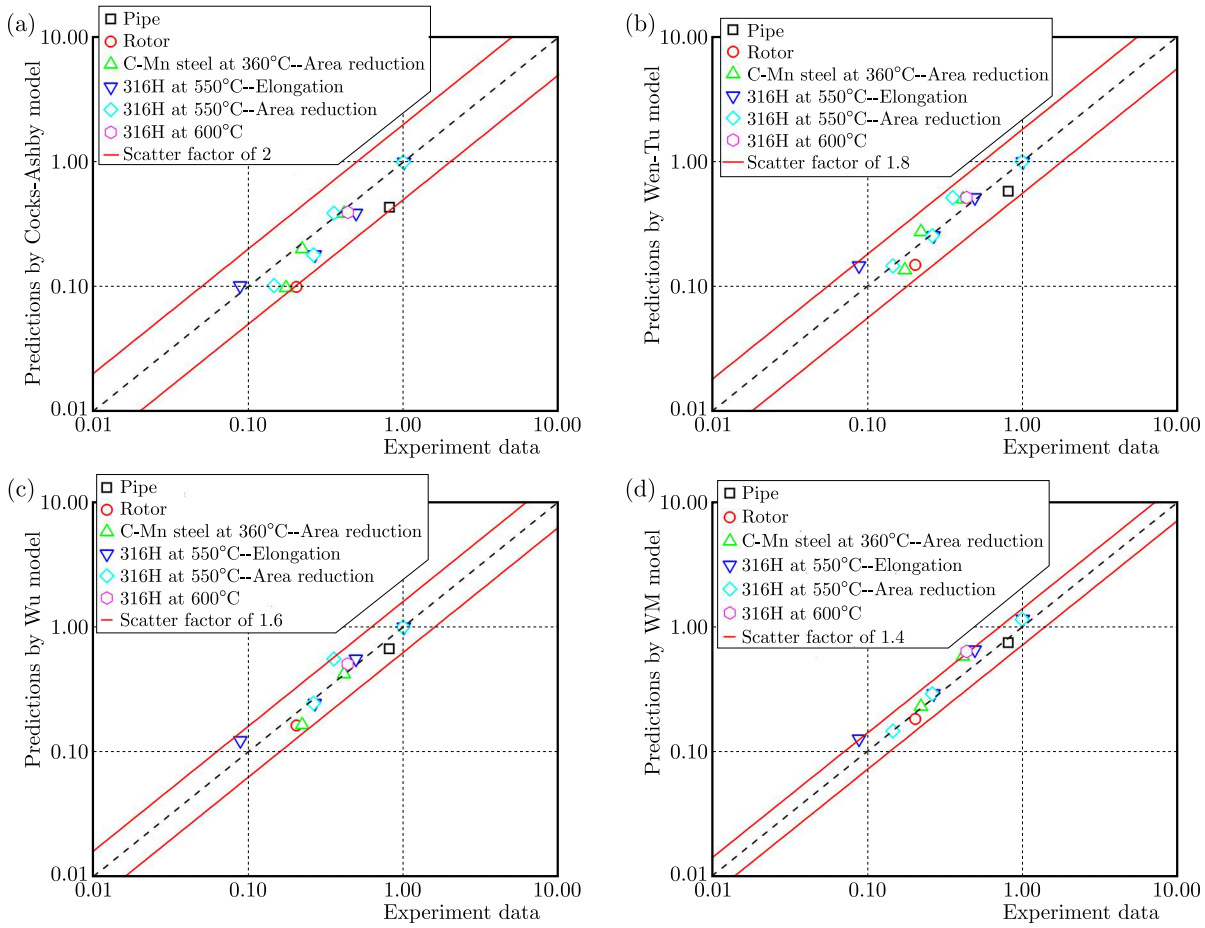

Fig. 8. Comparison of predictions and experimental data of *MDF*: (a) for Cocks-Ashby model, (b) for Wen-Tu model, (c) for Wu model, (d) for WM model

- The theoretical expression for multiaxial ductility factor *MDF* could also be established. By fitting theoretical curves of *MDF* against stress traiaxiality σ_m/σ_{eq}, another predicting model MDF_{WM} could be developed.
- Predictions of these two novel multiaxial ductility factor models as well as C-A and W-T models were compared with experimental data. The accuracy of MDF_{Wu} and MDF_{WM} models was obviously enhanced, especially for the MDF_{WM} with a scatter factor of only 1.4.

Acknowledgements

This research work was financially supported by the Scientific Research Program of Tianjin Education Commission (Grant No. 2021KJ053).

References

1. Alang N.A., Nikbin K., 2018, An analytical and numerical approach to multiscale ductility constraint based model to predict uniaxial/multiaxial creep rupture and cracking rates, *International Journal of Mechanical Sciences*, **135**, 342-352
2. Al-Rifaie H., Studziński R., Gajewski T., Malendowski M., Sumelka W., Sielicki P.W., 2021, A new blast absorbing sandwich panel with unconnected corrugated layersnumerical study, *Energies*, **14**, 1

3. Al-Rifaie H., Sumelka W., 2019, The development of a new shock absorbing uniaxial graded auxetic damper (UGAD), *Materials*, **12**, 16

4. Cocks A.C.F., Ashby M.F., 1980, Intergranular fracture during power-law creep under multiaxial stresses, *Metal Science Journal*, **14**, 8-9, 395-402

5. Davies C., 2006, *Crack Initiation and Growth at Elevated Temperatures in Engineering Steels*, Imperial College London

6. Holdsworth S.R., 1992, Initiation and early growth of creep cracks from pre-existing defects, *Materials at High Temperatures*, **10**, 2, 127-137

7. Manjoine M.J., 1975, Ductility indices at elevated temperature, *Journal of Engineering Materials and Technology*, **97**, 2, 156-161

8. McClintock F.A., 1968, A criterion for ductile fracture by the growth of holes, *Journal of Applied Mechanics*, **35**, 2, 363-371

9. Rice J.R., Tracey D.M., 1969, On the ductile enlargement of voids in triaxial stress fields, *Journal of the Mechanics and Physics of Solids*, **17**, 3, 201-217

10. Spindler M.W., 2004a, The multiaxial and uniaxial creep ductility of Type 304 steel as a function of stress and strain rate, *Materials at High Temperatures*, **21**, 1, 47-54

11. Spindler M.W., 2004b, The multiaxial creep ductility of austenitic stainless steels, *Fatigue and Fracture of Engineering Materials and Structures*, **27**, 4, 273-281

12. Spindler M.W., Hales R., Skelton R.P., 2001, Multiaxial creep ductility of an ex-service type 316 H stainless steel, *9th International Conference on Creep and Fracture of Engineering Materials and Structure*, 679-688

13. Tan J.P., Tu S.T., Wang G.Z., Xuan F.Z., 2013, Effect and mechanism of out-of-plane constraint on creep crack growth behavior of a Cr-Mo-V steel, *Engineering Fracture Mechanics*, **99**, 324-334

14. Wen J.F., Tu S.T., 2014, A multiaxial creep-damage model for creep crack growth considering cavity growth and microcrack interaction, *Engineering Fracture Mechanics*, **123**, 197-210

15. Wen J.F., Tu S.T., Xuan F.Z., Zhang X.W., Gao X.L., 2016, Effects of stress level and stress state on creep guctility: evaluation of different models, *Journal of Materials Science and Technology*, **32**, 8, 695-704

16. Wichtmann A., 2002, Evaluation of creep damage due to void growth under triaxial stress states in the design of steam turbine components, *JSME International Journal*, **45**, 1, 72-76

17. Wu D., Jing H., Xu L., 2020, Engineering application of enhanced C*-Q* two parameter approaches for predicting creep crack initiation times, *European Journal of Mechanics – A/Solids*, **82**, 104013

18. Wu D., Jing H., Xu L., Zhao L., Han Y., 2018a, Analytical approaches of creep crack initiation prediction coupled with the residual stress and constraint effect, *European Journal of Mechanics – A/Solids*, **71**, 1-15

19. Wu D., Jing H., Xu L., Zhao L., Han Y., 2018b, Numerical analysis of the creep crack constraint effects and the creep crack initiation for pressurized pipelines with circumferential surface cracks, *Advances in Engineering Software*, **115**, 40-51

20. Wu D., Jing H., Xu L., Zhao L., Han Y., 2018c, Theoretical and numerical analysis of the creep crack initiation time considering the constraint effects for pressurized pipelines with axial surface cracks, *International Journal of Mechanical Sciences*, **141**, 262-275

21. Wu D., Jing H., Xu L., Zhao L., Han Y., 2018d, Theoretical and numerical analysis of creep crack initiation combined with primary and secondary stresses, *Theoretical and Applied Fracture Mechanics*, **95**, 143-154

22. Wu D., Jing H., Xu L., Zhao L., Han Y., 2018e, Two-parameter approach of creep crack initiation times considering the constraint effect induced by specimen geometry, *Theoretical and Applied Fracture Mechanics*, **96**, 31-44

23. Wu D., Jing H., Xu L., Zhao L., Han Y., 2019, Enhanced models of creep crack initiation prediction coupled the stress-regime creep properties and constraint effect, *European Journal of Mechanics – A/Solids*, **74**, 145-159

24. Yatomi M., Bettinson A.D., O'Dowd N.P., Nikbin K.M., 2004, Modelling of damage development and failure in notched-bar multiaxial creep tests, *Fatigue and Fracture of Engineering Materials and Structures*, **27**, 4, 283-295

25. Yatomi M., Tabuchi M., 2010, Issues relating to numerical modelling of creep crack growth, *Engineering Fracture Mechanics*, **77**, 15, 3043-3052

26. You B.R., Lee S.B., 1996, A critical review on multiaxial fatigue assessments of metals, *International Journal of Fatigue*, **18**, 4, 235-244

Manuscript received February 22, 2022; accepted for print April 26, 2023

JOURNAL OF THEORETICAL AND APPLIED MECHANICS
61, 3, pp. 495-507, Warsaw 2023
https://doi.org/10.15632/jtam-pl/166562

A GRIFFITH CRACK MODEL IN A GENERALIZED NONHOMOGENEOUS INTERLAYER OF BONDED DISSIMILAR HALF-PLANES

Aibing Zhang, Jia Lou

Piezoelectric Device Laboratory, School of Mechanical Engineering and Mechanics, Ningbo University, Ningbo, China
corresponding author Aibing Zhang, e-mail: zhangaibing@nbu.edu.cn

Baolin Wang

School of Engineering, Design and Built Environment, Western Sydney University, Penrith, Australia

Ji Wang

Piezoelectric Device Laboratory, School of Mechanical Engineering and Mechanics, Ningbo University, Ningbo, China

The Griffith crack problem in bonded dissimilar half-planes is examined. To eliminate the unrealistic oscillatory stress near the interface crack tips, the interfacial transition zone is modeled by a very thin nonhomogeneous interlayer whose elastic properties vary continuously between the bonded materials and adhesive material. The interlayer thickness is assumed to be the sum of the maximum heights of asperities at the two bonded material surfaces. The crack problem is reduced to a set of Cauchy integral equations which can be solved numerically. The applicability of the generalized nonhomogeneous interlayer model is investigated by comparing it with the classical interface crack model.

Keywords: generalized nonhomogeneous interlayer, Griffith crack, stress intensity factors, fracture mechanics

1. Introduction

Interfaces are intrinsic to many modern composite materials since they are always layered. The structural performance of such materials is generally dependent on their interfaces which are heterogeneities such as discontinuities in elastic and thermal properties as well as residual stresses. Fracture mechanics of layered materials has been extensively used to characterize the initiation and propagation of delamination (Hutchinson and Suo, 1992; Suo, 1990; Wang *et al.*, 2021; Zhang and Wang, 2016). The classical model for an idealized (or perfect) bonding bimaterial structure containing an interface crack was established by Williams (1959) by assuming the zero-thickness interface, which means that the stress and displacement vary continuously across the interface. However, analytical solutions for interface crack problems show that there is an oscillatory singularity which is physically unreasonable and results in material interpenetration near the ends of the interface crack (England, 1965; Erdogan, 1965; Williams, 1959). In order to eliminate the unrealistic oscillatory singularity, a closed crack tip model was developed by Comninou (1977) based on classical solutions which assumed that the surfaces of interface crack contact was frictionless near the tips. This model was further applied to interfacial fracture analysis of anisotropic materials (Ayatollahi *et al.*, 2022; Herrmann and Loboda, 1999), piezoelectric materials (Govorukha *et al.*, 2000; Sheveleva *et al.*, 2015), thermopiezoelectric materials (Qin and Mai, 1999). A modified interface dislocation model for interface fracture analysis was presented by Zhang and Wang (2013), which represented an inverse square-root singularity at the interface crack tips and avoided the oscillatory behavior.

The idealized interface model for the fracture problem in bonded dissimilar homogeneous materials may be too unrealistic from the micromechanical point of view, and it does not capture any effect of mechanical characteristics of the real transition layer (i.e., interlayer) between the materials on the stress and displacement distribution. In fact, an interlayer forms whatever the actual mechanism of binding is, and should be taken into account as a distinct chemical species or a distinct phase. Physical properties in a thin interlayer are highly nonhomogeneous with the steeply varying composition profile. The layer thickness ranges from nanometers to fractions of a millimeter (Yang and Shih, 1994). Two attractive features emerge when the nonhomogeneous interlayer model is used to the interface crack problems. Firstly, the stress oscillatory singularity is removed so that the local mode mixity is independent of the distance ahead the crack tip. Secondly, the conventional stress intensity factors (SIFs) can be defined as the crack problems in a homogeneous medium. The nonhomogeneous interlayer model considering the interpenetration or interdiffusion of molecules in the interfacial zone was first theoretically developed by Delale and Erdogan (1988) and successfully applied to fracture problems in bimaterial structures (Erdogan *et al.*, 1991; Ozturk and Erdogan, 1995). A more generalized interlayer model introducing a distribution parameter independent of interlayer thickness and material properties was presented by Wang *et al.* (1996, 1997), and the Erdogan's interlayer model could be obtained when the distribution parameter tends to infinity.

On the other hand, there exist various roughnesses and asperities at each bonded material surface, and the third material used as an adhesive may be filled with gaps between the surfaces of two primary components as shown in Fig. 1a. As a result, a more generalized nonhomogeneous interlayer containing adhesive materials may also be emerged instead of the Erdogan's interlayer. The elastic constants of this nonhomogeneous interlayer are not only dependent on the physical properties of bonded materials but also on those of the adhesive material. Thus, the purpose of this paper is to develop a theoretical model of the Griffith crack in a generalized nonhomogeneous interlayer considering the influence of surface roughness of bonded materials and elastic properties of the adhesive material.

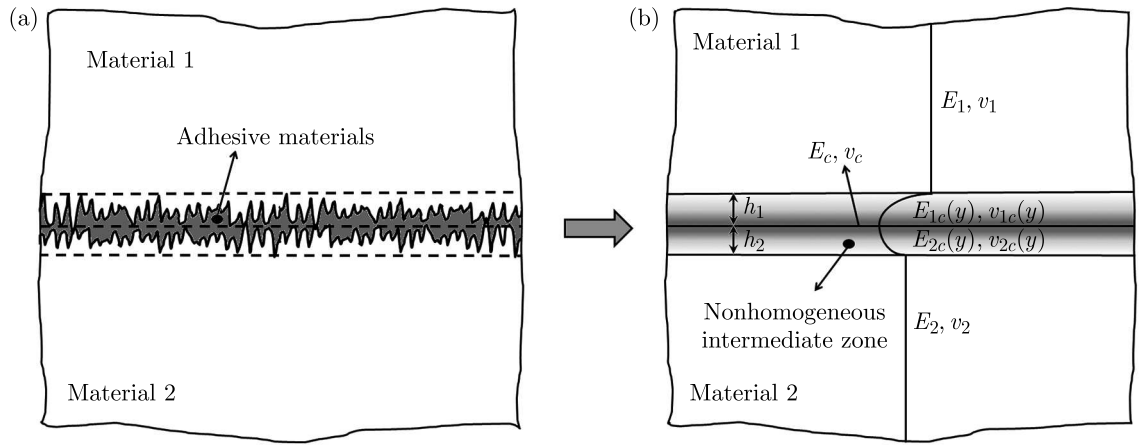

Fig. 1. The generalized nonhomogeneous interlayer model: (a) microstructures of the bonding zone between two homogeneous elastic half-planes, (b) the effective nonhomogeneous interlayer

2. Mathematical model for a Griffith crack in a generalized nonhomogeneous interlayer

2.1. Formulation of the generalized nonhomogeneous interlayer

Consider an interface mechanical problem in a bimaterial structure composed of two isotropic and homogeneous materials with elastic moduli E_1 and E_2, and Poisson's ratios ν_1 and ν_2. The

thickness of the nonhomogeneous interlayer is assumed to be the sum of the maximum heights of asperities at the two bonded material surfaces, assuming that the adhesive layer is much thinner than the interlayer. It is noted that the assumption of the zero-thickness adhesive layer is consistent with the classical model of interface mechanics (England, 1965; Erdogan, 1965; Williams, 1959). In order to facilitate the complicated interfacial transition zone, a generalized nonhomogeneous interlayer model with the thickness of $h = h_1 + h_2$ is developed as shown in Fig. 1b. The mechanical properties of the interlayer may vary steeply, but it is crucial to maintain continuity at the interfaces with the adjacent materials. Delale and Erdogan (1988) introduced an interlayer model with material constants that exhibited an exponential variation, which ensured an inverse square-root singularity at the crack tips and made the problem analytically tractable. Therefore, in this paper, the material parameters along such an interlayer are assumed to be only dependent on y, and the elastic modulus has a form of

$$E_{jc}(y) = E_c \mathrm{e}^{\lambda_j y} \tag{2.1}$$

where $j = 1, 2$ and E_c is the elastic modulus of the adhesive material, subscripts $1c$ and $2c$ are corresponding to regions $0 \leqslant y \leqslant h_1$ and $-h_2 \leqslant y < 0$, respectively. The parameter λ_j can be determined from the continuity conditions for $E_{1c}(h_1) = E_1$ and $E_{2c}(-h_2) = E_2$, that is

$$\lambda_j = \begin{cases} \dfrac{1}{h_1} \ln \dfrac{E_1}{E_c} & 0 \leqslant y \leqslant h_1 \\ -\dfrac{1}{h_2} \ln \dfrac{E_2}{E_c} & -h_2 \leqslant y < 0 \end{cases} \tag{2.2}$$

Introducing Airy stress functions $F_{jc}(x, y)$ as

$$\sigma_{xx}^{jc} = \frac{\partial^2 F_{jc}(x,y)}{\partial y^2} \qquad \sigma_{yy}^{jc} = \frac{\partial^2 F_{jc}(x,y)}{\partial x^2} \qquad \sigma_{xy}^{jc} = -\frac{\partial^2 F_{jc}(x,y)}{\partial x \partial y} \tag{2.3}$$

Considering that the functions E_{jc} and ν_{jc} are independent of x, the compatibility condition is expressed as

$$\begin{aligned} &\nabla^4 F_{jc}(x,y) - 2\lambda_j \frac{\partial}{\partial y} \nabla^2 F_{jc}(x,y) + \lambda_j^2 \frac{\partial^2 F_{jc}(x,y)}{\partial y^2} \\ &\quad - \Big[\frac{d^2 \nu_{jc}(y)}{dy^2} - 2\lambda_j \frac{d\nu_{jc}(y)}{dy} + \lambda_j^2 \nu_{jc}(y) \Big] \frac{\partial^2 F_{jc}(x,y)}{\partial x^2} = 0 \end{aligned} \tag{2.4}$$

It is known that Poisson's ratios do not influence the SIFs significantly (Delale and Erdogan, 1983; 1988). Thus, we further assume that

$$\begin{aligned} &\nabla^4 F_{jc}(x,y) - 2\lambda_j \frac{\partial}{\partial y} \nabla^2 F_{jc}(x,y) + \lambda_j^2 \frac{\partial^2 F_{jc}(x,y)}{\partial y^2} = 0 \\ &\frac{d^2 \nu_{jc}(y)}{dy^2} - 2\lambda_j \frac{d\nu_{jc}(y)}{dy} + \lambda_j^2 \nu_{jc}(y) = 0 \end{aligned} \tag{2.5}$$

By means of Eq. $(2.5)_2$, Poisson's ratios are obtained as follows

$$\nu_{jc}(y) = (\nu_c + \nu_{j0} y) \mathrm{e}^{\lambda_j y} \tag{2.6}$$

where $\nu_{10} = (E_c\nu_1 - E_1\nu_c)/(E_1 h_1)$ and $\nu_{20} = -(E_c\nu_2 - E_2\nu_c)/(E_2 h_2)$. Now, the elastic properties and geometric dimensions of the generalized nonhomogeneous interlayer are totally determined.

2.2. Griffith crack model in the generalized nonhomogeneous interlayer

Attention is now focused on the Griffith crack problem with a generalized nonhomogeneous interlayer as shown in Fig. 2, where the physical length of the crack is designated by $2c$. The origin of the rectangular coordinate system x-y is fixed at the middle point of the crack and the x-axis coincides with the crack line. The elastic properties are constant for $y > h_1$ and $y < -h_2$, and the plane elasticity problem can be formulated by assuming that each material is perfectly bonded along the planes $y = h_1$, $y = 0$ and $y = -h_2$ except for the crack.

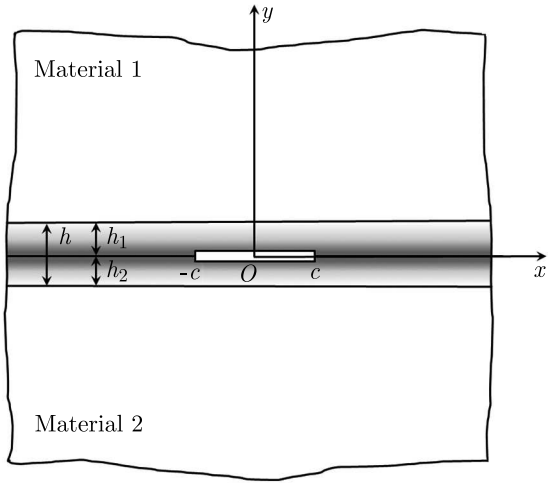

Fig. 2. Geometry of the Griffith crack problem with a generalized nonhomogeneous interlayer

By using the Fourier transform technique, the solutions for Airy stress functions $F_{jc}(x, y)$ in the generalized nonhomogeneous interlayer and $F_j(x, y)$ in the homogeneous materials have forms of

$$\begin{aligned} F_{jc}(x,y) &= \frac{1}{2\pi}\int_{-\infty}^{\infty}\Big\{[A_{j1}(\xi)+A_{j2}(\xi)y]\mathrm{e}^{m_{j1}y}+[A_{j3}(\xi)+A_{j4}(\xi)y]\mathrm{e}^{m_{j2}y}\Big\}\mathrm{e}^{-\mathrm{i}\xi x}\,d\xi \\ F_j(x,y) &= \frac{1}{2\pi}\int_{-\infty}^{\infty}[B_{j1}(\xi)+B_{j2}(\xi)y]\mathrm{e}^{-\delta_j|\xi|y-\mathrm{i}\xi x}\,d\xi \end{aligned} \tag{2.7}$$

where $A_{jk}(\xi)$ $(k = 1, 2, 3, 4)$ and $B_{jl}(\xi)$ $(l = 1, 2)$ are unknown functions, m_{jk} and δ_j are defined as

$$\begin{aligned} &m_{j1} = m_{j3} = \frac{\lambda_j}{2} - \sqrt{\xi^2+\frac{\lambda_j^2}{4}} \qquad m_{j2} = m_{j4} = \frac{\lambda_j}{2} + \sqrt{\xi^2+\frac{\lambda_j^2}{4}} \\ &\delta_j = \begin{cases} -1 & y > h_1 \\ 1 & y < -h_2 \end{cases} \end{aligned} \tag{2.8}$$

By substituting Airy stress functions (2.7) into Eq. (2.3) and using the constitutive equations and stain-displacement relations, the stress fields and displacements in the bimaterial structure are obtained as follows

$$
\begin{aligned}
\sigma_{yy}^{jc}(x,y) &= -\frac{1}{2\pi}\int\limits_{-\infty}^{\infty}\xi^2[(A_{j1}+A_{j2}y)\mathrm{e}^{m_{j1}y}+(A_{j3}+A_{j4}y)\mathrm{e}^{m_{j2}y}]\mathrm{e}^{-\mathrm{i}\xi x}\,d\xi\\
\sigma_{xy}^{jc}(x,y) &= \frac{1}{2\pi}\int\limits_{-\infty}^{\infty}\mathrm{i}\xi\Big\{[m_{j1}A_{j1}+(1+m_{j1}y)A_{j2}]\mathrm{e}^{m_{j1}y}\\
&\quad+[m_{j2}A_{j3}+(1+m_{j2}y)A_{j4}]\mathrm{e}^{m_{j2}y}\Big\}\mathrm{e}^{-\mathrm{i}\xi x}\,d\xi\\
\sigma_{xx}^{jc}(x,y) &= \frac{1}{2\pi}\int\limits_{-\infty}^{\infty}\Big\{[m_{j1}^2A_{j1}+(2+m_{j1}y)m_{j1}A_{j2}]\mathrm{e}^{m_{j1}y}\\
&\quad+[m_{j2}^2A_{j3}+(2+m_{j2}y)m_{j2}A_{j4}]\mathrm{e}^{m_{j2}y}\Big\}\mathrm{e}^{-\mathrm{i}\xi x}\,d\xi
\end{aligned}
\tag{2.9}
$$

$$
\begin{aligned}
\sigma_{yy}^{j}(x,y) &= -\frac{1}{2\pi}\int\limits_{-\infty}^{\infty}\xi^2(B_{j1}+B_{j2}y)\mathrm{e}^{-\delta_j|\xi|y-\mathrm{i}\xi x}\,d\xi\\
\sigma_{xy}^{j}(x,y) &= \frac{1}{2\pi}\int\limits_{-\infty}^{\infty}\mathrm{i}\xi[-\delta_j|\xi|B_{j1}+(1-\delta_j|\xi|y)B_{j2}]\mathrm{e}^{-\delta_j|\xi|y-\mathrm{i}\xi x}\,d\xi\\
\sigma_{xx}^{j}(x,y) &= \frac{1}{2\pi}\int\limits_{-\infty}^{\infty}[\xi^2B_{j1}+(\xi^2y-2\delta_j|\xi|)B_{j2}]\mathrm{e}^{-\delta_j|\xi|y-\mathrm{i}\xi x}\,d\xi
\end{aligned}
\tag{2.10}
$$

$$
\begin{aligned}
u_x^{jc}(x,y) &= -\frac{1}{2\pi}\int\limits_{-\infty}^{\infty}\frac{1}{\mathrm{i}\xi E_{jc}(y)}\Big\{\Big[\Big(m_{j1}^2+\xi^2\nu_{jc}(y)\Big)A_{j1}\\
&\quad+[(2+m_{j1}y)m_{j1}+\xi^2y\nu_{jc}(y)]A_{j2}\Big]\mathrm{e}^{m_{j1}y}+\Big[\Big(m_{j2}^2+\xi^2\nu_{jc}(y)\Big)A_{j3}\\
&\quad+[(2+m_{j2}y)m_{j2}+\xi^2y\nu_{jc}(y)]A_{j4}\Big]\mathrm{e}^{m_{j2}y}\Big\}\mathrm{e}^{-\mathrm{i}\xi x}\,d\xi\\
u_y^{jc}(x,y) &= -\frac{1}{2\pi E_c}\int\limits_{-\infty}^{\infty}\Big\{\Big[\Big(\frac{\xi^2}{m_{j1}-\lambda_j}\mathrm{e}^{-\lambda_jy}+m_{j1}(\nu_c+\nu_{j0}y)-\nu_{j0}\Big)A_{j1}\\
&\quad+\Big(\frac{(m_{j1}-\lambda_j)y-1}{(m_{j1}-\lambda_j)^2}\xi^2\mathrm{e}^{-\lambda_jy}+(\nu_c+\nu_{j0}y)m_{j1}y+\nu_c\Big)A_{j2}\Big]\mathrm{e}^{m_{j1}y}\\
&\quad+\Big[\Big(\frac{\xi^2}{m_{j2}-\lambda_j}\mathrm{e}^{-\lambda_jy}+m_{j2}(\nu_c+\nu_{j0}y)-\nu_{j0}\Big)A_{j3}\\
&\quad+\Big(\frac{(m_{j2}-\lambda_j)y-1}{(m_{j2}-\lambda_j)^2}\xi^2\mathrm{e}^{-\lambda_jy}+(\nu_c+\nu_{j0}y)m_{j2}y+\nu_c\Big)A_{j2}\Big]\mathrm{e}^{m_{j2}y}\Big\}\mathrm{e}^{-\mathrm{i}\xi x}\,d\xi
\end{aligned}
\tag{2.11}
$$

$$
\begin{aligned}
u_x^{j}(x,y) &= -\frac{1}{2\pi E_j}\int\limits_{-\infty}^{\infty}\frac{1}{\mathrm{i}\xi}\Big\{(1+\nu_j)\xi^2B_{j1}+[(1+\nu_j)\xi^2y-2\delta_j|\xi|y]B_{j2}\Big\}\mathrm{e}^{-\delta_j|\xi|y-\mathrm{i}\xi x}\,d\xi\\
u_y^{j}(x,y) &= \frac{1}{2\pi E_j}\int\limits_{-\infty}^{\infty}\Big\{(1+\nu_j)\delta_j|\xi|B_{j1}+[(1+\nu_j)\delta_j|\xi|y-\nu_j+1]B_{j2}\Big\}\mathrm{e}^{-\delta_j|\xi|y-\mathrm{i}\xi x}\,d\xi
\end{aligned}
\tag{2.12}
$$

The boundary conditions of the Griffith crack problem are expressed as

$$
\begin{aligned}
&u_x^{1c}(x,0)=u_x^{2c}(x,0) \qquad u_y^{1c}(x,0)=u_y^{2c}(x,0) \qquad |x|>c\\
&\sigma_{yy}^{1c}(x,0)=\sigma_{yy}^{2c}(x,0) \qquad \sigma_{xy}^{1c}(x,0)=\sigma_{xy}^{2c}(x,0) \qquad |x|<\infty\\
&\sigma_{yy}^{1c}(x,0)=-p(x) \qquad \sigma_{xy}^{1c}(x,0)=-q(x) \qquad |x|\leqslant c
\end{aligned}
\tag{2.13}
$$

and

$$\begin{aligned} &u_x^{1c}(x,h_1)=u_x^1(x,h_1) \qquad u_y^{1c}(x,h_1)=u_y^1(x,h_1) \qquad |x|<\infty \\ &\sigma_{yy}^{1c}(x,h_1)=\sigma_{yy}^1(x,h_1) \qquad \sigma_{xy}^{1c}(x,h_1)=\sigma_{xy}^1(x,h_1) \qquad |x|<\infty \end{aligned} \tag{2.14}$$

and

$$\begin{aligned} &u_x^{2c}(x,-h_2)=u_x^2(x,-h_2) \qquad u_y^{2c}(x,-h_2)=u_y^2(x,-h_2) \qquad |x|<\infty \\ &\sigma_{yy}^{2c}(x,-h_2)=\sigma_{yy}^2(x,-h_2) \qquad \sigma_{xy}^{2c}(x,-h_2)=\sigma_{xy}^2(x,-h_2) \qquad |x|<\infty \end{aligned} \tag{2.15}$$

where $p(x)$ and $q(x)$ are known functions.

2.3. Integral equations and stress intensity factors

We now introduce functions $f_j(x)$ at the crack plane

$$f_1(x)=\frac{\partial}{\partial x}[u_x^{1c}(x,0)-u_x^{2c}(x,0)] \qquad f_2(x)=\frac{\partial}{\partial x}[u_y^{1c}(x,0)-u_y^{2c}(x,0)] \tag{2.16}$$

The stress and displacement on the crack line for a bimaterial structure can be obtained based on Eqs. (2.9) and (2.11), then the functions $A_{jk}(\xi)$ are determined by making use of boundary conditions (2.13)-(2.15), and after some lengthy manipulations, we have

$$A_{jk}(\xi)=\gamma_{k1}^{jc}(\xi)g_1(\xi)+\gamma_{k2}^{jc}(\xi)g_2(\xi) \tag{2.17}$$

where $j=1,2$, $k=1,2,3,4$, and

$$g_1(\xi)=E_c\int_{-\infty}^{\infty}f_1(t)\mathrm{e}^{\mathrm{i}\xi t}\,dt \qquad g_2(\xi)=E_c\int_{-\infty}^{\infty}f_2(t)\mathrm{e}^{\mathrm{i}\xi t}\,dt \tag{2.18}$$

The functions $\gamma_{k1}^{jc}(\xi)$ and $\gamma_{k2}^{jc}(\xi)$ are not given here due to tediousness, and can be obtained by solving 12 linear algebraic equations in terms of $g_1(\xi)$ and $g_2(\xi)$ based on the boundary conditions. By substituting Airy functions Eqs. (2.7), and Eq. (2.17) into Eq. (2.3), the stresses on the crack line are obtained as follows

$$\begin{aligned} \sigma_{yy}^{1c}(x,0)&=-\frac{E_c}{2\pi}\int_{-c}^{c}\int_{-\infty}^{\infty}[P_{11}(\xi)f_1(t)+P_{12}(\xi)f_2(t)]\mathrm{e}^{\mathrm{i}\xi(t-x)}\,d\xi\,dt \\ \sigma_{xy}^{1c}(x,0)&=-\frac{E_c}{2\pi}\int_{-c}^{c}\int_{-\infty}^{\infty}[P_{21}(\xi)f_1(t)+P_{22}(\xi)f_2(t)]\mathrm{e}^{\mathrm{i}\xi(t-x)}\,d\xi\,dt \end{aligned} \tag{2.19}$$

where

$$\begin{aligned} &P_{11}(\xi)=\xi^2[\gamma_{11}^{1c}(\xi)+\gamma_{31}^{1c}(\xi)] \qquad P_{12}(\xi)=\xi^2[\gamma_{12}^{1c}(\xi)+\gamma_{32}^{1c}(\xi)] \\ &P_{21}(\xi)=-\mathrm{i}\xi[m_{11}\gamma_{11}^{1c}(\xi)+\gamma_{21}^{1c}(\xi)+m_{12}\gamma_{31}^{1c}(\xi)+\gamma_{41}^{1c}(\xi)] \\ &P_{22}(\xi)=-\mathrm{i}\xi[m_{11}\gamma_{12}^{1c}(\xi)+\gamma_{22}^{1c}(\xi)+m_{12}\gamma_{32}^{1c}(\xi)+\gamma_{42}^{1c}(\xi)] \end{aligned} \tag{2.20}$$

It should be noted that $P_{11}(\xi)$, $P_{22}(\xi)$ are even functions and $P_{12}(\xi)$, $P_{21}(\xi)$ are odd functions with respect to ξ. In addition, the following asymptotic properties of $P_{11}(\xi)$, $P_{12}(\xi)$, $P_{21}(\xi)$ and $P_{22}(\xi)$ are further given

$$\lim_{\xi\to+\infty}P_{12}(\xi)=\lim_{\xi\to+\infty}P_{21}(\xi)=-\frac{1}{4} \qquad \lim_{\xi\to+\infty}P_{11}(\xi)=\lim_{\xi\to+\infty}P_{22}(\xi)=0 \tag{2.21}$$

Therefore, the Griffith crack problem with a generalized nonhomogeneous interlayer can be reduced to the first kind singular integral equations based on the analysis of Eq. (2.21) rather than the second kind ones which represent physically unreasonable stress oscillatory singularity and lead to overlapping near the ends of the crack surfaces. Using boundary condition Eq. $(2.13)_3$, the Cauchy singular integral equations are obtained as follows

$$\begin{aligned}
&\frac{E_c}{\pi}\int_{-c}^{c}[Q_{11}(t,x)f_1(t)+Q_{12}(t,x)f_2(t)]\,dt-\frac{E_c}{4\pi}\int_{-c}^{c}\frac{f_2(t)}{t-x}\,dt=p(x)\\
&\frac{E_c}{\pi}\int_{-c}^{c}[Q_{21}(t,x)f_1(t)+Q_{22}(t,x)f_2(t)]\,dt-\frac{E_c}{4\pi}\int_{-c}^{c}\frac{f_1(t)}{t-x}\,dt=q(x)
\end{aligned}\tag{2.22}$$

where

$$\begin{aligned}
Q_{11}(t,x)&=\int_0^\infty P_{11}(\xi)\cos[\xi(t-x)]\,d\xi & Q_{12}(t,x)&=\int_0^\infty\Big[\mathrm{i}P_{12}(\xi)+\frac{1}{4}\Big]\sin[\xi(t-x)]\,d\xi\\
Q_{21}(t,x)&=\int_0^\infty\Big[\mathrm{i}P_{21}(\xi)+\frac{1}{4}\Big]\sin[\xi(t-x)]\,d\xi & Q_{22}(t,x)&=\int_0^\infty P_{22}(\xi)\cos[\xi(t-x)]\,d\xi
\end{aligned}\tag{2.23}$$

It is clear from condition $(2.13)_1$ that

$$\int_{-c}^{c}f_1(t)\,dt=0\qquad\qquad\int_{-c}^{c}f_2(t)\,dt=0\tag{2.24}$$

Integral Eqs. (2.22)-(2.24) can be solved numerically by using the method developed by Erdogan (1975). Furthermore, the undetermined functions $f_1(x)$ and $f_2(x)$ are of conventional inverse square-root singularity at $x=\pm c$ according to the singular integral equation theory. Normalizing the interval $(-c,c)$ by changing variables as $t=c\widetilde{t}$ and $x=c\widetilde{x}$, integral equations of (2.22)-(2.24) have solutions in the following form

$$f_1(t)=\frac{H_1(\widetilde{t})}{\sqrt{1-\widetilde{t}^2}}=\frac{\sum_{i=0}^{n-1}D_{1i}T_i(\widetilde{t})}{\sqrt{1-\widetilde{t}^2}}\qquad f_2(t)=\frac{H_2(\widetilde{t})}{\sqrt{1-\widetilde{t}^2}}=\frac{\sum_{i=0}^{n-1}D_{2i}T_i(\widetilde{t})}{\sqrt{1-\widetilde{t}^2}}\tag{2.25}$$

where $H_1(\widetilde{t})$ and $H_2(\widetilde{t})$ are continuous bounded functions defined in the interval $|\widetilde{t}|\leqslant 1$, $T_i(\widetilde{t})$ is the first kind Chebyshev polynomial, and the coefficients D_{1i} and D_{2i} are constants as yet to be determined. After discretization, the singular integral equations can be rewritten as

$$\begin{aligned}
&\frac{E_c}{n}\sum_{k=1}^{n}\Big[Q_{11}(\widetilde{t}_k,\widetilde{x}_r)H_1(\widetilde{t}_k)+Q_{12}(\widetilde{t}_k,\widetilde{x}_r)H_2(\widetilde{t}_k)-\frac{H_2(\widetilde{t}_k)}{4(\widetilde{t}_k-\widetilde{x}_r)}\Big]=p(\widetilde{x}_r)\\
&\frac{E_c}{n}\sum_{k=1}^{n}\Big[Q_{21}(\widetilde{t}_k,\widetilde{x}_r)H_1(\widetilde{t}_k)+Q_{22}(\widetilde{t}_k,\widetilde{x}_r)H_2(\widetilde{t}_k)-\frac{H_1(\widetilde{t}_k)}{4(\widetilde{t}_k-\widetilde{x}_r)}\Big]=q(\widetilde{x}_r)\\
&\sum_{k=1}^{n}H_1(\widetilde{t}_k)=0\qquad\qquad\sum_{k=1}^{n}H_2(\widetilde{t}_k)=0
\end{aligned}\tag{2.26}$$

where the discretization points $\widetilde{t}_k$ and $\widetilde{x}_r$ are defined by

$$\begin{aligned}
\widetilde{t}_k&=\cos\Big(\frac{2k-1}{2n}\pi\Big)\qquad & k&=1,2,\ldots,n\\
\widetilde{x}_r&=\cos\Big(\frac{r}{n}\pi\Big)\qquad & r&=1,2,\ldots,n-1
\end{aligned}\tag{2.27}$$

The equation system in (2.26) includes $2n$ linear algebraic equations in terms of $H_1(\widetilde{t}_k)$ and $H_2(\widetilde{t}_k)$, and the coefficients D_{1i} and D_{2i} can be easily solved. The SIFs at the crack tip are of interest and are defined as

$$\begin{aligned} K_1(c) &= \sqrt{2\pi(x-c)}\sigma_{yy}^{1c}(x,0) = -\frac{E_c}{4}\sqrt{\pi c}\sum_{i=1}^{n-1} D_{2i} \\ K_2(c) &= \sqrt{2\pi(x-c)}\sigma_{xy}^{1c}(x,0) = -\frac{E_c}{4}\sqrt{\pi c}\sum_{i=1}^{n-1} D_{1i} \end{aligned} \tag{2.28}$$

where the following integral property of the Chebyshev polynomial is used

$$\frac{1}{\pi}\int_{-1}^{1}\frac{1}{\widetilde{t}-\widetilde{x}}\frac{T_i(\widetilde{t})}{\sqrt{1-\widetilde{t}^2}}\,dt = -\frac{|\widetilde{x}|}{\widetilde{x}\sqrt{\widetilde{x}^2-1}}\Big(\widetilde{x}-\frac{|\widetilde{x}|}{\widetilde{x}}\sqrt{\widetilde{x}^2-1}\Big)^i \qquad |\widetilde{x}|>1 \tag{2.29}$$

The definition of fracture mode mixity is

$$\psi = \arctan\frac{K_2(c)}{K_1(c)} \tag{2.30}$$

The energy release rate for crack propagation at the crack tip can then be calculated by using the crack closure concept as

$$G(c) = \frac{1}{E_c}[K_1^2(c)+K_2^2(c)] \tag{2.31}$$

3. Numerical results and discussions

The influence of elastic property and thickness of the generalized nonhomogeneous interlayer on the SIFs is investigated in numerical examples. The material combination used is as follows (Delale and Erdogan, 1988)

$$\begin{aligned} E_1 &= 20.685\cdot 10^{10}\ \frac{\mathrm{N}}{\mathrm{m}^2} \qquad \nu_1 = 0.3 \\ E_2 &= 6.895\cdot 10^{10}\ \frac{\mathrm{N}}{\mathrm{m}^2} \qquad \nu_1 = 0.3 \end{aligned} \tag{3.1}$$

Poisson's ratio of the adhesive material is $\nu_c = 0.3$ since it has very little effect on the SIFs. Without loss of any generality, we set

$$p(x) = p_0 \qquad q(x) = q_0 \tag{3.2}$$

in the following numerical analysis. It is noted that the developed model for Griffith crack problems in bonded dissimilar elastic half-planes can be reduced to the interfacial region model (Delale and Erdogan, 1988) and the classical interface crack model (Williams, 1959) if the elastic modulus of the adhesive material is given as $E_c = E_1(E_2/E_1)^{h_1/h}$ and the thickness $h \to 0$, respectively. To verify validity of the presented theoretical model, the normalized SIFs for a Griffith crack with the thickness ratio $h_1/h = 0.5$ are given in Table 1, and the corresponding results calculated by Delale and Erdogan (1988) are also listed. The results show that the present scheme achieves a good agreement of the accuracy.

Both Figs. 3 and 4 plot the influence of the elastic modulus of the adhesive material and thickness ratio h_1/c on the normalized SIFs at the crack tip with $K_0 = \pi c\sqrt{p_0^2+q_0^2}$, for different combinations of $p(x)$ and $q(x)$. It is found that pure far-field uniform tension can produce mode II

Table 1. Normalized SIFs calculated based on the generalized nonhomogeneous interlayer model and the interfacial region model for $h_1/h = 0.5$

c/h	Delale and Erdogan (1988)		Present results	
	$K_1(c)/(p_0\sqrt{\pi c})$	$K_2(c)/(p_0\sqrt{\pi c})$	$K_1(c)/(p_0\sqrt{\pi c})$	$K_2(c)/(p_0\sqrt{\pi c})$
0.1	1.004	0.023	1.0041	0.0257
0.25	1.014	0.058	1.0141	0.0584
0.5	1.026	0.092	1.0263	0.0924
1	1.036	0.127	1.0360	0.1223
5	1.046	0.169	1.0452	0.1661

SIF and a pure far-field uniform shear loading can also produce mode I SIF at the crack tip based on the generalized nonhomogeneous interlayer model. This behavior is similar to the classical interface crack problem. In addition, it may observed that the normalized SIFs tend to increase as the elastic modulus of the adhesive material increases, and the thickness ratio h_1/c has a very significant effect on the crack-tip stress fields especially for small values of h_1/c.

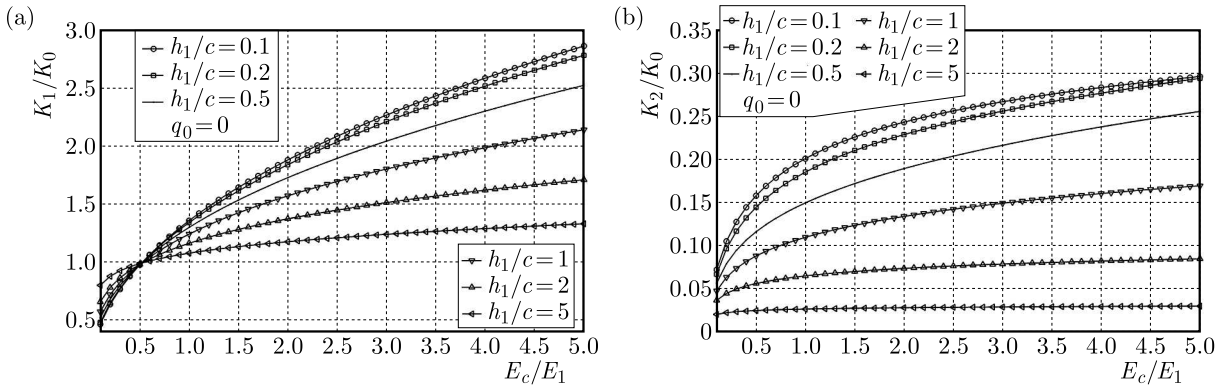

Fig. 3. Effect of the elastic modulus of the adhesive material on normalized (a) mode I and (b) mode II SIFs, with $p(x) = p_0$, and $q(x) = 0$

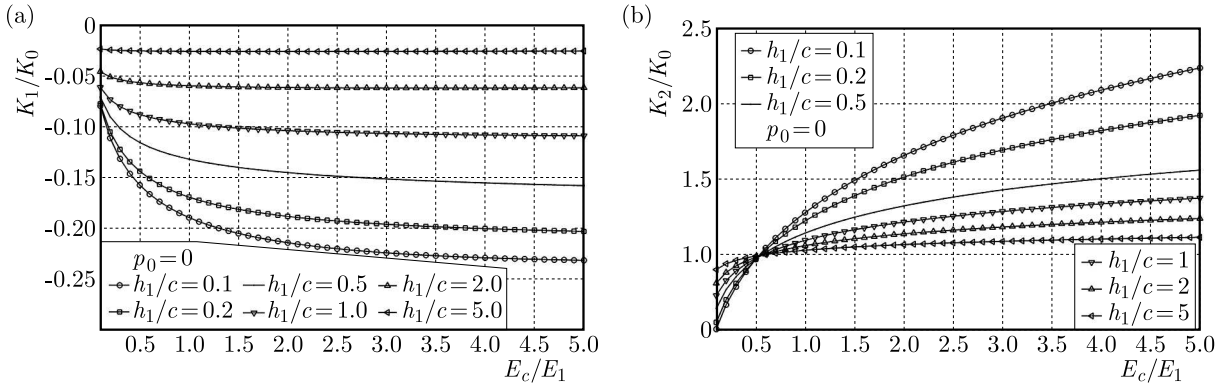

Fig. 4. Effect of the elastic modulus of the adhesive material on normalized (a) mode I and (b) mode II SIFs, with $p(x) = 0$, and $q(x) = q_0$

It is worth noting that the developed theoretical model introduces three new parameters, namely h_1, h_2 and E_c, which have clear physical significance and can be measured. The singularity obtained based on the classical interface crack model may result in a complex number (as shown in Eq. (3.3)) and lead to stress oscillations and displacement interference at the crack tips. However, the energy release rate is largely uninfluenced and has great practical guidance for

the criteria of crack propagation. To better understand the numerical results discussed below, it may be worthwhile to recall the crack-tip fields in the classical interface fracture mechanics. The SIFs at crack tip are given as (Sun and Jih, 1987)

$$K_1(c) + \mathrm{i}K_2(c) = (p_0 + \mathrm{i}q_0)\sqrt{\pi c}(1 + 2\mathrm{i}\varepsilon)(2c)^{-\mathrm{i}\varepsilon} \tag{3.3}$$

where

$$\begin{aligned} &\varepsilon = \frac{1}{2\pi}\ln\frac{1-\beta}{1+\beta} \qquad \beta = \frac{\mu_2(\kappa_1-1)-\mu_1(\kappa_2-1)}{\mu_2(\kappa_1+1)+\mu_1(\kappa_2+1)} \\ &\kappa_j = 3-4\nu_j \qquad \mu_j = \frac{E_j}{2(1+\nu_j)} \qquad j=1,2 \end{aligned} \tag{3.4}$$

The energy release rate for crack propagation in the interface is (Malyshev and Salganik, 1965)

$$G(c) = \frac{1-\beta^2}{E^*}[K_1^2(c) + K_2^2(c)] \tag{3.5}$$

with $1/E^* = (1/E_1 + 1/E_2)/2$, and $\overline{E}_j = E_j/(1-\nu_j^2)$ for plane strain, $\overline{E}_j = E_j$ for plane stress.

The SIFs obtained by Eqs. (2.28) cannot be directly compared to those calculated using the classical interface crack approach due to different singularities at the crack tips. However, the energy release rates calculated based on the developed model can also offer an important reference, similar to the classical interface crack model. The elastic modulus E_c of the adhesive should be predetermined in real adhesively bonded components when the developed model in this paper is used. On the other hand, if E_c is regarded as a more generalized parameter that depends only on the physical properties of bonded materials, the applicability of the model may be broader. Furthermore, the fracture criteria based on the energy release rates in the classical interface crack problems agree well with the experimental results. Therefore, the elastic modulus of the adhesive material can be determined as

$$E_c = \frac{E^*}{1-\beta^2} \tag{3.6}$$

by comparing with Eqs. (2.31) and (3.5). Figure 5 shows the influence of h_1/c and E_c on the normalized energy release rates G/G_0, where $G_0 = 10^{-10}(p_0^2+q_0^2)c$. It can be seen that values of G/G_0 obtained based on both models have little difference for the pure tension case when Eq. (3.6) holds, especially for small values of h_1/c.

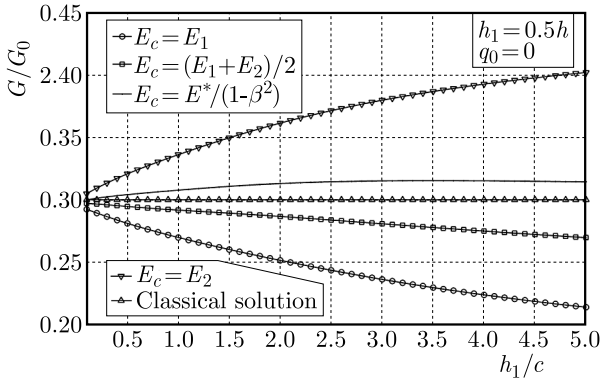

Fig. 5. Effect of the length ratio h_1/c between the generalized nonhomogeneous interlayer and crack on the normalized energy release rate

The influence of loading ratio q_0/p_0 for different thickness ratios of the interlayer h_1/h on the normalized SIFs, mode mixity and normalized energy release rate are plotted in Fig. 6 with

$E_c = E^*/(1-\beta^2)$. The results indicate that the mode II SIF K_2/K_0 and mode mixity ψ increase, while mode I SIF K_1/K_0 decreases with an increasing value of q_0/p_0. These tendencies are similar to the experimental results of Liechti and Chai (1992). From Fig. 6d, we can see that differences in the energy release rate G/G_0 between the generalized nonhomogeneous interlayer model and classical interface crack model are minimal when the thickness ratio of the interlayer is 0.75. Moreover, these differences can be further significantly reduced by selecting an appropriate value of h_1/h between 0.5 and 0.75.

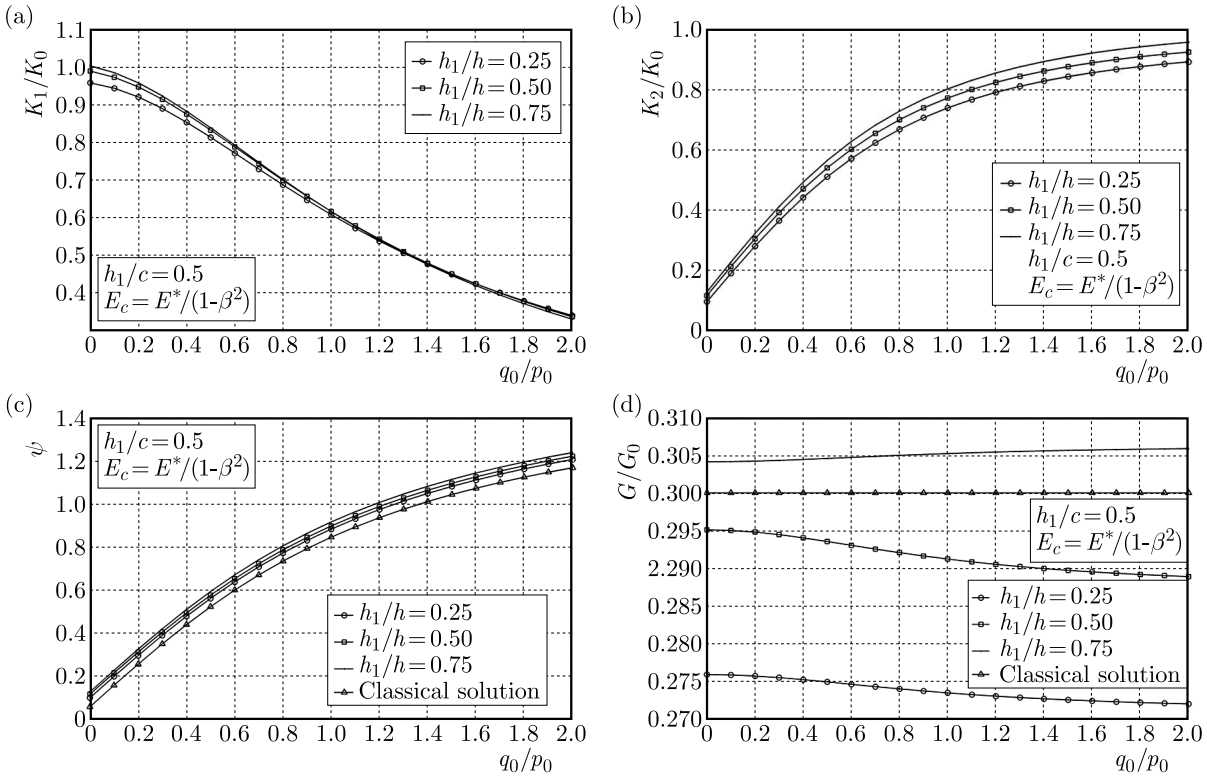

Fig. 6. Effect of the loading ratio q_0/p_0 on (a) normalized mode I SIF, (b) normalized mode II SIF, (c) mode mixity, and (d) normalized energy release rate

Finally, it should be noted that dimensions of SIFs of the classical interface crack model given by Eq. (3.3) depend on a complex factor $i\varepsilon$, hence, it is challenging to employ SIFs to develop a suitable fracture criterion for interface crack problems. However, the SIFs determined using Eqs. (2.28) overcome this limitation and can be used to establish the SIF-based fracture criterion. A quasi mode I (or quasi mode II) crack can be defined when the crack is subjected to simple tension (or pure shear) at a remote distance since the singular crack tip field is dominated by mode I (or mode II) fracture. Therefore, the SIF-based fracture criteria for quasi mode I and II cracks respectively take the form

$$K_1 = K_{1C} \qquad K_2 = K_{2C} \tag{3.7}$$

where K_{1C} and K_{2C} are the critical SIFs to be determined by experiments. For the mixed mode crack, the criterion may be taken in the elliptical form as

$$\Big(\frac{K_1}{K_{1C}}\Big)^2 + \Big(\frac{K_2}{K_{2C}}\Big)^2 = 1 \tag{3.8}$$

4. Conclusions

This paper proposes a Griffith crack model for two bonded dissimilar homogeneous isotropic elastic half-planes, taking into account roughness at each material surface and the effect of the adhesive material. A generalized nonhomogeneous interlayer is developed to model the adhesive interface, where it is assumed that all material properties vary continuously between those of the bonded materials and the adhesive material, and depend only on exponential functions of the coordinate y (perpendicular to the interface). The Griffith crack problem is then reduced to a set of singular integral equations which can be solved numerically. The influence of elastic property and thickness of the interlayer on mode I and II SIFs, mode mixity and energy release rate is studied through numerical results. The applicability of the developed crack model with the generalized nonhomogeneous interlayer is also investigated by comparing it with the classical interface crack model. It is found that the energy release rates calculated by the two models are very close when the elastic modulus and geometric dimensions of the generalized nonhomogeneous interlayer are appropriately selected.

Acknowledgements

The research was supported by the Natural Science Foundation of Zhejiang Province of China (LY21A020004), the Natural Science Foundation of Ningbo (2022J095) and the China Scholarship Council (202208330228).

References

1. Ayatollahi M.R., Nejati M., Ghouli S., 2022, Crack tip fields in anisotropic planes: a review, *International Journal of Fracture*, **234**, 113-139
2. Comninou M., 1977, The interface crack, *Journal of Applied Mechanics*, **44**, 631-636
3. Delale F., Erdogan F., 1983, The crack problem for a nonhomogeneous plane, *Journal of Applied Mechanics*, **50**, 609-614
4. Delale F., Erdogan F., 1988, On the mechanical modeling of the interfacial region in bonded half-planes, *Journal of Applied Mechanics*, **55**, 317-324
5. England A.H., 1965, A crack between dissimilar media, *Journal of Applied Mechanics*, **32**, 400-402
6. Erdogan F., 1965, Stress distribution in bonded dissimilar materials with cracks, *Journal of Applied Mechanics*, **32**, 403-410
7. Erdogan F., 1975, Complex function technique, [In:] *Continuum Mechanics of Single-Substance Bodies*, Eringen C. (Edit.), Academic, New York, 523-603
8. Erdogan F., Kaya A.C., Joseph P.F., 1991. The mode III crack problem in bonded materials with a nonhomogeneous interfacial zone, *Journal of Applied Mechanics*, **58**, 419-427
9. Govorukha V.B., Munz D., Kamlah M., 2000, On the singular integral equations approach to the interface crack problem for piezoelectric materials, *Archives of Mechanics*, **52**, 247-273
10. Herrmann K.P., Loboda V.V., 1999, On interface crack models with contact zones situated in an anisotropic bimaterial, *Archive of Applied Mechanics*, **69**, 317-335
11. Hutchinson J.W., Suo Z., 1992, Mixed mode cracking in layered materials, *Advances in Applied Mechanics*, **29**, 63-191
12. Liechti K.M., Chai Y.S., 1992, Asymmetric shielding in interfacial fracture under inplane shear, *Journal of Applied Mechanics*, **59**, 295-304
13. Malyshev B.M., Salganik R.L., 1965, The strength of adhesive joints using the theory of cracks, *International Journal of Fracture Mechanics*, **1**, 114-128

14. Ozturk M., Erdogan F., 1995. An axisymmetric crack in bonded materials with a nonhomogeneous interfacial zone under torsion, *Journal of Applied Mechanics*, **62**, 116-125

15. Qin Q.H., Mai Y.W., 1999. A closed crack tip model for interface cracks in thermopiezoelectric materials, *International Journal of Solids and Structures*, **36**, 2463-2479

16. Sheveleva A., Lapusta Y., Loboda V., 2015, Opening and contact zones of an interface crack in a piezoelectric bimaterial under combined compressive-shear loading, *Mechanics Research Communications*, **63**, 6-12

17. Sun C.T., Jih C.J., 1987, On strain energy release rates for interfacial cracks in bi-material media, *Engineering Fracture Mechanics*, **28**, 13-20

18. Suo Z.G., 1990, Singularities, interfaces and cracks in dissimilar anisotropic media, *Proceedings of the Royal Society of London*, **A427**, 331-358

19. Wang W.D., De Freitas S.T., Poulis J.A., Zarouchas D., 2021, A review of experimental and theoretical fracture characterization of bi-material bonded joints, *Composites Part B: Engineering*, **206**, 108537

20. Wang X.Y., Wang D., Zou Z.Z., 1996. On the Griffith crack in a nonhomogeneous interlayer of adjoining two different elastic materials, *International Journal of Fracture*, **79**, R51-R56

21. Wang X.Y., Zou Z.Z., Wang D., 1997, On the penny-shaped crack in a nonhomogeneous interlayer of adjoining two different elastic materials, *International Journal of Solids and Structures*, **34**, 3911-3921

22. Williams M.L., 1959, The stresses around a fault or crack in dissimilar media, *Bulletin of the Seismological Society of America*, **49**, 199-204

23. Yang W., Shih C.F., 1994, Fracture along an interlayer, *International Journal of Solids and Structures*, **31**, 985-1002

24. Zhang A.B., Wang B.L., 2013, An opportunistic analysis of the interface crack based on the modified interface dislocation method, *International Journal of Solids and Structures*, **50**, 15-20

25. Zhang A.B., Wang B.L., 2016, Temperature and electric potential fields of an interface crack in a layered thermoelectric or metal/thermoelectric material, *International Journal of Thermal Sciences*, **104**, 396-403

Manuscript received February 1, 2023; accepted for print May 12, 2023

JOURNAL OF THEORETICAL AND APPLIED MECHANICS
61, 3, pp. 509-520, Warsaw 2023
https://doi.org/10.15632/jtam-pl/166533

EXPERIMENTAL AND NUMERICAL ANALYSIS OF BOLTED TWO PLATES USING A DEVELOPED SHEAR THEORY

Kürşat Tanriver, Mustafa Ay
Institute of Pure and Applied Sciences, Marmara University, Istanbul, Turkey, and
Faculty of Technology, Marmara University, Istanbul, Turkey
corresponding author Kürşat Tanriver, e-mail: k.tanriver@hotmail.com

In this study, a software has been developed for calculating static strength of bolted steel plates. This software has been developed by adding equations covering the bending moment that occurs during a tensile test as well as under real loading conditions. In order to test the accuracy of this program, 5 samples with the M6 bolt connection were prepared. In addition, the simulation result was compared with the experimental work performed with tensile tests and the finite element analysis made in Ansys.

Keywords: bolt connection, MATLAB software, experimental work, finite element analysis

1. Introduction

When we examine fasteners in general, we notce that there are many fastening methods, and some of them are used as main methods. Firstly rivets, then bolts, and then welded joints are used (Albiez *et al.*, 2022).

Shear stress has a significant impact on structural behaviour of bolted steel construction assemblies. There are studies using bolted plates to increase the bending capacity of beams (Yao *et al.*, 2022). Bolts are known to show significant differences in strength under combined loads (Pitrakkos *et al.*, 2021). The aim of this study is to create an algorithm that analytically calculates both the plate material and bolt strength under static loading conditions when the same type of plates are connected by bolts and to investigate its industrial applicability. Ribeiro dos Santos *et al.* (2022) presented a study on the behaviour of bolts. Zhou *et al.* (2022) investigated buckling of stainless-steel pipes due to bending and carried out a study that numerically determined them. Considering bolted parts, Rakotondrainibe *et al.* (2022) potentially optimized the shape and topology of each part as well as the position and number of the bolts. Li and Young (2021) conducted an experimental study on open section members under an eccentric load used in steel structures. Fink and Camanho (2011) investigated how composite materials affect joint stiffness of metal plywood sheets, which were made of the same material as the fastener, to increase strength in metal bolt/rivet connections. Qi *et al.* (2021) simulated experimentally materials with Abaqus software and compared the results. He *et al.* (2021) studied the high-temperature load distribution of a bolt joint structure. A two-dimensional asymmetrical model of the bolt connection structure was created and a modification of the standard metric thread profile was made according to the thread load distribution, taking into account certain properties. Giannella *et al.* (2021) carried out finite element analysis by modeling three different connections of bolts that connected various components in gasoline engines. The results were compared in terms of preprocessing time and accuracy. Li *et al.* (2020) performed calculations of dynamic stiffness of mounted beam structures and connection surfaces according to an empirical formula. They created an equivalent model of bolted connections using springs and dampers and virtual material addition methods in the Ansys software. In addition, they conducted a

modal test of the beam structure. The simulation results obtained from the theoretical modeling method were compared with modal test results. Accordingly, they demonstrated that the modeling method using spring and damping elements had higher accuracy. Guzas *et al.* (2015) created a finite element model for bolts. They conducted physical experiments involving static and dynamic stress tests. They verified the models based on test data for static and dynamic stress experiments and reported achieving a good correlation. Ibrahim (2020) worked on a finite element model of a standard bolted connection using Siemens NX software. It was observed that the modal frequencies of the three simplified models were accurately captured. Additionally, the study emphasized the effects of beam discretization and computation time. Żyliński and Buczkowski (2010) conducted an analysis of bolted connections using the finite element method. Nonlinear stiffness properties for the bolt and flange with gaskets were developed. Furthermore, they compared the finite element analysis results with experimental results. Kim *et al.* (2007) proposed four types of bolt models as finite element modeling techniques for a bolted connection. The effectiveness and usability of the bolt models were validated by comparing static experiments and modal test results. Piscan *et al.* (2010) conducted research on deformation of the contact surface of a bolted connection using finite element analysis. In that study, the maximum stress that the bolt can withstand due to the maximum stress it may be exposed to, based on the bolt preload force, was determined. Additionally, the authors noted that surface contact stiffness exhibited a nonlinear variation. Ramires *et al.* (2012) worked on a connection technique they called a semi-rigid connection design. In this study, they optimized factors such as bolt diameters and positions, spring coefficients and plate thicknesses using a genetic algorithm. They managed to increase bolt stiffness while maintaining the same material cost.

2. Material and method

In this article, the aim is to examine the performance of plates of the same type connected with bolted connections under static loading conditions. The goal is to develop an algorithm that analytically calculates both the plate material and bolt strength. Today, metals, alloys and composites are used in various manufacturing processes by combining them with dissolvable connection techniques. In particular, quick assembly of different manufacturing plate-type connections in steel structures is facilitated by joining them with bolted connections. From the past to the present, bolts are frequently used as fasteners in steel construction assemblies, which is a common type of structure. With the advancement of technology, there has been a growing need for development of innovative designs of such bolts (Tanriver and Ay 2020).

Tensile tests can be performed to investigate tensile performance of fasteners (Guo *et al.*, 2020). In the literature, there are numerous studies where tensile load test results of bolts are both experimentally conducted and analyzed using the finite element method (Liu *et al.*, 2021).

In addition to these, in this study, calculations were made using software with an improved equation. Furthermore, the results were compared using a triple validation method. The ultimate goal here is to measure whether widely used fasteners can withstand static forces. The accuracy of the software developed in this study was assessed by comparing the experimental results and the finite element method.

2.1. Material

For this article, 5 test specimens of the same type and characteristics were prepared. As a sample, two ST 37 plates with 10 mm thickness (h_1, h_2), 100 mm width l_e, and 100 mm length l were used. The ST 37 plate has a modulus of elasticity of 210 GPa, yield strength of 235 MPa and tensile strength of 375 MPa.

A zinc-coated M6 steel bolt was used at the exact center of the plates for connection. The bolts have a length of 60 mm and were selected as hex head, 8.8 quality, and fully threaded according to the DIN 933 standard. The test specimen is shown in Fig. 1.

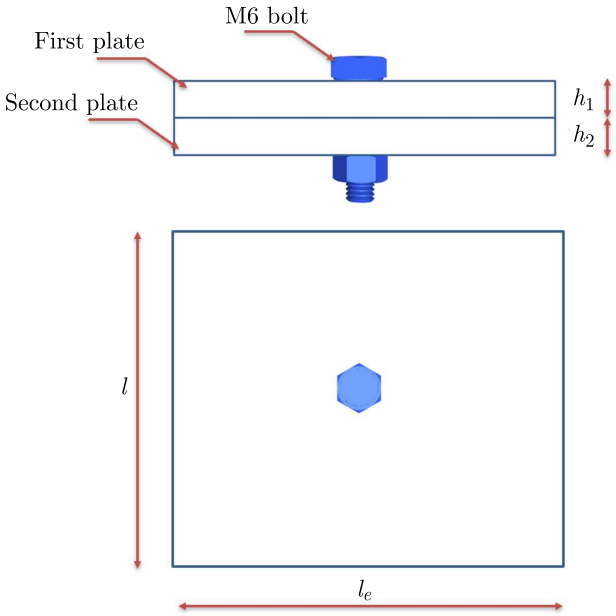

Fig. 1. Test sample

2.2. Method

The international standards currently used in tensile tests of metal materials include ISO 6892-1: 2016 and ASTM E8: 2016 standards. The test setup for this article was prepared in accordance with the ISO 6892-1: 2016 standard. The experiments were performed on the Instron 5569 tensile testing machine. The test specimen consists of two plates placed on top of each other and connected by a single bolt in the exact center. In this case, five specimens with the same properties were subjected to tensile load successively, with the lower jaw fixed and the upper jaw moving, forcing the bolt to be cut between the two plates. For each specimen, the tensile speed was set to 2 mm/min, and the load was gradually increased until the bolts were cut, ending the test. The first test specimen during the test and a visual of the test device are shown in Fig. 2. The test specimens were named M6-Cv1, M6-Cv2, M6-Cv3, M6-Cv-4, M6-Cv-5, respectively. The tensile test was applied to test specimens one by one in the order mentioned above.

Additionally, to investigate the static behaviour of bolted connections, analytical methods that provide stress distribution can be developed, and finite element models can be used to check their suitability. In Ansys, which is the software using these methods, numerical analysis of experimental studies on the buckling of shells and the shear load can be performed (Karasev *et al.*, 2020).

To examine the static behaviour of bolted connections, analytical methods that provide stress distribution can be developed, and finite element models can be used to verify their appropriateness (Hammami, 2022). In this article, finite element analysis was carried out using the structural Ansys R19.2 analysis module. The shear stresses were investigated afterwards.

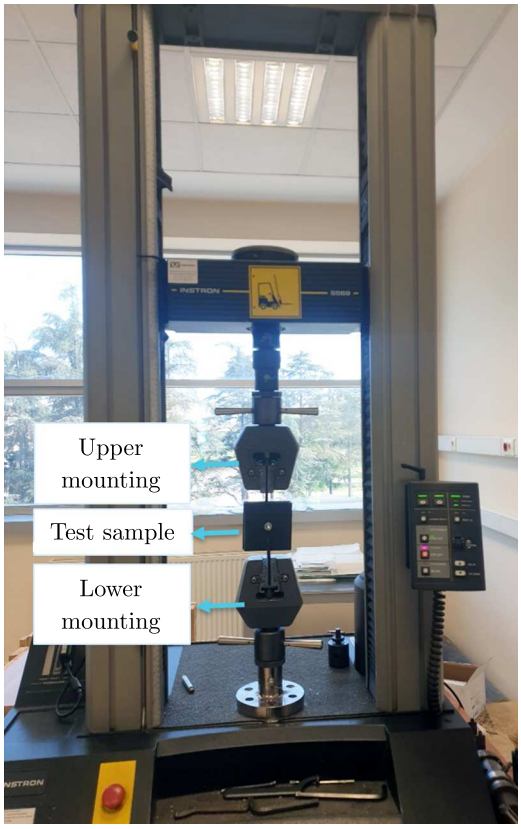

Fig. 2. Test sample

3. Result and discussion

3.1. Experimental study and finite element analysis

Before performing the stress analysis, it is necessary to examine the loads applied to the structure. The stress-strain curves obtained from the tensile tests of the specimens are given in Fig. 3, respectively.

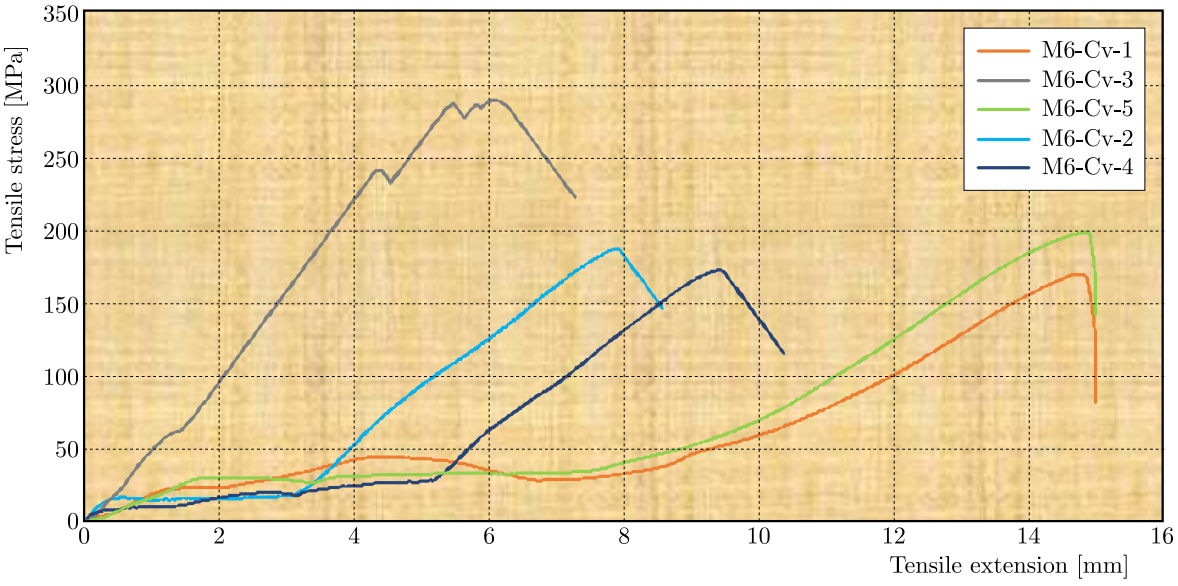

Fig. 3. Stress-extension curves

Although the test specimens were geometrically identical to each other before the tensile test, they showed differences in the test results. Some of them exhibited much more elongation resulting in fracture at lower tensile forces compared to others. In some cases, more noticeable bending occurred. A summary of the test results is given in Table 1.

Table 1. Tensile test results summary

Test specimen	Tensile extension [mm]	Tensile stress [MPa]	Load [N]
M6-Cv-1	14.73	170.08	10204.56
M6-Cv-2	7.85	187.69	11261.14
M6-Cv-3	12.10	289.94	17379.37
M6-Cv-4	9.37	172.81	10368.61
M6-Cv-5	14.83	198.89	11933.46
Average value		203.88 MPa	12229.42 N

Based on these results, the arithmetic mean of tensile stresses of the 5 test specimens with M6 bolt connections is found to be 203.88 MPa. Similarly, taking the average of shear forces of the bolts according to the same results, the shear force is determined to be 12229.42 N. In this study, the data obtained from the experimental results are planned to be used in both the finite element Ansys R19.2 analysis and a MATLAB code for the targeted studies. Therefore, in the "Software" Section, it is aimed to write a code based on the equations developed for this study using the MATLAB code. In Ansys R19.2 structural analysis module, simulation was performed by applying an average shear force of 12229.42 N obtained from the experimental results for the same test specimen. The analysis used a total of 235 804 finite elements and 985 717 nodes. The sweep meshing method was used, and the mesh size was set to 1 mm. The contact between the plates was defined as a surface-to-surface contact. Similarly, the connection contact between the plate-groove and the bolt threads was also defined as the surface-to-surface contact. Furthermore, for the surface-to-surface contact, tangential and normal behaviour were defined as the penalty friction and hard contact, respectively. To simulate the real constraints in the tests and to limit the displacement of one of the plates, fixed support was defined in the Y-direction. The problem was solved using the Maximum Shear Stress method. The finite element model is shown in Fig. 4.

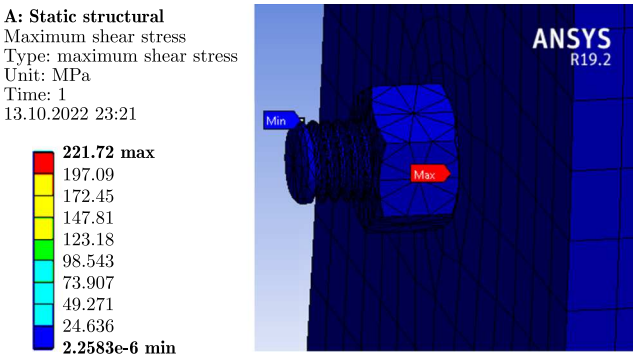

Fig. 4. Maximum shear stress analysis

Accordingly, in the finite element analysis, the maximum shear stress was found to be 221.72 MPa. The ratio between the average of the experimental results in Table 1 and the finite element result is 1.09. When we examine the studies conducted in the literature, the ratio between the experimental results and the finite element results appears to be 1.77 (Guo *et al.*, 2020), 1.08 (Rajanyam *et al.*, 2020) and 1.02 (Nguyen *et al.*, 2022). It seems that the value in this article is among the values in the current studies.

3.2. Modeling the plate under moment

In the literature review, it has been indicated that bolt geometry and generation of moments are improved when loads are connected eccentrically (Ansari *et al.*, 2023; Esmaeili *et al.*, 2014; Hammami, 2022; Pitrakkos *et al.*, 2021). However, no study formulating and explaining these findings through additional formulas has been found.

There are studies that claim that the load exerted on bolted connections is not actually proportional to the number of bolts and model and compare it with experimental results (Kontoleon *et al.*, 2003). Actually, it should be noted that this is because of inability to perform axial tension. The contact surface of the bolt holes providing the bolt-plate interaction should be taken into account (Ye *et al.*, 2022).

When plates are subjected to a tensile load, it is assumed that they are subjected to tensile stress in the y-axis plane as shown in Fig. 5a, and calculations are made accordingly. However, in tensile tests, it is known that this cannot be the case under real loading conditions, and the eccentricity ratio in the load test can reduce load carrying capacities (Nguyen *et al.*, 2022). Due to a non-central application of the tensile load, the plates are forced to bend, and a moment is generated.

When the stresses generated by this moment are added to simulations while calculating the shear load on the bolts, and the calculations become more accurate. The bending moment occurs at an angle in the section plane. The plate model under the moment loading is shown in Fig. 5b.

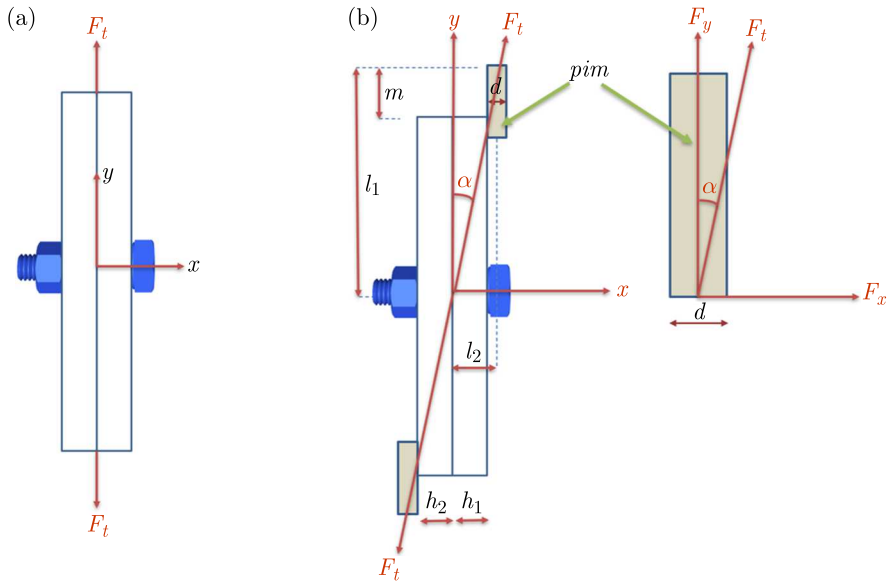

Fig. 5. The model of the plate under the moment: (a) theoretical (b) real condition

The angle α that will occur in the section plane, distance l_1 of the vertical force to the pivot point, distance l_2 of the horizontal force to the pivot point, the vertical force F_y, the horizontal force F_x generated by these forces, and the moments M_1 and M_2 formed by these forces are given below

$$\begin{aligned} &\alpha = \tan^{-1}\frac{l_2}{l_1} \qquad l_1 = \frac{l}{2} + m \qquad l_2 = h + m \qquad h = h_1 = h_2 \\ &F_x = F_T \sin\alpha \qquad F_y = F_T \cos\alpha \\ &M_1 = F_x l_1 \qquad M_2 = F_y l_2 \end{aligned} \tag{3.1}$$

Here, h represents plate thickness, l – length of the plate under tension, d – diameter of the bolt to which the tension jaws are connected, m effective length of tension connection, and F_T – tensile force.

The designed software consists of two stages. The first one is to determine whether the plate can withstand the forces it is subjected to, and the second one is to investigate whether the constructive strength of any bolts to be used as fastener is appropriate. In the first stage, it is necessary to calculate whether the plates can withstand the tensile force statically, and then to calculate the shear stress for bolt strength. The area affected by the tensile force A, moment of inertia I_z, stress σ to which the plates are exposed, the safety stress σ_{saf} and the plate material strength condition are given below

$$\begin{aligned} &A = l_e h \qquad I_z = l_e \frac{h^3}{12} \\ &\sigma = \frac{F_y}{A} + \frac{M_1}{I_z} h \qquad \sigma_{saf} = \frac{\sigma_y}{s} \qquad \sigma \leqslant \sigma_{saf} \end{aligned} \tag{3.2}$$

Here, h represents plate thickness, l_e – plate width, F_y – force acting on the plates in the y-axis, I_z – moment of inertia, M_1 – moment, σ_y – yield stress of the plate material, and s – safety factor.

Now, we need to examine whether the constructive strength of any of the bolts to be used as fasteners is appropriate, which is the second stage of the designed software. Due to the angled effect of the tensile force, the M_1 and M_2 moments were generated in the plates. Since the directions of these moments are opposite to each other, the resulting net moment M_{net}, and the tensile-compressive stress σ_{tc} generated by this moment are given as

$$M_{net} = M_2 - M_1 \qquad \sigma_{tc} = \frac{M_{net}}{I_z} h \tag{3.3}$$

Here, h represents plate thickness and I_z – coefficient of the moment of inertia.

As a result of the tensile-compressive stress σ_{tc} generated in the plates, an additional virtual shear force will be generated that acts in the opposite direction to the bolts in the plates. The F_{im} virtual force is the maximum force that will act when the stress profile is assumed to be triangular. The intensity of the bolt within the plates changes in proportion to the area of this triangle. Therefore, the average force corresponding to the area of the triangle will be a half of the F_{im} force. The virtual force F_{im} is shown in Fig. 6.

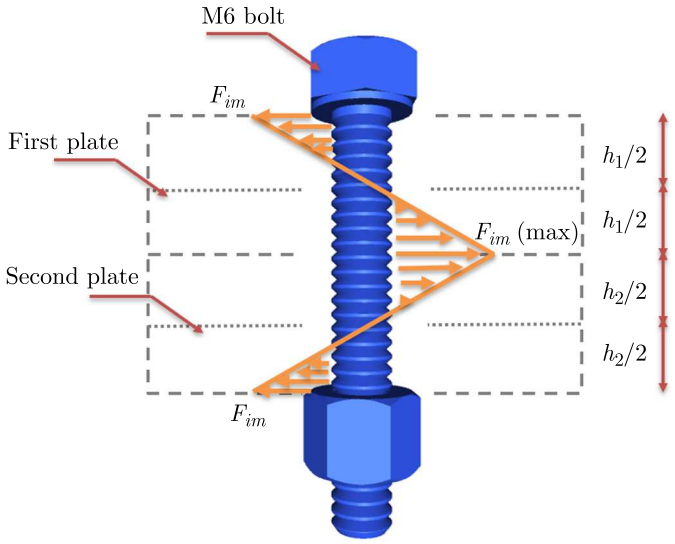

Fig. 6. Imaginary force

The crushing area A_{cr} and the virtual shear force F_{im}, with plate thickness h, are expressed by the following equations

$$F_{im} = \sigma_{tc} A_{cr} \qquad A_{cr} = h D_{bolt} \tag{3.4}$$

Here, h represents plate thickness, and D_{bolt} – diameter of the bolt.

The total shear force per bolt F_{sh}, cross-sectional area per bolt A_{bolt}, net shear stress per bolt τ_{net}, and the bolt shear stress strength condition are given below

$$\begin{aligned} F_{sh} &= \frac{F_y}{n} + \frac{F_{im}}{2} \qquad A_{bolt} = \pi \frac{D_{bolt}^2}{4} \\ \tau_{net} &= \frac{F_{sh}}{A_{bolt}} \qquad \tau_{saf} = \frac{\tau_s}{s} \qquad \tau_{net} \leqslant \tau_{saf} \end{aligned} \tag{3.5}$$

Here, n represents the number of bolts, D_{bolt} represents diameter of the bolt, F_y represents the force acting on the plates in the y-axis, F_{im} is the virtual force, τ_s – shear stress of the bolt material, and s is the safety factor.

3.3. Software

In this Section, the equations involving bending moment have been transferred into the MATLAB code, and the code has been executed on a sample model. Additionally, to measure its accuracy, the software results have been compared with both experimental and finite element results. In the previous Section, the arithmetic average of the tensile test results for 5 samples with M6 connections, shown in Table 1, was 12229.42 N for the F_{real} load. This load was used in the Ansys maximum shear stress analysis, and the resulting stress value τ_{ans} was 221.72 MPa.

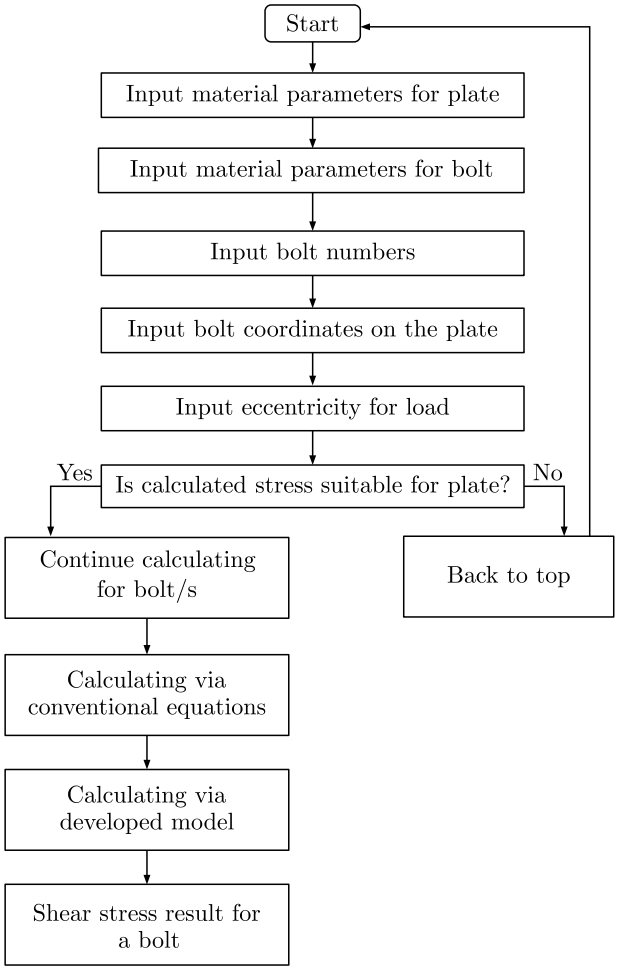

Fig. 7. Flowchart of the software procedure and result

Now, to make a proper comparison, the MATLAB program has been run on the same model dimensions shown in Fig. 1, which were used in the tensile test and finite element analysis. The load used was again the arithmetic average of the tensile test results for the 5 samples with M6 connections, shown in Table 1, with a F_{real} load of 12229.42 N. As a result, the critical stress calculated by MATLAB was 220.70 MPa. The flowchart of the software procedure and the result is shown in Fig. 7.

According to the results obtained here, the output of the MATLAB software designed for this study is 16.70 MPa higher than the average τ_{real} (203.88 MPa) of the experimental results for the M6 bolted connection samples conducted in the laboratory environment. Additionally, it is observed that the result is 1.18 MPa lower than the output of the Ansys finite element analysis. The error rates of the MATLAB results have been determined based on both the experimental and Ansys finite element method results. The error rate relative to the laboratory test results is given as *Err test Rate*, while the error rate relative to the Ansys finite element results is given as *Err ans Rate*. The error rates are provided below

$$Err\ test\ Rate = \frac{\tau_{net} - \tau_{real}}{\tau_{real}} \tag{3.6}$$

Here, with $\tau_{net} = 220.70$ MPa and $\tau_{real} = 203.88$ MPa, the error rate *Err test Rate* is found to be +8.2%

$$Err\ ans\ Rate = \frac{\tau_{net} - \tau_{ans}}{\tau_{ans}} \tag{3.7}$$

Here, with $\tau_{net} = 220.70$ MPa and $\tau_{ans} = 221.72$ MPa, the error rate *Err ans Rate* is found to be −0.46%.

If this innovation and change was made, the simple shear stress would be given in the equation below

$$A_{bolt} = \pi \frac{D_{bolt}^2}{4} \qquad \tau_{bolt-old} = \frac{F_T}{A_{bolt}} \tag{3.8}$$

Here, with the bolt diameter D_{bolt} being 6 mm, the bolt cross-sectional area A_{bolt} is found to be 28.27 mm^2.

If the lowest stress value in Table 1, 10204.56 N F_T force in M6-Cv-1 sample, is considered, $\tau_{bolt-old}$ is found to be 288.48 MPa. When considering the average value of 12229.42 N F_T force, $\tau_{bolt-old}$ is calculated as 432.58 MPa. If the highest stress value in M6-CV-5 sample, 17379.37 N F_T force, is taken into account, $\tau_{bolt-old}$ is found to be 614.76 MPa. Since 288.48 MPa is a closer value, the error rate is expressed below considering this value

$$Err\ test\ Rate = \frac{\tau_{net} - \tau_{real}}{\tau_{real}} \tag{3.9}$$

Here, with $\tau_{bolt-old} = 288.48$ MPa and $\tau_{real} = 203.88$ MPa, the error rate *Err test Rate* is found to be +41.5%.

As can be seen here, if the conventional bolt shear stress calculation was done, the current error rate would be 41.4%. However, with the modifications and calculations done by using the MATLAB program, the error rate is found to be 8.2%. The new calculation provides 33.3% more accurate results compared to the old calculation, offering designers a safer margin and benefits in terms of staying within the safety zone. In addition to all of these, a regression analysis has been performed between the values of different bolt diameters with the average force of 12229.42 N using the program. The regression analysis graph is shown in Fig. 8.

Accordingly, the determination coefficient R^2 is found to be 0.9816, approaching 1. With a constant load of 12229.42 N, the equation predicts the critical stress per bolt with the independent variable of bolt diameter at a rate of 98.16%. The critical stress values written opposite the bolt diameter are taken from the MATLAB algorithm; therefore, it can be concluded that the code provides a correct stress value at a rate of 98.16%.

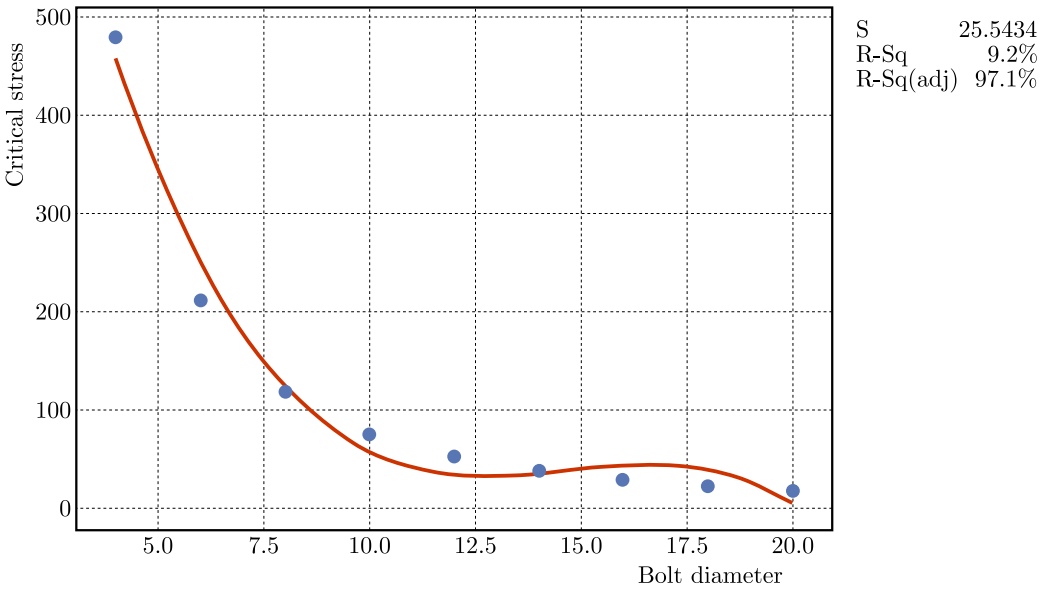

Fig. 8. Regression analysis graph

4. Conclusion

In the literature review, there are studies that show the improvement of bolt geometry and the formation of moments when the loads are connected eccentrically when compared with existing models. However, no study has been found that develops and explains this by converting these quantities into equations and adding additional formulas. For that reason, codes have been added to the MATLAB software in order to calculate the moments formed by eccentricity during tension, in addition to conventional studies, and the software has been improved. The designed software consists of two stages. The first stage is to determine whether the plate used can withstand the forces it is subjected to, and the second stage is to investigate whether the constructive strength of any of the bolts used as fasteners is appropriate.

In order to investigate tensile performance of fasteners, tensile tests are performed. Generally, there are studies comparing experimental results with finite element results. There are also studies that validate numerical and experimental results for estimating the shear capacity of bolted connections. In this study, additionally, calculations are made with the help of the MATLAB software, and the results are compared in a triple validation method with both finite element and experimental method.

Although the specimens were geometrically identical to each other before tensile tests, they showed differences in the test results. In some of them, elongation was much greater compared to others, resulting in failure at lower tensile forces. In others, more visible bending occurred. According to the test results, an arithmetic average of stresses of 5 M6 connected samples with the same properties was taken, and the average stress was found to be 203.88 MPa. Also, based on the same results, the average shear load was determined to be 12229.42 N. The finite element analysis in the Ansys R19.2 structural analysis module was performed using the average shear load of 12229.42 N. Consequently, the maximum shear stress in the finite element analysis was found to be 221.72 MPa. Considering these values, the ratio between the average of the test results and the finite element analysis was 1.09. It is a value within the range of ratios between experimental and finite element results found in the literature.

Additionally, the code written with the added equations was run in MATLAB using the average shear load, which indicated a critical stress of 220.70 MPa. Based on these results, the MATLAB software developed with the improved additional formulas has error rates of +8.2%

when considering the experimental results and −0.46% when considering Ansys finite element results.

If this innovation was not made and the conventional bolt shear stress calculation was used, the current error rate would be 41.4%. The new calculation offers a 33.3% more accurate estimate compared to the old calculation, providing designers with a safer margin and benefiting them by staying within the safety zone.

In addition to these, a regression analysis has been performed for different bolt diameters. Accordingly, the coefficient R^2 was found to be close to 1, 0.9816 in exact. With a constant load of 12229.42 N, the critical stress per bolt, with the bolt diameter as an independent variable, was predicted with an accuracy of 98.16%. Since these values were obtained in MATLAB, it wae also concluded that the code provided stress values with an accuracy of 98.16%.

In the future, it is aimed to develop the presented study by adding an optimization module. Thus, by preparing constraint functions for plates and bolts, the most suitable coordinates for the bolts can be determined. This will provide a more efficient and effective design process, ensuring that the connections are optimized for a specific application and requirements.

References

1. Albiez M., Damm J., Ummenhofer T., Kaufmann M., Vallée, T., Myslicki S., 2022, Hybrid joining of jacket structures for offshore wind turbines – Determination of requirements and adhesive characterisation, *Engineering Structures*, **259**, 114186
2. Ansari R., Hassani R., Gholami Y., Rouhi H., 2023, Numerical nonlinear bending analysis of FG-GPLRC plates with arbitrary shape including cutout, *Structural Engineering and Mechanics*, **85**, 2, 147-161
3. Esmaeili F., Zehsaz M., Chakherlou T., 2014, Investigation the effect of tightening torque on the fatigue strength of double lap simple bolted and hybrid (boltedbonded) joints using volumetric method, *Materials and Design*, **63**, 349-359
4. Fink A., Camanho P., 2011, Reinforcement of composite bolted joints by means of local metal hybridization, *Composite Joint and Connections*, 3-34
5. Giannella V., Sepe R., Citarella R., Armentani E., 2021, FEM modelling approaches of bolt connections for the dynamic analyses of an automotive engine, *Applied Sciences*, **11**, 10, 4343, 1-12
6. Guo X., Zong S., Gao S., Zhu S., Zhang Y., 2020, Ductile failure of occlusive high strength bolt connections under shear force, *Journal of Constructional Steel Research*, **168**, 105982
7. Guzas E., Behan K., Davis J., 2015, 3D finite element modeling of single bolt connections under static and dynamic tension loading, *Shock and Vibration*, article ID 205018
8. Hammami C., 2022, Nmerical investigation of static behavior of bolted joints, *Journal of Theoretical and Applied Mechanics*, **60**, 3, 385-394
9. He L., Zhang B., Guo C., Shi W., 2021, Stress and load distribution analysis in bolt connection with modified thread profile under high temperature conditions, *Journal of Theoretical and Applied Mechanics*, **59**, 469-480
10. Ibrahim A., 2020, *On the Effective Finite Element Simplification of Bolted Joints: Static and Modal Analyses*, Dubai: Master Thesis, Rochester Institute of Technology
11. Karasev A., Varianychko M., Bessmertnyi Y., Krasovsky V., Karasev G., 2020, Numerical analysis of experimental research on buckling of closed shallow conical shells under external pressure, *Journal of Theoretical and Applied Mechanics*, **58**, 1, 117-126
12. Kim J., Yoon J.-C., Kang B.-S., 2007, Finite element analysis and modeling of structure with bolted joints, *Applied Mathematical Modelling*, **31**, 895-911

13. Kontoleon M., Kaziolas D., Zygomalas M., Baniotopoulos C., 2003, Analysis of steel bolted connections by means of a nonsmooth optimization procedure, *Computers and Structures*, **81**, 2455-2465

14. Li P., Li W., Wei P., Wang Q., 2020, Research on finite element analysis and modelling of bolted joint, *IOP Conference Series: Materials Science and Engineering*, Bristol, UK: IOP Publishing Ltd., 156-167

15. Li Q., Young B., 2021, Tests of cold-formed steel built-up open section members under eccentric compressive load, *Journal of Constructional Steel Research*, **184**, 1-12

16. Liu Y., Li M., Lu X., Li Q., Zhu X., 2021, Pull-out performance and optimization of a novel Interference-fit rivet for composite joints, *Composite Structures*, **269**, 114041

17. Nguyen T.-T., Thai H.-T., Li D., Wang J., Uy B., Ngo T., 2022, Behaviour and design of eccentrically loaded CFST columns with high strength materials and slender sections, *Journal of Constructional Steel Research*, **188**, 1-16

18. Piscan I., Predincea N., Pop N., 2010, Finite element analysis of bolted joint, *Proceedings in Manufacturing Systems*, **5**, 167-172

19. Pitrakkos T., Tizani W., Cabrera M., Salh N.F., 2021, Blind bolts with headed anchors under combined tension and shear, *Journal of Constructional Steel Research*, **179**, 106546

20. Qi H., Chen S., Zou J., Zhang H., Liu M., Ju J., Sang X., 2021, Numerical study on the dynamic response of a concrete fillet steel tubular long column under axial impact by a rigit body, *Journal of Theoretical and Applied Mechanics*, **59**, 551-563

21. Rajanayagam H., Gunawardena T., Mendis P., Pologanathan K., Gatheeshgar P., Dissanayake M., Corradi M., 2022, Evaluation of inter-modular connection behaviour under lateral loads: An experimental and numerical study, *Journal of Constructional Steel Research*, **194**, 1-16

22. Rakotondrainibe L., Desai J., Orval P., Allaire G., 2022, Coupled topology optimization of structure and connections for bolted mechanical systems, *European Journal of Mechanics – A Solids*, **93**, 104499

23. Ramires F., Andrade S., Silva Vellasco P.C.G.D.S., de Lima L.R.O., 2012, Genetic algorithm optimization of composite and steel endplate semi-rigid joints, *Engineering Structures*, **45**, 177-191

24. Ribeiro Dos Santos L., Barreto Caldas R., Prates J.A., Rodrigues F.C., Cardoso H., 2022, Design procedure to bearing concrete failure in composite cold-formed steel columns with riveted bolt shear connectors, *Engineering Structures*, **256**, 114003

25. Tanriver K., Ay M., 2020, Topology optimization of a steel construction bolt under boundary conditions, *Euroasia Journal of Mathematics, Engineering, Natural and Medical Sciences*, **7**, 12, 31-47

26. Yao Y., Huang H., Zhang W., Ye Y., Xin L., Liu Y., 2022, Seismic performance of steel-PEC spliced frame beam, *Journal of Constructional Steel Research*, **197**, 1-11

27. Ye J., Quan G., Yun X., Guo X., Chen J., 2022, An improved and robust finite element model for simulation of thin-walled steel bolted connections, *Engineering Structures*, **250**, 113368

28. Zhou F., Huang L., Li H.-T., 2022, Cold-formed stainless steel SHS and RHS columns subjected to local-flexural interactive buckling, *Journal of Constructional Steel Research*, **188**, 106999

29. Żylinski B., Buczkowski R., 2010, Analysis of bolt joint using the finite element method, *Archive of Mechanical Engineering*, **LVII**, 3, 275-292

Manuscript received October 20, 2022; accepted for print May 11, 2023

JOURNAL OF THEORETICAL AND APPLIED MECHANICS
61, 3, pp. 521-531, Warsaw 2023
https://doi.org/10.15632/jtam-pl/166652

AN UNSTEADY VEHICLE-ROAD COUPLING DYNAMIC RESPONSE OF A MULTI-LAYER PLATE ON A VISCOELASTIC HALF-SPACE FOUNDATION

Shao-Qi Li
Shijiazhuang Tiedao University, School of Transportation, Shijiazhuang, China
e-mail: llishaoqi@163.com

Zhan-You Yan
Shijiazhuang Tiedao University, State Key Laboratory of Mechanical Behavior in Traffic Engineering Structure and System Safety, Shijiazhuang, China, and
Shijiazhuang Tiedao University, School of Civil Engineering, Shijiazhuang, China
corresponding author, e-mail: yanzhanyou@163.com

Yong-Chang Cui, Xue-Ke Hou, Zi-Jun Wang
Shijiazhuang Tiedao University, School of Transportation and School of Civil Engineering, Shijiazhuang, China
e-mail: 749018248@qq.com, 2294232910@qq.com, 1151699829@qq.com

To study the dynamic response of roads under non-stationary random excitation, a dynamic differential equation is constructed firstly based on a two-axle half car model, and white noise to simulate road roughness is then filtered. Finally, non-stationary responses of different vehicle acceleration conditions are obtained. An infinite multi-layer plate on a viscoelastic half-space foundation as a model of the road structure and an analytical solution for the road dynamic response are obtained. Based on a numerical example, the dynamic response of a four-layer road model under vehicle loads is discussed. The study fills the gap in the theory of multi-wheel vehicle models.

Keywords: non-stationary filtered white noise, viscoelastic half-space, multi-layer plate, vehicle-road coupling

1. Introduction

With the continuous improvement of the national economic level and the rapid development of the road transportation industry, the number and types of various heavy-duty vehicles on the road are increasing, and damage to the road is particularly serious. Among them, vibration is an unavoidable topic when vehicles are driving on the road. Due to technical levels and other uncontrollable factors, the road surface cannot be completely flat because it leads to excitation of the road surface during driving of the vehicle. The vehicle vibration and its own gravity influence also produce complex dynamic response problems on the road surface (Rahman and Kibria, 2014; Awal *et al.*, 2017). How to establish a more realistic and effective model to reflect the dynamic response of the road under heavy loads has become a hot topic in the current road research.

At present, the dynamic response of the pavement under an external load is generally selected for a constant speed, and the upper load is described as a dead load or harmonic load. For the pavement structure model, early scholars usually simplified it to a Kirchhoff's thin plate on a viscoelastic foundation. Dieterman and Metrikine (1997) studied the dynamic response of single-layer soil under the action of a moving load as a simple harmonic load. Kim and Roesset (1998) and Kim (2004) studied the dynamic response of the infinite Kirchhoff thin plate on

the Kelvin foundation under a moving dead load and harmonic load by using the fast Fourier transform method. Sun (2007) used the integral transformation and Green function method to find the integral analytical solution of the transient deflection and the steady-state deflection of the plate under the moving load. Later, Cai *et al.* (2009) and Cao and Boström (2013) extended the road structure to an elastic half-space and porous saturated soil half-space volume models on the basis of Sun (2007). Li (2011) and Li *et al.* (2013) optimized the pavement structure model again: the infinite two-layer plate model on the viscoelastic half-space foundation was proposed, and the dynamic response of the two-layer plate structure under the moving load was studied. A relationship between the dynamic response of the plate structure and the elastic modulus of the material was obtained. Si (2017) extended the virtual excitation method to deal with random vibration of the viscoelastic half-space foundation under a train load, and used the evolutionary power spectrum and corresponding standard deviation to express time-varying random characteristics of the system. Mirsaidov and Mamasoliev (2020) established a mathematical model and a calculation method of the internal force coefficient of a multi-layer strip plate on an elastic foundation under various static loads and proved regularity of infinite algebraic equations and obtained the corresponding estimation. Hamidi *et al.* (2021) utilized the state space method in the Laplace domain. The influence of the elastic foundation and viscoelastic interface on dynamic behavior of laminated magneto electro elastic rectangular plates with simply supported boundary conditions was studied. The dynamic response of three--dimensional displacement, stress, electric displacement and magnetic displacement phase in the thickness direction and orthotropic behavior under harmonic stress was analyzed. However, the current speed of vehicles on the road is always changing, especially acceleration and deceleration when the vehicle starts and stops, which result in that the load on the road can not be simply described as a dead or harmonic loads.

The article combines the vehicle load with random road roughness excitation for the first time. The authors use a two-axle and half-car model to build dynamic differential equations, and used filtered white noise to simulate road roughness. At the same time, the viscoelastic half--space foundation model is further extended to a multi-layer plate on a viscoelastic half-space foundation model. Based on Green's function and Duhamel's integral, the analytical solution of the dynamic response of the infinite multi-layer plate on the viscoelastic half-space foundation under the action of moving vehicles is obtained, and the generalized integral calculation program for simulating singular and oscillating functions is compiled by using MATLAB software. Finally, the algorithm in this paper is created and the dynamic response of the road structure under non-stationary vehicle-road coupling conditions is obtained.

2. Vehicle and road model

2.1. Vehicle model

The vehicle model is a two-axle heavy vehicle, and the half-car model is shown in Fig. 1a. The tire damping is relatively small compared to suspension damping, and for convenience of numerical calculations, the vehicle model can be simplified as shown in Fig. 1b.

Based on the balance of the front and rear forces of the vehicle body, it is concluded that

$$\begin{aligned} &m_{2f}\ddot{z}_{2f} + m_{2c}\ddot{z}_c\frac{b}{L} + C_{2f}(\dot{z}_{2f} - \dot{z}_{1f}) + K_{2f}(z_{2f} - z_{1f}) = 0 \\ &m_{2r}\ddot{z}_{2r} + m_{2c}\ddot{z}_c\frac{a}{L} + C_{2r}(\dot{z}_{2r} - \dot{z}_{1r}) + K_{2r}(z_{2r} - z_{1r}) = 0 \end{aligned} \tag{2.1}$$

Adding Eqs. (2.1), we get

$$m_2\ddot{z}_c + C_{2f}(\dot{z}_{2f} - \dot{z}_{1f}) + C_{2r}(\dot{z}_{2r} - \dot{z}_{1r}) + K_{2f}(z_{2f} - z_{1f}) + K_{2r}(z_{1r} - z_{2r}) = 0 \tag{2.2}$$

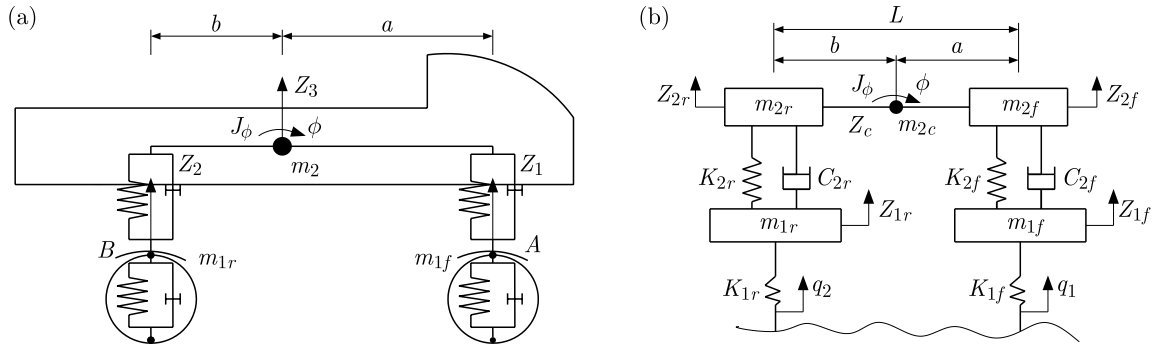

Fig. 1. Vehicle model: (a) two-axle half-car model, (b) simplified half-car model

Based on the balance of the front and rear forces of the non-suspended mass, it is concluded that

$$\begin{aligned} &m_{1f}\ddot{z}_{1f} + C_{2f}(\dot{z}_{1f} - \dot{z}_{2f}) + K_{2f}(z_{1f} - z_{2f}) + K_{1f}(z_{1f} - q_1) = 0 \\ &m_{1r}\ddot{z}_{1r} + C_{2r}(\dot{z}_{1r} - \dot{z}_{2r}) + K_{2r}(z_{1r} - z_{2r}) + K_{1r}(z_{1r} - q_2) = 0 \end{aligned} \tag{2.3}$$

Based on the principle of moment balance around the centroid, it is concluded that

$$J\ddot{\phi} - aC_{2f}(\dot{z}_{2f} - \dot{z}_{1f}) + bC_{2r}(\dot{z}_{2r} - \dot{z}_{1r}) - aK_{2f}(z_{2f} - z_{1f}) + bK_{2r}(z_{2r} - z_{1r}) = 0 \tag{2.4}$$

According to the literature (Zhang *et al.*, 2022), the road roughness of the front and rear wheels in the time domain is expressed as

$$\dot{q}_f(t) + \dot{s}2\pi n_c q(t) = 2\pi n_0 \sqrt{G_q(n_0)\dot{s}}W(t) \qquad \dot{q}_r(t) = -\frac{2v}{L}q_r(t) - \dot{q}_f(t) + \frac{2v}{L}q_f(t) \tag{2.5}$$

where $q(t)$ is the road roughness under unsteady conditions in the time domain, s is the distance traveled by the vehicle, n_c is the lower cut-off space frequency, $n_c = 0.011\,\mathrm{m}^{-1}$, $n_0 = 0.1\,\mathrm{m}^{-1}$ is the reference space frequency, $G_q(n_0)$ is the road roughness coefficient – if it is not stated in the text, it is taken as Class C pavement (ISO, 1990), $W(t)$ is the band-limited white noise, v is the vehicle running speed, L is the distance between the front and rear wheels.

2.2. A multi-layer plate on the viscoelastic half-space foundation

Figure 2 shows an infinite multi-layer plate model on a viscoelastic half-space foundation. The bottom layer shown in the figure is a viscoelastic half-space foundation and above it, is an infinite multi-layer plate.

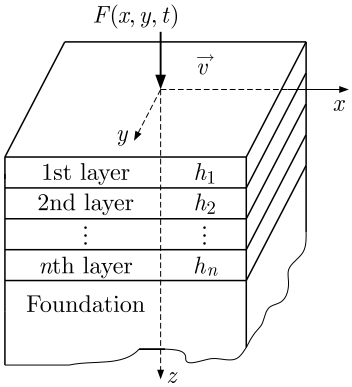

Fig. 2. An infinite multi-layer plate on a viscoelastic half-space foundation

The density, Poisson's ratio and elastic modulus of the viscoelastic half-space foundation are represented by ρ, μ and E, respectively. The displacement in three directions of x, y, z is represented by $u_i(u_x, v_y, w_z)$, and the control equation for a homogeneous isotropic viscoelastic half-space foundation represented by the displacement is

$$(\lambda + G)\nabla(\nabla \cdot u_j) + G\nabla^2 u_j = \rho \frac{\partial^2 u_j}{\partial t^2} \tag{2.6}$$

where: λ, G are Lamé constants, $\lambda = \mu E/[(1+\mu)(1-2\mu)]$, $G = E/[2(1+\mu)]$, ∇^2 is the Laplace operator.

However, in practice, soil (i.e. viscoelastic half-space) should also consider the influence of material damping. According to the linear hysteresis damping theory, material damping is introduced, namely

$$E^* = (1 + 2\mathrm{j}\xi)E \qquad G^* = (1 + 2\mathrm{j}\xi)G \qquad \lambda^* = (1 + 2\mathrm{j}\xi)\lambda \tag{2.7}$$

where j is the imaginary unit, $\mathrm{j}^2 = -1$, ξ is the material damping ratio, where $\xi = 0.05$ is taken.

Smooth contact between the plate and the viscoelastic half-space foundation is assumed. The thickness, elastic modulus, Poisson's ratio and density of each layer are h_i, E_i, μ_i, ρ_i $(i = 1, 2, 3)$. The upper surface of the uppermost plate is subjected to a moving load of $F(x, y, t)$. $P(x, y, t)$ is the vertical reaction of the viscoelastic half-space foundation acting on the plate. In reference (Yang *et al.*, 2010), the differential equation of motion expressed by the vertical displacement of the multi-layer plate is

$$D\Big(\frac{\partial^4 w_{zb}}{\partial x^4} + \frac{\partial^4 w_{zb}}{\partial y^4}\Big) + 2(D_{xy} + 2D_k)\frac{\partial^4 w_{zb}}{\partial x^2 \partial y^2} + m_b \frac{\partial^2 w_{zb}}{\partial t^2} = F(x, y, t) - P(x, y, t) \tag{2.8}$$

where w_{zb} is vertical displacement of the multi-layer plate, $m_b = \sum_{i=1}^{n} \rho_i h_i$ is mass per unit area of the multi-layer plate, D is bending stiffness of the plate in either the x or y direction, D_{xy} is bending stiffness in both the x and y directions, D_k is torsional stiffness. Its expression is

$$\begin{aligned}
D &= \int_{h_0-h_1}^{h_0} \frac{E_1}{1-\mu_1^2} z^2\, dz + \int_{h_0-h_1-h_2}^{h_0-h_1} \frac{E_2}{1-\mu_2^2} z^2\, dz + \cdots + \int_{h_0-\sum_{i=1}^{n} h_i}^{h_0-\sum_{i=1}^{n-1} h_i} \frac{E_n}{1-\mu_n^2} z^2\, dz \\
D_{xy} &= \int_{h_0-h_1}^{h_0} \frac{E_1\mu_1}{1-\mu_1^2} z^2\, dz + \int_{h_0-h_1-h_2}^{h_0-h_1} \frac{E_2\mu_2}{1-\mu_2^2} z^2\, dz + \cdots + \int_{h_0-\sum_{i=1}^{n} h_i}^{h_0-\sum_{i=1}^{n-1} h_i} \frac{E_n\mu_n}{1-\mu_n^2} z^2\, dz \\
D_k &= \int_{h_0-h_1}^{h_0} \frac{E_1}{2(1+\mu_1)} z^2\, dz + \int_{h_0-h_1-h_2}^{h_0-h_1} \frac{E_2}{2(1+\mu_2)} z^2\, dz + \cdots + \int_{h_0-\sum_{i=1}^{n} h_i}^{h_0-\sum_{i=1}^{n-1} h_i} \frac{E_n}{2(1+\mu_n)} z^2\, dz
\end{aligned} \tag{2.9}$$

where h_0 is the distance between the neutral layer of the multi-layer plate and the upper surface of the uppermost plate. Since the stress in the neutral layer is zero (Hung and Yang, 2001), the expression can be deduced as follows

$$h_0 = \left[E_1 h_1^2 + E_2(2h_1 + h_2)h_1 + E_3(2h_1 + 2h_2 + h_3)h_3 + \cdots + E_n\left(2\sum_{i=1}^{n-1} h_i + h_n\right)h_n\right] \frac{1}{n\sum_{i=1}^{n} E_i h_i} \tag{2.10}$$

The boundary conditions and initial conditions of the problem can be expressed as

$$\begin{aligned}
&\lim_{x\to\pm\infty} \frac{\partial^n w_{zb}}{\partial x^n} = 0 \qquad \lim_{y\to\pm\infty} \frac{\partial^n w_{zb}}{\partial y^n} = 0 \qquad n = 0, 1, 2, \ldots \\
&w_{zb}(x, y, t)\big|_{t=0} = \frac{\partial w_{zb}(x, y, t)}{\partial t}\Big|_{t=0} = 0
\end{aligned} \tag{2.11}$$

2.3. Description of the vehicle-road coupling system

The article studies the dynamic response of road structures based on the vehicle-road coupling. The coupling relationship between the vehicle and the road surface can be described as follows: when the vehicle passes through the road at a certain speed, the vehicle generates vibration due to excitation of the road roughness, and the road structure also vibrates under the dynamic load of the vehicle, and the vibration of the road surface causes secondary coupling vibration of the vehicle.

In order to more accurately describe the interaction between the tire and road surface, the vertical load force $F(x,y,t)$ consists of two parts, namely the static load Mg (M is mass distributed on the tire by the whole vehicle) and the dynamic load F_d (Lu *et al.*, 2021)

$$F = Mg + F_d \tag{2.12}$$

where F_d is the reaction force generated by the unsteady road excitation on the vehicle.

3. Analytical solution of the dynamic response

According to the Helmholtz theorem, the displacement vector of a viscoelastic half-space foundation in a rectangular coordinate system can be decomposed into

$$\mathbf{u}_i(u_x, v_y, w_z) = \nabla\Phi + \nabla \times \mathbf{\Psi}_i(\Psi_1, \Psi_2, \Psi_3) \tag{3.1}$$

where u_x, v_y and w_z are displacements in the three directions x, y and z of the viscoelastic half-space foundation, respectively, Φ is the scalar potential of displacement $\mathbf{u}_i$, $\mathbf{\Psi}_i$ is the vector potential of the displacement $\mathbf{u}_i$.

By using Green's function and generalized Duhamel's integral, an analytical solution of the dynamic response of an infinite four-layer plate on a viscoelastic half-space foundation under moving loads can be obtained. The expression for the generalized Duhamel integral is (Li *et al.*, 2013)

$$u_{ki}(x,y,z,t) = \int\limits_S \int\limits_0^t F(\zeta_1, \zeta_2, \tau) G_{ki}(x-\zeta_1, y-\zeta_2, z, t-\tau)\, d\tau\, dS \tag{3.2}$$

where on the right-hand there is a convolution integral of the moving load and Green's function.

According to reference (Li *et al.*, 2013), the vertical displacement of the viscoelastic half-space foundation under the moving load can be obtained

$$\begin{aligned} w = {} & \frac{F}{(2\pi)^2 G} \mathrm{e}^{\mathrm{j}\omega_0 t} \int\limits_{-\infty}^{+\infty}\int\limits_{-\infty}^{+\infty} \frac{\sin(k_1 l_1)}{k_1 l_1} \frac{\sin(k_2 l_2)}{k_2 l_2} \frac{1}{\Delta} [B_p(k_1^2 + k_1^2 + B_s^2)\mathrm{e}^{-B_p z} \\ & - 2B_p(k_1^2 + k_2^2)\mathrm{e}^{-B_s z}]\mathrm{e}^{\mathrm{j}[k_1(x-vt)+k_2 y]}\, dk_1\, dk_2 \end{aligned} \tag{3.3}$$

where ω_0 is the loading frequency of harmonic loads, $\omega_0 = 0$ represents the moving dead load, $l_1 = 0.11$, $l_2 = 0.16$ are the rectangular areas of contact force distribution between the wheel and ground. The rectangular area is $\{-l_1 \leqslant x \leqslant l_1,\ -l_2 \leqslant x \leqslant l_2\}$, and B_p, B_s, Δ are intermediate transition expressions. The derivation is more complex and will not be repeated, see Li *et al.* (2013). v is the driving speed of the vehicle, and the range of it is 0-45 m/s.

4. Numerical calculation

4.1. Vehicle and road model parameters

The analytical solution for the multi-layer plate on the viscoelastic half-space foundation has been given in Section 3. Next, the authors completed simulation of the dynamic response using MATLAB (Xue, 2019; Kreines and Kreines, 2020). In fact, the making use of four layer plates such as surface layer, base, subbase and cushion layer is sufficient to meet the needs of the project. That is, $n = 4$ in Eqs. (2.9) and (2.10). The article takes the road structure of Laiqu section of Taihang Mountain Expressway as the example (Yan *et al.*, 2020), see Table 1 for material parameters of the viscoelastic half-space foundation and the four-layer plate structure. The parameter information of the two-axle heavy vehicle is given in Table 2 (Kim *et al.*, 2005).

Table 1. Material parameters of the road structure

Pavement structure	Thickness [m]	Elastic modulus [MPa]	Poisson's ratio	Density [kg/m^3]
AC-13C	0.04	9000	0.25	2300
ARHM-20	0.06	10000	0.25	2300
ATB-25	0.1	8000	0.25	2400
Subbase	0.54	9000	0.25	2300
Foundation	$+\infty$	60	0.40	1850

Table 2. Parameters of the two-axle heavy vehicle

Parameter	Numerical value	Parameter	Numerical value
Front wheel mass [kg]	500	Rear suspension damping [Ns/m]	$3.3420 \cdot 10^7$
Rear wheels mass [kg]	725	Front suspension stiffness [N/m]	$1.577 \cdot 10^6$
Vehicle mass [kg]	28500	Rear suspension stiffness [N/m]	$4.724 \cdot 10^6$
Wheel base [m]	4	Front wheel stiffness [N/m]	$3.146 \cdot 10^6$
Front suspension damping [Ns/m]	$1.120 \cdot 10^7$	Rear wheels stiffness [N/m]	$4.724 \cdot 10^6$

4.2. Road surface excitation in an unsteady state

The roughness parameters corresponding to A-D grade roads refer to the current standard GB/T 7031-2005 (Li *et al.*, 2006), see Table 3. According to equations $(2.5)_2$ and (2.6), filtered white noise is used to simulate road roughness at the front and rear wheel positions.

Table 3. A-D pavement grade parameters in GB/T 7031-2005

Pavement grade	Unevenness parameter $G_d(n_0)$ $[10^{-6}(\mathrm{m}^2/\mathrm{m}^{-1})]$		
	minimum	geometric mean	maximum
A	–	16	32
B	32	64	128
C	128	256	512
D	512	1024	2048

Figure 3a shows the time history response of road roughness of different pavement grades in an unsteady state. The vehicle speed uniformly increases from 0 m/s to 45 m/s. Negative

values represent a situation below the road reference plane. At 12 seconds, the time history response of road roughness under four different pavement grades A, B, C and D based on band--limited white noise is 7.855 mm, 15.710 mm, 31.420 mm and 62.840 mm, respectively. They are all extreme values in 15 seconds. Except for A-level pavement, all of them are doubled on the basis of the previous grade. Taking the D-level pavement as an example, a small speed from 0 s to 2 s produces a small displacement response, and the response increases with an increase of speed. When the speed is greater than 7 m/s, its amplitude fluctuates within the range of 0 mm to 62.840 mm. Figure 3b shows the time history response of road roughness at the front tire and rear tire positions under non-stationary conditions. As shown in the figure, from 0 s to 15 s, the road roughness curves at the front and rear wheel positions appear successively, and the two curves gradually overlap as the vehicle speed increases. However, from 0 s to 2 s, the two curves differ from the above conclusion due to wheelbase length of the front and rear wheels. Figure 3c shows the road roughness with different accelerations. From the slopes of the two curves in the figure, it can be seen that the greater the acceleration, the stronger the increase (or decrease) in the amplitude of road roughness. This phenomenon conforms to Newton's second law which it states that the magnitude of the force acting (road roughness in the article) on an object is proportional to acceleration.

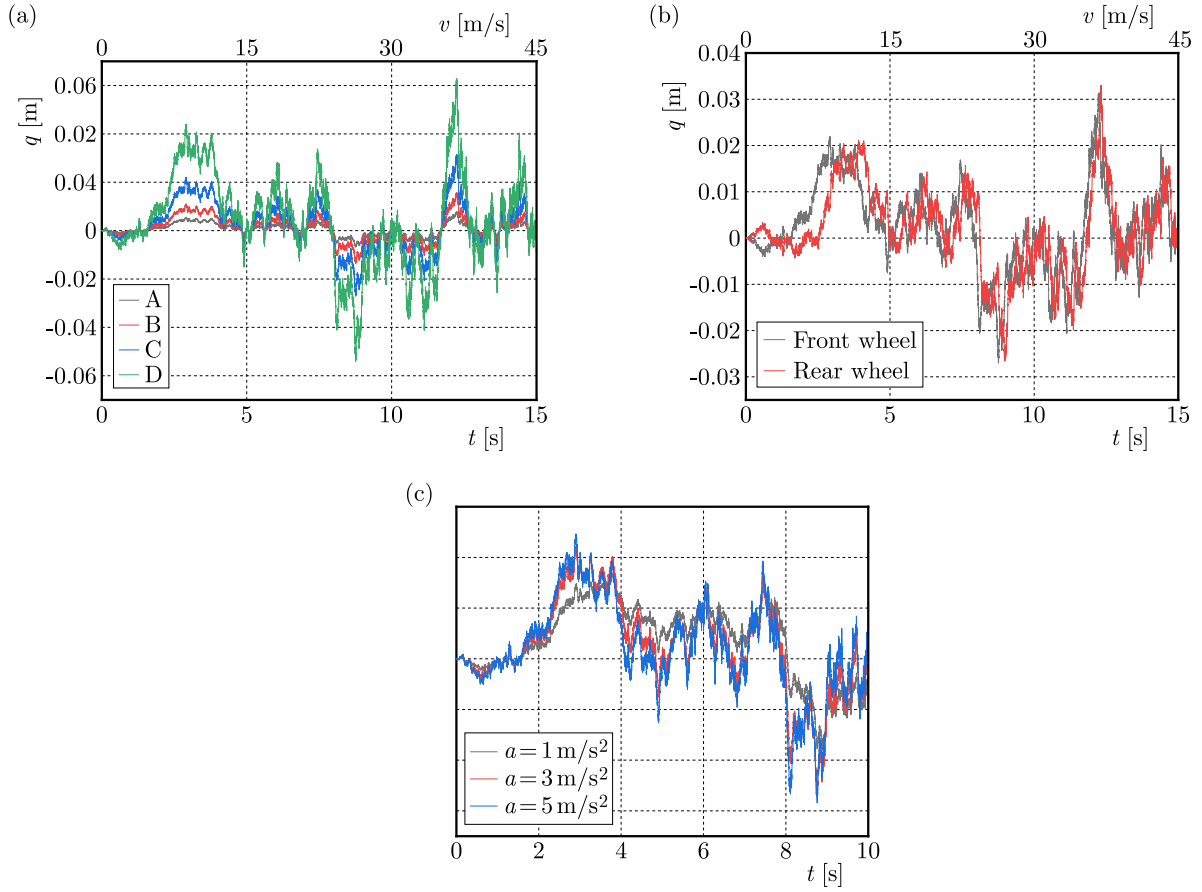

Fig. 3. Road roughness: (a) of different pavement grades, (b) under various tires, (c) with different accelerations

Figure 4a shows the vertical vibration time-history response of the unsprung mass of the front axle. Its amplitude fluctuates around the $w = 0$ axis and increases with an increase of the vehicle speed, which has a strong correlation with the road roughness response. According to equation (2.12), the C-level road excitation under the non-stationary vehicle load, as shown in Fig. 4b, can be obtained. Its amplitude fluctuates up and down around the static load generated

by the vehicle self weight ($Mg/4 = 7.5827 \cdot 10^7$ N), which shows an increasing trend as the vehicle speed increases. From 0 s to 15 s, the maximum and minimum values of the road excitation are $7.584 \cdot 10^7$ N and $7.581 \cdot 10^7$ N, respectively. The difference between them is only 0.04%. Its value directly affects the result of vertical displacement of the pavement.

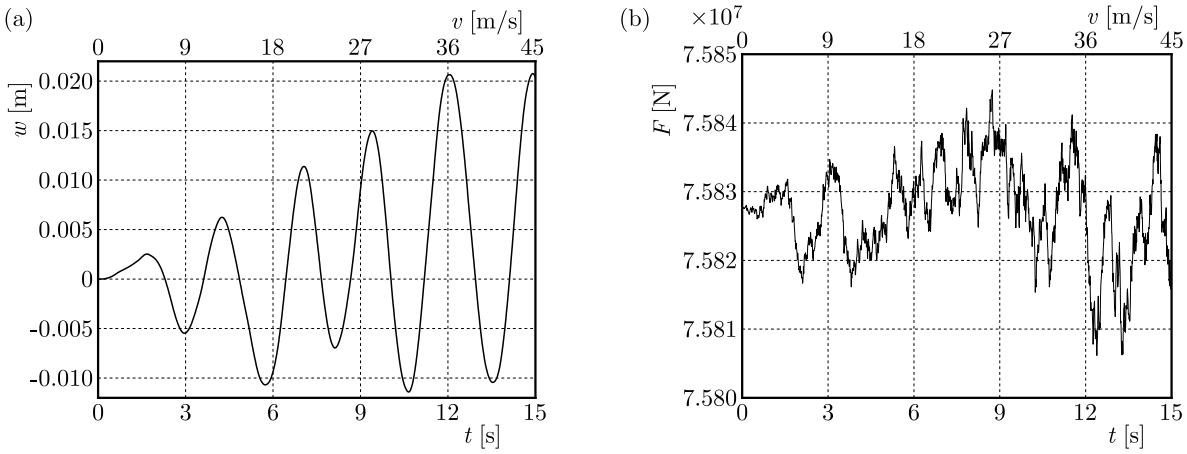

Fig. 4. (a) Unsprung mass vertical vibration of the front axle; (b) road excitation in an unsteady state

4.3. Dynamic response of the vehicle-road coupling in an unsteady state

4.3.1. Algorithm validation

Hung used the direct integral transformation method to calculate the dynamic response of a viscoelastic half-space foundation (Hung and Yang, 2001). Next, the article uses a self-made MATLAB program to study the dynamic response of road structures. Some model parameters in Hung's article are as follows: $v = 50$ km/h, $F = 5 \cdot 10^4$ N, $G = 20$ MPa, $\mu = 0.25$, $\rho = 2000$ kg/m^3, $\xi = 0.02$. To verify the correctness of the self-made MATLAB program, see Fig. 5, where a comparison of the time-history response results of the vertical displacement W of viscoelastic the half-space foundation is shown. The method in this paper is consistent with the calculation results of Hung. Li *et al.* (2015) established a layered road structure using Ansys software and verified the correctness of the algorithm proposed in this paper.

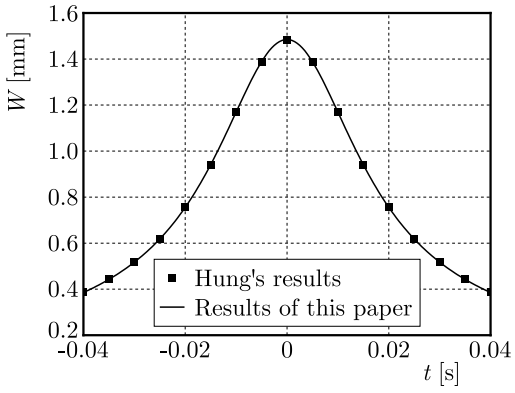

Fig. 5. Comparison of the vertical displacement results

4.3.2. Displacement response of the four-layer plate under an unsteady state

The force exerted by driving vehicles on the road surface can cause vertical displacement of the road surface. This Section focuses on the displacement w of a four-layer plate on a viscoelastic half-space foundation.

Figure 6a shows the time history curve of the vertical displacement of the road surface, four curves represent four different vehicle speeds. When the speed is 5 m/s, 10 m/s, 20 m/s, and 30 m/s, the vertical displacements are ±0.6 s are 0.131 mm, 0.057 mm, 0.027 mm, and 0.018 mm, respectively. Figure 6b shows the vertical displacement under a single wheel in the direction of x (driving direction) and y (perpendicular to the driving direction) when the moving speed is 10 m/s. At 6 m from the reference point, their vertical displacement is $5.677 \cdot 10^{-2}$ mm and $5.796 \cdot 10^{-2}$ mm, respectively, with a difference of only 2.096%. For the observation point, the vertical displacement gradually increases when the vehicle arrives, and decreases when the vehicle leaves. Generally, it presents a "V" shape with flat ends and steep middle. Figure 6c shows three curves representing the vertical displacement of the road surface at the front wheel position, where the rear wheel and the front wheel act alone, and the front and rear wheels act together ($v = 10$ m/s). The maximum vertical displacement of a single wheel is 0.094 mm, 0.340 mm respectively, and the maximum vertical displacement caused by the combined action of two wheels is 0.434 mm.

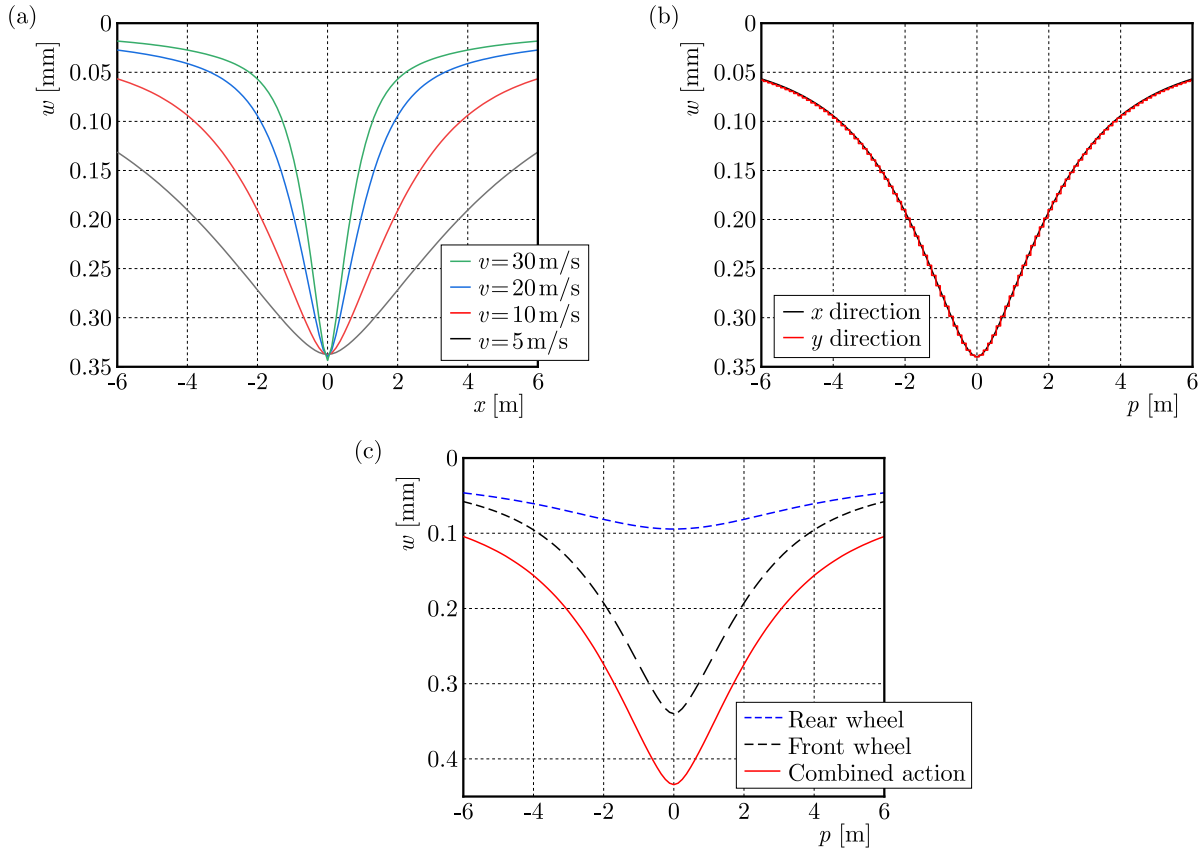

Fig. 6. (a) Time history curve of vertical displacement at different speeds; (b) vertical displacement in x and y directions; (c) vertical displacement of each tire at the front wheel position

Figure 7a shows the vertical displacement response nephogram of the four-layer plate caused by the single-wheel action. Figure 7b shows the interaction of the front and rear wheels ($v = 15$ m/s). The maximum vertical displacement is 0.340 mm, 0.438 mm, respectively. The combined action of the front and rear wheels is 1.288 times of a single wheel. The vertical displacement effect of a single wheel set on the pavement is shown as a "circle" extending from the inside out on a plane. During the double-wheel action, due to the two "circular" coherent effects, it gradually transits to "8-shaped" and "oval", and finally approaches to "circular" infinitely.

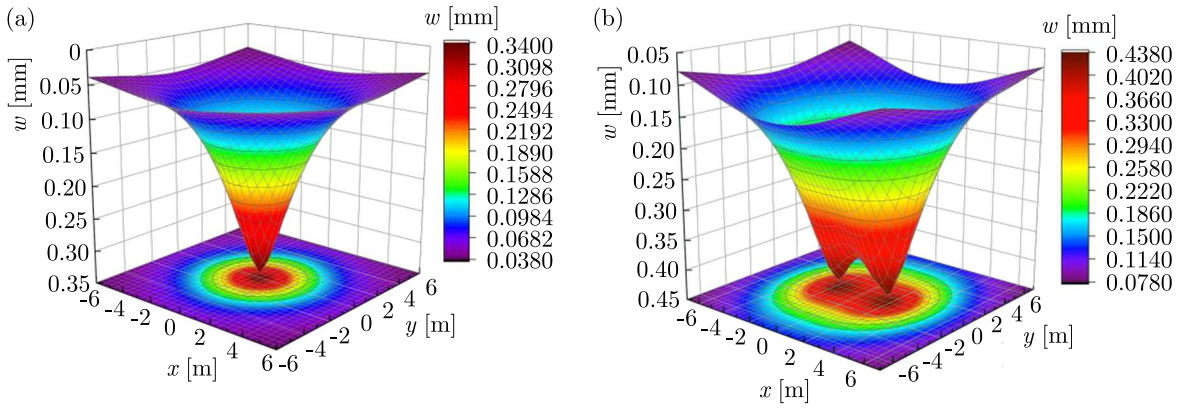

Fig. 7. Nephogram of vertical displacement: (a) under the action of a single wheel, (b) under the coherent action of the front and rear wheels

5. Conclusions

By establishing a mathematical model and rigorous theoretical derivation, the unsteady vehicle--road coupling dynamic response of a multi-layer plate on a viscoelastic half space foundation is studied, and the following conclusions are drawn:

- Based on band-limited white noise to simulate road roughness, the response of road roughness is small at a low speed, but increases significantly with speed. At high speeds, the response of road roughness is relatively large, but the increase in speed is relatively small, and there may even be a decrease.
- Based on the non-steady road excitation of accelerating vehicles, its amplitude fluctuates around the static load generated by the vehicle own weight, and increases with an increase of vehicle speed.
- The vertical displacement effect of the vehicle load on the ground is almost the same in the longitudinal direction (driving direction) and the transverse direction (perpendicular to the driving direction). The transverse displacement at 6m from the loading position is only 2.096% higher than the longitudinal displacement, and this effect decreases rapidly with an increase of distance.
- The vertical displacement effect of a single wheel set on the pavement is shown as a "circle" extending from the inside out on a plane. During the double-wheel action, due to the two "circular" coherent effects, it gradually transits to "8-shaped" and "oval", and finally approaches to "circular" infinitely.

References

1. Awal M.A., Ouelha S., Dong S., Boashash B., 2017, A robust high-resolution time-frequency representation based on the local optimization of the short-time fractional Fourier transform, *Digital Signal Processing*, **70**, 125-144

2. Cai Y.Q., Cao Z.G., Sun H.L., Xu C., 2009, Dynamic response of pavements on poroelastic half-space soil medium to a moving traffic load, *Computers and Geotechnics*, **36**, 52-60

3. Cao Z.G., Boström A., 2013, Dynamic response of a poroelastic half-space to accelerating or decelerating trains, *Journal of Sound and Vibration*, **332**, 2777-2794

4. Dieterman H.A., Metrikine A., 1997, Critical velocities of a harmonic load moving uniformly along an elastic layer, *Journal of Applied Mechanics – ASME*, **64**, 596-600

5. Hamidi M., Zaki S., Aboussaleh M., 2021, Modeling and numerical simulation of the dynamic behavior of magneto-electro-elastic multilayer plates based on a Winkler-Pasternak elastic foundation, *Journal of Intelligent Material Systems and Structures*, **32**, 832-846
6. Hung H.H., Yang Y.B., 2001, Elasitc waves in visco-elastic half-space generated by various vehicle loads, *Solid Dynamics and Earthquake Engineering*, **21**, 1-17
7. ISO 8606:1990 – Plastics – Prepregs – Bulk moulding compound (BMC) and dough moulding compound (DMC) – Basis for a specification
8. Kim C.W., Kawatani M., Kim K.B., 2005, Three-dimensional dynamic analysis for bridge-vehicle interaction with roadway roughness, *Computers and Structures*, **83**, 1627-1645
9. Kim S.M., 2004, Influence of horizontal resistance at plate bottom on vibration of plates on elastic foundation under moving loads, *Engineering Structures*, **26**, 519-529
10. Kim S.M., Roesset J.M., 1998, Moving loads on a plate on elastic foundation, *Journal of Engineering Mechanics*, **124**, 1010-1017
11. Kreines M.G., Kreines E.M., 2020, Matrix models of texts: models of text collections, *Mathematical Models and Computer Simulations*, **12**, 37-57
12. Li H.Y., 2011, *Research on Pavement Structure Dynamics under the Interaction between Vehicle and Pavement* (in Chinese), Beijing Jiaotong University
13. Li H.Y., Qi Y.Q., Liu J., 2013, Dynamic responses of a two-layer plate on viscoelastic half-space foundation under moving loads (in Chinese), *Geotechnical Mechanics*, **34**, 28-34
14. Li H.Y., Yang S.P., Liu J., Si C.D., 2015, Dynamic response in multilayered viscoelastic medium generated by moving distributed loads (in Chinese), *Engineering Mechanics*, **32**, 120-127
15. Li S.C., Wang S.Y., Zhao J.Y., 2006, Mechanical vibration road surface spectrum measurement data report: GB/T7031-2005 (in Chinese), Beijing: China Standards Press
16. Lu Y.J., Zhang J.N., Li H.Y., Ma Z.Z., 2021, Study on coupling dynamics of tire-road system based on non-uniform contact (in Chinese), *Journal of Mechanical Engineering*, **57**, 87-98
17. Mirsaidov M., Mamasoliev Q., 2020, Contact problems of multilayer slabs interaction on an elastic foundation, *IOP Conference Series: Earth and Environmental Science*, **614**, 1-14
18. Rahman M.S., Kibria K.M.G., 2014, Investigation of vibration and ride characteristics of a five degrees of freedom vehicle suspension system, *Procedia Engineering*, **90**, 96-102
19. Si L.T., 2017, *Random Vibration Analysis of Linear Continuous System under Moving Random Load* (in Chinese), Dalian University of Technology
20. Sun L., 2007, Steady-state dynamic response of a Kirchhoffs slab on viscoelastic Kelvin's foundation to moving harmonic loads (in Chinese), *Journal of Applied Mechanics*, **74**, 1212-1224
21. Xue D.Y., 2019, *MTALAB Calculus* (in Chinese), Beijing: Tsinghua University Press
22. Yan Z.Y., Zhao X.L., Zhao G.F., Zhao Y., Zhao G.Y., 2020, Dynamic response of asphalt pavement under multi-wheel dynamic load (in Chinese), *Journal of China Highway*, **33**, 119-132
23. Yang S.P., Li S.H., Lu Y.J., 2010, Investigation on dynamical interaction between a heavy vehicle and road pavement, *Vehicle System Dynamics: International Journal of Vehicle Mechanics and Mobility*, **48**, 923-944
24. Zhang B.Y., Dai T., Tan C.A., Li J., Zhang Y., Li S.H., 2022, Research on the non-stationary virtual excitation method of suspension system vibration characteristics (in Chinese), *Vibration. Test and Diagnosis*, **42**, 227-234

Manuscript received February 8, 2023; accepted for print May 16, 2023

JOURNAL OF THEORETICAL AND APPLIED MECHANICS
61, 3, pp. 533-544, Warsaw 2023
https://doi.org/10.15632/jtam-pl/167475

FAILURE ANALYSIS AND OPTIMIZATION DESIGN OF SUSPENSION SUPPORT HOLES FOR GEARBOX CASES

Leyu Wei
School of Materials Science and Engineering, North China University of Water Resources and Electric Power, Zhengzhou, China; corresponding author, e-mail: 34523626@qq.com

Xinmeng Liu
Zhengzhou Yutong Bus Co., Ltd., Zhengzhou 450001, China

Jie Yang, Linjian Shangguan
School of Mechanical Engineering, North China University of Water Resources and Electric Power, Zhengzhou, China

Xingxing Wang
School of Materials Science and Engineering, North China University of Water Resources and Electric Power, Zhengzhou, China

Jizhe Mao
Zhengzhou Research Institute of Mechanical Engineering Co., Ltd., Zhengzhou, China

The suspension hole of a gearbox case was cracked after the mining test vehicle has covered 7000 km. In order to analyze and solve this problem, in this paper, based on the modal analysis of the suspension system and failure analysis of the faulty parts, the finite element model of the powertrain system was established using Ansys, and strength analysis of the gearbox case was carried out. According to the analysis results, improvement and optimization measures were proposed. The analysis results show that the maximum stress of the optimized gearbox case was reduced by 6.9%, and the test vehicle could operate for 50 000 km without failure after the improvement, which verified the effectiveness of those measures. Accumulating experience in the gearbox case design and simulation, modal analysis and finite element analysis were combined to quickly identify the failure causes of the suspension support hole, and targeted improvement measures were taken, which effectively shortened the research and development cycle and saved production costs.

Keywords: gearbox case, modal analysis, failure analysis, optimization design, suspension support holes

1. Introduction

The gearbox is mainly composed of gears, bearings, shafts, and case among other parts. It is an important component of the vehicle powertrain and is widely used in machinery (Vilan *et al.*, 2010). As the main supporting part of the gearbox, the case is bolted to the motor externally and supported on the vehicle frame by a suspension structure. The gearbox case of a complex structure and large size is subjected to loads such as shock and vibration from complex road conditions, as well as torque and gear meshing reaction forces applied to the bearing holes by the internal drive shaft of the gearbox through bearings (Dong, 2011). Once the gearbox case ruptures under complex loads, it will affect the performance and life of the vehicle and, in serious conditions, it may cause accidents and generate significant economic losses (Li and Chen, 2017; Liu, 2018; Fu *et al.*, 2010; Hu *et al.*, 2017; Wilk *et al.*, 2011). Therefore, it is necessary to analyze and study the strength of the gearbox case to ensure its reliability and structural strength.

Xue (2019) conducted appearance analysis, metallographic structure analysis, hardness testing, macroscopic fracture analysis and SEM analysis on a fractured part of the gearbox suspension. Chen *et al.* (2018) carried out testing, diagnosis and finite element analysis, and found that the mounting bracket at gearbox surface exhibited a high resonance at the corresponding frequency, which negatively affected the mounting stability and increased interior noise of the vehicle. Xiao established a dynamic model for the suspension system of the EV powertrain. Through experiments, the researcher obtained inertia parameters of a pure EV powertrain and a static stiffness curve of the suspension. He also examined the excitation force on the EV powertrain (Xiao, 2021). Wang *et al.* (2018) studied the influence of polygonal wear of wheels on the dynamic performance of the gearbox housing of a high-speed train. Wu *et al.* (2019) established a three-dimensional multibody system (MBS) railway vehicle model by considering the flexibility of the gearbox shell and wheel set as well as nonlinear wheel rail contact, and studied the effect of wheel polygonization on the fatigue of a gearbox shell installed on the wheel set of a high-speed train. In order to reduce the radiated noise of the gearbox of agricultural electric vehicles, Son *et al.* (2020) optimized the shape of the gearbox shell. There is great space for optimization of the gearbox housing (Jin *et al.*, 2021; Huang *et al.*, 2021), but there are few literatures items that specify or analyze suspension support holes of gearboxes. Therefore, in this study, we carried out failure analysis and optimization design for the suspension support hole of the gearbox housing. In this paper, upon the analysis of failure causes of suspension holes of a gearbox, improvement and optimization measures are proposed, and the strength analysis of the gearbox case is carried out by employing a simulation analysis method to verify the effectiveness of the improvement measures, which is of great significance to promote vehicle research and development.

2. Fault description and detection

During the durability test of a pure electric mining test vehicle, when the vehicle covered 7000 km, the problem of rupture of the suspension hole of the gearbox case appeared. The inspection of the powertrain found that there were oil stains on the surface of the gearbox shell, and the support holes on the left side of the shell (flange direction) were damaged. Two support holes were broken in the middle of the screw thread, with the fracture not structurally loose. Figure 1

Fig. 1. Rupture position of the support hole

shows the lower left and upper right support holes. One support hole steel wire thread sleeve and the inner wall of the hole were damaged in the middle of the thread against the lower end. Figure 1 shows the lower right support hole. The thread of the broken support hole measured up

to 10 mm in depth, and the damaged support hole wall measured up to 10 mm in depth. Still, 1/2 was unscrewed as shown in Fig. 2.

Fig. 2. Support hole thread the gearbox case

The inspection of the threaded holes was passed. The technical requirements of the four-hole thread were M14, 20 mm of thread depth, 25 mm of hole depth; the outer circle of the tab was ∅30, and the height of the tab was 30 mm. The support hole without damage was tested as: M14, thread depth being 20 mm, hole depth 27 mm; the outer circle of the small end of the tab 30.7 mm, and the height of the tab 15.3 mm (to the rib), which passed. After physical and chemical analysis of the shell, the structure was free of defects, and the measured hardness was 105 HB, which met the technical requirements (Liu *et al.*, 2021).

The current bolt specification used is M14×25, with the actual screw-in size at about 15 mm. The effective thread connection length of aluminum alloy material is required to be 1.5-2 times of the outer diameter of the thread. The preliminary judgment of the failure phenomenon is that the cause of the failure is that the upper left and lower right bolts are loose and missing, leading to a sudden increase in the load on the single bolt hole, which in turn leads to rupture of the shell. In addition, there is a slight collision trace at the position of the suspension limit, which can be determined that there was a rigid collision at the suspension limit during the operation.

3. Materials and methods

The gearbox housing is made of cast aluminum alloy with the modulus $6.9 \cdot 10^4$ MPa, Poisson's ratio $\nu = 0.3$, and density 2.7 g/cm^3. The suspension bracket is made of Q235, with the modulus $2.5 \cdot 10^5 4$ MPa, Poisson's ratio $\nu = 0.28$, and density 7.7 g/cm^3. All parameters have been set in the material properties of Ansys.

Compared with traditional fuel vehicles, vibration of electric vehicles, which is produced by the power transmission system, has significantly decreased. However, there are still various vibration problems with the motor operation due to limitations of processing technology and precision constraints. To analyze causes of cracking in the connection hole between the gearbox of a mining vehicle and the suspension bracket, this article conducts modal analysis of the powertrain suspension bracket. It analyzes the frequency and mode of vibration of the bracket and performs finite element loading analysis on the overall model. By obtaining strength of each component, it identifies the causes of problems for further optimization of the design.

4. Results of finite element analysis

4.1. Modal analysis of the suspension bracket

The modal analysis is mainly used to determine dynamic characteristics of structural systems to clearly calculate frequencies and vibration patterns of each order, and to further optimize the performance of products in use. Currently, there are wide applications of modal analysis for improvement of vehicle frames, power systems and other components (Fan and Pan, 2010; Guo *et al.*, 2015; Korka and Gillich, 2017; Liu and Gao, 2017; Wang *et al.*, 2022; Walunj *et al.*, 2015); Zhang *et al.*, 2022).

The powertrain suspension bracket is simulated by PSHELL unit, and the basic size of the unit is 4 mm. The finite element modal analysis models of gearbox suspension bracket 1 and 2 are established as showm in Fig. 3a and 3b, respectively.

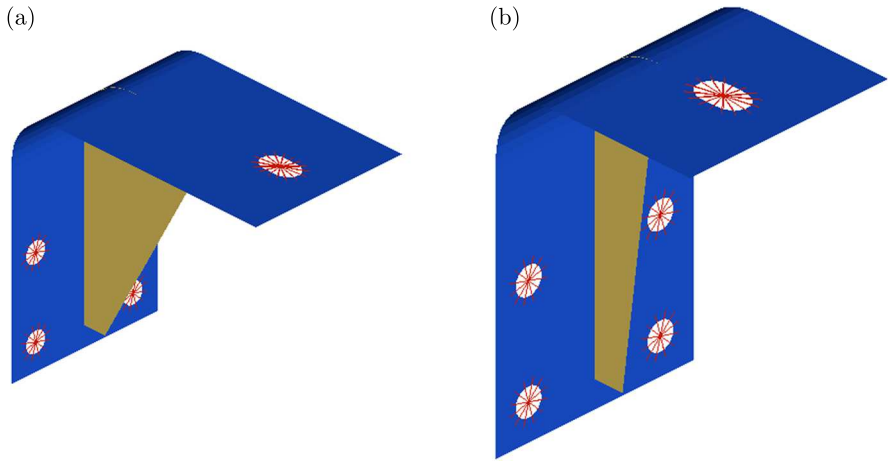

Fig. 3. The finite element model of the bracket: (a) gearbox suspension bracket 1, (b) gearbox suspension bracket 2

To constrain the six degrees of freedom at the connection between the bracket and the powertrain, the third-order constrained modes of vertical vibration, advection and torsion are solved. The first 3 order frequencies of each model are shown in Table 1, and the first 3 order modes and vibration patterns of each model are shown in Fig. 4.

Table 1. The inherent frequency of the first 3 orders of each model

No.	Vibration type	Frequency of gearbox bracket 1 [Hz]	Frequency of gearbox bracket 2 [Hz]	Target value [Hz]
1	Vertical vibration	382.3	583.2	$\geqslant 350$
2	Horizontal vibration	521.3	704.7	
3	Torsional vibration	1089	1332	

From Table 1 and Fig. 4, it can be seen that differences in the inherent frequencies of each order of different models are significant, indicating that the working conditions of different frequencies have a large impact on the modal characteristics of the bracket, and the inherent frequencies of each model under torsional working conditions peak. The inherent frequencies of each order of suspension bracket 1 and 2 are greater than the target value of 450 Hz. The analysis shows that the cracking problem of the connection hole between the gearbox and the suspension bracket of the mine car is not caused by vibration of the bracket (Yang *et al.*, 2022).

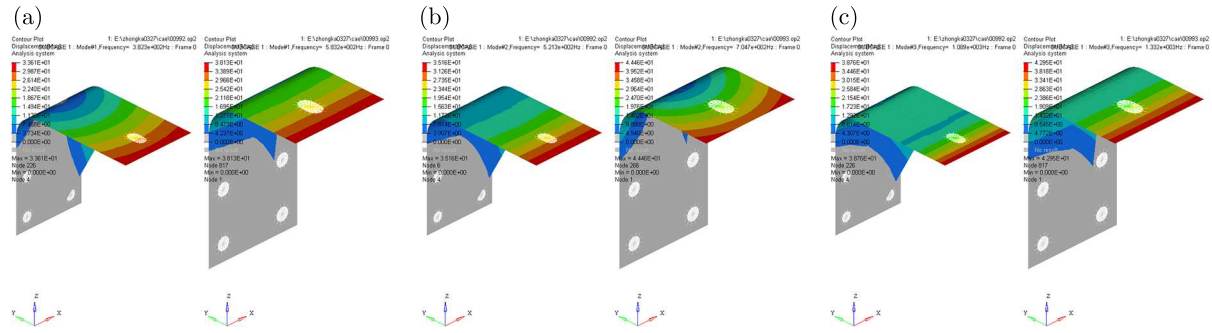

Fig. 4. (a) 1st order, (b) 2nd order and (c) 3rd order of each model

4.2. Powertrain strength analysis

For the problem of cracking of the connection hole between the gearbox case and the suspension bracket, it is proposed to conduct strength analysis of the powertrain, focusing on the stress distribution of the gearbox case to provide a basis for design of the optimized structure of the case. Therefore, a finite element analysis model is established for the whole powertrain as shown in Fig. 5.

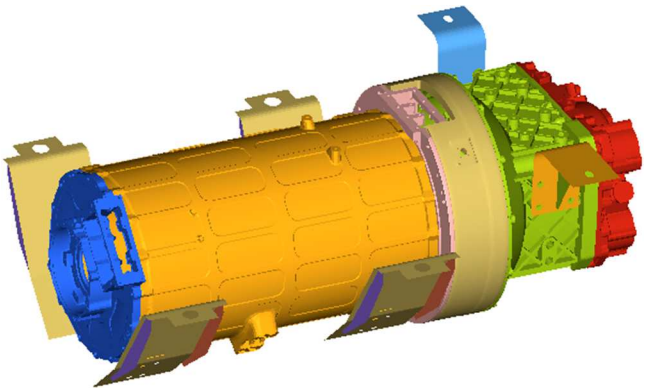

Fig. 5. Finite element analysis model of the powertrain

In this paper, the finite element analysis is based on Ansys, and the suspension bracket of the powertrain is simulated by PSHELL unit with a basic unit size of 4 mm. The bolts and welds are simulated by RBE2 unit; the suspension is simulated by CBUSH unit; mass of the powertrain is 670 kg, and is simulated by CONM2 unit (Fu *et al.*, 2010; Li and Wang, 2008; Shen etal, 2014). The gearbox case, suspension bracket and support arms are all made of cast aluminum alloy, and the bolt is made of steel. If linear elastic properties of the materials are considered alone in the model calculation, the materials are isotropic (Zhang *et al.*, 2014; Zhang and Wang, 2020).

In the powertrain finite element model, 6 degrees of freedom are constrained at the connection between the bracket and the body end, and 9 normal and 4 extreme conditions are selected based on strength analysis. When the finite element method model is calculated, the maximum bolt preload force needs to be considered, and the load information of specific working conditions is shown in Table 2. All working conditions are considered for the self-weight of the powertrain. The yield strength of the gearbox case material is 120 MPa, tensile strength 295 MPa, fatigue strength 126 MPa, and the stress results are shown in Table 3 as follows.

As can be seen from Table 3, the cracking areas of the support holes are smaller than the yield limit, and the stress clouds under each working condition are shown in Figs. 6 and 7 down below. The maximum von Mises stress of the gearbox shell is concentrated at the bolt hole under each working condition, and the maximum value is 69.153 MPa in working condition 9.

Table 2. Strength working conditions

No.	Description	Loading			Target value [MPa]
		$X(G)$	$Y(G)$	$Z(G)$	
1	To the right $1G$		1	−1	⩽ 126 MPa (general working conditions)
2	Vertical downward $3G$			−3	
3	Vertical downward $3G$, forward $1G$	−1		−3	
4	Vertical downward $3G$, backward $1G$	1		−3	
5	Forward $3G$	−3		−1	
6	Backward $3G$	3		−1	
7	To the left $3G$		−3	−1	
8	To the right $3G$		3	−1	
9	Peak torque (12000 Nm)		3	−1	
10	Vertical backward $3G$, upward $4G$			4	
11	Vertical downward $6G$			−6	⩽ 295 MPa (extreme work. cond.)
12	Vertical downward $6G$, to the left $3G$		−3	−6	
13	Vertical downward $6G$, to the right $3G$		3	−6	

Table 3. Strength stress results

No.	Description	Loading			Transmission case maximum stress [MPa]	Target value [MPa]	Maximum deform. of suspension [mm]	Target value [MPa]
		$X(G)$	$Y(G)$	$Z(G)$				
1	To the right $1G$		1	−1	10.044	⩽ 126 MPa (general working conditions)	0.462	⩽ 5 mm
2	Vertical downward $3G$			−3	14.843		1.814	
3	Vertical downward $3G$, forward $1G$	−1		−3	19.618		2.271	
4	Vertical downward $3G$, backward $1G$	1		−3	16.135		1.686	
5	Forward $3G$	−3		−1	27		2.815	
6	Backward $3G$	3		−1	24.134		2.369	
7	To the left $3G$		−3	−1	28.636		3.718	
8	To the right $3G$		3	−1	22.511		3.882	
9	Peak torque (14406 Nm)		3	−1	69.153		5.908	
10	Vertical backward $3G$, upward $4G$			4	19.791		2.418	
11	Vertical downward $6G$			−6	29.696	⩽ 295 MPa (extreme working conditions)	3.627	
12	Vertical downward $6G$, to the left $3G$		−3	−6	52.743		4.847	
13	Vertical downward $6G$, to the right $3G$		3	−6	42.072		5.566	

The maximum stress of the gearbox shell is less than the fatigue strength of the material in each working condition, which meets the design requirements. The deformation of the suspension pad is larger in working condition 9 and 13, and the deformation is 5.908 mm and 5.566 mm respectively, which is larger than the target value. Therefore, working condition 9 is selected for further optimization.

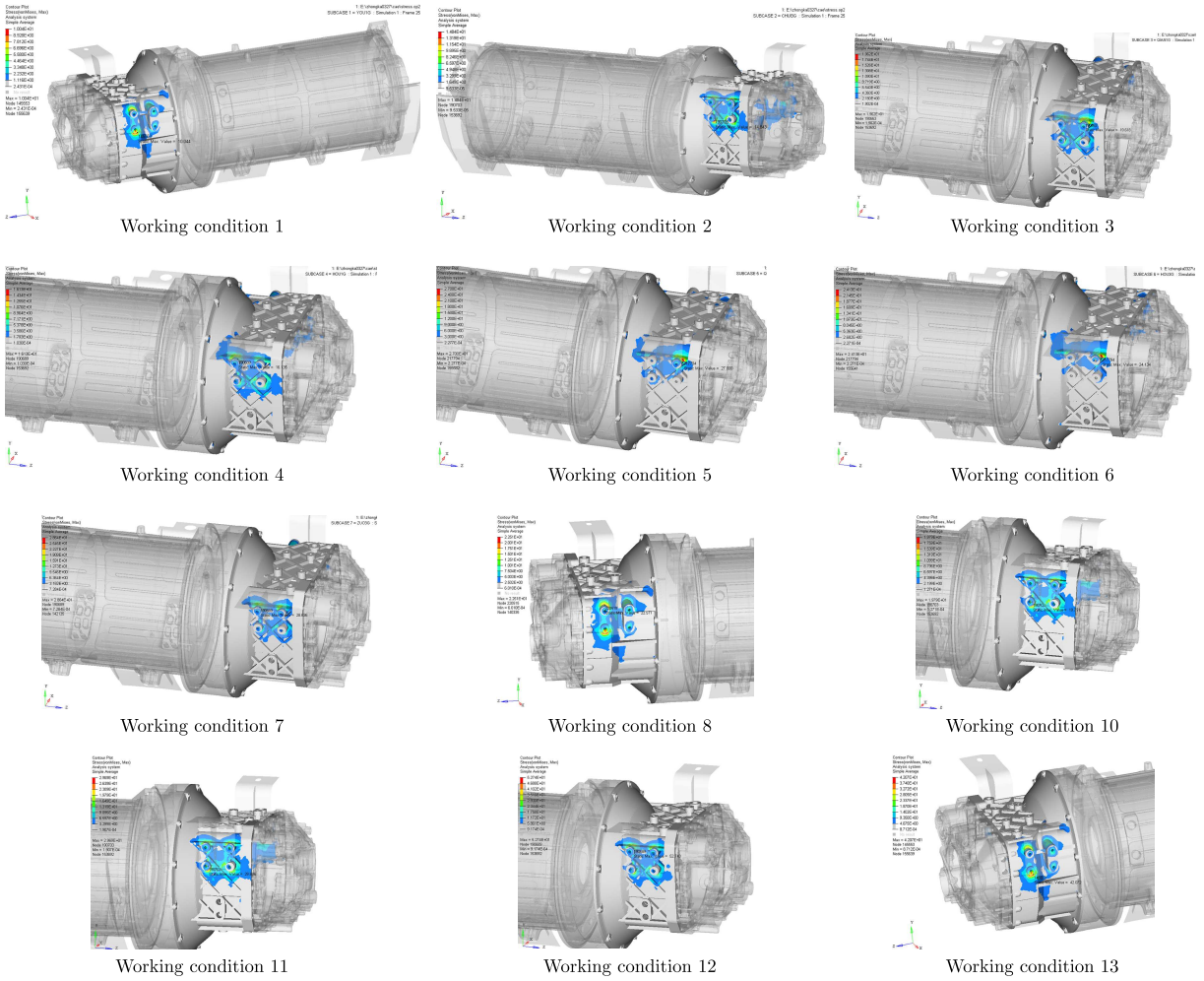

Fig. 6. Stress cloud for each working condition except for 9

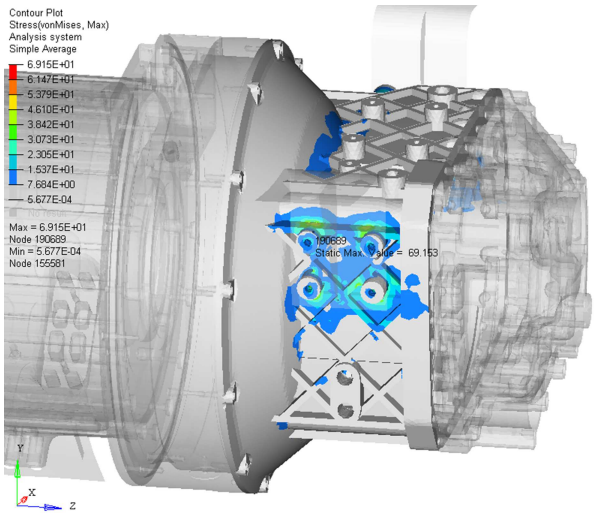

Fig. 7. Stress cloud for working condition 9

In working condition 9, if the suspension rubber pad at the suspension bracket of the gearbox is rigidized, the simulated suspension rubber pad is compressed to the limit, and the "iron touching iron" situation occurs. As it can be seen from stress cloud 9, the maximum stress of the original gearbox shell is 69.153 MPa, and the maximum stress of the gearbox shell after rigidization is 267.075 MPa, which exceeds the allowable target value for the material. Therefore, the limit gap size must be adjusted to avoid the collision between the rubber pad and the limit block, as shown in Fig. 8.

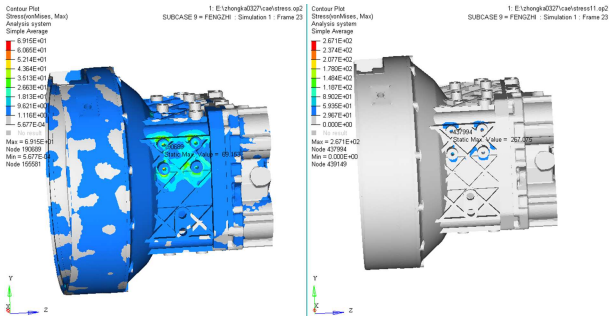

Fig. 8. Stress cloud before and after rigidization of the suspension rubber pad under working condition 9

Under working condition 9, the effect of increased length of the bolt on the case stress is analyzed. The bolt is simulated with RBE2 rigidity, the length of the bolt is increased (by about 10 mm), and the maximum stress of the gearbox case is compared and analyzed. The maximum stress of the original case is 77.064 MPa, and after the bolt is increased by 10 mm, the maximum stress of the case is 69.153 MPa, which is reduced by about 11.4%, which is shown in Fig. 9.

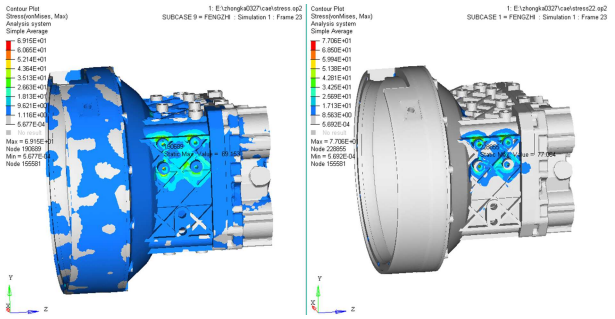

Fig. 9. Stress cloud before and after reducing the bolt length under working condition 9

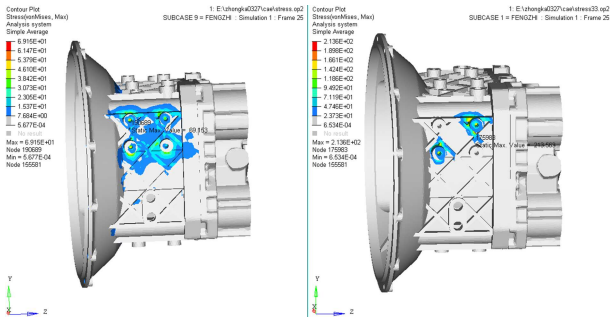

Fig. 10. Stress cloud before and after cancellation of diagonal bolts under working condition 9

The case stresses are compared and analyzed by simulating working conditions with the loss of diagonal bolts at the gearbox cases under working condition 9, as shown in Fig. 10. The maximum stress in the gearbox case when the diagonal 2 screws were not lost was 69.153 MPa,

and the stress in the gearbox case after the loss of the diagonal 2 screws was 213.563 MPa, which all exceeded the allowable target value of the material.

In summary, the limit size of the mount foot pads, the connection length of the bolts, and the number of bolt connections have a greater influence on strength of the bolt hole area of the gearbox housing. According to the simulation analysis of the limit size of the suspension foot pad, connection length of the bolts, and the number of bolt connections, these three factors have a great influence on strength of the bolt hole area of the gearbox housing.

4.3. Validation of the optimized solution

Through fault tree analysis, problems such as material defects and machining process of the gearbox shell were excluded. The causes of cracks, based on preliminary analysis of the cracking location, testing data and bracket modal analysis of the integrated support holes of the gearbox case, are: (1) the bolt length and screwing depth are not enough; (2) the bolt is loose and lost, which results in an increase of individual bolt load-bearing beyond the limit; (3) the suspension spacing is limited, resulting in "hard contact" in between.

In response to the aforementioned test and cause analysis, the following improvement and optimization measures were taken: (1) bolt length increased by 10 mm; (2) reinforcement bars at the suspension position of the shell increased; (3) height of the limit block adjusted to 8 mm, which is greater than the maximum runout under normal working conditions.

The improved scheme was imported into the model of the original scheme and strength analysis was performed. According to the results shown in Table 3, only the case under the most severe working condition 9 is compared and analyzed.

Under working condition 9, the support holes of the gearbox case were reinforced with additional ribs, and the maximum stress of the case before and after the reinforcement was compared, see Fig. 11. The original maximum stress of the gearbox case was 69.153 MPa, and the maximum stress of the gearbox case after optimization was 64.364 MPa, which was reduced by 6.9%.

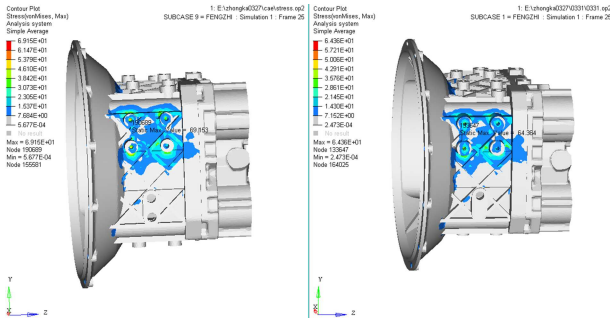

Fig. 11. Stress cloud before and after installation of additional reinforcing ribs under working condition 9

Fig. 12. Before the verification

Fig. 13. Loaded status

Figures 12 and 13 show the gearboxes before and after loading verification, respectively. The improved gearbox case has successfully completed the loading test and undergone a 50 000 km road durability test, indicating that the optimized gearbox case meets the requirements of the design target.

5. Conclusion

This paper adopts a simulation analysis method to determine the specific cause of the cracking problem at the connection hole between the gearbox case and suspension brackets by establishing a finite element analysis model for the powertrain to carry out strength analysis. According to the cause of failure, an optimization strategy of the gearbox case was proposed, and the optimized gearbox case was verified to comply with the design requirements by simulation. With the solution to this problem, we come to the following conclusions accordingly:

- The modal analysis of the suspension bracket was carried out with the help of a finite element analysis software, and the results showed that the working frequency of the bracket was staggered with the intrinsic frequency, so that the resonance could be avoided, thus excluding the cause of cracking at the connecting holes caused by non-bracket vibration.
- Based on the modal analysis of the bracket, strength analysis of the powertrain was carried out by means of finite element simulation. Inspection and testing accurately identified the cause of failure and the structure of the gearbox case was optimized. By comparing the stress of the gearbox case before and after the improvement, the effectiveness of optimization measures was verified, and the R&D cycle and cost were effectively reduced.
- The improved gearbox case the completed a road durability test of 50 000 km and reached the design target. The method proposed in this study solved practical problems for enterprises and reduced their economic losses. Currently, the product is widely used and accepted by the industry.

Acknowledgements

This research project was funded by the Major Science and Technology Special Projects in Henan "Development and Industrialization of Industrial Robot Precision Reducer" (project No. 161100210100)

and the High-level Talent Scientific Research Start-up Project of North China University of Water Resources and Electric Power "Research on Anti-fatigue Design and Manufacturing of Harmonic Reducer Based on Flexible Deformation" (project No. 201909008).

References

1. Chen D., Chen Q.SH., Deng L., et al., 2018, Optimization design analysis of a certain SUV transmission suspension bracket, *Modern Manufacturing Engineering*, **8**, 3-5
2. Dong X.L., 2011, Analysis and optimization design of transmission case cracking, *Mechanical Engineering and Automation*, **7**, 180-182
3. Fan J.D., Pan H.M., 2010, Finite element modal and experimental modal analysis of gearbox case, *Coal Mining Machinery*, **31**, 5, 92-93
4. Fu J.S., Wang J.F., Wang J., 2010, Finite element static analysis on heavy-duty truck gearbox housing, *Applied Mechanics and Materials*, **37-38**, 491-495
5. Guo M., Li B., Yang J., Liang S., 2015, Study of experimental modal analysis method of machine tool spindle system, *Journal of Vibroengineering*, **17**, 6, 3173-3186
6. Hu W.G., Liu Z.M., Liu D.K., Hai X., 2017, Fatigue failure analysis of high speed train gearbox housings, *Engineering Failure Analysis*, **73**, 57-71
7. Huang N., Chen Q., Cai G., Xu D., Zhang L., Zhao W., 2021, Fault diagnosis of bearing in wind turbine gearbox under actual operating conditions driven by limited data with noise labels, *IEEE Transactions on Instrumentation and Measurement*, **70**, 1-10
8. Jin B., Li H.P., Yan W.S., Cao M., 2021, Distributed model predictive control and optimization for linear systems with global constraints and time-varying communication, *IEEE Transactions on Automatic Control*, **66**, 7, 3393-3400
9. Korka Z.I., Gillich N., 2017, Modal analysis of helical gear pairs with various ratios and helix angles, *Romanian Journal of Acoustics and Vibration*, **14**, 91-96
10. Li J., Wang L., 2008, Finite element analysis of 1.5 MW wind power gearbox housing, *Acta Energiae Solaris Sinica*, **29**, 11, 1438-1443
11. Li L.Y., Chen Y., 2017, Research and countermeasures of transmission case cracking problem, *Research and Development*, **8**, 56-58
12. Liu C., Zhao Y., Wang Y., Zhang T., Jia H., 2021, Hybrid dynamic modeling and analysis of high-speed thin-rimmed gears, *Journal of Mechanical Design*, **143**, 12, 123401
13. Liu W.G., 2018, Analysis and improvement of front shell cracking, *Times Automotive*, **7**, 116-119
14. Liu Z.H., Gao Q.H., 2017, In-plane vibration modal analysis of heavy-loaded radial tire with a larger flat ratio, *Journal of Vibroengineering*, **19**, 7, 5327-5345
15. Shen G., Xiang D., Mou P., Jiang J., Gao L., 2014, Analysis of vibration characteristics for wind turbine gearbox, *Applied Mechanics and Materials*, **496-500**, 962-968
16. Son G.H., Kim B.S, Cho S.J., Park Y.J., 2020, Optimization of the housing shape design for radiated noise reduction of an agricultural electric vehicle gearbox, *Applied Sciences-Basel*, **10**, 23, 8414
17. Vilán J.A.V., Robleda A.S., Lago M.L., Ruiz E.C., 2010, Feasible geometrical configurations for split torque gearboxes with idler pinions, *Journal of Mechanical Design*, **132**, 12, 121011-121018
18. Walunj P.S., Chougule V.N., Mitra A.C., 2015, Investigation of modal parameters on planetary gearbox using finite element analysis to minimize vibration, *International Journal of Analytical, Experimental and Finite Element Analysis*, **2**, 4, 147-152

19. Wang H., Wu X., Zheng X., Yuan X., 2022, Virtual voltage vector based model predictive control for a nine-phase open-end winding PMSM with a common DC bus, *IEEE Transactions on Industrial Electronics (1982)*, **69**, 6, 5386-5397

20. Wang Z.W., Mei G.M., Zhang W.H., Cheng Y., Zou H., Huang G., Li F., 2018, Effects of polygonal wear of wheels on the dynamic performance of the gearbox housing of a high-speed train, *Proceedings of the Institution of Mechanical Engineers Part F – Journal of Rail and Rapid Transit*, **232**, 6, 1852-1863

21. Wilk A., Madej H., Figlus T., 2011, Analysis of the possibility to reduce vibroactivity of the gearbox housing, *Eksploatacja i Niezawodność – Maintenance and Reliability*, 42-49

22. Wu H., Wu P.B., Li F.S., Shi H., Xu K., 2019, Fatigue analysis of the gearbox housing in high-speed trains under wheel polygonization using a multibody dynamics algorithm, *Engineering Failure Analysis*, **100**, 351-364

23. Xiao B., 2021, *Research on the Dynamic Characteristics of the Transient Impact Conditions of the Electric Vehicle Powertrain Suspension System*, Ph.D. Thesis, South China University of Technology, Guang Zhou

24. Xue X.C., 2019, Analysis of the causes of fracture in automobile transmission suspension, *Failure Analysis and Prevention*, **14**, 6, 5

25. Yang J., Liu H., Ma K., Yang B., Guerrero J.M., 2022, An optimization strategy of price and conversion factor considering the coupling of electricity and gas based on three-stage game, *IEEE Transactions on Automation Science and Engineering*, **20**, 2, 878-891

26. Zhang C., Wang H., 2020, Swing vibration control of suspended structures using the Active Rotary Inertia Driver system: Theoretical modeling and experimental verification, *Structural Control and Health Monitoring*, **27**, 6, 25-43

27. Zhang Q., Du W.H., Ma W.J., et al., 2014, Finite element and experimental modal analysis of light truck transmission case, *Mechanical Design and Manufacture*, **7**, 149-151

28. Zhang X., Wang Y., Yuan X., Shen Y., Lu Z., Wang Z., 2022, Adaptive dynamic surface control with disturbance observers for battery/supercapacitor-based hybrid energy sources in electric vehicles, *IEEE Transactions on Transportation Electrification*

Manuscript received February 17, 2023; accepted for print May 25, 2023

JOURNAL OF THEORETICAL AND APPLIED MECHANICS
61, 3, pp. 545-557, Warsaw 2023
https://doi.org/10.15632/jtam-pl/166338

STUDY ON CONSTRAINT EFFECT AND CREEP CRACK INITIATION OF PLATE CONTAINING ELLIPTICAL EMBEDDED CRACKS

Dongquan Wu, Zixiang Liu, Yupeng Li, Dinghe Li

Sino-European Institute of Aviation Engineering, Civil Aviation University of China, Tianjin, China

corresponding author Dongquan Wu, e-mail: dqwu@cauc.edu.cn

Zhiqiang Zhang

Aviation Engineering Institute, Civil Aviation University of China, Tianjin, China

In this study, a plate structure containing elliptical embedded cracks loaded under high temperature is studied. The constraint effect and creep crack initiation of the plate containing embedded cracks are discussed by using the finite element method based on the creep ductility exhaustion model. It is indicated that the highest constraint level or the load-independent parameter Q^* is observed at the endpoint of the ellipse major axis of an elliptical embedded crack, and the constraint levels increase with crack length or depth, which represents a worse condition for the structure, such as higher stress concentration and greater danger of failure for a larger crack depth ratio a/t or crack length ratio a/c. Moreover, under the creep condition, the embedded crack with a larger a/t, a/c or loadings is accompanied with a higher crack driving force, which can accelerate creep damage, creep cracking initiation (CCI) and shorten the creep crack initiation (CCI) time. Additionally, an empirical prediction equation and engineering approach to the constraint parameter and the CCI time for elliptical embedded cracks are proposed, and the engineering approach to the CCI time is validated.

Keywords: elliptical embedded crack, creep crack initiation time, creep ductility exhaustion model, constraint parameter

Highlights:

(1) The constraint effect and creep crack initiation of a plate containing embedded cracks are discussed by using the finite element method based on the creep ductility exhaustion model.
(2) The highest constraint level is observed at the endpoint of the ellipse major axis of the elliptical embedded crack, and the constraint levels increase with crack length or depth, while the creep crack initiation time exhibits a contrary trend.
(3) An empirical prediction equation and engineering approach of the constraint parameter and creep crack initiation (CCI) time is proposed, and the engineering approach is validated.

1. Introduction

In recent years, the modern industrial core equipment (such as aeroengines, ultra supercritical generator sets, nuclear power generator sets, etc.) with higher energy conversion efficiency and lower pollution emission rate is vigorously developed in order to conserve energy, reduce pollution emission and protect the environment. To continuously improve energy conversion efficiency, all of the modern industrial core equipment is designed for operating under higher temperature, which will lead to increasingly harsh in-service conditions of the hot side components (Chen *et al.*, 2004).

The integrity assessment of high temperature in-service components such as power plants and aeroengines is generally inseparable from reliable prediction of creep properties and creep life. For

steam pipes, aeroengines and other structures operating in elevated temperature environment, initial defects such as cracks may occur during their processing (such as welding) or after a long time service, which will have a significant influence on components safety in the subsequent service. Creep crack initiation and creep crack propagation are important failure mechanisms for high temperature structures containing cracks, which usually leads to failure or fracture of these structures before their allowable service life (Yamamoto *et al.*, 2010; Murakami *et al.*, 1988; Zhao *et al.*, 2012). Specially, the creep crack initiation time is the critical and longest period of the whole creep life for high-temperature components. To ensure safety and reliability of high-temperature service structures, taking investigation on the creep crack initiation time is extremely important (Davies *et al.*, 2007). The creep crack initiation time is generally defined as the time when initial microcracks (or micro cavities) in the structure or material begin to connect and form the main crack under the creep condition. The generation, growth and connection processes of creep micro cavities and creep microcracks are referred as to creep damage. A large number of theories and experiments have proved that the creep cracks initiation and creep cracks propagation are the main failure forms of structures (Holdsworth, 1992).

Among the current evaluation methods of creep cracks initiation time, the finite element simulation method or an analytical prediction model based on the continuous damage approach have special advantages. The creep damage model mainly includes two types: one is the damage constitutive model based on the stress variable (Hosseini *et al.*, 2013), and the other is the damage constitutive model based on the strain variable (Yatomi *et al.*, 2004). The former typical type of model are the Kachanov Rabotnov (K-R) model (Rabotnov *et al.*, 1970) and Liu Murakami (L-M) model (Liu and Murakami, 1998). For example, Mao *et al.* (2004), You *et al.* (2004) and Chen *et al.* (2014) used K-R and L-M models to analyze creep damage and creep life prediction of materials and structures by the finite element method, respectively, which allowed obtaining satisfactory research results. In the latter type of model, the classic creep ductility exhaustion model proposed by Cocks and Ashby (1980) adopts one single parameter as the damage variable and involves few material parameters, so the model is simple and convenient to be applied in engineering fields. The basic principle of the damage model is that when the cumulative creep strain of a micro-element on the material reaches the creep fracture strain (or creep ductility), it is considered that the damage of this micro-element reaches the critical value and fails. Riedel and Rice (1980) were first to propose a definition of the creep crack initiation time under steady state creep by using the critical equivalent strain produced at a specified distance, that is, when all the microelements at a given distance fail, it is considered that the creep crack initiation time has been reached. Davies (2006) established a prediction method of creep crack initiation time under different stress states based on the creep ductility exhaustion model, Norton's constitutive law and crack tip fracture parameters. Among these theoretical models, the accuracy of the model under transient creep condition was the best.

Wu *et al.* (2020) then applied the C^*-Q^* two parameter method of the crack tip stress field considering constraint parameters into the damage model, and proposed a two parameter prediction approach of the creep crack initiation time. Because of considering the influence of the constraint effect, this approach could be well applied to predict the creep crack initiation time for different structures containing cracks. However, this prediction model is only applied to predict the creep crack initiation time for some standard laboratory specimens or specific pipeline structures containing surface cracks, while its applicability to other structures containing other kinds of cracks needs further study.

The constraint effect refers to the influence of such factors as size and shape of a specimen, crack size and loading configuration on the analytical stress field or strain field at the crack tip, which will further affect the predicting accuracy of creep crack damage or creep crack life. The results of theoretical and experimental studies showed that the geometrical shape, size and loading configurations could all have different effects on the process of creep crack initiation,

crack propagation and creep failure. For this reason, the HRR field based on a single parameter cannot accurately characterize the stress field at the crack tip for different cracked structures (Shih and German, 1981). In order to establish a theoretical modification to accurately describe the stress field at the crack tip, researchers have focused on various two-parameter models of the stress field considering the constraint effect which is suitable for elasto-plastic or creep conditions. Budden and Ainsworth (1999) proposed an in-plane constraint parameter Q suitable for high temperature conditions, and the C^*-Q two-parameter model describing the stress field at the creep crack tip for a high-temperature cracked structure. Xu *et al.* (2016) proposed a load--independent constraint parameter Q^*, and the C^*-Q^* two-parameter creep stress field applicable to structures containing surface cracks at elevated temperature.

At present, the creep crack growth behavior is mainly focused on two-dimensional through--wall specimen cracks and surface cracks, but the research on embedded cracks is relatively rare, while the embedded cracks are difficult to detect before failure and they are especially dangerous crack types. Therefore, it is of great significance to investigate the distribution of creep stress, creep damage, constraint effect and creep life for structures containing embedded cracks. In this paper, based on a typical creep ductility exhaustion model, the finite element method is used to simulate the creep damage of the plate structure containing embedded cracks. The distribution law of the load-independent constraint parameter Q^* along the crack front and the influence of crack size on the creep crack initiation time are analyzed. Finally, the engineering prediction methods of the constraint parameter Q^* and creep crack initiation time are established by fitting a mathematical relationship between the constraint parameter Q^* and creep crack initiation time as well as geometrical sizes of embedded cracks (i.e. crack length ratio a/c and crack depth ratio a/t). The study provides a technical support and theoretical basis for creep crack life assessment of high temperature service components containing embedded cracks.

2. Methodology

2.1. Creep ductility exhaustion approach

In this study, the strain-based creep ductility exhaustion approach proposed by Cocks and Ashby (1980) is used to evaluate creep damage ahead of the crack tip. The typical form of the creep damage rate can be described as follows

$$\dot{\omega} = \frac{\dot{\varepsilon}_c}{\varepsilon_f^*} \tag{2.1}$$

where $\dot{\varepsilon}_c$ and ε_f^* are the creep strain rate and multiaxial creep ductility, respectively. For the creep strain rate, Norton model is adopted

$$\dot{\varepsilon}_c = A\sigma^n \tag{2.2}$$

The multiaxial creep ductility can be obtained by multipying the uniaxial creep ductility and multiaxial creep ductility factor ($MCDF$)

$$\varepsilon_f^* = MCDF\varepsilon_f \tag{2.3}$$

where the uniaxial creep ductility is generally taken as a constant, and multiaxial creep ductility factor ($MCDF$) can be effectively assessed by the Wen-Tu model (Wen and Tu, 2014)

$$MCDF = \frac{\exp\left(\frac{2}{3}\frac{n-0.5}{n+0.5}\right)}{\exp\left(2\frac{n-0.5}{n+0.5}h\right)} \tag{2.4}$$

where h is the stress triaxiality which can be calculated by

$$h = \frac{\sigma_m}{\overline{\sigma}} \tag{2.5}$$

where σ_m is hydrostatic stress and $\overline{\sigma}$ is equivalent stress.

The above creep ductility exhaustion model can be compiled into Abaqus software as a Creep subroutine using Fortran language. When submitting the finite element simulation, the subroutine is loaded into the finite element model through the relevant interface for calculation, so as to realize the simulation of creep damage (Wu *et al.*, 2020). In this study, the creep crack initiation (CCI) time is defined as the time when the damage value ω at 0.05 mm ahead of the crack tip reaches unity (Murakami *et al.*, 1988). These CCI data are extracted from the output of finite element simulation results.

In this study, the material properties of P92 heat-resistant steel under 650°C in-service temperature are used in the finite element model, and P92 steel is widely used in ultra supercritical units. The details of the mechanical properties of P92 steel at 650°C are summarized in Table 1, where mainly elasto-plastic and creep parameters are given (Wu *et al.*, 2020). The uniaxial creep ductility is taken as a constant of 20%, as used in reference (Wu *et al.*, 2020).

Table 1. Material properties of P92 steel at 650°C

Young modulus E [MPa]	Yielding stress σ_0 [MPa]	Creep coefficient A [MPa^{-n}h^{-1}]	Creep exponent n	Uniaxial creep ductility ε_f [%]
125000	180	$2.6353 \cdot 10^{-16}$	5.23	20

2.2. Constraint parameter

Budden and Ainsworth (1999) proposed an in-plane constraint parameter Q suitable for high temperature conditions, as well as a C^*-Q two-parameter model describing the stress field

$$\sigma_{ij} = \sigma_0 \Big(\frac{C^*}{\dot{\varepsilon}_0 \sigma_0 I_n r} \Big)^{\frac{1}{n+1}} \widetilde{\sigma}_{ij}(\theta; n) + Q \sigma_0 \delta_{ij} \tag{2.6}$$

where C^* integral represents the fracture parameter under a steady state creep condition at the crack front, which is extracted from the finite element simulation results. $\dot{\varepsilon}_0$ and σ_0 are the normalized creep strain rate and yield stress, respectively. r is the distance away from the crack tip, and θ is the angle between the crack direction and research position. $\widetilde{\sigma}_{ij}(\theta; n)$ is a dimensionless function of n and θ, and I_n is a parameter related to the creep stress-hardening exponent n. δ_{ij} is the Kronecker delta function ($\delta_{ij} = 1$ for $i = j$ and $\delta_{ij} = 0$ for $i \neq j$). The constraint parameter Q is always determined by the difference of crack opening stress between the specimen structure and the analytical creep stress field

$$Q = \frac{\sigma_{22}^{FEM}(r, 0) - \sigma_{22}(r, 0)}{\sigma_0} \tag{2.7}$$

where $\sigma_{22}^{FEM}(r, 0)$ is the crack opening stress obtained from finite element simulation, and $\sigma_{22}(r, 0)$ is the theoretical creep stress field calculated by

$$\sigma_{ij} = \sigma_0 \Big(\frac{C^*}{\dot{\varepsilon}_0 \sigma_0 I_n r} \Big)^{\frac{1}{n+1}} \widetilde{\sigma}_{ij}(\theta; n) \tag{2.8}$$

Xu *et al.* (2016) then proposed a load-independent constraint parameter Q^* and a C^*-Q^* two--parameter creep stress field

$$Q^* = \left(\frac{C^*}{\dot{\varepsilon}_0\sigma_0 I_n L}\right)^{\frac{-1}{n+1}} Q = \left(\frac{C^*}{\dot{\varepsilon}_0\sigma_0 I_n L}\right)^{\frac{-1}{n+1}} \frac{\sigma_{22}^{FEM}(r,0) - \sigma_{22}(r,0)}{\sigma_0}$$
$$\frac{\sigma_{ij}}{\sigma_0} = \left(\frac{C^*}{\dot{\varepsilon}_0 L I_n \sigma_0}\right)^{\frac{1}{n+1}} \left[\left(\frac{L}{r}\right)^{\frac{1}{n+1}} \widetilde{\sigma}_{ij}(\theta;n) + Q^*_{RRss}\delta_{ij}\right] \tag{2.9}$$

where L is the normalized length generally set as 1 mm (Xu *et al.*, 2016).

In this study, the mechanical parameters of P92 steel at 650°C are used, and more related high temperature properties are summarized in Table 2.

Table 2. Mechanical parameters of P92 steel at 650°C

Normalized creep strain rate $\dot{\varepsilon}_0$ [1]	Constant parameter I_n	Dimensionless function $\widetilde{\sigma}_{ij}(\theta;n)$	Normalized length L [mm]
$8.8183 \cdot 10^{-5}$	4.99	0.48	1

2.3. Finite element method

A flat plate structure containing embedded cracks is used as the research objective in this study. In general, non-penetration cracks are usually simplified as elliptical in engineering applications, as shown in Fig. 1. According to symmetry of the plate structure, only one eighth of the plate structure is taken in the finite element model for simulation. The three-dimensional finite element model is shown in Fig. 2. The length, width and thickness of the model are 50 mm, 15 mm and 2.5 mm ($= t/2$), respectively. a is a half of the crack depth of the elliptical crack along the thickness direction of the plate, and c is a half of the crack length along the width direction of the plate. In order to conveniently characterize the distribution of constraint parameters at the front of elliptical crack, the angle between the center of the ellipse and any point on the elliptical crack front is denoted as Φ. For convenience of describing the position of the research point, the center of the elliptical crack is taken as the origin, of which $2\Phi/\pi = 0$ represents the rightmost endpoint of the elliptical crack, where there is a intersection of the elliptical crack and the center line of the plate. $2\Phi/\pi = 1$ represents the uppermost endpoint of the elliptical crack, which is the shallowest position of the elliptical crack in the structural thickness direction. Note that in this study, the center of the elliptical crack is just set in the center position of the plate structure. According to the symmetry, symmetrical constraints are set in the three symmetry planes, respectively, and the uniformly distributed load along the length direction is set in the section where it is far from the crack end to realize the loading process, as shown in Fig. 2.

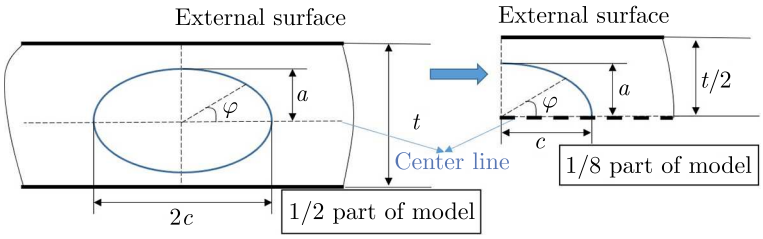

Fig. 1. Geometrical illustrations of the plate structure containing an embedded crack

Figure 3 shows mesh distribution of the three-dimensional finite element model of the plate structure containing the elliptical embedded crack. The area around the crack front adopts a local refined mesh with the minimum mesh size of 0.01 mm. This is to ensure that it is easy to

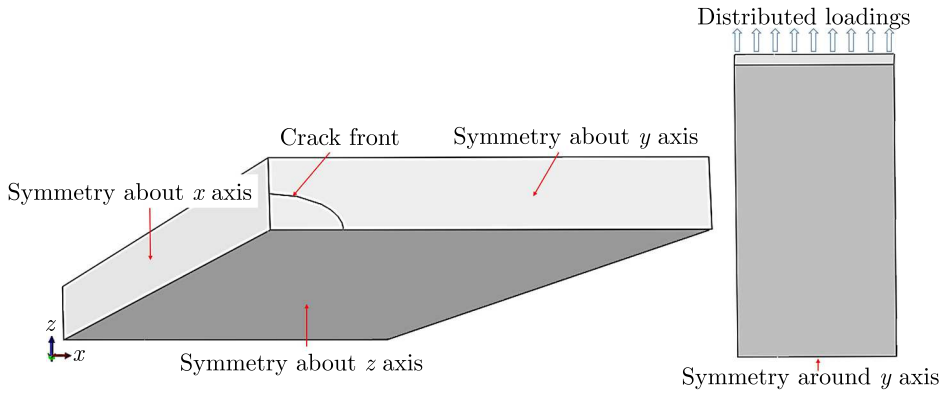

Fig. 2. 1/8 finite element model of the plate structure containing an embedded crack

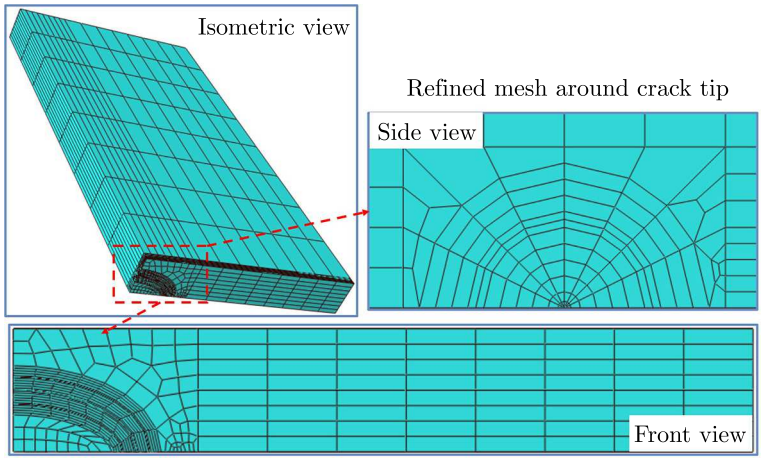

Fig. 3. Mesh of the finite element model of the plate structure containing an embedded crack

obtain the critical distance in the FE model (Wu *et al.*, 2020) for extracting the creep initiation time. The mesh size at other locations is about 0.1 mm-2 mm. The element type of the eight node reduced integral (C3D8R) element is adopted for the model, which exhibits good mechanical calculation accuracy for three-dimensional solid models. The total number of elements of all finite element models with different embedded crack sizes is similar (Wu *et al.*, 2020), because the finite element models use the same mesh refinement size near the crack tip. The total number of elements is about 1800-2100, and the total number of nodes is about 2500-2700.

3. Results and discussion

3.1. Results and analysis of constraint parameters

In order to avoid the influence of the plastic zone ($r < 0.1$ mm) around the crack tip and to ensure that the value of r is within the effective zone of stress concentration at the crack tip, the constraint parameter Q^* is defined by referring to the fixed distance $r = 0.2$ mm (Wu *et al.*, 2020; Xu *et al.*, 2016), and then a large Q^* value can be obtained to ensure the accuracy of calculation, as shown in Fig. 4.

Figure 5 compares the distribution of the constraint parameter Q^* varied with the angle position ($0 \leqslant 2\Phi/\pi \leqslant 1$) ahead of the elliptical crack front with the crack depth ratio $a/t = 0.25$ and the crack length ratio $a/c = 0.5$, 0.7, 1.0, 1.2, 1.5. It can be seen from the figure that at the position of $2\Phi/\pi = 1$, i.e the intersection point of the crack front and the center line of the plate

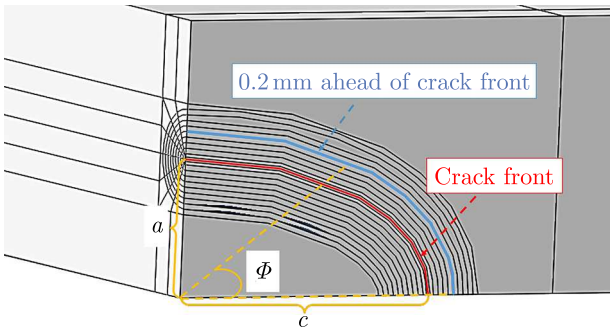

Fig. 4. Research position of the constraint parameter

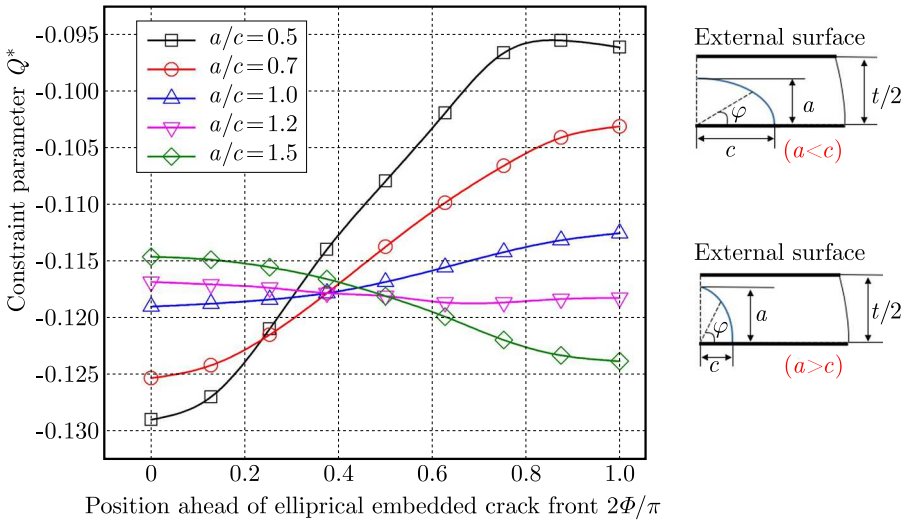

Fig. 5. Distributions of the constraint parameter ahead of the crack front for embedded cracks with various a/c and $a/t = 0.25$

or the rightmost endpoint of the elliptical crack, the constraint parameter Q^* decreases with an increase of the crack length ratio a/c, while at the position of $2\Phi/\pi = 0$, i.e the shallowest position of the crack in the thickness direction of the plate or the uppermost endpoint of the elliptical crack, the constraint parameter Q^* increases with the crack length ratio a/c.

In addition, for an elliptical embedded crack with the same crack depth ratio a/t, the distribution of the maximum constraint parameter Q^* is affected by the crack length ratio a/c. For the elliptical embedded crack with the transverse length c larger than the longitudinal length a (i.e. $a/c \leqslant 1.0$, refers to the three curves with $a/c = 0.5$, 0.7 and 1.0 in Fig. 5), the long axis of the elliptical crack front is distributed laterally (the shape of the elliptical crack is shown at the top right in Fig. 5), and the maximum value of the constraint parameter Q^* is distributed at the position of $2\Phi/\pi = 1$ (i.e. the uppermost endpoint of the elliptical crack front), and the constraint parameter Q^* at the position $2\Phi/\pi = 0$ (i.e. the rightmost endpoint of the elliptical crack front) is the minimum. For the elliptical embedded crack with the transverse length c less than the longitudinal length a (i.e. $a/c \geqslant 1.0$, refers to the three curves with $a/c = 1.2$ and 1.5 at the bottom right in Fig. 5), the long axis of the elliptical crack front is longitudinally distributed (the shape of the elliptical crack is shown at the top right in Fig. 5), and the maximum value of the constraint parameter Q^* is distributed at the position of $2\Phi/\pi = 0$ (i.e. the rightmost endpoint of the elliptical crack front), and the constraint parameter Q^* at the position $2\Phi/\pi = 1$ (i.e. the uppermost endpoint of the elliptical crack front) is the minimum.

Therefore, the maximum constraint level around the crack front always appears near the endpoint of the actual major axis of the elliptical crack, while the minimum constraint level

always appears at the endpoint of the actual minor axis of the elliptical crack, no matter whether the major axis is distributed laterally or longitudinally. This phenomenon is caused by the maximum crack propogation under tension at the end of the long axis of the crack. Briefly, with an increase of the crack length ratio a/c, the constraint parameter at the end of the long axis of the elliptical crack increases continuously, which means that the stress concentration here is more severe, the material here is more endangered, and creep crack initiation occurs first. Such conclusions are similar to those of other researchers on the distribution of constraint parameters of semi elliptical surface cracks (Wu *et al.*, 2020; Xu *et al.*, 2016).

Taking the relevant data at the location where creep initiation is most likely to occur, the relationship between the constraint parameter Q^* and crack length a/c can be established with a fixed crack depth $a/t = 0.25$. The specific formula obtained after fitting is as follows

$$Q^* = \alpha + (1-\alpha)\Big\{1 - \exp\Big[-\beta_1 \frac{a}{c} - \beta_2 \Big(\frac{a}{c}\Big)^2 - \beta_3 \Big(\frac{a}{c}\Big)^3\Big]\Big\} \tag{3.1}$$

where α, β_1, β_2 and β_3 are fitting coefficients respectively, and the corresponding values are $\sigma = -3.273 \cdot 10^{-1}$, $\beta_1 = 7.323 \cdot 10^{-1}$, $\beta_2 = -9.20 \cdot 10^{-1}$, $\beta_3 = 3.566 \cdot 10^{-1}$. The constraint parameters at other positions also basically satisfy this formula, but coefficients are different.

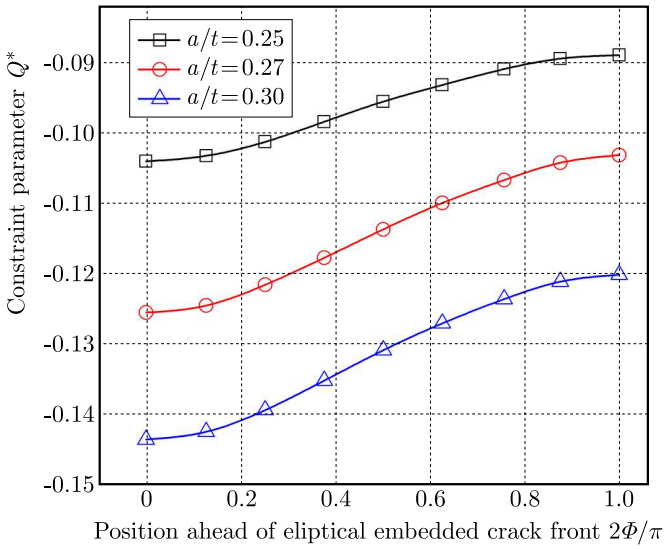

Fig. 6. Distributions of the constraint parameter ahead of the crack front for cracks with various depths with $a/c = 0.7$

Figure 6 compares the distribution of the constraint parameter Q^* varied with the angle position ($0 \leqslant 2\Phi/\pi \leqslant 1$) ahead of the elliptical crack front with the crack length ratio $a/c = 0.7$ and depth ratio $a/t = 0.25$, 0.30, 0.35, 0.40. It can be concluded that the variation of crack depth ratio a/t has a negative correlation with the constraint parameter Q^* around the crack front, that is, the larger the crack longitudinal length a is, the smaller the constraint parameter Q^* is. This is due to the fact that with an increase of a, the outline of elliptical crack front is closer to a circle, and the tension stress will be smaller at the endpoint of the crack front. Since the model is only 1/8 part of the plate structure, the critical crack size must meet $a/t < 0.5$ according to the actual value of a and t (that is, the crack length a in the plate thickness direction cannot exceed half of the plate thickness $t/2$). By analyzing each group of data of the constraint parameter with a fixed depth ratio, it can be found that the change of the constraint parameter Q^* varies with the angle $2\Phi/\pi$ showing an upward trend, which is similar with what discussed in Fig. 5. For the elliptical embedded crack with $a/c \leqslant 1.0$, the maximum value of the constraint parameter Q^* is distributed at the position of $2\Phi/\pi = 1$, and for the elliptical embedded crack with $a/c \geqslant 1.0$,

the maximum value of the constraint parameter Q^* is distributed at the position of $2\Phi/\pi = 0$. Additionally, with an increase of the crack depth ratio a/t, the constraint parameter at the deepest point of the crack (the endpoint of the long axis of the elliptical crack) is larger, which means that the stress concentration is more serious and the location is more dangerous.

3.2. Results and analysis of creep crack initiation

To study creep damage accumulation along the elliptical embedded crack front and to determine creep crack initiation time, it is necessary to define the critical distance ahead of the crack tip, which will be used in the finite element model to obtain the damage value and creep crack initiation time. The definition of the critical location of creep crack initiation time should follow the detailed principles: (i) firstly to determine the angle $2\Phi/\pi$ ahead of the crack front (that is, the maximum angle position of the constraint parameter obtained from analysis in the previous Section), (ii) then a critical distance away from the crack front also needs to be chosen as the research position of the creep crack initiation process, which is generally selected as the characteristic grain size of P92 heat-resistant steel about $d = 0.05$ mm. The details are depicted by using the example shown in Fig. 7.

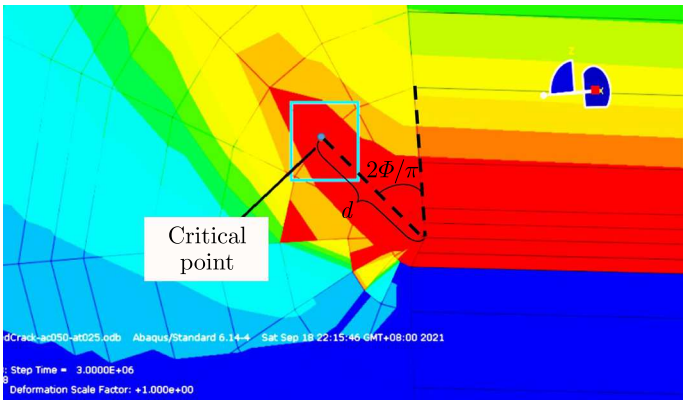

Fig. 7. Definition of the critical position of creep crack initiation time in the FE model

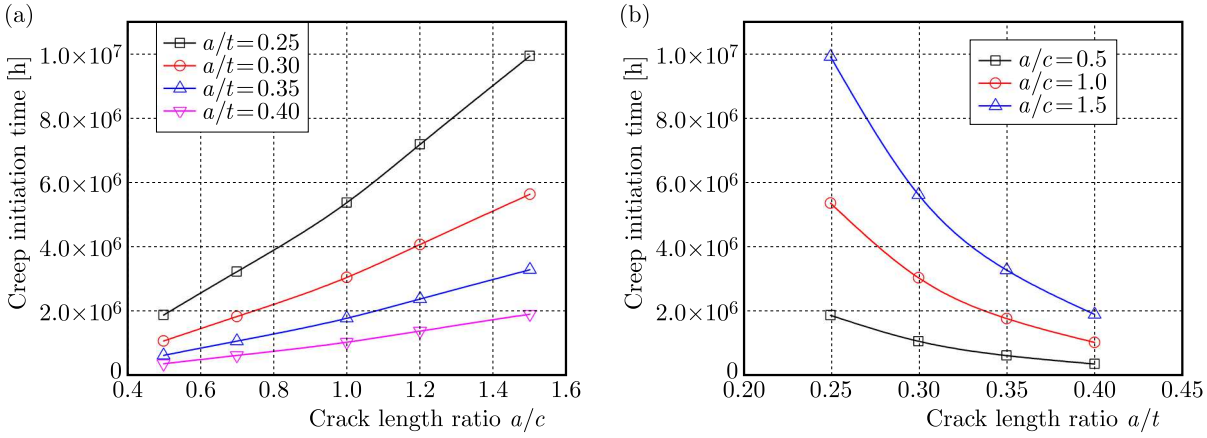

Fig. 8. Variations of the creep crack initiation time with: (a) a/c, (b) a/t

Figure 8a compares the relationship between the crack length ratio a/c and the creep crack initiation time when the crack depth ratio a/t is fixed. The results show that the creep crack initiation time decreases with a decrease of the crack length ratio a/c, which is similar with the change of constraint levels. Figure 8b compares the relationship between the crack depth

ratio a/t and the creep crack initiation time when the crack length ratio a/c is fixed. With an increase of crack depth ratio a/t, the creep crack initiation time is shortened, which also keeps consistent with the change of the constraint level. Therefore, it can be indicated that the longer the crack length and the deeper the crack depth are, the stronger the constraint effect ahead of the crack front is, the faster accumulation of creep damage and creep crack cracking, as well as the shorter the creep crack initiation time, and the more endangered the structure. Note that in this Section, the constant distributed load of 30 MPa is applied for different sizes of embedded cracks.

Meanwhile, it can be found from Fig. 8 that the relationship between the creep crack initiation time t_i and crack depth ratio a/t meets an exponential law. By fitting the data in Fig. 8a, the engineering calculation method between the creep crack initiation time t_i and crack depth ratio a/t under different crack length ratio a/c can be established respectively

$$t_i = \begin{cases} 3E + 7\exp\left(-11.06\dfrac{a}{t}\right) & \text{for} \quad \dfrac{a}{c} = 0.5 \\ 8E + 7\exp\left(-11.05\dfrac{a}{t}\right) & \text{for} \quad \dfrac{a}{c} = 1.0 \\ 2E + 8\exp\left(-11.05\dfrac{a}{t}\right) & \text{for} \quad \dfrac{a}{c} = 1.5 \end{cases} \tag{3.2}$$

It can be found that the above formulas are basically similar, so the engineering calculation method between the creep crack initiation time t_i and crack depth ratio a/t can be summarized by a unified expression

$$t_i = A\exp\left(B\frac{a}{t}\right) \tag{3.3}$$

where the exponent terms of the formula are basically the same $-11.05a/t$, that is, the exponent coefficient $B = -11.05$. The coefficient term A of the formula is related to the crack length ratio a/c. The relationship between A and a/c basically meet an exponential law, and it can be fitted as follows

$$A = 1E + 7\exp\left(1.8971\frac{a}{c}\right) \tag{3.4}$$

By taking Eq. (3.4) into Eq. (3.3), the relationship between the creep crack initiation time t_i and crack depth ratio a/t as well as crack length ratio a/c can be further written as

$$t_i = \left[1E + 7\exp\left(1.8971\frac{a}{c}\right)\right]\exp\left(-11.05\frac{a}{t}\right) \tag{3.5}$$

In addition, the variation of creep crack initiation time under different loads is also studied. Taking the model with crack sizes of $a/c = 0.5$, $a/t = 0.3$ as an example, the simulation results of the creep crack initiation time for different loads are shown in Fig. 9. It is obvious that, with an increase of load P, the creep crack initiation time of the plate structure decreases gradually, and it changes linearly in the logarithmic coordinate. Based on the findings, we can draw a conclusion that the load is an important factor which leads to a rapid increase of creep damage and a reduction of creep life of the plate structure containing an elliptical embedded crack.

Moreover, it can be found that the relationship between creep crack initiation time t_i and load P satisfies the exponential relationship, namely, the engineering calculation method for the creep crack initiation time and load can be expressed by the following formula

$$t_i = 1.263E + 9\exp(-0.23P) \tag{3.6}$$

Since the curves for creep crack initiation time t_i against the load P under different crack sizes are similar and show the exponential law, the relationship between creep the crack initiation

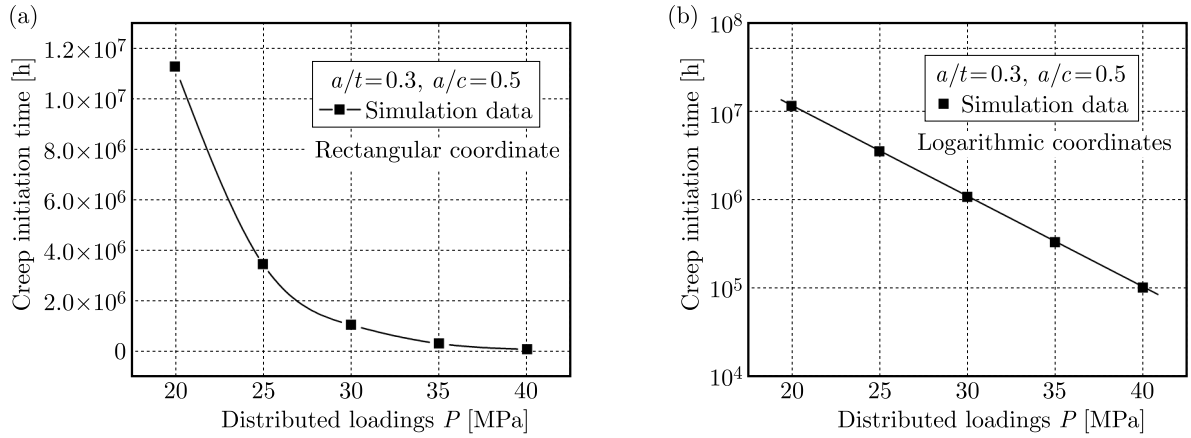

Fig. 9. Variations of the creep crack initiation time under different loadings: (a) in rectangular coordinate, (b) in logarithmic coordinate

time and crack depth ratio a/t as well as crack length ratio a/c and load P can be established by referring to Eq. (3.5) and Eq. (3.6)

$$t_i = 1.124E + 8\exp\Big(0.94855\frac{a}{c} - 5.525\frac{a}{t} - 0.115P\Big) \tag{3.7}$$

Based on the above engineering prediction formula, the creep crack initiation time of the plate structure containing the elliptical embedded crack with a specified crack size and load can be predicted. In the following study, four groups of non-fitting data of plate structures with embedded cracks are selected for finite element simulation as summarized in Table 3, and the results are compared with the calculation results of the engineering prediction formula, see Fig. 10. It can be found that the engineering predictions for different control groups have better accuracy than the simulation results, and the error can be kept within ±5%, which verifies the validity of the engineering prediction formula for the creep crack initiation time.

Table 3. Comparison of creep crack initiation times between FE results and predictions for different conditions

Specimen	Parameter					
	a/t	a/c	P [MPa]	Simulation results [h]	Predictions from equation [h]	Error [%]
1	0.32	0.8	23	$2.997 \cdot 10^6$	$2.911 \cdot 10^6$	−2.8
2	0.38	1.2	38	$5.329 \cdot 10^5$	$5.437 \cdot 10^5$	2.0
3	0.38	0.8	38	$3.795 \cdot 10^5$	$3.721 \cdot 10^5$	−1.9
4	0.32	1.2	23	$4.167 \cdot 10^6$	$4.252 \cdot 10^6$	2.0

4. Conclusion

In this study, a high temperature plate structure containing elliptical embedded cracks is taken as the research object. Based on the creep ductility exhaustion model, the constraint effect and creep crack initiation times are studied by using the three-dimensional (3D) finite element method. The results show that:

- When the crack depth ratio a/t is fixed, with an increase of the crack length ratio a/c, the constraint parameter near the shallowest point of the crack front (about $2\Phi/\pi = 1$) increases continuously. Whether the major axis of an elliptical crack is distributed transversely or

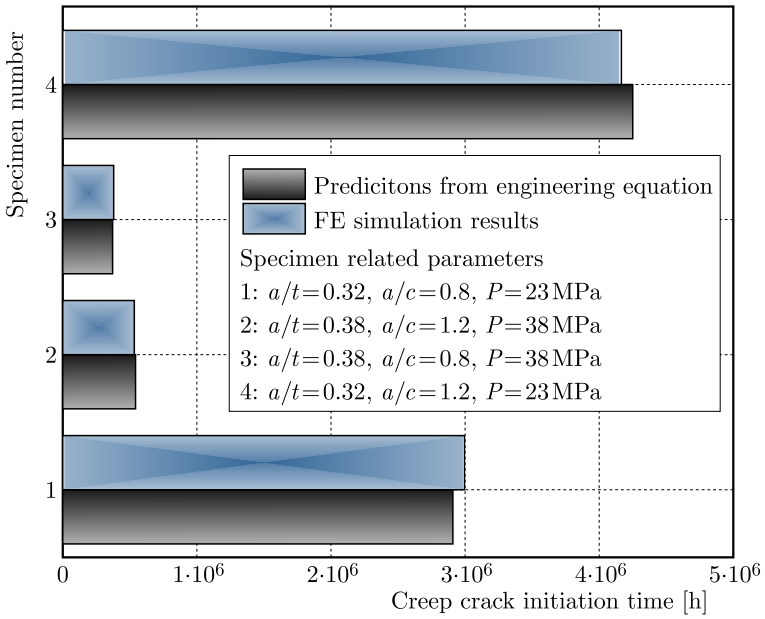

Fig. 10. Comparison of creep crack initiation times between FE results and predictions for different conditions

longitudinally, the maximum constraint level always appear at the endpoint of the actual major axis of the elliptical crack, and the minimum constraint level always appear at the end of the minor axis. When the crack length a/c is fixed, the constraint parameter decreases with an increase of the crack depth ratio a/t, which is due to the fact that the outline of the crack is close to circular.

- With a decrease of the crack length ratio a/c or an increase of the crack depth ratio a/t, the creep crack initiation times decrease significantly. That is, with an increase of the transverse crack length c or the longitudinal crack length a, the creep damage accumulation rate increases, the creep crack initiation time shortens, and the lower the safety of the plate structure is , the easier the creep crack propagation cracking occurs.
- The empirical relationship between the constraint parameter Q^* and embedded crack length and depth is established. The engineering prediction method of creep crack initiation times is also established and validated with the influence of the embedded crack length, crack depth as well as load taken into consideration.

Acknowledgements

The authors would like to acknowledge the support from the Scientific Research Program of Tianjin Education Commission (Grant No. 2021KJ053).

References

1. Budden P.J., Ainsworth R.A., 1999, The effect of constraint on creep fracture assessments, *International Journal of Fracture*, **97**, 1, 237-247
2. Chen L., Jiang T., Xie L., 2004, Overview of life prediction methods for turbine blades under creep fatigue interaction, *Aviation Manufacturing Technology*, **12**, 61-64
3. Chen X., Zhou G., Tu S., 2014, Finite element analysis of creep crack propagation of T-type brazing joints, *Journal of Mechanical Strength*, **5**, 790-796
4. Cocks A.C.F., Ashby M.F., 1980, Intergranular fracture during power-law creep under multi-axial stresses, *Metal Science*, **14**, 8/9, 395-402

5. Davies C.M., 2006, *Crack Initiation and Growth at Elevated Temperatures in Engineering Steels*, Department of Mechanical Engineering, Imperial College London, 1-200
6. Davies C.M., O'Dowd N.P., Nikbin K.M., Webster G.A., 2007, An analytical and computational study of crack initiation under transient creep conditions, *International Journal of Solids and Structures*, **44**, 1823-1843
7. Holdsworth S.R., 1992, Initiation and early growth of creep cracks from pre-existing defects, *Material High Temperature*, **10**, 127-137
8. Hosseini E., Holdsworth S., Mazza E., 2013, Stress regime-dependent creep constitutive model considerations in finite element continuum damage mechanics, *International Journal of Damage Mechanics*, **22**, 8, 1186-1205
9. Liu Y., Murakami S., 1998, Damage localization of conventional creep damage models and proposition of a new model for creep damage analysis, *JSME International Journal Series A*, **41**, 1, 57-65
10. Mao X., Liu Z., Yang K., *et al.*, 2004, Creep damage calculation model based on time-harden theory, *Journal of Mechanical Strength*, **26**, 1, 105-108
11. Murakami S., Kawai M., Rong H., 1988, Finite element analysis of creep crack growth by a local approach, *International Journal of Mechanical Sciences*, **30**, 7, 491-502
12. Rabotnov Y.N., Leckie F.A., Prager W., 1970, Creep problems in structural members, *Journal of Applied Mechanics*, **37**, 1, 249
13. Riedel H., Rice J.R., 1980, Tensile cracks in creeping solids, *ASTM STP 700, American Society for Testing and Materials*, **1**, 112-130
14. Shih C.F., German M.D., 1981, Requirements for a one parameter characterization of crack tip fields by the HRR singularity, *International Journal of Fracture*, **17**, 27-43
15. Wen J.F., Tu S.T., 2014, A multiaxial creep-damage model for creep crack growth considering cavity growth and microcrack interaction, *Engineering Fracture Mechanics*, **123**, 197-210
16. Wu D.Q., Jing H.Y., Xu L.Y., 2020, Engineering application of enhanced C^*-Q^* two parameter approaches for predicting creep crack initiation times, *European Journal of Mechanics - A/Solids*, **82**, 104013
17. Xu L.Y., Zhang X.F., Zhao L., Han Y., Jing H., 2016, Quantifying the creep crack-tip constraint effects using a load-independent constraint parameter Q^*, *International Journal of Mechanical Sciences*, **119**, 320-332
18. Yamamoto M., Miura N., Ogata T.K., 2010, Applicability of C^* parameter in assessing Type IV creep cracking in Mod. 9Cr-1Mo steel welded joint, *Engineering Fracture Mechanics*, **77**, 15, 3022-3034
19. Yatomi M., Bettinson A.D., O'Dowd N.P., Nikbin K.M., 2004, Modelling of damage development and failure in notched-bar multiaxial creep tests, *Fatigue and Fracture of Engineering Materials and Structures*, **27**, 4, 283-295
20. You Y., Ling X., Tu S., 2004, Finite element analysis of creep damage of small punch test specimen at elevated temperature, *Journal of Mechanical Strength*, **26**, 2, 183-187
21. Zhao L., Jing H., Xu L., Han Y., Xiu J., 2012, Analysis of creep crack growth behavior of P92 steel welded joint by experiment and numerical simulation, *Materials Science and Engineering A*, **558**, 119-128

Manuscript received October 31, 2022; accepted for print April 17, 2023

JOURNAL OF THEORETICAL AND APPLIED MECHANICS
61, 3, pp. 559-571, Warsaw 2023
https://doi.org/10.15632/jtam-pl/168072

BUCKLING AND VIBRATION OF POROUS SIGMOID FUNCTIONALLY GRADED CONICAL SHELLS

Xiaolin Huang, Jiaheng Wang, Nengguo Wei, Chengzhe Wang, Bin Ma
School of Architecture and Transportation Engineering, Guilin University of Electronic Technology, Guilin, China
corresponding author Bin Ma, e-mail: 780227067@qq.com

In this study, the buckling and vibration of a sigmoid functionally graded material (S-FGM) shells are investigated. Two types of porosity distributions, even and uneven, are taken into account. The material properties are estimated by a new modified rule of mixture. In the framework of the classic thin shell theory, the governing equations are derived and Galerkin's integrate technique is employed to compute the critical load and natural frequency of porous S-FGM shells. The influence of pores, ceramic mass fraction and materials power index are discussed in detail.

Keywords: functionally graded materials, pore, conical shell, buckling, vibration

1. Introduction

In the past two decades, many studies have been devoted to the buckling and vibration of functionally graded conical shells (Sofiyev, 2019). Sofiyev and his coauthors have made a prominent contribution to those studies. By using the Donnell shell theory and the Galerkin method, they obtained a series of analytical solutions to buckling loads and lowest natural frequencies of non-homogeneous orthotropic conical shells (Sofiyev *et al.*, 2009a), FGM cylindrical shells (Sofiyev, 2007; Sofiyev and Kuruoglu, 2014), FGM conical shells (Sofiyev, 2009; Sofiyev and Schnack, 2012), and FGM hybrid truncated shells (Sofiyev *et al.*, 2008a,b; Sofiyev, 2019) subjected to mechanical and thermal loads. In their studies, two-parameter elastic foundations were sometimes considered. The effects of foundation, materials and geometric parameters on the buckling pressures and lowest natural frequencies were investigated in detail. Naj *et al.* (2008) employed a first-order shell theory and Sander's nonlinear kinematics equations to study mechanical and thermal buckling behavior of FGM truncated conical shells. They found that the semi-vertex angle, length-to-thickness ratio and radius-to-thickness ratio had significant effects on the buckling mechanical and thermal loads. After investigating dynamic buckling characteristics of imperfect FGM conical shells subjected to an impact load, Zhang and Li (2010) found that the maximal dynamic deflection of an imperfect shell was larger than that of the corresponding perfect shell. By studying buckling behavior of FGM hybrid conical shells reinforced with stiffeners, Dung and Chan (2017) and Duc *et al.* (2018) found that the number of stiffeners could significantly affect the critical loads. The vibration analysis of functionally graded conical and cylindrical shell structures was presented by Tornabene (2009) and Qu *et al.* (2013). The FGMs with a four-parameter power-law distribution was proposed. Vibration characteristics of FGM conical shell panels were investigated by Zhao and Liew (2011). In their study, two types of FGMs, Al/ZrO_2 and Ti-6Al-4V aluminum oxide were taken into account. Using the differential quadrature method (DQM), Heydarpour *et al.* (2014) studied vibration behavior of FGM truncated conical shells subjected to internal pressures. For rotating FGM conical shells, Malekzadeh and Heydarpour (2013) and Dey *et al.* (2015) discussed the effect of rotational speed on natural frequencies. They found that the influence of Coriolis acceleration on the frequency depends

on the shell boundary conditions. Using the variational principle in conjunction with the modified Fourier series, Su *et al.* (2014) obtained an analytical solution of thick FGM conical shells, cylindrical shells and annular plate structures. In addition, vibration of FGM conical shells was studied by Deniz *et al.* (2016) and Zarei *et al.* (2020).

In the above-mentioned studies, the conical shells were treated as perfect structures without pores. However, porosities inevitably appear inside the materials in the process of fabricating FGMs (Wu *et al.*, 2020) and affect Young's moduli (Sofiyev *et al.*, 2009b). Hence, it is necessary to investigate the influence of internal pores on buckling and vibration characteristics of FGM conical shells. Hoa *et al.* (2020) investigated the effects of pores on the critical load of FGM conical shells on elastic foundations. Buckling and vibration characteristics of porous FGM conical shells were also studied by Cuong-Le *et al.* (2021) and Yan *et al.* (2020). All of the results showed that the porosity distributions and porosity volume fraction could affect the statics and dynamics of FGM conical shells. Moreover, the used model for evaluating FGM material properties was based on the model of estimating typical mechanical properties of metal foams, and not the law of mixture.

A sigmoid functionally graded material (S-FGM) is a new kind of composite in which the ceramic volume fraction is described by a sigmoid distribution law. Compared with typical FGMs, S-FGMs have the advantage of eliminating stress concentration in some interfaces where the materials are continuous but quickly varying. Hence, S-FGMs can be used in some engineering structures subjected to impact and thermal loads to avoid concentration of stress. Up to now, few studies have been devoted to buckling and vibration of S-FGM truncated conical shells (Dung *et al.*, 2019; Nemati and Mahmoodabadi, 2020).

As reviewed above, the number of studies on the buckling and vibration of S-FGM conical shells is still rather scarce. According to the authors' knowledge, no previous research work has been done for the buckling and vibration of porous S-FGM shells. Hence, the present study attempts to present a modified model of estimating material properties and investigate the effect of internal pores on the buckling and vibration of porous S-FGM conical shells.

2. A porous S-FGM truncated conical shell

As depicted in Fig. 1, a porous S-FGM truncated conical shell subjected to external pressures P_1 and P_2 is considered. A curvilinear coordinate system (s, θ, z) is set in the middle surface of the cone. s and θ axes lie along the generator and in the circumferential direction. The z axis is perpendicular to the s-θ curve. The radii of the cone at the small and large ends are S_1 and S_2, respectively. L, h and γ denote length, thickness and semi-vertex, respecively. The truncated conical shell is made of ceramic and metal materials. Two types of porosity distributions, even and uneven, are considered (see, Fig. 2).

In the previous open literature, the pore volume fraction α is usually assumed to be very small $\alpha \ll 1$ and neglected in calculating the total volume of porous structures, i.e. $V_c + V_m = 1$, in which V_c and V_m denote the ceramic and metal volume fractions. To eliminate the assumption, we now let $V_c + V_m + \alpha = 1$ and $W_c + W_m = 1$, in which W_c and W_m are the ceramic and metal mass fractions, respectively. Thus, V_c can be calculated as follows

$$V_c = (1 - \alpha)\frac{W_c/\rho_c}{W_c/\rho_c + W_m/\rho_m} \tag{2.1}$$

where ρ_c and ρ_m are the ceramic and metal mass densities.

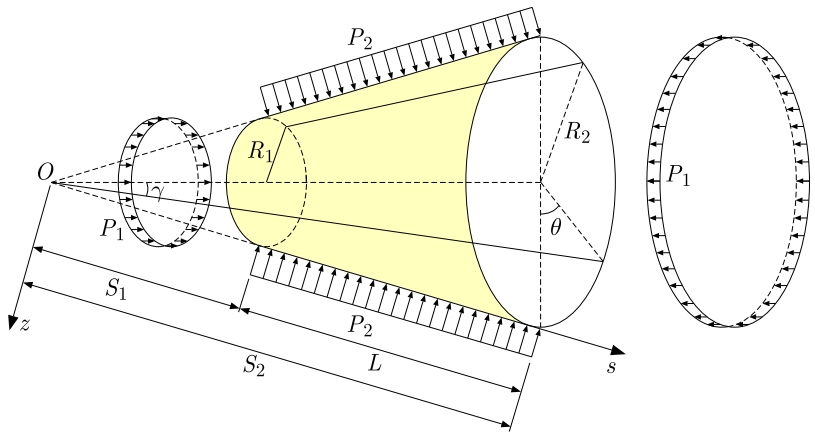

Fig. 1. Scheme of a S-FGM truncated conical shell

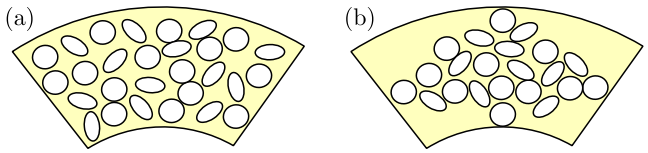

Fig. 2. Porosity distributions: (a) even, (b) uneven

The ceramic volume distribution V_c^* of the S-FGMs is assumed to be

$$V_c^*(z) = \begin{cases} V_{c1}\Big(1 - \dfrac{1}{2}\Big(\dfrac{h/2 - z}{h/2}\Big)^N\Big) & \text{for} \quad 0 \leqslant z \leqslant \dfrac{h}{2} \\ \dfrac{1}{2}V_{c1}\Big(\dfrac{h/2 + z}{h/2}\Big)^N & \text{for} \quad -\dfrac{h}{2} \leqslant z \leqslant 0 \end{cases} \tag{2.2}$$

but $V_c{}^*$ for typical FGMs is

$$V_c^* = V_{c2}\Big(1 + \frac{2z}{h}\Big)^N \tag{2.3}$$

where N is the material volume index. The coefficients V_{c1} and V_{c2} can be calculated by

$$\int_{-0.5h}^{0.5h} V_c^*(z)\, dz = \int_{-0.5h}^{0.5h} V_c\, dz \tag{2.4}$$

Applying the modified rule of mixture, the effective Young's modulus $E(z)$, mass density $\rho(z)$ and Poisson's ratio $\nu(z)$ of the conical shell can be expressed as follows

$$\begin{aligned} E(z) &= E_c V_c^*(z) + E_m[1 - V_c^*(z) - \alpha^*(z)] \\ \rho(z) &= \rho_c V_c^*(z) + \rho_m[1 - V_c^*(z) - \alpha^*(z)] \\ \nu(z) &= \nu_c V_c^*(z) + \nu_m[1 - V_c^*(z) - \alpha^*(z)] \end{aligned} \tag{2.5}$$

where E_c and ν_c are Young's modulus and Poisson's ratio of the ceramics. E_m and ν_m are the corresponding values of the metals. The porosity volume distributions α^* for the even distribution (ED) is assumed to be

$$\alpha^*(z) = \alpha \tag{2.6}$$

and the uneven distribution (UD) is assumed to be

$$\alpha^*(z) = \alpha_1\Big(1 - \frac{2|z|}{h}\Big) \tag{2.7}$$

Assuming that the total porosity fractions for different distributions are equivalent, the coefficient α_1 can be determined as follows

$$\int_{-0.5h}^{0.5h} \alpha_1\Big(1-\frac{2|z|}{h}\Big)\,dz = \int_{-0.5h}^{0.5h} \alpha\,dz \tag{2.8}$$

3. Formulations

3.1. Governing equations

In the framework of the classical thin shell theory, the stress-strain relationship of the S-FGM conical shell can be expressed as follows

$$\begin{bmatrix}\sigma_s\\ \sigma_\theta\\ \sigma_{s\theta}\end{bmatrix} = \frac{E(z)}{1-\nu^2(z)}\begin{bmatrix}1 & \nu(z) & 0\\ \nu(z) & 1 & 0\\ 0 & 0 & 1-\nu(z)\end{bmatrix}\begin{bmatrix}\varepsilon_s - z\dfrac{\partial^2 W}{\partial s^2}\\ \varepsilon_\theta - z\Big(\dfrac{1}{s^2}\dfrac{\partial^2 W}{\partial \psi^2}+\dfrac{1}{s}\dfrac{\partial W}{\partial s}\Big)\\ \varepsilon_{s\theta} - z\Big(\dfrac{1}{s}\dfrac{\partial^2 W}{\partial s\partial \psi}-\dfrac{1}{s^2}\dfrac{\partial W}{\partial \psi}\Big)\end{bmatrix} \tag{3.1}$$

in which σ_s, σ_θ and $\sigma_{s\theta}$ are the stresses of the middle surface, ε_s, ε_θ and $\varepsilon_{s\theta}$ are the corresponding strains, W is the displacement in the circumferential direction and $\psi = \theta\sin\gamma$.

The membrane forces $(N_s, N_\theta, N_{s\theta})$ and moments $(M_s, M_\theta, M_{s\theta})$ are calculated as

$$[(N_s, N_\theta, N_{s\theta}), (M_s, M_\theta, M_{s\theta})] = \int_{-h/2}^{h/2} [1, z](\sigma_s, \sigma_\theta, \sigma_{s\theta})\,dz \tag{3.2}$$

Introducing stress function $F(s,\psi,t)$, the membrane forces are expressed as

$$(N_s, N_\theta, N_{s\theta}) = \left(\frac{1}{s^2}\frac{\partial^2 F}{\partial\psi^2}+\frac{1}{s}\frac{\partial\psi}{\partial s}, \frac{\partial^2 F}{\partial s^2}, -\frac{1}{s}\frac{\partial^2 F}{\partial s\partial\psi}+\frac{1}{s^2}\frac{\partial F}{\partial\psi}\right) \tag{3.3}$$

On the condition that the truncated conical shell is subjected to external pressures P_1 and P_2, the initial membrane forces are given as (Sofiyev, 2009)

$$N_s^0 = -\frac{1}{2}P_1 s\tan\gamma \qquad N_\theta^0 = -P_2 s\tan\gamma \qquad N_{s\theta}^0 = 0 \tag{3.4}$$

Combined with the effects of the initial membrane forces N_s^0, N_θ^0 and $N_{s\theta}^0$, the dynamic equilibrium equations and the strain compatibility equations are built as follows

$$\begin{aligned}&\frac{\partial^2 M_s}{\partial s^2}+\frac{2}{s}\frac{\partial M_s}{\partial s}+\frac{2}{s}\frac{\partial^2 M_{s\theta}}{\partial s\partial\psi}-\frac{1}{s}\frac{\partial M_\theta}{\partial s}+\frac{2}{s^2}\frac{\partial M_{s\theta}}{\partial\psi}+\frac{1}{s^2}\frac{\partial^2 M_\theta}{\partial\psi^2}+\frac{N_\theta}{s}\cot\gamma\\ &\quad+N_s^0\frac{\partial^2 W}{\partial s^2}+\frac{N_\theta^0}{s}\Big(\frac{1}{s}\frac{\partial^2 W}{\partial\psi^2}+\frac{\partial W}{\partial s}\Big)+2N_{s\theta}^0\frac{\partial}{\partial s}\Big(\frac{1}{s}\frac{\partial W}{\partial\psi}\Big)-\rho_t h\frac{\partial^2 W}{\partial t^2}=0\\ &\frac{\cot\gamma}{s}\frac{\partial^2 W}{\partial s^2}-\frac{2}{s}\frac{\partial^2 e_{s\theta}}{\partial s\partial\psi}-\frac{2}{s^2}\frac{\partial e_{s\theta}}{\partial\psi}+\frac{\partial^2 e_\theta}{\partial s^2}+\frac{1}{s^2}\frac{\partial^2 e_s}{\partial\psi^2}+\frac{2}{s}\frac{\partial e_\theta}{\partial s}-\frac{1}{s}\frac{\partial e_s}{\partial s}=0\end{aligned} \tag{3.5}$$

where $\rho_t = \int_{-0.5}^{0.5}\rho(z)\,dz$.

Substituting Eqs. (3.1)-(3.4) into equations (3.5) and introducing the independent variable $x = \ln(s/s_2)$, the governing equations of the S-FGM conical shell can be derived as follows

$$\begin{aligned}&L_1(F)+L_2(W)+P_1L_3(W)+P_2L_4(W)-\rho_t h s_2^4\frac{\partial^2 W}{\partial t^2}=0\\ &L_5(F)+L_6(W)=0\end{aligned} \tag{3.6}$$

where the linear operators L_i $(i=1,\ldots,6)$ are given in Appendix A.

3.2. The solution of the governing equations

In the present study, The free supported boundary conditions are assumed to be

$$s = s_1 \qquad \text{and} \qquad s = s_2 \qquad \Rightarrow \qquad W = M_s = T_s = 0 \tag{3.7}$$

The solution to the governing equations is assumed as

$$\begin{aligned} W &= w(t)\mathrm{e}^{\mu x}\sin(\beta_1 x)\cos(\beta_2\psi) \\ F &= f(t)\mathrm{e}^{(\mu+1)x}\sin(\beta_1 x)\cos(\beta_2\psi) \end{aligned} \tag{3.8}$$

where β_1 and β_2 are the coefficients of the vibration mode (m, n), defined by

$$\beta_1 = \frac{m\pi}{x_0} \qquad \beta_2 = \frac{n}{\sin\gamma} \qquad x_0 = \ln\frac{s_2}{s_1} \tag{3.9}$$

The parameter μ is introduced to obtain the minimum values of the critical pressure and lowest frequency. Multiplying Eq. $(3.6)_1$ by $s_2^2\exp[(\mu+2)x]\sin(\beta_1 x)\cos(\beta_2\psi)$ and $(3.6)_2$ by $s_2^3\exp[(\mu+3)x]\sin(\beta_1 x)\cos(\beta_2\psi)$, then applying Galerkin's method over the shell area $0 \leqslant \psi \leqslant 2\pi\sin\gamma$ and $-x_0 \leqslant x \leqslant 0$, the following differential equation with respect to time t can be derived

$$\frac{\partial^2 w}{\partial t^2} + \frac{1}{G_7}\Big(-\frac{G_1 G_6}{G_5} + G_2 + P_1 G_3 + P_2 G_4\Big)w(t) = 0 \tag{3.10}$$

where the coefficients G_i $(i = 1, \ldots, 7)$ are defined by

$$\begin{aligned}
G_1 &= \frac{1}{G_4}\int_{-x_0}^{0}\int_{0}^{2\pi\sin\gamma} L_1(F)s_2^2\mathrm{e}^{(\mu+2)x}\sin(\beta_1 x)\cos(\beta_2\psi)\,dx\,d\psi \\
G_2 &= \int_{-x_0}^{0}\int_{0}^{2\pi\sin\gamma} L_2(W)s_2^2\mathrm{e}^{(\mu+2)x}\sin(\beta_1 x)\cos(\beta_2\psi)\,dx\,d\psi \\
G_3 &= \int_{-x_0}^{0}\int_{0}^{2\pi\sin\gamma} L_3(W)s_2^2\mathrm{e}^{(\mu+2)x}\sin(\beta_1 x)\cos(\beta_2\psi)\,dx\,d\psi \\
G_4 &= \int_{-x_0}^{0}\int_{0}^{2\pi\sin\gamma} L_4(W)s_2^2\mathrm{e}^{(\mu+2)x}\sin(\beta_1 x)\cos(\beta_2\psi)\,dx\,d\psi \\
G_5 &= \int_{-x_0}^{0}\int_{0}^{2\pi\sin\gamma} L_5(F)s_2^3\mathrm{e}^{(\mu+3)x}\sin(\beta_1 x)\cos(\beta_2\psi)\,dx\,d\psi \\
G_6 &= \int_{-x_0}^{0}\int_{0}^{2\pi\sin\gamma} L_6(W)s_2^3\mathrm{e}^{(\mu+3)x}\sin(\beta_1 x)\cos(\beta_2\psi)\,dx\,d\psi \\
G_7 &= -\int_{-x_0}^{0}\int_{0}^{2\pi\sin\gamma} \rho_f h s_2^6\frac{\partial^2 W}{\partial t^2}\mathrm{e}^{(\mu+2)x}\sin(\beta_1 x)\cos(\beta_2\psi)\,dx\,d\psi
\end{aligned} \tag{3.11}$$

If the conical shell is free from external pressures $P_1 = P_2 = 0$, the frequency ω of the free vibration is obtained as

$$\omega = \sqrt{\frac{1}{G_7}\Big(-\frac{G_1 G_6}{G_5} + G_2\Big)} \tag{3.12}$$

According to equation (3.10), the critical hydraulic buckling pressures $P_1 = P_2 = P_{Hcr}$ and lateral buckling pressures $P_1 = 0$, $P_2 = P_{L\,cr}$ are obtained as

$$P_{H\,cr} = -\frac{G_1G_6 - G_2G_5}{G_5(G_3 + G_4)} \qquad P_{L\,cr} = -\frac{G_1G_6 - G_2G_5}{G_5G_4} \tag{3.13}$$

It is noted that the minimum values of buckling pressure and frequency obtained by Eqs. (3.12) and (3.13) depend on the parameters m, n and μ. In the present study, the minimum value of the shape mode (m, n) can be found by changing the value of the parameter μ from 0 to 5 with the step 0.1 (Sofiyev, 2009).

4. Results and discussion

4.1. Comparison studies

To validate the present method, two numerical examples are tested and the results are listed in Tables 1 and 2.

Example 1. The buckling behavior of a typical FGM truncated conical shell is studied in this example. The critical loads $P_{H\,cr}$ and $P_{L\,cr}$ are displayed in Table 1. The materials properties for silicon nitride (Si_3N_4) are $E_c = 0.32227\,\text{TPa}$, $\rho_c = 2370\,\text{kg/m}^3$ and $\nu_c = 0.24$. Those for stainless steel (SUS304) are $E_m = 0.2077877\,\text{TPa}$, $\rho_m = 8166\,\text{kg/m}^3$ and $\nu_m = 0.317756$. The geometric parameters are $R_1 = 1.0\,\text{m}$, $R_2 = 3.0\,\text{m}$, $R_2/h = 200$ and $\gamma = 30^\circ$. It can be observed that the present results agree well with those given by Sofiyev (2009). The maximum error is only 0.5%.

Table 1. Comparison of the critical pressures $P_{H\,cr}$ and $P_{L\,cr}$ for a typical FGM truncated conical shell

N	Method	$P_{H\,cr}(n,\mu)$ [MPa]	$P_{L\,cr}(n,\mu)$ [MPa]
Si_3N_4 $(N = 0)$	Sofiyev (2009)	0.741(8,2.1)	0.779(8,1.9)
	Present	0.739(8,2.1)	0.776(8,1.9)
	Discrepancy	0.3%	0.4%
1.0	Sofiyev (2009)	0.578(8,2.1)	0.607(8,1.9)
	Present	0.575(8,2.1)	0.604(8,1.9)
	Disfrepancy	0.5%	0.5%
2.0	Sofiyev (2009)	0.551(8,2.1)	0.579(8,1.9)
	Present	0.548(8,2.1)	0.577(8,1.9)
	Discrepancy	0.5%	0.3%

Example 2. The free vibration of a typical FGM truncated conical is studied in the example. The materials properties for silicon nitride (Si_3N_4) are $E_c = 0.32227\,\text{TPa}$, $\rho_c = 2370\,\text{kg/m}^3$ and $\nu_c = 0.24$, and the those for Nicknel (Ni) are $E_m = 0.205098\,\text{TPa}$, $\rho_m = 8900\,\text{kg/m}^3$ and $\nu_m = 0.31$. The geometric parameters of the shell are $R_2/h = 100$, $L = 2R_1$ and $\gamma = 30^\circ$. The dimensionless fundamental frequency $\Omega_1 = \omega_1 R_2\sqrt{(1-\nu_c^2)\rho_c/E_c}$ is calculated and listed in Table 2. It can be seen that the maximum deviation between the present results and those given by Sofiyev and Schnack (2012) is 0.6%.

4.2. Parametric studies

After the present method is validated, the effects of the porosity volume fraction, porosity distribution, material volume index, semi-vertex angle on the critical buckling loads and the

Table 2. Comparison of the dimensionless fundamental frequency Ω_1 for a typical FGM truncated conical shell

Method	N_i	$N = 1.0$	$N = 2.0$	Si_3N_4
Sofiyev and Schnack (2012)	0.0723(7)	0.0997(7)	0.0887(7)	0.1763(7)
Present	0.0725(7,1.1)	0.1002(7,1.0)	0.0892(7,1.1)	0.1757(7,1.1)
Discrepancy	0.3%	0.5%	0.6%	0.4%

lowest natural frequencies of porous S-FGM truncated conical shells are discussed in this Subsection. The material and geometric parameters are given in Example 1. Unless specially stated, the following parameters are used: $W_c = 0.3$, $\alpha = 0.1$ and $N = 1.0$.

Tables 3 and 4 list the first five buckling pressures $P_{H\,cr}$, $P_{L\,cr}$ and natural frequency ω of the porous conical shell. The two kinds of pore distributions, even distribution (ED) and uneven distribution (UD) are taken into account. It can be found that the minimum values of the buckling pressures are obtained in mode (1,7). However, the lowest frequency is obtained in mode (1,5). Also, it can be observed that the parameter μ for the critical buckling pressures is about 2.7, but that for the lowest frequency it is 1.1. Moreover, it can be found that the minimum values of the buckling pressures $P_{H\,cr}$, $P_{L\,cr}$ and frequency ω for the even distribution are smaller than the corresponding values for the uneven distribution, respectively. It can be proved that the effective rigidity for the even distribution is larger than that for the uneven one.

Table 3. Buckling pressures $P_{H\,cr}$, $P_{L\,cr}$ and frequency ω of different modes (m, n) for a porous S-FGM truncated conical shell with evenly distributed pores

(m, n)	(1,7)	(1,6)	(1,8)	(1,5)	(2,8)
$P_{H\,cr}(\mu)$ [MPa]	0.442(2.7)	0.447(1.7)	0.462(3.8)	0.542(0.8)	0.574(3.0)
$P_{L\,cr}(\mu)$ [MPa]	0.461(2.6)	0.465(1.6)	0.485(3.6)	0.567(0.8)	0.624(2.7)
(m, n)	(1,5)	(1,6)	(1,4)	(1,7)	(1,8)
$\omega(\mu)$ [Hz]	51.791(1.1)	54.699(1.9)	59.401(0.5)	61.732(3.0)	70.702(4.0)

Table 4. Buckling pressures $P_{H\,cr}$, $P_{L\,cr}$ and frequency ω of different modes (m, n) for a porous S-FGM truncated conical shell with unevenly distributed pores

(m, n)	(1,7)	(1,6)	(1,8)	(1,5)	(2,8)
$P_{H\,cr}(\mu)$ [MPa]	0.460(2.6)	0.462(1.7)	0.482(3.7)	0.557(0.8)	0.594(3.1)
$P_{L\,cr}(\mu)$ [MPa]	0.481(2.7)	0.484(1.7)	0.507(3.7)	0.582(0.8)	0.645(2.7)
(m, n)	(1,5)	(1,6)	(1,4)	(1,7)	(1,8)
$\omega(\mu)$ [Hz]	52.461(1.1)	55.685(2.0)	59.706(0.5)	62.986(3.0)	72.231(4.1)

For the sake of revealing the effect of the parameter μ on the buckling and vibration behavior of the truncated conical shell, the curves of the buckling pressure $P_{H\,cr}$ and $P_{L\,cr}$ versus the parameter μ are displayed in Fig. 3a. As the parameter μ changes from 0.0 to 2.7, the buckling pressures $P_{H\,cr}$ and $P_{L\,cr}$ decrease. However, the buckling pressures increase as the parameter changes from 2.7 to 5.0. Thus, it can be found that the critical buckling pressures can be obtained at $\mu \approx 2.7$. A similar variation of the natural frequency versus the parameter μ is observed in Fig. 3b, but the lowest frequency ω can be obtained at $\mu \approx 1.1$.

The curves of the buckling pressures $P_{H\,cr}$, $P_{L\,cr}$ and lowest frequency ω versus the ceramic mass fraction W_c are shown in Figs. 4a and 4b. From the two figures, it can be observed that the values of $P_{H\,cr}$, $P_{L\,cr}$ and ω are increased with an increase in W_c. It is due to the fact that Young's modulus of Si_3N_4 is higher than that of Ni. Also, it can be seen that the critical buckling

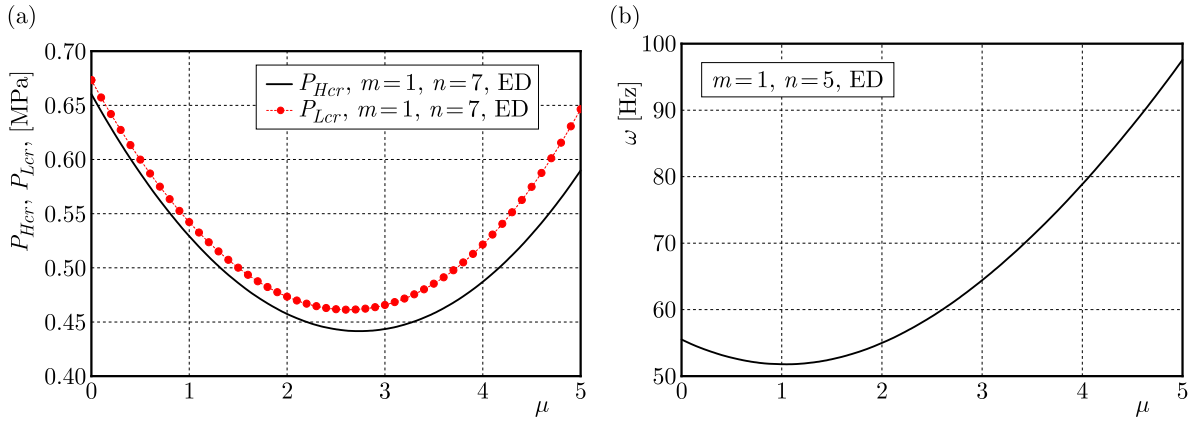

Fig. 3. Effect of the parameter on: (a) critical buckling pressures, (b) lowest frequency

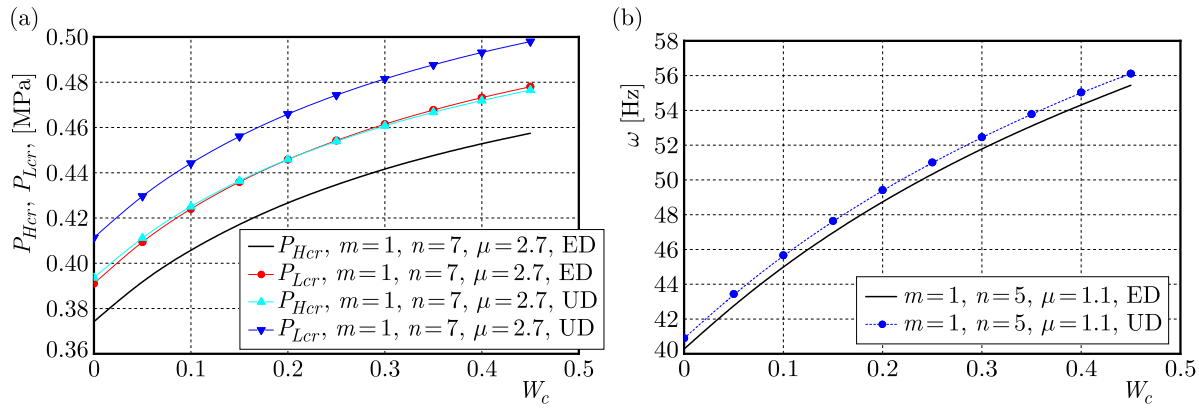

Fig. 4. Effect of the ceramic mass fraction W_C on: (a) buckling pressures $P_{H\,cr}$ and $P_{L\,cr}$, (b) lowest frequency ω

pressure $P_{H\,cr}$ for the even distribution is very close to the critical lateral pressure $P_{L\,cr}$ for the uneven distribution. The lowest frequency for the uneven distribution is higher than that for the even porosity distribution. Also, this demonstrates that the effective rigidity of the former is larger than that of the latter.

In Fig. 5a, the influence of the porosity volume fraction α on the buckling pressures $P_{H\,cr}$ and $P_{L\,cr}$ is revealed. It is clear that the values of $P_{H\,cr}$ and $P_{L\,cr}$ decreased with an increasing value of α. The decrease in the buckling hydraulic pressure $P_{H\,cr}$ is more significant than that of the buckling lateral pressure $P_{L\,cr}$. If the value of α varies from 0 to 0.3, the value of $P_{H\,cr}$ for the uneven and even distribution decreases by about 21% and 32%, respectively. It is evident that the effect of the porosity volume fraction on the buckling hydraulic pressure for the even porosity distribution is more significant than that for uneven porosity distribution.

The variation curves of the lowest frequency ω versus porosity volume fraction α are shown in Fig. 5b. It can be observed that the variation is different for different porosity distributions. The lowest frequency ω for the even distribution is decreased by increasing α. On the contrary, the lowest frequency ω for the uneven distribution is increased as α increases. Also, one can notice the turning point of the variation curves for the uneven distribution at $\alpha = 0.24$. Furthermore, the value of ω for $\alpha > 0.4$ increases more slowly than that for $\alpha < 0.24$.

The effects of the material index N on the buckling pressures $P_{H\,cr}$ and $P_{L\,cr}$ are shown in Fig. 6a. It is clear that the values of buckling pressures are decreased with an increase of the index N. This is because the increase of N indicates a decrease in the volume fraction of Si_3N_4, which leads to a decrease in the shell effective rigidity. As expected, the curve of buckling

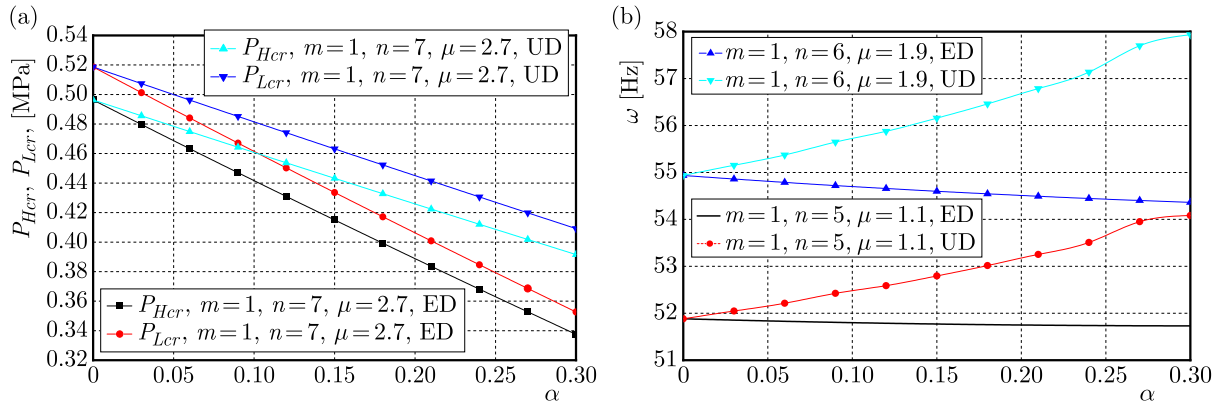

Fig. 5. Effect of the pore volume fraction α on: (a) buckling pressures $P_{H\,cr}$ and $P_{L\,cr}$, (b) lowest frequency ω

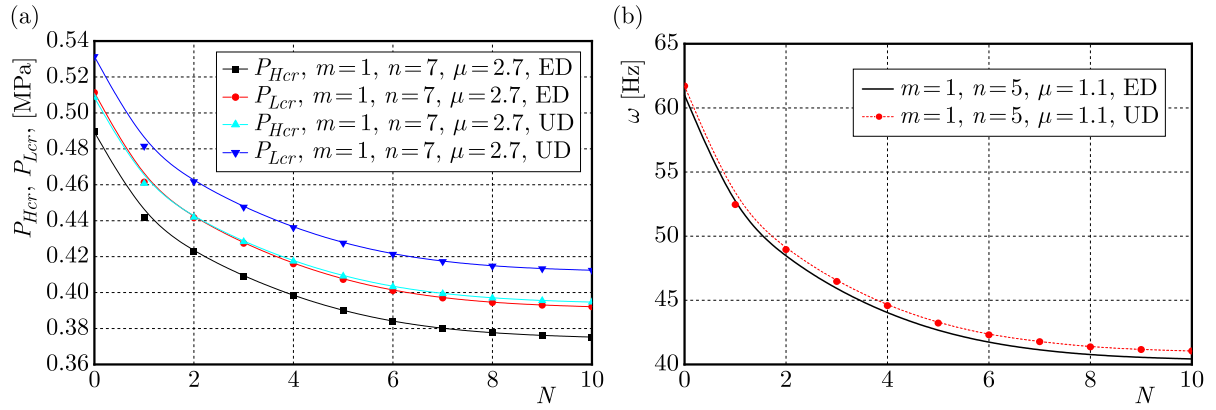

Fig. 6. Effect of the material index N on: (a) buckling pressures $P_{H\,cr}$ and $P_{L\,cr}$, (b) lowest frequency ω

hydraulic pressure $P_{H\,cr}$ for the uneven distribution is very close to the curve of buckling lateral pressure $P_{L\,cr}$ for the even distribution. This proves that the effective rigidity of the former nearly equals that of the latter. Figure 6b shows the effect of the material index N on the lowest frequency ω. It is seen that the value of ω can be decreased by increasing the index N. This is due to the fact that an increase in N leads to a decrease in the effective rigidity of the truncated conical shell.

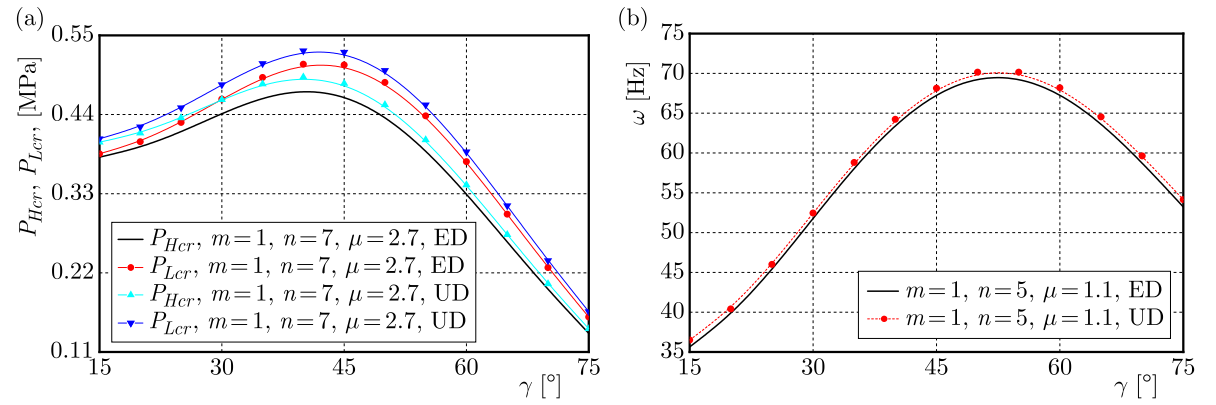

Fig. 7. Effect of the semi-vertex angle γ on: (a) buckling pressures $P_{H\,cr}$ and $P_{L\,cr}$, (b) lowest frequency ω

The curves of the buckling pressures $P_{H\,cr}$ and $P_{L\,cr}$ versus semi-vertex angle γ are shown in Fig. 7a. From the figure, it can be seen that the maximum values of buckling pressures $P_{H\,cr}$, $P_{L\,cr}$ and frequency ω are obtained at $\gamma \approx 40°$, which implies that the maximum of the shell effective rigidity is obtained at $\gamma \approx 40°$. The variation of the lowest frequency ω varying with the semi-vertex angle γ are shown in Fig. 7b. It can be observed that the maximum value of the lowest frequency ω is reached at $\gamma \approx 50°$. Also, it can be observed that the porosity distribution has an insignificant effect on the lowest frequency. The maximum difference is about 2.4%.

5. Conclusion

This paper presents a new reliable model to evaluate material properties of sigmoid functionally graded materials. The buckling and vibration of porous S-FGM truncated conical shells are investigated. The present results are compared with those available in the open literature. In the parametric studies, the effects of ceramic mass fraction, porosity volume fraction, porosity distribution, material index and semi-vertex angle are discussed in detail. The results show that both the porosity volume fraction and distribution have significant effects on the buckling pressures and lowest frequency. The buckling pressures and lowest frequency for the even porosity distribution are decreased as the porosity volume fraction rises. However, the lowest frequency for the uneven porosity distribution is increased. By increasing the ceramic mass fraction, the values of buckling pressures and lowest frequency can be raised. As the semi-vertex angle γ changes from 15° to 75°, the critical buckling pressure and lowest frequency are obtained at about 40° and 50°, respectively.

A. Appendix

$$
\begin{aligned}
L_1(F) &= A_1 \mathrm{e}^{-4x}\Big(\frac{\partial^4 F}{\partial x^4} - 4\frac{\partial^3 F}{\partial x^3} + 4\frac{\partial^2 F}{\partial x^2} + 2\frac{\partial^2 F}{\partial \psi^2} + \frac{\partial^4 F}{\partial \psi^4}\Big)\\
&\quad - s_2 \mathrm{e}^{-3x}\cot\gamma\frac{\partial F}{\partial x} + s_2 \mathrm{e}^{-3x}\cot\gamma\frac{\partial^2 F}{\partial x^2} + A_2 \mathrm{e}^{-4x}\Big(\frac{\partial^4 F}{\partial x^2 \partial \psi^2} - 2\frac{\partial^3 F}{\partial x \partial \psi^2} + \frac{\partial^2 F}{\partial \psi^2}\Big)\\
L_2(W) &= -A_3 \mathrm{e}^{-4x}\Big(\frac{\partial^4 W}{\partial x^4} - 4\frac{\partial^3 W}{\partial x^3} + 4\frac{\partial^2 W}{\partial x^2} + 2\frac{\partial^2 W}{\partial \psi^2} + \frac{\partial^4 W}{\partial \psi^4}\Big)\\
&\quad - A_4 \mathrm{e}^{-4x}\Big(\frac{\partial^4 W}{\partial x^2 \partial \psi^2} - 2\frac{\partial^3 W}{\partial x \partial \psi^2} + \frac{\partial^2 W}{\partial \psi^2}\Big)\\
L_3(W) &= \frac{1}{2}s_2^3 \mathrm{e}^{-x}\tan\gamma\Big(\frac{\partial W}{\partial x} - \frac{\partial^2 W}{\partial x^2}\Big) \qquad L_4 W = -s_2^3 \mathrm{e}^{-x}\tan\gamma\Big(\frac{\partial W}{\partial x} + \frac{\partial^2 W}{\partial \psi^2}\Big) \qquad \text{(A.1)}\\
L_5(F) &= B_1 \mathrm{e}^{-4x}\Big(\frac{\partial^4 F}{\partial x^4} - 4\frac{\partial^3 F}{\partial x^3} + 4\frac{\partial^2 F}{\partial x^2} + 2\frac{\partial^2 F}{\partial \psi^2} + \frac{\partial^4 F}{\partial \psi^4}\Big)\\
&\quad + B_2 \mathrm{e}^{-4x}\Big(\frac{\partial^4 F}{\partial x^2 \partial \psi^2} - 2\frac{\partial^3 F}{\partial x \partial \psi^2} + \frac{\partial^2 F}{\partial \psi^2}\Big)\\
L_6(W) &= -B_3 \mathrm{e}^{-4x}\Big(\frac{\partial^4 W}{\partial x^4} - 4\frac{\partial^3 W}{\partial x^3} + 4\frac{\partial^2 W}{\partial x^2} + 2\frac{\partial^2 W}{\partial \psi^2} + \frac{\partial^4 W}{\partial \psi^4}\Big)\\
&\quad + B_4 \mathrm{e}^{-4x}\Big(\frac{\partial^4 W}{\partial x^2 \partial \psi^2} - 2\frac{\partial^3 W}{\partial x \partial \psi^2} + \frac{\partial^2 W}{\partial \psi^2}\Big) + s_2 \mathrm{e}^{-3x}\cot\gamma\Big(\frac{\partial^2 W}{\partial x^2} - \frac{\partial W}{\partial x}\Big)
\end{aligned}
$$

In which coefficients A_i and B_i are defined by

$$
\begin{aligned}
&A_1 = c_{12} \qquad A_2 = 2(c_{11} - c_{31}) \qquad A_3 = c_{13} \qquad A_4 = 2(c_{14} + c_{32})\\
&B_1 = b_{11} \qquad B_2 = 2(b_{31} + b_{12}) \qquad B_3 = b_{14} \qquad B_4 = 2(b_{32} - b_{13})
\end{aligned}
$$

$$
\begin{aligned}
&c_{11} = a_{11}^1 b_{11} + a_{12}^1 b_{12} \qquad c_{12} = a_{11}^2 b_{12} + a_{12}^1 b_{12} \qquad c_{13} = a_{11}^1 b_{13} + a_{12}^1 b_{14} + a_{11}^2 \\
&c_{14} = a_{11}^1 b_{14} + a_{12}^1 b_{13} + a_{12}^2 \qquad c_{31} = a_{66}^1 b_{31} \qquad c_{32} = a_{66}^1 b_{32} + a_{66}^2
\end{aligned} \tag{A.2}
$$

$$
\begin{aligned}
&b_{11} = a_{11}^0 d_0 \qquad b_{12} = -a_{12}^0 d_0 \qquad b_{13} = (a_{12}^0 a_{12}^1 - a_{11}^1 a_{11}^0) d_0 \\
&b_{14} = (a_{12}^0 a_{11}^1 - a_{12}^1 a_{11}^0) d_0 \qquad b_{31} = \frac{1}{a_{66}^0} \qquad b_{32} = -\frac{a_{66}^1}{a_{66}^0} \\
&d_0 = \frac{1}{a_{11}^0 a_{11}^0 - a_{12}^0 a_{12}^0}
\end{aligned}
$$

In Eqs. (A.2), the coefficients a_{ij}^k are defined as follows

$$
\begin{aligned}
&a_{11}^k = \int_{-0.5h}^{0.5h} z^k \frac{E(z)}{1-\nu^2(z)}\, dz \qquad a_{12}^k = \int_{-0.5h}^{0.5h} z^k \frac{\nu(z)E(z)}{1-\nu^2(z)}\, dz \\
&a_{66}^k = \int_{-0.5h}^{0.5h} z^k \frac{E(z)}{2[1+\nu(z)]}\, dz
\end{aligned} \tag{A.3}
$$

Acknowledgment

The authors are grateful for the financial support of the National Natural Science Foundation of China (No. 12162010) and the Natural Science Foundation of Guangxi (No. 2021GXNSFAA220087).

References

1. Alizada A.N., Sofiyev A.H., 2011, Modified Young's moduli of nano-materials taking into account the scale effects and vacancies, *Meccanica*, **46**, 915-920
2. Chi S.H., Chung Y.L., 2002, Cracking in sigmoid functionally graded coating, *Journal of Mechanics*, **18**, 41–53
3. Cuong-Le T., Nguyen K.N., Nguyen-Trong N., Khatir S., Nguyen-Xuan H., Abdel--Wahab M., 2021, A three-dimensional solution for free vibration and buckling of annular plate, conical, cylinder and cylindrical shell of FG porous-cellular materials using IGA, *Composite Structures*, **259**, 113216
4. Deniz A., Zerin Z., Karaca Z., 2016, Winkler-Pasternak foundation effect on the frequency parameter of FGM truncated conical shells in the framework of shear deformation theory, *Composites: Part B*, **104**, 57-70
5. Dey S., Sarkar S., Das A., Karmakar A., Adhikari S., 2015, Effect of twist and rotation on vibration of functionally graded conical shells, *International of Journal of Mechanics and Material Design*, **11**, 425-437
6. Duc N.D., Kim S.E., Chan D.Q., 2018, Thermal buckling analysis of FGM sandwich truncated conical shells reinforced by FGM stiffeners resting on elastic foundations using FSDT, *Journal of Thermal Stresses*, **41**, 3, 331-365
7. Dung D.V., Chan D.Q., 2017, Analytical investigation on mechanical buckling of FGM truncated conical shells reinforced by orthogonal stiffeners based on FSDT, *Composite Structures*, **159**, 827-841
8. Dung D.V., Nga N.T., Vuong P.M., 2019, Nonlinear stability analysis of stiffened functionally graded material sandwich cylindrical shells with general Sigmoid law and power law in thermal environment using third-order shear deformation theory, *Journal of Sandwich Structures and Materials*, **21**, 3, 938-972

9. Heydarpour Y., Malekzadeh P., Aghdam M.M., 2014, Free vibration of functionally graded truncated conical shells under internal pressure, *Meccanica*, **49**, 267-282

10. Hoa L.K., Phi B.G., Chan D., Dang V.D., 2020, Buckling analysis of FG porous truncated conical shells resting on elastic foundations in the framework of the shear deformation theory, *Advances in Applied Mathematics and Mechanics*, **14**, 1, 218-247

11. Malekzadeh P., Heydarpour Y., 2013, Free vibration analysis of rotating functionally graded truncated conical shells, *Composite Structures*, **97**, 176-188

12. Naj R., Boroujerdy M.S., Eslami M.R., 2008, Thermal and mechanical instability of functionally graded truncated conical shells, *Thin-Walled Structures*, **46**, 65-78

13. Nemati A.R., Mahmoodabadi M.J., 2020, Effect of micromechanical models on stability of functionally graded conical panels resting on Winkler-Pasternak foundation in various thermal environments, *Archives of Applied Mechanics*, **90**, 5, 883-915

14. Qu Y.G., Long X.H., Yuan G.Q., Meng G., 2013, A unified formulation for vibration analysis of functionally graded shells of revolution with arbitrary boundary conditions, *Composites: Part B*, **50**, 381-402

15. Sofiyev A.H., 2007, Vibration and stability of composite cylindrical shells containing a FG layer subjected to various loads, *Structural Engineering and Mechanics*, **27**, 365-391

16. Sofiyev A.H., 2009, The vibration and stability behavior of freely supported FGM conical shells subjected to external pressure, *Composite Structures*, **89**, 356-366

17. Sofiyev A.H., 2019, Review of research on the vibration and buckling of the FGM conical shells, *Composite Structures*, **211**, 301-317

18. Sofiyev A.H., Aksogan O., Schnack E., Avcar M., 2008a, The stability of a three-layered composite conical shell containing a FGM layer subjected to external pressure, *Mechanics of Advanced Materials and Structures*, **15**, 461-466

19. Sofiyev A.H., Korkmaz K.A., Mammadov Z., Karmanli M., 2009a, The vibration and buckling of freely supported non-homogeneous orthotropic conical shells subjected to different uniform pressures, *International Journal of Pressure Vessels and Piping*, **86**, 661-668

20. Sofiyev A.H., Kuruoglu N., 2014, Buckling and vibration of shear deformable functionally graded orthotropic cylindrical shells under external pressures, *Thin-Walled Structures*, **78**, 121-130

21. Sofiyev A.H., Kuruoglu N., Turkmen M., 2009b, Buckling of FGM hybrid truncated conical shells subjected to hydrostatic pressure, *Thin-Walled Structures*, **47**, 61-72

22. Sofiyev A.H., Schnack E., 2012, The vibration analysis of FGM truncated conical shells resting on two-parameter elastic foundations, *Mechanics of Advanced Materials and Structures*, **19**, 241-249

23. Sofiyev A.H., Zerin Z., Korkmaz A., 2008b, The stability of a thin three-layered composite truncated conical shell containing a FGM layer subjected to non-uniform lateral pressure, *Composite Structures*, **85**, 105-115

24. Su Z., Jin G.Y., Shi S.G., Ye T.G., Jia X.T., 2014, A unified solution for vibration analysis of functionally graded cylindrical, conical shells and annular plates with general boundary conditions, *International Journal of Mechanical Sciences*, **80**, 62-80

25. Torabi J., Ansari R., 2018, A higher-order isoparametric superelement for free vibration analysis of functionally graded shells of revolution, *Thin-Walled Structures*, **133**, 169-179

26. Tornabene F., 2009, Free vibration analysis of functionally graded conical, cylindrical shell and annular plate structures with a four-parameter power-law distribution, *Computer Methods of Applied Mechanics and Engineering*, **198**, 2911-2935

27. Wu H., Yang J., Kitipornchal S., 2020, Mechanical analysis of functionally graded porous structures: a review, *International Journal of Structural Stability and Dynamics*, **20**, 2041015

28. Yan K., Zhang Y., Cai H., Tahouneh V., 2020, Vibrational characteristic of FG porous conical shells using Donnell's shell theory, *Steel and Composite Structures*, **35**, 2, 249-260

29. Zarei M., Rahimi G.H., Hemmatnezhad M., 2020, Free vibrational characteristics of grid-stiffened truncated composite conical shells, *Aerospace Science and Technology*, **99**, 105717

30. Zhang J.H., Li S.R., 2010, Dynamic buckling of FGM truncated conical shells subjected to non-uniform normal impact load, *Composite Structures*, **92**, 2979-2983

31. Zhao X., Liew K.M., 2011, Free vibration analysis of functionally graded conical shell panels by a meshless method, *Composite Structures*, **93**, 649-664

Manuscript received February 19, 2023; accepted for print May 31, 2023

JOURNAL OF THEORETICAL AND APPLIED MECHANICS
61, 3, pp. 573-583, Warsaw 2023
https://doi.org/10.15632/jtam-pl/166461

DETERMINATION OF CONTACT PRESSURE DISTRIBUTION ON FRICTIONLESS ROUGH SURFACES USING AN OPTIMISATION APPROACH: A ONE-DIMENSIONAL STUDY

Milagros Noemi Quintana Castillo
Department of Mathematics, State University of Santa Catarina, Joinville, Brazil
e-mail: milla.quicas@gmail.com

Marco Antonio Luersen
Department of Mechanical Engineering, Federal University of Technology – Parana, Curitiba, Brazil
e-mail: luersen@utfpr.edu.br (corresponding author)

Francisco José Profito
Department of Mechanical Engineering, Polytechnic School of the University of São Paulo, Brazil
e-mail: fprofito@usp.br

Determining pressures and stresses that arise when mechanical components come into contact is crucial for analysis of surface-related failures. In real situations, determining contact pressure and stress distributions is challenging and depends on several factors, such as load, material properties and surface characteristics. This paper describes the determination of contact pressure on rough surfaces using a one-dimensional approach. Elastic, frictionless, unilateral, normal contact between a rough surface and a smooth surface is considered. Linear elastic half-space theory is used, and the contact pressure distribution is obtained by solving an associated optimisation problem. Results are given for a virtual wavy profile and two engineering roughness profiles.

Keywords: frictionless normal contact, rough surface, optimisation

1. Introduction

Contact problems in engineering have been studied for decades, particularly those related to elastic contact between deformable bodies. Research in this field is of considerable importance in mechanics since contact occurs between all interacting bodies that transmit forces and motion. When two bodies are pressed against each other, a contact area is formed in the interface between them, and a challenge is to determine the interfacial pressure and stress distributions developed in the vicinity of the contact zone (Zhao *et al.*, 2014). Jackson and Green (2006) and He *et al.* (2021) noted that stress analysis in materials in contact is of significant importance for design of mechanical components. According to Persson (2006), the study of contact between surfaces is also essential due to its influence on heat transfer, wear, friction and adhesion phenomena that significantly affect efficiency and durability of engineering systems.

All natural or manufactured surfaces are rough at the microscopic level and exhibit asperities at various length scale regardless of how they have been produced and even if they appear smooth macroscopically (Rey and Bleyer, 2018). The surface roughness also affects contact characteristics with a significant impact on the interfacial pressure and stress distributions and, consequently, on friction, wear and superficial damage behaviour (Jackson and Green, 2006). Therefore, it is essential to understand the nature of roughness and its effect on contact problems to analyse situations that correspond more closely to real applications (Weber *et al.*, 2018). According to Josso *et al.* (2002), surface topographies can be described as a superposition of

three components: form, waviness, and roughness. The contact mechanics between rough surfaces aims at explaining the complex interactions between asperities of the roughness component. Understanding the nature of these interactions is of great practical interest as they play a vital role in the tribological performance of different systems. However, understanding the relationship between the contact variables – such as interfacial pressure, stresses, real contact area, contact stiffness and many other aspects depending on morphological properties of the surfaces – remains challenging (Hills *et al.*, 1993; Bemporad and Paggi, 2015; Zhang *et al.*, 2019; Fu *et al.*, 2020).

In order to calculate the contact pressure distribution, the present work uses theory of elastic half-spaces to describe the normal frictionless contact problem between two bodies. Then, the contact regions of the bodies are discretised, resulting in a linear complementarity problem (LCP), which is converted into an optimisation problem and solved with a classic optimiser algorithm. Recently, LCPs have been used to solve optimisation problems, and in the last 20 years, elastoplastic analysis problems have also been solved by converting them into LCPs, which have emerged as a unified solution for quadratic and linear programming. According to Cottle *et al.* (1992) and Sushun (1995), the complementarity and linearity of an LCP provide necessary fundamental elements for the analysis and understanding of the complex nature of mathematical programming and equilibrium problems.

The contribution of this paper is twofold. First, it presents contact pressure solutions of real roughness profiles, which are not extensively used in studies with rough surfaces that usually represent asperities by analytic functions. The paper also uses an approach based on solving an associated optimisation problem, performed numerically by quadratic programming, a method that has not been widely used in the study of normal contact problems.

2. Formulation of the contact problem

2.1. Mathematical modelling of the contact problem

Two smooth non-conforming isotropic elastic bodies are considered to be initially in contact at a single point P. After applying an external normal force, both bodies deform in the vicinity of P, as shown in Fig. 1. At the interface between the bodies, contact pressures arise. The math-

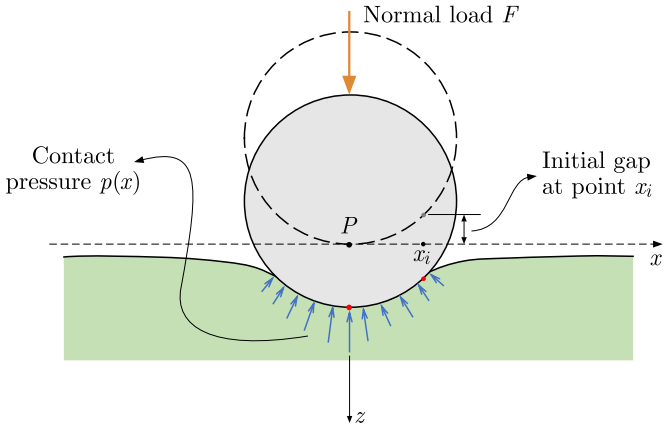

Fig. 1. Schematic representation of two smooth elastic bodies in contact

ematical formulation adopted in the present work to calculate the contact pressure distribution at the interface is based on the elastic half-space theory for normal frictionless line contact problems (Johnson, 1985; Zhao *et al.*, 2014). According to this theory, when two homogeneous linear elastic bodies with positive radii of curvature are brought into contact, and their deformations

are small enough for the theory of linear elasticity to be applicable, the dimensions of the corresponding contact area will be small compared with the radii of curvature of the undeformed surfaces. Since the region of interest is located in the vicinity of the contact area, the stresses can be calculated to a good approximation by considering each body as a semi-infinite elastic solid bounded by a flat surface, i.e., an elastic half-space. In addition, the following conditions for normal contact problems are considered: (i) there is no penetration between the two bodies, and thus the distance between the two surfaces is zero in the contact area and positive outside it; (ii) the pressure is zero outside the contact area. Mathematically

$$\begin{aligned} &e(x) = 0 \qquad p(x) \geqslant 0 \qquad \text{(points in the contact area)} \\ &e(x) > 0 \qquad p(x) = 0 \qquad \text{(points outside the contact area)} \end{aligned} \tag{2.1}$$

In the above equations, $p(x)$ is the interfacial pressure at the point x, $e(x) = u(x) + g(x)$ is the normal distance between the points on the surfaces after deformation, $g(x)$ is the initial gap between the surfaces before deformation, and $u(x)$ is the normal displacement at the point x. Considering elastic half-spaces, the normal displacement at the point x, induced by the pressure $p(x)$ distributed in the interval $I = [x_a, x_b]$ is given by Wang and Zhu (2020) as

$$u(x) = \frac{-4}{\pi E'} \int_{x_a}^{x_b} \ln|x - x'| p(x')\, dx' \tag{2.2}$$

where E' is the effective Young's modulus $E' = 2/[(1-\nu_1^2)/E_1 + (1-\nu_2^2)/E_2]$, E_1 and E_2 are Young's moduli, and ν_1 and ν_2 are Poisson's ratios of the materials of body 1 and body 2, respectively. The total normal force F is calculated as

$$F = \int_I p(x)\, dx \tag{2.3}$$

The solution of the contact problem should satisfy the contact conditions of Eqs. (2.1) and involves calculation of Eq. (2.2), which is generally obtained numerically by discretising the interval I with a uniform mesh and approximating the pressure profile by a piecewise constant function (see, for instance, Venner, 1991). Thus, the discretised form of Eq. (2.2) can be written as

$$u_i = u(x_i) = \sum_{j=1}^{j=N} K_{ij} p_j \qquad \text{or} \qquad \mathbf{u} = \mathbf{K}\mathbf{p} \tag{2.4}$$

where N is the number of discrete points and K_{ij} are the influence coefficients that compound the influence matrix $\mathbf{K}$, i.e.

$$\begin{aligned} K_{ij} = \frac{-4}{\pi E'} \int_{x_j - h/2}^{x_j + h/2} \ln|x_i - x'|\, dx' = \frac{-4}{\pi E'} \Big\{ \Big|x_i - \Big(x_j + \frac{h}{2}\Big)\Big| \Big[\ln\Big|x_i - \Big(x_j + \frac{h}{2}\Big)\Big| - 1\Big] \\ - \Big|x_i - \Big(x_j - \frac{h}{2}\Big)\Big| \Big[\ln\Big|x_i - \Big(x_j - \frac{h}{2}\Big)\Big| - 1\Big] \Big\} \end{aligned} \tag{2.5}$$

To solve the numerical problem, an N-dimensional vector $\mathbf{x} = [x_1, x_2, \ldots, x_N]$ is constructed with the coordinates of discrete points in the interval $I = [x_a, x_b]$. Likewise, the values of pressure $p(x)$, the gap between the surfaces before deformation $g(x)$, the normal displacement $u(x)$ and the gap between the surfaces after deformation $e(x)$ at each point x_i are also represented by the N-dimensional vectors $\mathbf{p}$, $\mathbf{g}$, $\mathbf{u}$ and $\mathbf{e}$, respectively.

In the present approach, the initial gap at the reference point g_0 must be provided. Therefore, the vector $\mathbf{g}$ containing the initial gap can be calculated based on the shapes (radii of curvature) of the contacting bodies as

$$\mathbf{g} = g_0\mathbf{1} + \mathbf{g}_s \tag{2.6}$$

where $\mathbf{g}_s$ is the normal distance between the contact surfaces defined from the reference point, and $\mathbf{1}$ is an N-dimensional unit vector. The normal force is obtained from Eq. (2.3) after the solution of $p(x)$ is found. Notice that for smooth surfaces, to have contact between the bodies, g_0 should be negative ($g_0 < 0$).

To account for the effect of surface roughness in the elastic half-space contact modelling approach, the function r describing the roughness heights is considered to define the initial gap. Accordingly, Eq. (2.6) can be rewritten as

$$\mathbf{g} = g_0\mathbf{1} + \mathbf{g}_s + \mathbf{r} \tag{2.7}$$

where $\mathbf{r}$ is the N-dimensional vector containing the roughness heights at the discrete points x_i.

Figure 2 depicts the initial undeformed contact geometry between a rough elastic flat surface (body 1 in Fig. 2) and a smooth rigid plane (body 2 in Fig. 2). It is important to remark that considering one of the surfaces smooth and rigid does not restrict the applicability of the current modelling approach, since two rough elastic surfaces can be transformed into the contact problem between a rough surface and a plane using equivalent parameters (Barber, 2018).

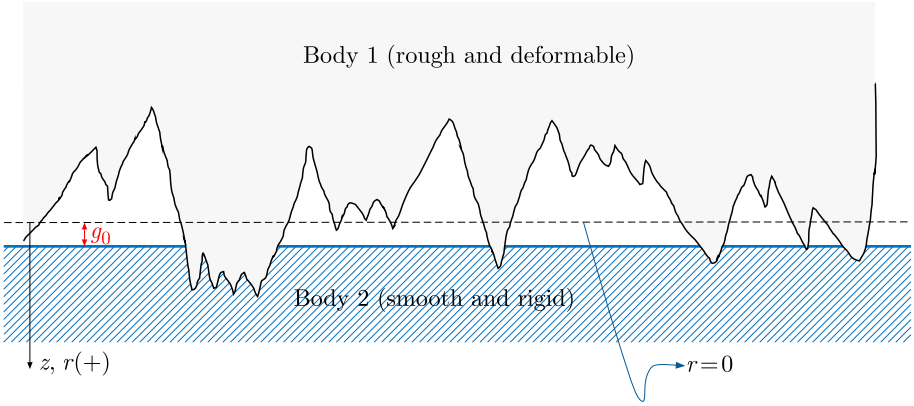

Fig. 2. Schematic representation of the initial undeformed contact gap between a rough flat elastic surface and a smooth rigid plane

2.2. Elastic normal contact problem as a linear complementarity problem

The contact conditions defined in Eqs. (2.1), and the distance between the contact surfaces after deformation can be written in discretised vector forms using Eq. (2.4) as

$$p_i e_i = 0 \rightarrow \mathbf{p}^{\mathrm{T}}\mathbf{e} = 0 \qquad \mathbf{e} = \mathbf{K}\mathbf{p} + \mathbf{g} \tag{2.8}$$

Therefore, to find the pressures at the discrete points, the following system of equations must be satisfied

$$\mathbf{e} = \mathbf{K}\mathbf{p} + \mathbf{g} \qquad \mathbf{p}^{\mathrm{T}}\mathbf{e} = 0 \qquad \mathbf{p}, \mathbf{e} \geqslant \mathbf{0} \tag{2.9}$$

The above equations can be identified as a linear complementarity problem (LCP). An important property of this LCP is that, as $\mathbf{K}$ is symmetric and positive definite, the solution is unique

(Bemporad and Paggi, 2015). The LCP described by Eq. (2.9) can be written as the following quadratic optimisation problem

$$\min_{\mathbf{p}} f(\mathbf{p}) \rightarrow \min_{\mathbf{p}}(\mathbf{p}^{\mathrm{T}}\mathbf{K}\mathbf{p} + \mathbf{p}^{\mathrm{T}}\mathbf{g})$$
$$\text{subject to: } \begin{cases} \mathbf{K}\mathbf{p} + \mathbf{g} \geqslant \mathbf{0} \\ \mathbf{p} \geqslant \mathbf{0} \end{cases} \tag{2.10}$$

The optimisation problem described in Eq. (2.10) is solved in Matlab using quadratic programming and an interior point algorithm presented in Byrd *et al.* (1999) and Nocedal and Wright (2006).

3. Numerical results and discussion

This Section discusses the numerical results obtained with the proposed calculation method for contact pressure of the three case studies. First, the profile of an analytical wavy surface is considered. Afterwards, the roughness profiles of two real engineering surfaces obtained from optical profilometry are analysed. For all cases, body 1 (the upper body) is assumed rough and body 2 (the lower one) smooth, following the formulation presented in Section 2.

3.1. Analytical wavy profile

This case evaluates the proposed calculation method for a wavy analytical profile. The geometric and material properties of the two contact bodies are shown in Table 1.

Table 1. Parameters for simulations of the analytical wavy profile

Body	Radius of curvature [mm]	Young's modulus [Pa]	Poisson's ratio [–]
1	20	$210 \cdot 10^9$	0.3
2	50	$210 \cdot 10^9$	0.3

The undulation of the wavy profile is chosen such that the peak heights are about 10 times smaller than the initial distance $g_0 = -0.01\,\mathrm{mm}$. Mathematically, this undulation is prescribed as

$$r(x) = 0.001\cos(50x) \qquad x \in [-1\,\mathrm{mm}, 1\,\mathrm{mm}] \tag{3.1}$$

To analyse the influence of the mesh discretization, simulations with meshes containing 64, 256 and 1024 nodes have been performed, and the results are summarised in Table 2. Figure 3 depicts the distance between the bodies in the initial condition. While the total force and contact width vary little as the number of nodes increases, the maximum pressure increases with the number of nodes. This increase can be explained by the highly accurate representation of the profile waviness as the mesh is refined, which yields a localized decrease in the real contact area and an increase in the local pressure.

Figures 4 show the pressure and gap distributions between the contact surfaces before and after contact for different meshes (64, 256 and 1024 nodes, respectively). The horizontal axis is normalised by a half-width of the Hertzian contact ($\overline{x} = x/b$). The contact pressure is normalised by its maximum value ($\overline{p} = p/p_{max}$) and is represented by the solid black line. The dotted blue and solid red lines represent the normalised initial ($\overline{g} = gR/b^2$) and final ($\overline{e} = eR/b^2$) gaps, respectively, where $R = 1/(R_1^{-1} + R_2^{-1})$ is the reduced radius of curvature, and R_1 and R_2 are the radii of curvature of body 1 and body 2.

Table 2. Simulation results of the analytical wavy profile.

No. of nodes	Normal force [N/mm]	Maximum pressure [MPa]	Contact width [mm]
64	856.7	2936	0.365
256	851.2	3991	0.341
1024	851.2	4036	0.333

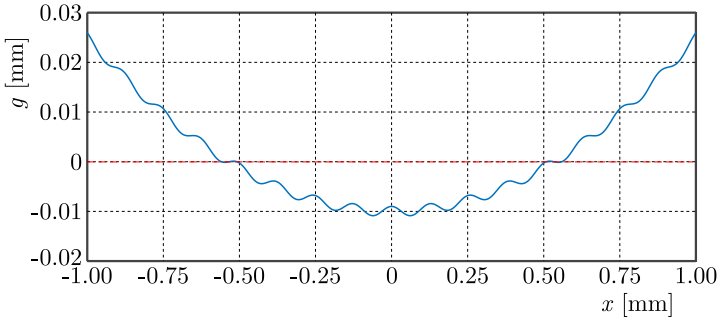

Fig. 3. Initial gap for the virtual wavy profile

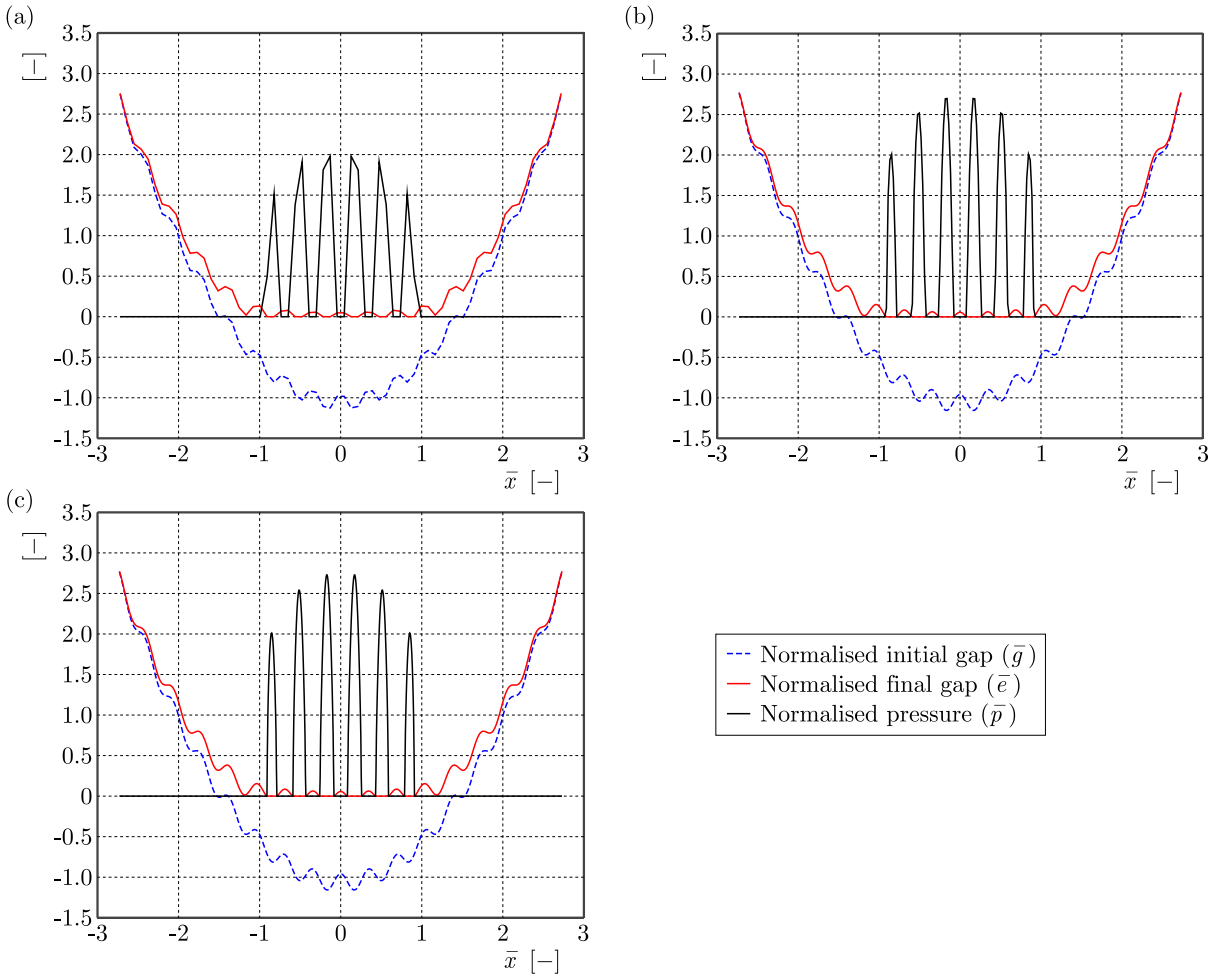

Fig. 4. Initial and final gaps and contact pressure for the analytical wavy profile. Results for meshes with (a) 64, (b) 256 and (c) 1024 nodes. All quantities are normalised

Overall, as can be observed in Fig. 4, wherever the pressure is nonzero and positive ($\overline{p} > 0$) the final gap is zero ($\overline{e} = 0$), and wherever the final gap is positive ($\overline{e} > 0$), the pressure is zero ($\overline{p} = 0$), thus satisfying the normal contact conditions of Eqs. (2.1). Figure 4 also shows the contact region between the normalised interval $\overline{x} \in [-1, 1]$. The pressure has a symmetrical distribution with six peaks, the largest being closer to the contact centre. Outside the contact region, as expected, the pressure is null. The pressure profile obtained with the 64-nodes mesh (Fig. 4a) is not smooth, and the maximum pressure is lower than those of the refined meshes. The pressure increases more smoothly with the 256-nodes mesh (Fig. 4b) but shows a flattening at the peaks. When the mesh discretization is increased to 1024 nodes (Fig. 4c), the entire pressure distribution becomes smooth, especially at the local maxima (peaks). In this latter case, the pressure peaks are also higher than those obtained with coarser meshes. This trend is because the greater the number of nodes, the more accurate the profile representation and solution near the peaks.

3.2. Real engineering surfaces

The cases presented below aim at evaluating the proposed calculation method for real engineering surfaces. To this end, a cylinder liner surface topography of an internal combustion engine and a 1200-grit sandpaper polished surface are considered. Both surfaces have been measured with 3D optical profilometry; the samples have 0.8×0.8 mm and 702×702 mesh points. The properties of the two surfaces are summarized in Table 3.

Table 3. Parameters for simulations of real engineering surfaces

Body	Radius of curvature [mm]	Young's modulus [Pa]	Poisson's ratio [–]
1	1000	$210 \cdot 10^9$	0.3
2	1000	$210 \cdot 10^9$	0.3

To perform 1D simulations, five profiles in the y-direction are considered. The initial distance g_0 is chosen to be approximately 0.2 times the standard deviation of the roughness heights. This value is defined following preliminary simulations and is intended to ensure that the real contact area is 4% to 10% of the apparent area. The real area is estimated by identifying and counting the regions of the discretized domain where the pressure is nonzero.

3.2.1. Surface of the cylinder of an internal combustion engine

Figure 5 shows, in three-dimensional and top views, the roughness profile obtained from measurements in a mesh of 702×702 points on a sample of the surface of the cylinder of an internal combustion engine.

In order to map the behaviour of the entire rough surface, analyses have been carried out in five cross-sections with discretization points corresponding to those used to measure the roughness profile (702 points). The sections were made parallel to the x axis, at positions $y = 0$; $y = 0.2$; $y = 0.4$; $y = 0.6$ and $y = 0.8$ mm. The initial reference gap value used was $g_0 = 9 \cdot 10^{-5}$ mm.

Table 4 shows, for different sections, the force and maximum pressure obtained in the simulations and height of the highest roughness peak in the section. The section where the highest contact force, 48 N/mm, occurs is the section with the highest roughness peak (section $y = 0.2$ mm), and sections that have the lowest force values (sections $y = 0.6$ and $y = 0.8$ mm) are also the sections where the highest roughness peaks are smaller than in the other sections. The same behaviour does not occur in the case of maximum pressure, i.e., there is no direct relationship

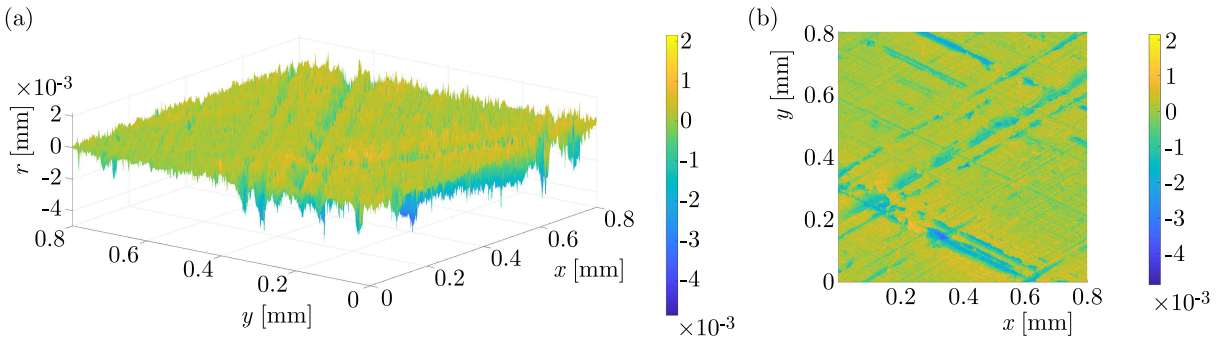

Fig. 5. Roughness profile of the surface of the cylinder of an internal combustion engine (702 × 702 mesh): (a) three-dimensional view, (b) top view – xy plane

Table 4. Results of simulations of the surface of the cylinder of an internal combustion engine

y [mm]	Force [N/mm]	Maximum pressure [MPa]	Highest roughness peak [mm]
0.0	35	6035	$7.0 \cdot 10^{-4}$
0.2	48	6480	$9.0 \cdot 10^{-4}$
0.4	32	8689	$7.2 \cdot 10^{-4}$
0.6	31	5181	$6.4 \cdot 10^{-4}$
0.8	31	5189	$6.4 \cdot 10^{-4}$

between the maximum pressure and the highest roughness peak, which occurs at $y = 0.4$ mm at the position $x = 0$.

Figure 6 shows, for the central section ($y = 0.4$ mm), the initial gap (dotted blue line) and the normal distance of each point on the surface after deformation (solid blue line) normalised by the maximum initial gap value[1]. The contact pressure (solid red line) normalised by its maximum

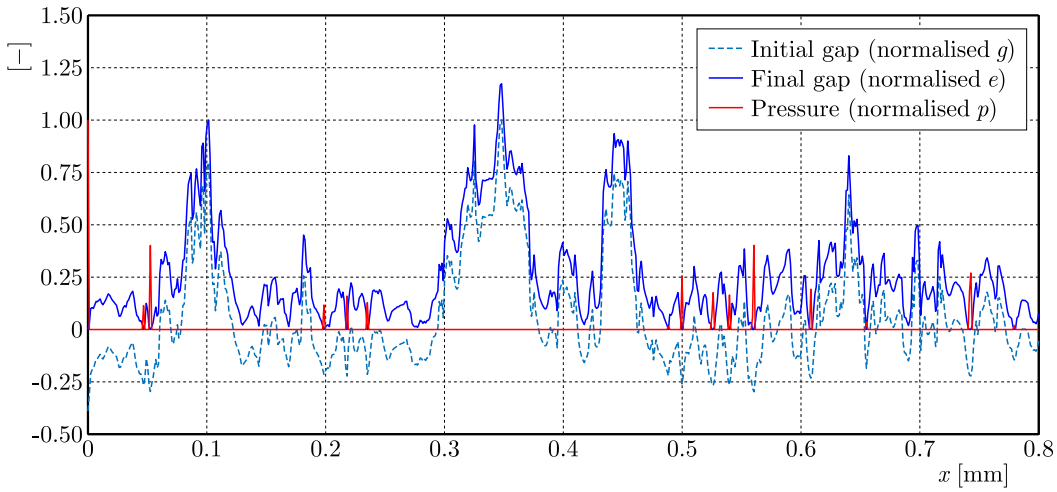

Fig. 6. Normalised initial and final gaps and normalised contact pressure for simulation of the surface of the cylinder of an internal combustion engine (section $y = 0.4$ mm)

value is also shown. From this figure, it can be noted that pressure occurs only where the final distance between the bodies is zero, i.e., where there is contact. Moreover, as expected, the final

[1]It is worth noting here that for this problem and the problem presented in Section 3.2.3 (i.e., for real engineering surfaces cases), the normalisation of the initial and final gaps (normalisations of g and e, respectively) are different from those used for the problem of Section 3.1. This is done aiming for clarity in presentation of the results.

shape of the piece undergoes changes. In addition, within a section, the point where the highest pressure occurs is the region with the highest roughness peaks, which corresponds to the highest initial "penetration", as can be seen when the initial gap (dotted blue line) and pressure (solid red line) are compared. For brevity, a graph of only a representative section is presented and discussed here and in Section 3.2.2.

3.2.2. Surface polished with 1200-grit sandpaper

Figure 7 presents, in three-dimensional and top views, the roughness profile obtained from measurements in a mesh of 702 × 702 points on a sample of a surface polished with a 1200-grit sandpaper. Because of the polishing, the roughness peaks are smaller compared with those of the surface of the cylinder of an internal combustion engine.

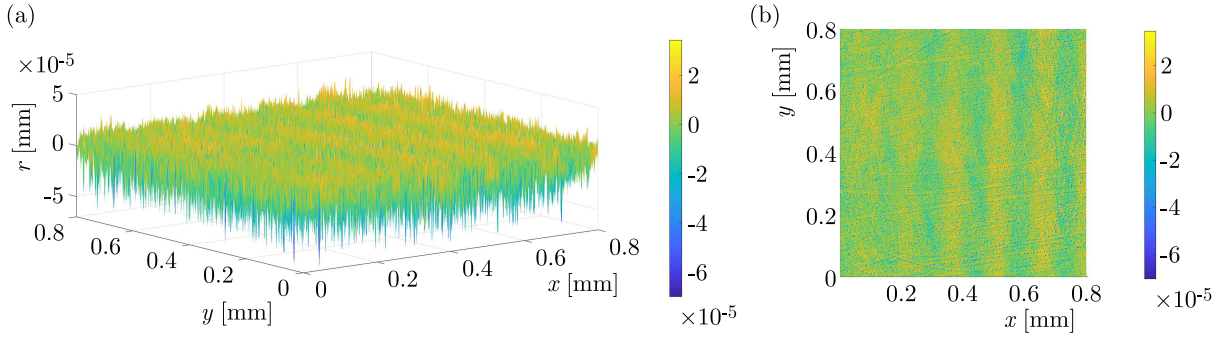

Fig. 7. Roughness profile of the surface polished with a 1200-grit sandpaper (702 × 702 mesh): (a) three-dimensional view, (b) top view – xy plane

As performed for the surface of the cylinder, simulations have been carried out in five sections. The initial reference gap value used was $g_0 = 1.4 \cdot 10^{-6}$ mm.

Table 5 presents, for different sections, the force and maximum pressure obtained from the simulations and the height of the highest roughness peak in the section.

Table 5. Results of simulations of the surface polished with a 1200-grit sandpaper

y [mm]	Force [N/mm]	Maximum pressure [MPa]	Highest roughness peak [mm]
0.0	1.11	309	$2.0 \cdot 10^{-5}$
0.2	1.04	153	$1.6 \cdot 10^{-5}$
0.4	1.20	203	$2.0 \cdot 10^{-5}$
0.6	1.11	310	$2.0 \cdot 10^{-5}$
0.8	0.86	114	$1.3 \cdot 10^{-6}$

Figure 8 shows, for the central section ($y = 0.4$ mm), the initial gap (dotted blue line) and the normal distance of each point on the surface after deformation (solid blue line) normalised by the maximum initial gap value. The contact pressure normalised by its maximum value is also shown (solid red line).

Because the surface has been polished, the roughness peaks have similar heights in all the sections, and there are only a few isolated peaks. This can also be observed in Table 5, where there are three sections, $y = 0$ mm, $y = 0.4$ mm and $y = 0.6$ mm: the highest peak measures $2.0 \cdot 10^{-5}$ mm, and two other sections have lower values, but still close ($1.3 \cdot 10^{-5}$ and $2.0 \cdot 10^{-5}$ mm). Thus, there is no significant variation in the contact force between the sections, and the highest value is at $y = 0.4$ mm. The highest maximum pressure occurs in the section with the highest

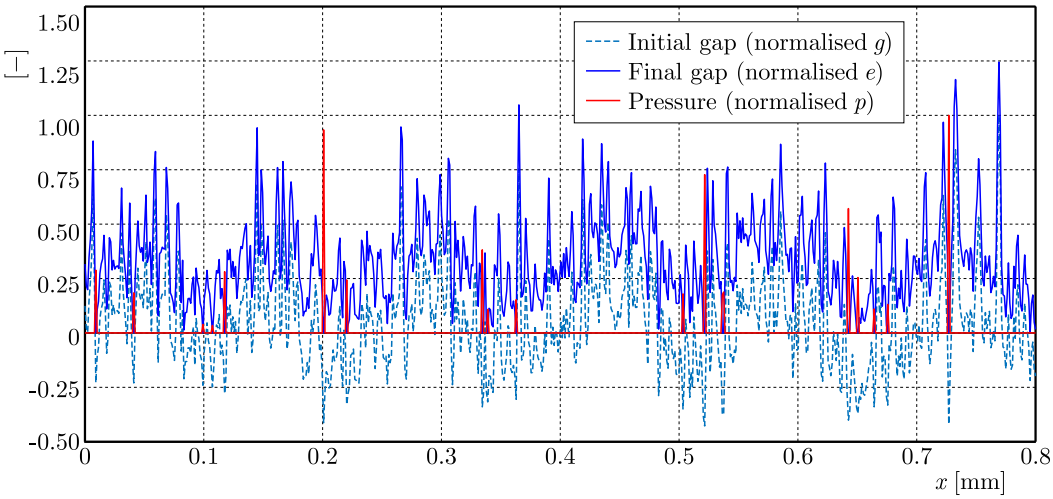

Fig. 8. Normalised initial and final gaps and normalised contact pressure for simulation of the surface polished with a 1200-grit sandpaper (section $y = 0.4\,\text{mm}$)

roughness peak ($y = 0.6\,\text{mm}$). As the heights of the peaks are more homogeneous than the peaks on the surface of the cylinder engine, the relationship between maximum the pressure and highest roughness peak is not so clear.

4. Concluding remarks

This work aims at developing and apply an efficient technique for determining contact pressure distribution between elastic bodies with rough surfaces. The corresponding problem is formulated as a linear complementarity problem (LCP), which is associated with an optimisation problem, and this is then solved using a quadratic programming strategy.

Problems with rough surfaces in a one-dimensional domain are analysed. Initially, a virtual surface is considered, i.e., with roughness generated by an analytic function, and then profiles of real engineering surfaces based on experimental roughness measurements are evaluated. Overall, the numerical results are coherent with what is observed in practice: the section where the highest contact force occurs is the one with the highest roughness peak, and the surfaces with higher roughness peaks have higher maximum pressures.

References

1. Barber J.R., 2018, Contact of rough surfaces, [In:] *Contact Mechanics. Solid Mechanics and its Applications*, Springer, **250**, 329-394

2. Bemporad A., Paggi M., 2015, Optimization algorithms for the solution of the frictionless normal contact between rough surfaces, *International Journal of Solid and Structures*, **69-70**, 94-105

3. Byrd R.H., Hribar M.E., Nocedal J., 1999, An interior point algorithm for large-scale non-linear programming, *SIAM Journal on Optimization*, **9**, 4, 877-900

4. Cottle R., Pang J., Stone R., 1992, *The Linear Complementarity Problem*, Philadelphia: Society for Industrial and Applied Mathematics

5. Fu S., Kor W.S., Cheng F., Seah L.K., 2020, In-situ measurement of surface roughness using chromatic confocal sensor, *Procedia CIRP*, **94**, 780-784

6. He X., Liu Z., Ripley L.B., Swensen V.L., Griffin-Wiesner I.J., Gulner B.R., Mcandrews G.R., Wieser R.J., Borovsky B.P., Wang Q.J., Kim S.H., 2021, Empirical relationship between interfacial shear stress and contact pressure in micro and macro-scale friction, *Tribology International*, **155**, 106780
7. Hills D.A., Nowell D., Sackfield A., 1993, *Mechanics of Elastics Contacts*, Butterworth-Heinemann
8. Jackson R.L., Green I., 2006, A statistical model of elasto-plastic asperity contact between rough surfaces, *Tribology International*, **39**, 9, 906-914
9. Johnson K.L., 1985, *Contact Mechanics*, Cambridge University Press
10. Josso B., Burton D.R., Lalor M.J., 2002, Frequency normalized wavelet transform for surface roughness analysis and characterization, *Wear*, **252**, 5-6, 491-500
11. Nocedal J., Wright S.J., 2006, *Numerical Optimization*, New York: Springer, 2a ed.
12. Persson B.N.J., 2006, Contact mechanics for randomly rough surfaces, *Surface Science Reports*, **61**, 4, 201-227
13. Rey V., Bleyer J., 2018, Stability analysis of rough surfaces in adhesive normal contact, *Computational Mechanics*, **62**, 1155-1167
14. Sushun K., 1995, The existence of the solution for linear complementary problem, *Applied Mathematics and Mechanics*, **16**, 7, 683-685
15. Venner C.H., 1991, Multilevel solution of the EHL line and point contact problems, PhD Thesis, University of Twente, Enschede, The Netherlands
16. Wang J., Zhu D., 2020, *Interfacial Mechanics: Theories and Methods for Contact and Lubrication*, New York: CRC Press, 1st ed.
17. Weber B., Suhina T., Junge T., Pastewka L., Brouwer A.M., Bonn D., 2018, Molecular probes reveal deviations from Amontons' law in multi-asperity frictional contacts, *Nature Communications*, **9**, 1, 888
18. Zhang F., Liu J., Ding X., Wang R., 2019, Experimental and finite element analyses of contact behaviors between non-transparent rough surfaces, *Journal of the Mechanics and Physics of Solids*, **126**, 87-100
19. Zhao J., Vollebregt E.A.H., Oosterlee W.C., 2014, A full multigrid method for linear complementarity problem arising from elastic normal contact problems, *Mathematical Modelling and Analysis*, **19**, 2, 216-240

Manuscript received March 20, 2022; accepted for print April 27, 2023

JOURNAL OF THEORETICAL AND APPLIED MECHANICS
61, 3, pp. 585-597, Warsaw 2023
https://doi.org/10.15632/jtam-pl/166466

SENSITIVITY TO GAUSS QUADRATURE OF ISOGEOMETRIC BOUNDARY ELEMENT METHOD FOR 2D POTENTIAL PROBLEMS

Ahlem Alia

Université de Lille, Centre National de la Recherche Scientifique, Centrale Lille,

Unité Mixte de Recherche 9013-LaMcube-Laboratoire de Mécanique, Multiphysique, Multiéchelle, Lille, France

e-mail: ahlem.alia@univ-lille.fr

Hasna Ben Said

Faculté des Sciences de Gafsa, Département des Filières Technologiques, Tunisia

IsoGeometric Analysis (IGA) is widely used because it links exact geometry to analysis. When IGA is applied within the Boundary Element framework (IGBEM), and under certain boundary conditions, discretization errors can be suppressed leading to an accurate estimation of the integration errors. By using the IGBEM for potential problems, the effect of Gauss quadrature on the accuracy of each term arising in the IGBEM is studied for smooth geometry under constant boundary conditions. The results show that the method of computing singular integrals in the IGBEM is efficient. Results can be improved by selecting optimal numbers of Gauss points for both integrals.

Keywords: potential problems, isogeometric analysis, boundary element method, Gauss quadrature

1. Introduction

In recent years, there has been an increasing interest in applying IsoGeometric Analysis (IGA) for mechanical problems such as solid mechanics (Chasapi *et al.*, 2022; Peng and Lian, 2022), fluid mechanics (Opstal *et al.*, 2015; Yan *et al.*, 2019), acoustics (Coox *et al.*, 2017; Alia, 2020; Alia *et al.*, 2022) and contact (Temizer *et al.*, 2011; Matzen *et al.*, 2013; Khanyile *et al.*, 2022). IGA has shown a superior precision over the conventional Finite Element Method (FEM) and Boundary Element Method (BEM) for many applications (Hughes *et al.*, 2005, 2010; Simpson *et al.*, 2012; An *et al.*, 2018). Contrary to these standard methods, IGA is based on the exact geometry because it links between the geometry design and mechanical analysis environments.

Due to Hughes (Hughes *et al.*, 2005), this numerical method uses NURBS basis functions of geometry to approximate unknowns. Since that pioneer work, other basis functions like Bsplines and Bézier have been used, and other specific algorithms have been developed for IGA. In fact, to discretize a problem, IGA is based on a patch, knot vector, control points and control variables entities. The control entities are not physical but only fictive entities. They are used to interpolate physical nodes and variables by using NURBS, Bsplines or Bézier functions. This is why, for instance, a new contact algorithm knot-to-surface has been specifically developed for IGA (Temizer *et al.*, 2011).

Studies on the accuracy of the standard BEM focused on some specific aspects such as the commonly applied rule of six elements per wavelength in acoustics for continuous elements (Marburg, 2002) and the position of collocation points on discontinuous elements (Marburg and Nolte, 2008). For 2D acoustic applications, Treeby and Pan (2009) have presented an interesting classification of BEM errors into three categories. The first category of errors originates from

discretization that is due to approximation of boundary variables, geometry, and their discontinuities. The second category of errors concerns quadrature ones because of the approximate evaluation of regular, singular and nearly singular integrals. Finally, the last category of errors is related to system resolution which exhibits ill-conditioned matrices at some irregular frequencies as well as additional errors due to the iterative solver. These three categories of errors are related to each other, so it is difficult to separate them. This is why Treeby and Pan (2009) proposed to set a global error constraint supposed to be appropriate within the engineering applications. Then they discussed precision of the method when that global error was maintained.

Some numerical aspects related to errors in IGA were analyzed in previous works (Simpson *et al.*, 2012; An *et al.*, 2018; Kostas *et al.*, 2017) including development of new quadrature formulae (Aimi *et al.*, 2018; Calabrò *et al.*, 2018) and the effect of Gauss quadrature on the accuracy of singular integrals (Peng and Lian, 2022). In fact, even if the geometry is exact, a small number of Gauss points can lead to wrong results as shown in (Alia, 2020) because the Gauss points play the role of acoustic source points. To our knowledge, there was no direct interest in estimating integration errors of different terms occurring in the boundary integral equation of potential problems when solved by the IsoGeometric Boundary Element Method (IGBEM) in the case of a standard Gauss quadrature.

The objective of this study is to identify the effect of the number of Gauss points on the accuracy of integral involving Green's function and the derivative of Green's function, separately. In fact, since in IGA simulation is performed on the exact geometry instead of the approximated one, we suppress the discretization errors by choosing constant boundary variables on a smooth geometry. In this article, before exploring in details the motioned numerical method (Section 3), we review the conventional BEM in Section 2. Finally, we validate the IGBEM results in Section 4 for an annular region before studying the influence of Gauss quadrature on the accuracy of integrals in the case of a circular domain.

2. Boundary element method for potential problems

Both the Laplace equation and the Green function are fundamental for the boundary integral formulation of potential problems (Katsikadelis, 2016). Laplace equation (2.1) governs the potential field ϕ in many problems like steady state heat conduction and potential flow inside a domain V limited by a boundary S (Liu, 2009)

$$\Delta\phi = 0 \quad \text{in} \quad V \tag{2.1}$$

The Dirichlet and Neumann boundary conditions are given, respectively, by

$$\phi = \phi_D \quad \text{on} \quad S_D \qquad q = \frac{\partial\phi}{\partial n} = q_N \quad \text{on} \quad S_N \tag{2.2}$$

where $S = S_D \cup S_N$, n is the boundary normal pointing away the domain, and q is the normal derivative of ϕ.

By using the second Green identity, the well-known Boundary Integral Equation (BIE) can be derived from the preceding boundary value problem and expressed as in the following (Liu, 2009; Wu, 2000)

$$\int_S \Big(G(P,Q)\frac{\partial\phi(P)}{\partial n} - \phi(P)\frac{\partial G(P,Q)}{\partial n} \Big)\, dS(P) = C_Q\phi(Q)$$

$$C_Q = \begin{cases} 1 & Q \in V \\ \dfrac{1}{2} & Q \in S_{smooth} \\ 0 & Q \notin (S \cup V) \end{cases} \tag{2.3}$$

Green's function is expressed in two dimensions as $G(P,Q) = -(1/2\pi)\log r$ (Liu, 2009). Here r is the distance between two points Q and P. The BIE is to be used with the Neumann condition (describing $\partial\phi_N(P)/\partial n$ on S_N) and Dirichlet condition (describing $\phi_D(P)$ on S_D).

To solve numerically the BIE for unknown boundary variables, the geometry is discretized into ne elements and nd nodes. In the case of isoparametric boundary elements, both geometry and boundary variables are represented by the same Lagrange shape functions N_i. Over an element, a varying quantity f is approximated by $f = \sum_{i=1}^{\ell} f_i N_i(u)$ where u is the local coordinate $(-1 \leqslant u \leqslant 1)$ and ℓ is the number of nodes per Lagrange element. f can be the potential, derivative of the potential, or node position given by x and y. The discretized form of the BIE can be written as

$$\Big(\sum_{e=1}^{ne}\sum_{i=1}^{\ell}\int_{-1}^{\ell} G(P,Q)N_i J_e\, d\xi\Big)q_i + \Big(\sum_{e=1}^{ne}\sum_{i=1}^{\ell}\int_{-1}^{1}\frac{\partial G(P,Q)}{\partial n}N_i J_e\, d\xi\Big)\phi_i = C_Q\phi(Q) \tag{2.4}$$

where J_e is the Jacobian of transformation of the e-th element.

Despite the introduction of these boundary conditions, only half of the boundary values are known from the boundary conditions (Wu, 2000). The other half needs to be calculated by collocating the point Q on the entire boundary. Collocation consists in placing the point Q successively in each node i of the boundary. For each collocation node i and element S_j, the boundary integration based on Eq. (2.4) is performed to produce two elementary vectors in 2D problems denoted by g_i and h_i. After assembling the elementary vectors into global matrices and then arranging them in such a way that all the unknowns are located on the left-hand side, solving the obtained system enables one to calculate the boundary unknowns (Wu, 2000).

Usually, the used geometry introduces errors because it is not exact. In what follows, the exact geometry based on NURBS (Non-Uniform Rational BSplines) combined to BEM is adopted to suppress the errors due to domain approximation. The next Section concerns the definition of the NURBS basis functions and their introduction into the BEM.

3. Isogeometric boundary element method

3.1. Preliminary notions

Among the curves designed by control points, Bsplines and NURBS can be cited. It is known that Bsplines are very flexible in geometry design. Their flexibility is originating from their basis functions $N_{i,p}$ which have quasi-local control. These basis functions are different from the shape functions N_i of the standard BEM. Note the order of interpolation p in $N_{i,p}$. The basis functions $N_{i,p}$ are constructed for a knot vector, $\mathbf{E} = \{u_1, u_2, \ldots, u_{n+p+1}\}$, a non-decreasing sequence of coordinates in the parametric space. Each knot vector corresponds to a patch of elements. The knot vector can be uniform (nodes are equally-spaced in the parametric space) or not (repeated nodes) (Hughes *et al.*, 2005). It serves to divide the parametric space into elements and to modify the shape of the curve.

Equation (3.1) defines a Bspline curve T of the order p (Hughes *et al.*, 2005)

$$T(u) = \sum_{i=1}^{m} N_{i,p}(u)P_i = \mathbf{P}^{\mathrm{T}}\mathbf{N}(u) \tag{3.1}$$

where P_i are the Bspline control points, m is the number of both basis functions and control points. The basis functions $N_{i,p}$ are calculated by the following recursive expression (Hughes *et al.*, 2005)

$$N_{i,0}(u) = \begin{cases} 1 & u_i \leqslant u \leqslant u_{i+1} \\ 0 & \text{otherwise} \end{cases}$$
$$N_{i,p}(u) = \frac{u - u_i}{u_{i+p} - u_i} N_{i,p-1}(u) + \frac{u_{i+p+1} - u}{u_{i+p+1} - u_{i+1}} N_{i+1,p-1}(u) \qquad p \geqslant 1 \tag{3.2}$$

The most important properties of the Bspline basis functions are the partition of unity, Eq. (3.3), linear independence, Eq. $(3.3)_2$, and its quasi-local support because some control points influence $p+1$ elements

$$\sum_{i=1}^{m} N_{i,p}(u) = 1$$
$$\sum_{i=1}^{m} a_i N_{i,p}(u) = 0 \iff \forall i \quad a_i = 0 \tag{3.3}$$

The rational basis functions of NURBS are defined as following

$$R_{i,p}(u) = \frac{w_i N_{i,p}(u)}{\sum_{i=1}^{m} w_i N_{i,p}(u)} = \frac{\mathbf{WN}(u)}{W(u)} \tag{3.4}$$

where w_i is the weight of the i-th basis function and $W(u)$ is the weight function. Both Bsplines and NURBS shared the same properties listed above, and the NURBS curve is deduced by

$$T(u) = \sum_{i=1}^{m} R_{i,p}(u) P_i = \mathbf{P}^{\mathrm{T}} \mathbf{R}(u) \tag{3.5}$$

Besides the flexibility of Bsplines and NURBS, they present an important feature of easy refinement without deploying a great effort. In fact, three types of refinement can be used in IGA (Hughes *et al.*, 2005). In h-refinement, the knot insertion consists in adding new knots and, therefore, new elements. Each new element is located between knots of different values. During this process, the number of control points is increased by one after each knot insertion. Consequently, the control points require to be redefined at each new insertion. Moreover, the new basis functions have to be recalculated for the new knot vector. p-refinement consists of the order elevation by increasing the multiplicity of each knot component by one. This increases the number of control points and basis functions but keeps the geometry and parameterization unchanged. The last type, called k-refinement, is a combination of both knot insertion and order elevation.

3.2. Computational aspects related to IGBEM implementation

Now it is easy to link the geometry design and the analysis based on the BEM environment. Let us consider a geometry that is defined by NURBS. For a set of control points $P_i(x_i^P, y_i^P)$, the geometry of the domain is defined by

$$x = \sum_{i=1}^{m} R_{i,p}(u) x_i^P \qquad y = \sum_{i=1}^{m} R_{i,p}(u) y_i^P \tag{3.6}$$

where x, y are the coordinates of a boundary point, u is its parametric coordinate, and m is the number of control points per element.

In IGA, the potential and its normal derivative are expressed in Eq. (3.7) by the same basis functions that are used to define the geometry

$$\phi = \sum_{i=1}^{m} R_{i,p}(u) \phi_i^P \qquad \frac{\partial \phi}{\partial n} = q = \sum_{i=1}^{m} R_{i,p}(u) q_i^P \tag{3.7}$$

Unlike the traditional BEM, ϕ_i^p and q_i^p represent the potential and its normal derivative at the control points, respectively. For each collocation point P_i and element, S_j^e correspond two elementary vectors h_i and g_i given by

$$\begin{aligned} h_i &= \int\limits_{S_j^e} \frac{\partial G}{\partial n} R_{i,p}(u)\, dS = \int\limits_{-1}^{1} \frac{\partial G}{\partial n} R_{i,p} J_e\, du \\ g_i &= \int\limits_{S_j^e} G R_{i,p}(u)\, dS = \int\limits_{-1}^{1} G R_{i,p} J_e\, du \end{aligned} \tag{3.8}$$

Since the control points do not necessary belong to the boundary, they cannot play the role of collocation points in the IGBEM. Instead, Greville abscissae are used as collocation points for the IGBEM (Kostas *et al.*, 2017; Johnson, 2005). Their expression is given by

$$u_i^{col} = \sum_{j=1}^{p} \frac{u_{i+j}}{p} \tag{3.9}$$

where u_i is the i-th component of the knot vector.

When the collocation point Q_i does not belong to the element S_j^e, the integral is regular and Gauss quadrature can be used as expressed in Eq. (3.10). In Eq. (3.10), $f_i^{(1)} = (\partial G/\partial n) R_{i,p}(u_k) J_e$ and $f_i^{(2)} = G R_{i,p}(u_k) J$ are two functions evaluated at the k-th Gauss point u_k of weight w_k. Moreover, $nGpR$ represents the number of Gauss points used in the regular integration

$$h_i = \sum_{k=1}^{nGpR} f_i^{(1)} w_k \qquad g_i = \sum_{k=1}^{nGpR} f_i^{(2)} w_k \tag{3.10}$$

To show the superiority of the IGBEM over BEM in the case of regular integrals, we consider convergence of $I_0 = \int dS/r^2$ over a quarter circle of radius 2 (Fig. 1). The calculation of the L_2 norm of the relative error is based on the analytical scheme provided by Mahajerin (1983) for 19 points denoted by P in Fig. 1.

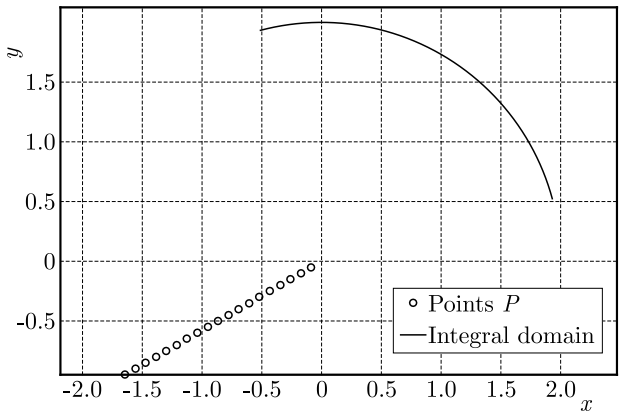

Fig. 1. Geometry of the quarter circle and location of points used to calculate integral $I_0 = \int dS/r^2$

Figure 2a represents a clear illustration of the accuracy of the IGBEM. Actually, only 4 elements and 4 Gauss points are required to integrate $1/r^2$ over the quarter circle. 4 Gauss points and 10 elements are sufficient to achieve an error of the machine precision order. With only 2 Gauss points and 10 elements, we obtain an error of the order of 10^{-8}. On the other hand, the BEM seems to be less accurate than the IGBEM. In fact, BEM errors are greater than those

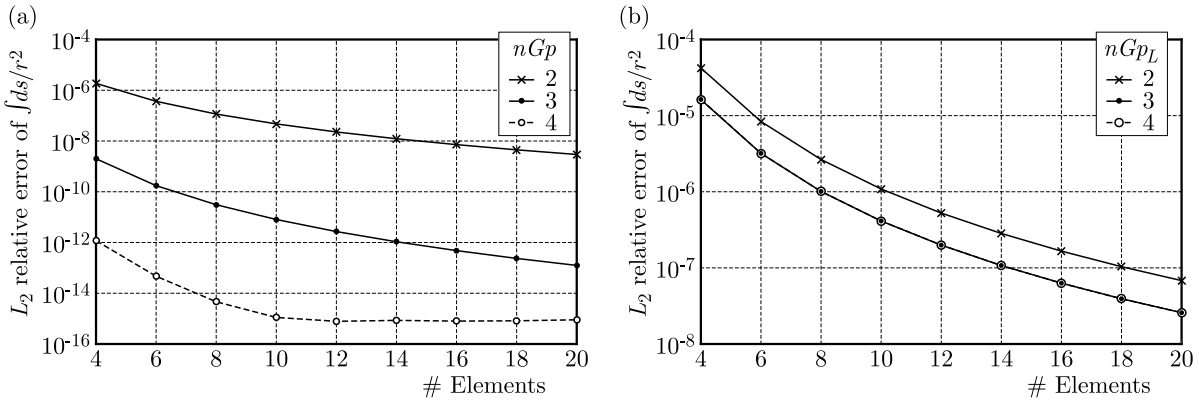

Fig. 2. Errors in the evaluation of $I_0 = \int dS/r^2$ over the quarter circle with respect to the elements number for different numbers of Gauss points in the case of (a) IGBEM and (b) BEM

of the IGBEM (Fig. 2b). In the BEM, the minimum error of the order of 10^{-7} is archived for 3 Gauss points and cannot be improved anymore by increasing the number of Gauss points.

When the collocation point Q_i belongs to the element S_j, the integral is singular. To overcome the singularity problem, the procedure proposed initially by Wu (2000) for the BEM is applied and adopted here to the IGBEM. It consists in dividing the element at the collocation point into left and right regions and improving the convergence rate by considering two successive changes of variables (1) $z^2 = \varepsilon(u_p - u)$, and (2) $z = \sqrt{1+\varepsilon u_p}(1+\eta)/2$ where u_p is the position of the collocation point in the parametric space. The integration over the left region $\varepsilon = +1$ is performed separately from the right region $\varepsilon = -1$ in Eq. (3.11). For both regions, we use the same number of Gauss points $nGpS$. These variable changes apply also to the elementary vector h_i. Therefore, Eq. (3.11) written for g_i can be extended to h_i by only replacing the Green function by its normal derivative

$$g_i^{(\varepsilon)} = \int_0^{\sqrt{1+\varepsilon u_p}} GR_{i,p} J_e 2z \, dz = \int_{-1}^{1} GR_{i,p} J_e 2z \frac{dz}{d\eta} \, d\eta \tag{3.11}$$

Finally, when the collocation point lies close to the element but not in, then the integral is nearly singular. In this paper, we choose to treat the nearly singular integrals exactly as the regular ones without any additional treatment. The consequences of this choice will be discussed later. In what follows, the number of degrees of freedom is denoted by $nDOF$ for IGBEM and $nDOF_L$ for the BEM, where L is used for Lagrange.

4. Results

The previous equations have been implemented to handle several patches and closed domains, and numerical simulation is performed only for quadratic elements. To validate the IGBEM result, we consider an annular region for which the potential field ϕ_a is prescribed on the inner boundary S_a of radius a. The outer boundary S_b of radius b is subjected to the normal derivative $\partial\phi_b/\partial n$.

The analytical solution of this axisymmetric problem is given by (Liu, 2009)

$$\phi(r) = \phi_a + b\frac{\partial \phi_b}{\partial n} \log \frac{r}{a}$$

In simulation, we used the following parameters: $a = 1$ with $\phi_a = 100$, and $b = 2$ with $\partial\phi_b/\partial n = 200$.

For a clear illustration of the IGBEM mesh, a small number of elements of the same length ($ne = 24$, $nDOF = 32$) have been used to plot Fig. 3a in the case of the IGBEM. Figure 3b shows the internal field points used to calculate the potential field inside the annular region. These internal field points are located between $r = 1.1$ and $r = 1.9$.

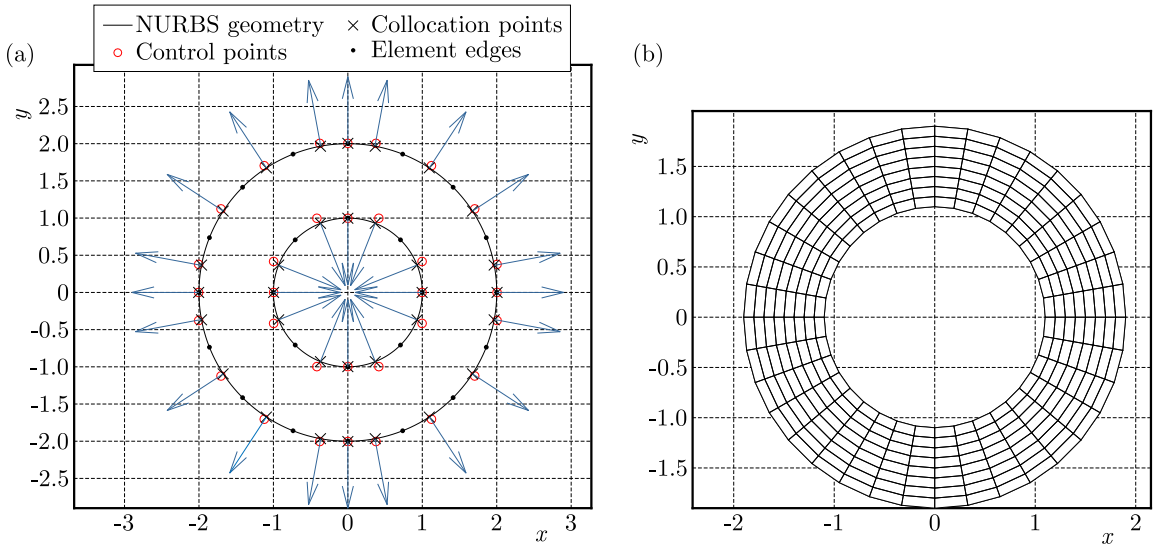

Fig. 3. (a) NURBS-based geometry and the IGBEM mesh of the annular region, (b) mesh of the internal points

Contrary to the BEM, IGBEM looks to be in good agreement with the analytical solution in terms of potential distribution inside the annular region (Fig. 4). Note that the BEM result has been obtained for the same number and type of elements, i.e. 24 quadratic elements but with $nDOF_L = 48$.

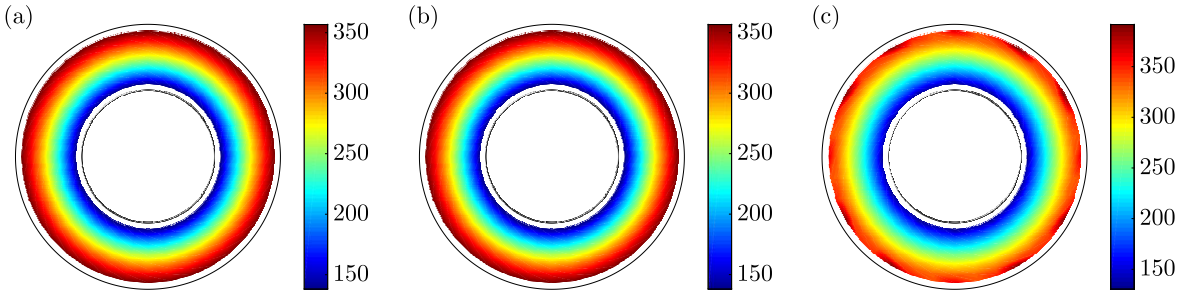

Fig. 4. (Color online) Potential distribution calculated: (a) analytically, (b) by IGBEM, (c) BEM

For a better comparison, the relative error for the field points located on x-axis is plotted in Fig. 5. One can see that the quality of the IGBEM solution is better than that of the BEM but the IGBEM appears less accurate for points close to the boundaries in comparison to points located far from the boundary. Consequently, we can conclude that: (1) nearly singular integrals are poorly integrated and (2) treatment of the singular integrals is sufficient. To check this initial conclusion, leting examine in detail the errors made separately on the integrals of the Green function and its derivative noted, respectively, by

$$I_1 = \int G(P,q)\, dS \qquad I_2 = \int \frac{\partial G}{\partial n}(P,q)\, dS$$

In what follows, instead of computing I_1 and I_2 over the annular region, the geometry is simplified. From now on, let us limit the geometry to only the outer boundary of the last example, i.e. a circle of radius 2 as shown in Fig. 6.

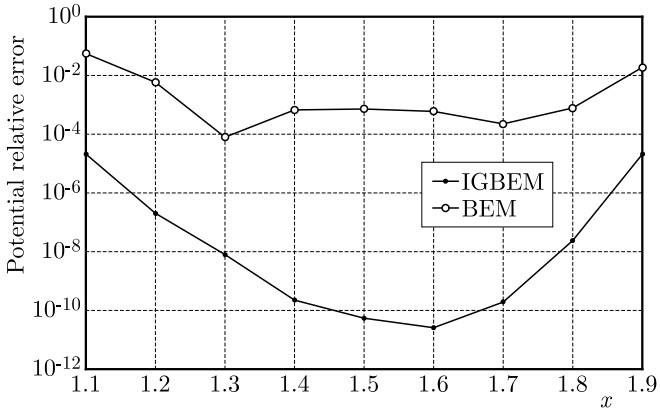

Fig. 5. Errors in the potential at internal field points located on the x-axis for IGBEM and BEM

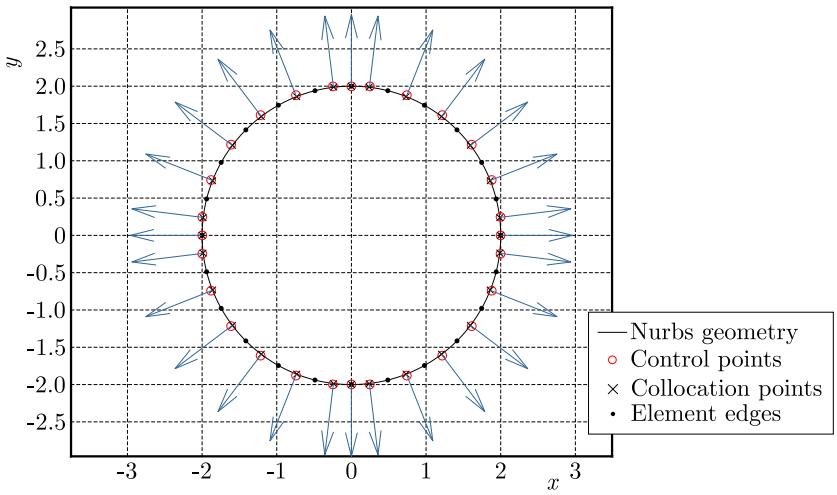

Fig. 6. NURBS-based geometry and the IGBEM mesh of the circle

4.1. Errors in $I_1 = \int [\partial G(Q,P)/\partial n]\, dS(P)$

To examine the quadrature errors, we considered the case of an internal potential problem consisting of a circle of radius 2. A simple way to study the quadrature error in the term involving the normal derivative of Green's function $I_1 = \int [\partial G(P,Q)/\partial n]\, dS(P)$ is to calculate $C_Q = -\int [\partial G(P,Q)/\partial n]\, dS(P)$. The exact value of C_Q is given by Eq. (2.3).

To show the superior precision of the IGBEM over BEM, the variation of the regular integral error of C_Q at an internal point as it gradually approaches the boundary of the circle along the x direction is plotted in Fig. 7a. Note that in this figure, x varies from -1.99 to 1.99 with a space step of 0.0025 in order to show all variations. As expected, the IGBEM behaves better than the BEM. In fact, to obtain the same error, the IGBEM requires almost a half of the number of degrees of freedom required by the BEM. When the point is far from the boundary, the regular integral error is of the order of the machine precision (Fig. 7a) but it increases as the mesh gets coarser (Fig. 7b).

For points close to the boundary, the integral is nearly singular. One way to improve the precision is to increase the number of Gauss points for all elements (Fig. 8a). The other way is to gradually increase the number of Gauss points as the point gets closer to the integration element (Fig. 8b). To limit the maximum value of error to 10^{-8} in Fig. 8b almost everywhere, 30 Gauss points have been used to the points close to the boundary (within the size of an element). According to their distance from the boundary, 8, 6, or 4 Gauss points have been considered for the other points.

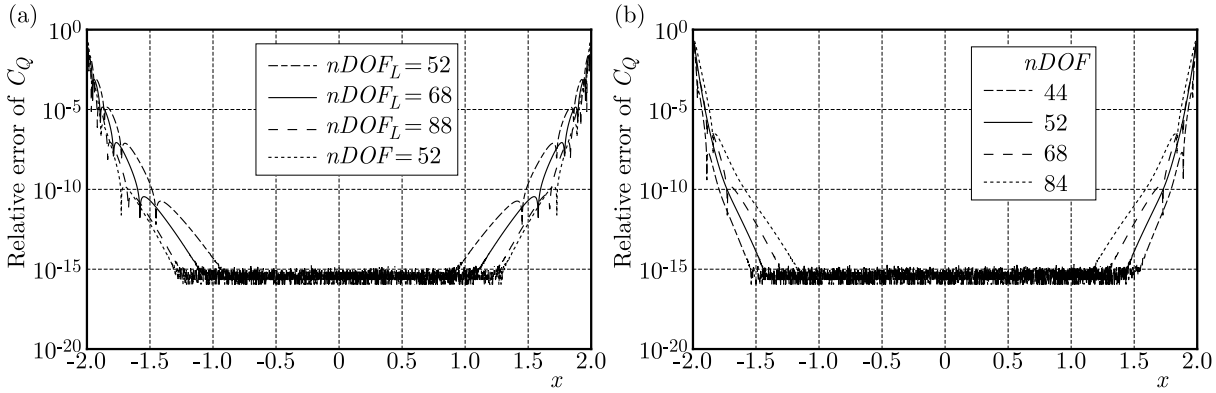

Fig. 7. Variation of errors of C_Q at an internal point as it gradually approaches the boundary of a circle: (a) comparison between the BEM and IGBEM for 6 Gauss points per quadratic element, (b) effect of DOF number for 6 Gauss points per quadratic element. $nDOF$ and $nDOF_L$ denote the DOF numbers in IGBEM and BEM, respectively

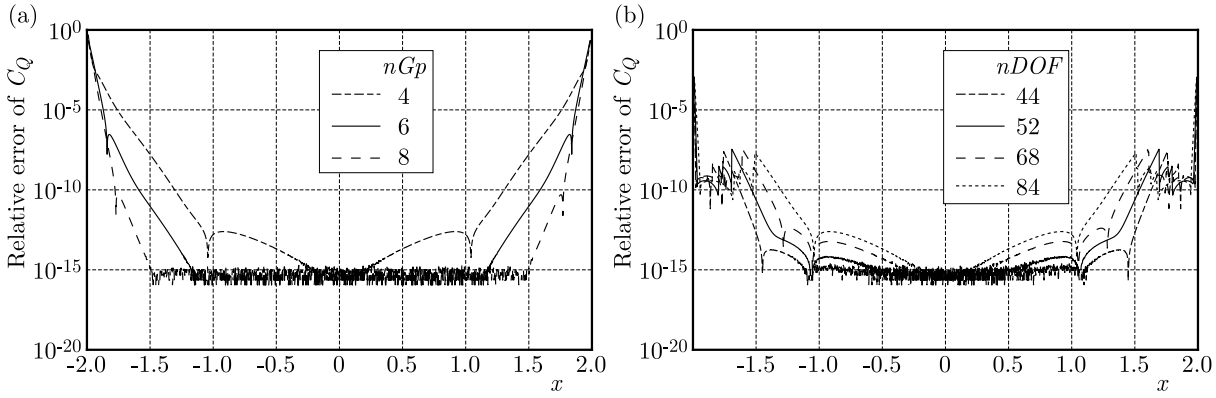

Fig. 8. Variation of errors of C_Q at an internal point as it gradually approaches the boundary of a circle: effect of (a) the number of Gauss points for 44 DOF and (b) gradual increase of the number of Gauss points as the internal point gets closer to the boundary

To our surprise, the variation of C_Q errors at collocation points presents an optimal number of Gauss points denoted by nGp^*. This optimal number increases when the mesh gets coarser as shown in Fig. 9a. For example, this optimal number is equal to 4 for 68 and 84 DOF. It is equal to 5 for 52 DOF.

To examine this result, we perform integration by using different numbers of Gauss points for singular and regular integrals that we denoted by $nGpS$ and $nGpR$, respectively, in Figs. 9b and 9c. These figures show variation of C_Q errors for 52 and 84 DOF. According to Fig. 9a, the error in the case of 84 DOF is minimal when $nGp^* = 4$. In Fig. 9b, we can see that by varying $nGpR$ from 2 to 20 in the case of 84 DOF while maintaining $nGpS = nGp^* = 4$, the error decreases in comparison to the case when $nGpS = nGpR$ and becomes constant for $nGpR \geqslant 4$. However, if $nGpR = nGp^* = 4$ then we obtain the same error as in the case of $nGpS = nGpR$ (see the case of 84 DOF in Fig. 9c). This is also true for 52 DOF.

We conclude that the overall error in I_1 is dominated by the contribution of quadrature errors of the singular integrals. The choice of the $nGpS$ number is crucial for obtaining a better precision. As soon as the optimal number nGp^* is chosen to be equal to the number of Gauss points for singular integrals, one can afford to use the lower number $nGpR$ and obtain the same quality of precision.

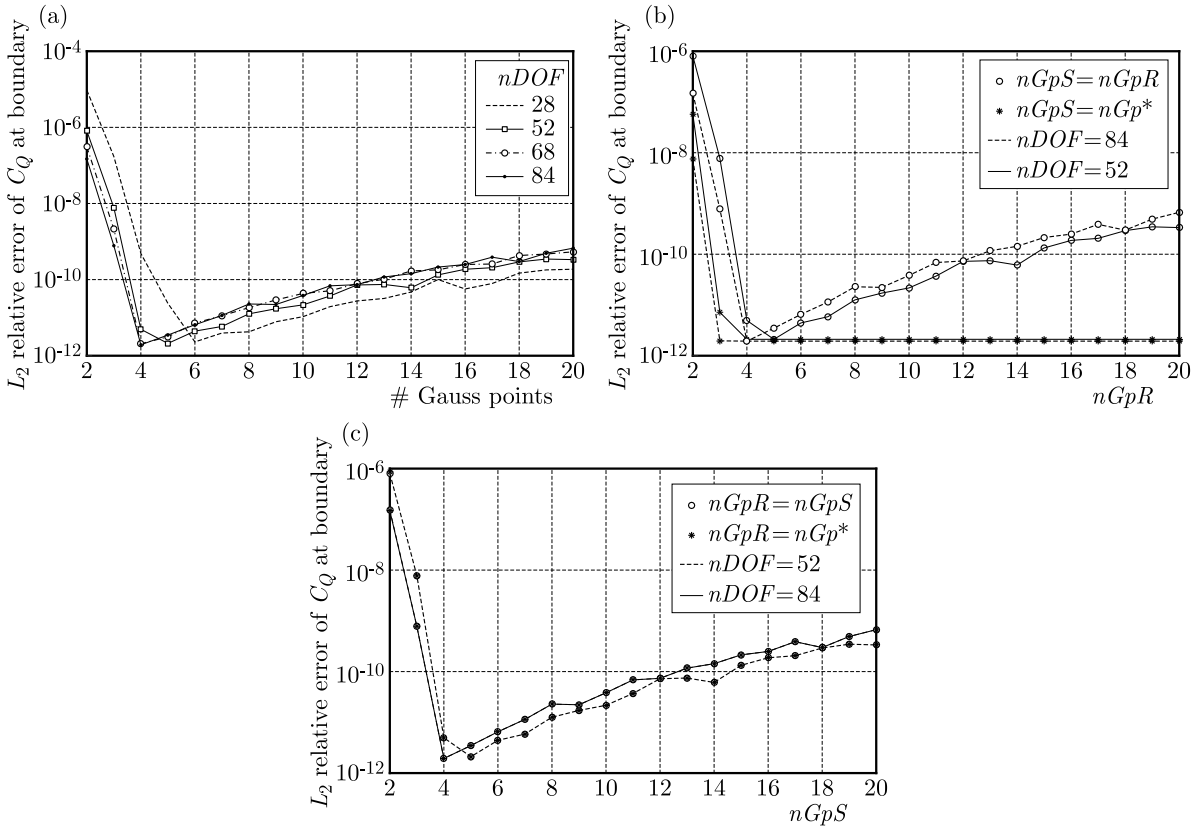

Fig. 9. Influence of the number of Gauss points on convergence of C_Q at collocation points: (a) identification of an optimal number of Gauss points nGp^* improving the convergence and effect of selection of the number of Gauss points on the precision of (b) regular integrals and (c) singular integrals for 52 and 84 DOF. $nGpS$ and $nGpR$ denote the number of Gauss points used in singular and regular integrals, respectively. nGp^* is the optimal number of Gauss points as obtained from Fig. 9a

4.2. Errors in $I_2 = \int G(Q,P)\, dS(P)$

In this Section, we study the quadrature error in the term involving Green's function denoted by $I_2 = \int G(Q,P)\, dS(P)$. The reference solution is computed using analytical integration on an arbitrary line segment proposed by Liu (2009). In Fig. 10 the variation of the regular integral error of I_2 is plotted at an internal point as it gradually approaches the boundary of the circle.

According to this figure, I_2 behaves like I_1 for internal points. Firstly, the IGBEM is more accurate than the BEM (see Figs. 7a and 10a). Secondly, when calculated with the IGBEM, the precision of I_2 can be improved by either increasing the number of Gauss points or by using fine meshes (see Figs. 10b and 10c). Another similarity with I_1 is that a better precision is achieved far from the boundary contrary to points situated near the boundary for which computing of nearly singular integrals is required. However, I_2 convergence is obtained with a higher error in comparison to I_1. Actually, by comparing Fig. 10b to Fig. 7b, we can see that for the same DOF number, the error is the highest in I_2. Moreover, the effect of the nearly singular integrals is less important in I_2 than in I_1: the range of points with the smallest error was wider in I_2 than in I_1. Therefore, far from the boundary, the regular terms in I_2 require more Gauss points than in I_1 (see Figs. 10c and 8a), but close to the boundary, I_2 behaves better than I_1.

I_2 behaves differently from I_1 when the collocation points are involved in the integral. From Fig. 11a, one can notice the absence of an optimal number of Gauss points. On the contrary, the error decreases by increasing either DOF or number of Gauss points. Moreover, I_2 convergence has a higher error than I_1 even by using 20 Gauss points in comparison, for example, to 10 in the

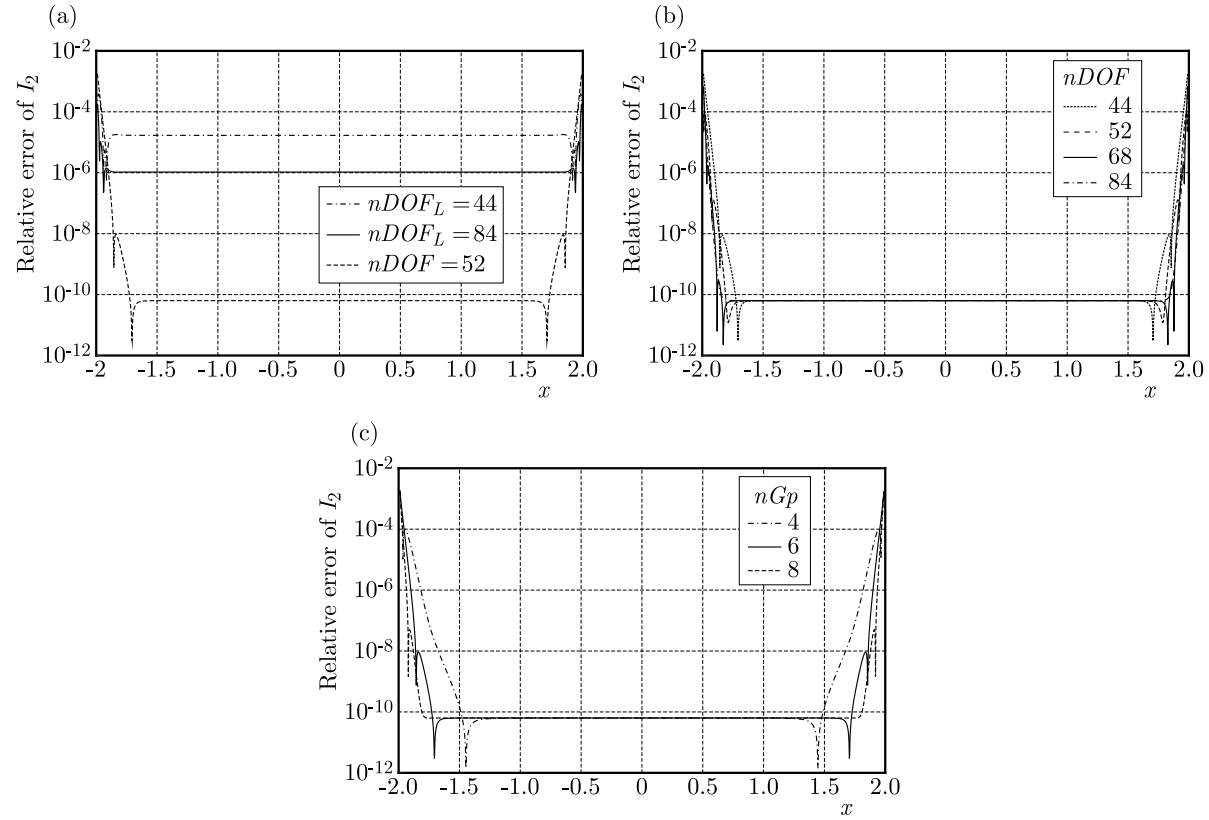

Fig. 10. Variation of I_2 errors at an internal point as it gradually approaches the boundary of a circle: (a) comparison between the BEM and IGBEM for 6 Gauss points per quadratic element, and the effect of (b) DOF number for 6 Gauss points per quadratic element and (c) the number of Gauss points for 44 DOF

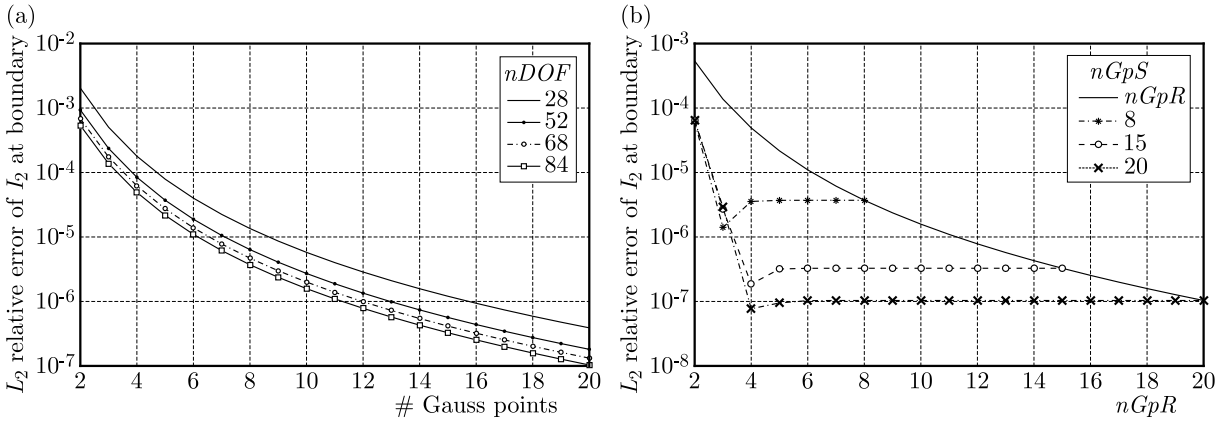

Fig. 11. Influence of the number of Gauss points on the convergence of I_2 at the collocation points: (a) for different DOF numbers and (b) effect of the number of Gauss points on errors for 84 DOF. *nGpS* and *nGpR* denote the number of Gauss points used in singular and regular integrals, respectively

case of I_1 (Fig. 9a). Since the regular integrals in I_2 give small errors, consequently, the noticed large error in Fig. 11a originates from the contribution of singular integrals. This conclusion can be confirmed by examining Fig. 11b according to which for a given *nGpS* number (for example 20) fewer nGpR Gauss points are needed (5 in our example) to obtain the same error. A more interesting result is that for a given *nGpS* number, there is an optimal *nGpR* number for which a smaller error is obtained (4 in our example).

5. Conclusion

Thanks to isogeometric analysis, the geometry is exact and its discretization errors in the IGBEM can be suppressed. This allows a better estimation of quadrature errors when constant boundary conditions are assumed over a smooth geometry. In this article, we have examined separately quadrature errors of the integral involving the derivative of Green's function (noted I_1) and that one involving Green's function itself (noted I_2) in the case of a 2D potential problem. We evaluated these integrals for points inside the domain (case of regular integrals only) and for points on the boundary (case of both regular and singular integrals).

Our important result is the identification of an optimal number of Gauss points for singular integrals of I_1. Moreover, although this number is absent in the case of singular integrals of I_2, we found that for each number of Gauss points chosen for singular integrals in I_2 there corresponds an optimal number of Gauss points for regular integrals. These results indicate that with a judicious choice of the number of Gauss points for the singular and regular integrals of I_1 and I_2 we can improve convergence of the IGBEM. Moreover, we found that I_1 is more accurate than I_2. Nevertheless, convergence remains dictated in both cases by the number of Gauss points used in the singular integrals.

In addition, the use of the Greville abscissae and the treatment of singularity by splitting the integration domain into two regions limits generalization of these conclusions. The study of the behavior of the errors for other techniques of singularity treatment and other collocation point positions deserves further investigations. Finally, our choice to compute the regular and nearly singular integrals in the same way led to large errors at points located near the boundary compared to the singular integrals. Hence, we need to give more importance to these integrals by treating them more rigorously.

References

1. Aimi A., Calabrò F., Diligenti M., Sampoli M.L., Sangalli G., Sestini A., 2018, Efficient assembly based on B-spline tailored quadrature rules for the IgA-SGBEM, *Computer Methods in Applied Mechanics and Engineering*, **331**, 327-342

2. Alia A., 2020, Ultrasonic diffraction by a circular transducer: Isogeometric analysis sensitivity to full Gauss quadrature points, *Journal of the Acoustical Society of America*, **147**, 2, EL74-EL79

3. Alia A., Khanyile N.P., Dufrénoy P., De Saxcé G., 2022, Vibration and acoustic radiation of an impacted plate: parametric study based on isogeometric analysis, *International Conference on Noise and Vibration Engineering (ISMA 2022)*

4. An Z., Yu T., Bui T.Q., Wang C., Trinh N.A., 2018, Implementation of isogeometric boundary element method for 2-D steady heat transfer analysis, *Advances in Engineering Software*, **116**, 36-49

5. Calabrò F., Falini A., Sampoli M.L., Sestini A., 2018, Efficient quadrature rules based on spline quasi-interpolation for application to IGA-BEMs, *Journal of Computational and Applied Mathematics*, **338**, 153-167

6. Chasapi M., Mester L., Simeon B., Klinkel S., 2022, Isogeometric analysis of 3D solids in boundary representation for problems in nonlinear solid mechanics and structural dynamics, *International Journal for Numerical Methods in Engineering*, **123**, 5, 1228-1252

7. Coox L., Atak O., Vandepitte D., Desmet W., 2017, An isogeometric indirect boundary element method for solving acoustic problems in open boundary domains, *Computer Methods in Applied Mechanics and Engineering*, **316**, 186-208

8. Hughes T.J.R., Cottrell J.A., Bazilevs Y., 2005, Isogeometric analysis: CAD, finite elements, NURBS, exact geometry and mesh refinement, *Computer Methods in Applied Mechanics and Engineering*, **194**, 39-41, 4135-4195

9. Hughes T.J.R., Reali A., Sangalli G., 2010, Efficient quadrature for NURBS-based isogeometric analysis, *Computer Methods in Applied Mechanics and Engineering*, **199**, 5-8, 301-313
10. Johnson R.W., 2005, Higher order B-spline collocation at the Greville abscissae, *Applied Numerical Mathematics*, **52**, 1, 63-75
11. Katsikadelis J.T., 2016, *The Boundary Element Method for Engineers and Scientists, Theory and Applications*, Academic Press
12. Khanyile N.P., Alia A., Dufrénoy P., De Saxcé G., 2022, Acoustic radiation simulation of forced vibrating plates using isogeometric analysis, *Journal of the Acoustical Society of America*, **152**, 1, 524-539
13. Kostas K.V., Ginnis A.I., Politis C.G., Kaklis P.D., 2017, Shape-optimization of 2D hydrofoils using an isogeometric BEM solver, *Computer-Aided Design*, **82**, 79-87
14. Liu Y., 2009, *Fast Multipole Boundary Element Method: Theory and Applications in Engineering*, Cambridge University Press, New York
15. Mahajerin E., 1983, Exact evaluation of $\int dSr^2$ over a circular element, *Applied Mathematical Modelling*, **7**, 4, 282-284
16. Marburg S., 2002, Six boundary elements per wavelength: is that enough? *Journal of Computational Acoustics*, **10**, 1, 25-51
17. Marburg S., Nolte B. (Editors), 2008, *Computational Acoustics of Noise Propagation in Fluids – Finite and Boundary Element Methods*, Springer, Heiderberg
18. Matzen M.E., Cichosz T., Bischoff M., 2013, A point to segment contact formulation for isogeometric, NURBS based finite elements, *Computer Methods in Applied Mechanics and Engineering*, **255**, 27-39
19. Opstal van T., Fonn E., Holdahl R., Kvamsdal T., Kvarving A.M., Mathisen K.M., Nordanger K., Okstad K.M., Rasheed A., Tabib M., 2015, Isogeometric methods for CFD and FSI-simulation of flow around turbine blades, *Energy Procedia*, **80**, 442-449
20. Peng X., Lian H., 2022, Numerical aspects of isogeometric boundary element methods: (nearly) singular quadrature, trimmed NURBS and surface crack modeling, *Computer Modeling in Engineering and Sciences*, **130**, 1, 513-542
21. Simpson R.N., Bordas S.P.A., Trevelyan J., Rabczuk T., 2012, A two-dimensional isogeometric boundary element method for elastostatic analysis, *Computer Methods in Applied Mechanics and Engineering*, **209-212**, 87-100
22. Temizer I., Wriggers P., Hughes T.J.R., 2011, Contact treatment in isogeometric analysis with NURBS, *Computer Methods in Applied Mechanics and Engineering*, **200**, 9-12, 1100-1112
23. Treeby B.E., Pan J., 2009, A practical examination of the errors arising in the direct collocation boundary element method for acoustic scattering, *Engineering Analysis with Boundary Elements*, **33**, 11, 1302-1315
24. Wu T.W., 2000, *Boundary Element Acoustics, Fundamentals and Computer Codes*, WIT Press, Southampton
25. Yan J., Lin S., Bazilevs Y., Wagner G.J., 2019, Isogeometric analysis of multi-phase flows with surface tension and with application to dynamics of rising bubbles, *Computers and Fluids*, **179**, 777-789

Manuscript received February 9, 2022; accepted for print May 9, 2023

JOURNAL OF THEORETICAL AND APPLIED MECHANICS
61, 3, pp. 599-611, Warsaw 2023
https://doi.org/10.15632/jtam-pl/168913

ANALYSIS OF THE CONTRIBUTION DEGREE OF VIBRATION TRANSMISSION OF BOLTED STRUCTURE

Shuai Liu

Harbin Engineering University, Harbin, China; and

Science and Technology on Reactor System Design Technology Laboratory, Chengdu, China

e-mail: liushuai_9105@163.com

Wanyou Li

Harbin Engineering University, Harbin, China

Xuan Huang, Furui Xiong, Xiaozhou Jiang, Zhipeng Feng, Liwei Deng, Zhihao Yuan, Guojiang Liao, Wanjun Wu

Science and Technology on Reactor System Design Technology Laboratory, Chengdu, China

In practical engineering, vibration transmission between bolted structures supported by cantilever beams involves many factors. The vibration transmission effect is the embodiment of coupling of various factors, so it is impossible to accurately and quantitatively evaluate the influence degree of various factors. In this paper, the influence factors of vibration between bolted plates in the form of a cantilever beam are studied by a numerical calculation method. The effects of the friction coefficient, bolt preload, temperature and pressure on vibration characteristics are studied. Finally, the contribution of different influencing factors to vibration transmission is given.

Keywords: bolted structures, vibration transmission, numerical calculation

1. Introduction

Bolt connection is a common connection form in large assemblies, which is widely used in mechanical structures such as nuclear power equipment. In numerical simulation of dynamic characteristics of mechanical structures, different models of bolted connection (Rogers and Boothroyd, 1975; Du *et al.*, 2018; Shen *et al.*, 2020) have a great influence on the process and results of numerical simulations. In a submersible interior, a power device is connected to the base through a support which is usually connected by elastic or bolt connection. In the environment of a deep sea, when connection with the base is by bolts, transmission of structural vibration (Tullini and Laudiero, 2008; Li *et al.*, 2017; Hao *et al.*, 2021) is affected by many factors, including the fit of bolts and holes, friction between the plate and plate joint surfaces, deformation of the shell base, etc. Simulation of vibration transmission under bolted connection is complex. The vibration transmission mechanism and simulation modes are not clear, which needs to be further studied. In this paper, vibration transmission between a submersible internal structure and the base is studied. The model of bolted connection is established and the influencing factors of vibration transmission are studied. The law of vibration of typical bolted connection is given from the perspective of numerical simulation, which can be used as a reference for design.

2. Simulation model of bolted connection

2.1. Geometric model

Taking a bolted plate structure as an example, the influence of various models of bolted connection on dynamic characteristics of the example is studied. By analysing the bolted structure, nonlinear factors mainly exist in the connection position. The friction coefficient, preload, temperature, pressure can lead to a change of vibration transmission in bolt connection. So the influence laws of the friction coefficient, preload, temperature, pressure and other parameters are studied. Combined with a vibration experimental model of the bolted plate structure, suggestions for numerical simulation mode and vibration transmission contribution of the bolted plate structure are given. The bolt connection mechanism model established in this paper is shown in Fig. 1.

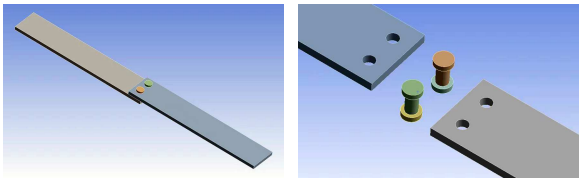

Fig. 1. The bolted plate

2.2. Size and coordinates of the model

The size of the flat plate is 200 mm×40 mm×5 mm (overlapping length is 20 mm). The diameter of the through hole at the connection is 6.5 mm and the diameter of the contact circle between the end face of the bolt or nut and the flat plate is about 10 mm. Both the flat plate and the bolt are made of steel, as shown in Fig. 2.

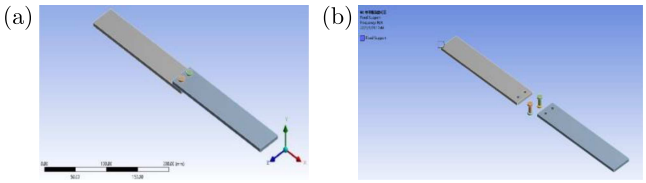

Fig. 2. Size and coordinates of the model: (a) coordinate, (b) boundary conditions

The coordinate system: X axis is along the length direction, Y axis is along the thickness direction, and Z axis is along the width direction of the plate. Rigid fixed constraints are adopted at one end of the length direction.

3. Research on simulation model

In order to obtain a proper simulation method of the bolted connection, different simulation methods are discussed. The bolt connection structure is complex, and it is inefficient to it in large and complex structures. Therefore, the bolt connection structure is usually reasonably simplified. This paper mainly studies the following five simplified models to explore the influence of the bolt simulation mode on structural dynamic characteristics when the bolted flat plate structure is connected. In the paper, the bolt is simulated by making use of five following elements:

1) Unthreaded solid element;
2) Cylinder solid element;
3) Byline element;

4) Beam element;
5) Joint element.

Referring to the five simplified models and distinguishing details in the model, the following 12 calculation models are established to analyze dynamic characteristics of bolted structures.

Model 1A: unthreaded solid model with bonded contact, as shown in Fig. 3a;
Model 1B: unthreaded solid model with nodes of the contact surface combined (Fig. 3b);
Model 2A: cylinder solid model with bonded contact (Fig. 4a);
Model 2B: cylinder solid model with nodes of the contact surface combined (Fig. 4b);
Model 3A: line element with contact (beam constraint) (Fig. 5a);
Model 3B: line element with MPC contact (multipoint constraint) (Fig. 5b);
Model 4A: beam element with stress on the through-hole cylinder face (Fig. 6a);
Model 4B: beam element with stress on the through-hole sideline (Fig. 6b);
Model 4C: beam element with stress on the bolt contact surface (Fig. 6c);
Model 5A: joint connection with stress on the through-hole cylinder face (Fig. 7a);
Model 5B: joint connection with stress on the through-hole cylinder sideline (Fig. 7b);
Model 5C: joint connection with stress on the bolt contact surface (Fig. 7c).

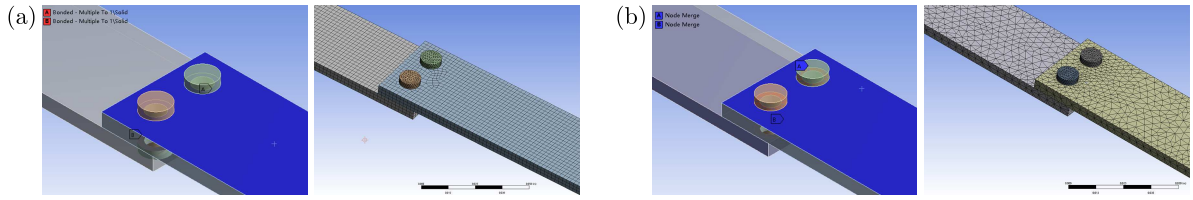

Fig. 3. Model 1A (a) and model 1B (b)

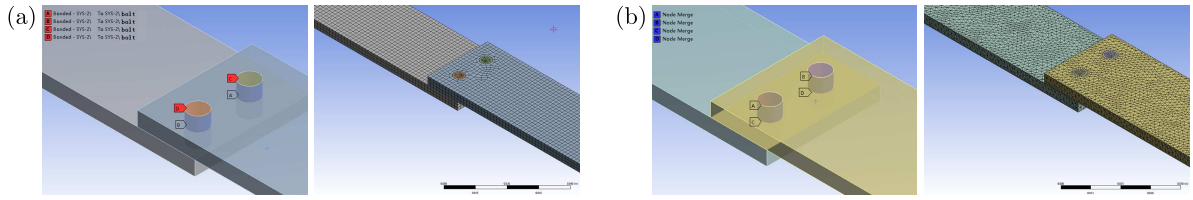

Fig. 4. Model 2A (a) and model 2B (b)

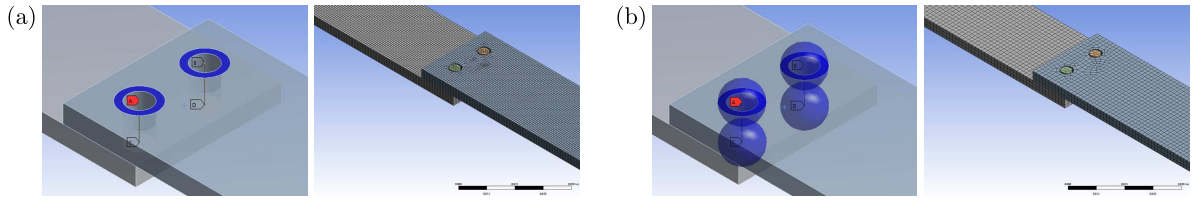

Fig. 5. Model 3A (a) and model 3B (b)

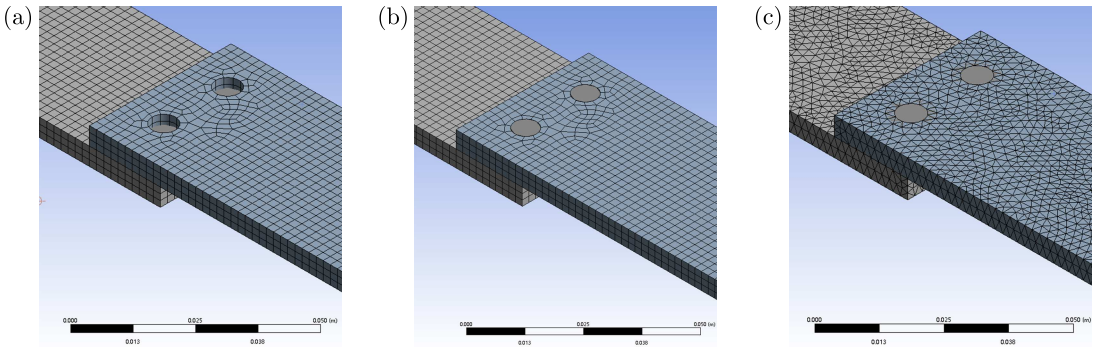

Fig. 6. Model 4A (a), model 4B (b) and model 4C (c)

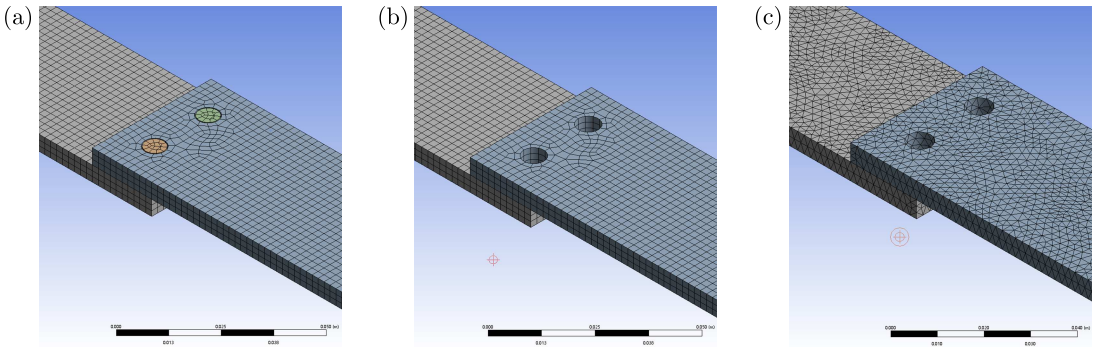

Fig. 7. Model 5A (a), model 5B (b) and model 5C (c)

4. Modal theory

4.1. Modal analysis theory

The essence of modal analysis is a coordinate transformation. Its purpose is to put the response vector originally described in the physical coordinate system into the so-called "modal coordinate system". Each basis vector of this coordinate system is just an eigenvector of the vibration system. In other words, in this coordinate, the vibration equation is a set of equations without coupling with each other, which respectively describe vibration forms of each order of the vibration system. Each coordinate can be solved separately to obtain a certain order of structural parameters of the system.

After discretization, the dynamic characteristics of the structure can be described by n-order matrix differential equation

$$\mathbf{M}\ddot{\mathbf{x}} + \mathbf{C}\dot{\mathbf{x}} + \mathbf{K}\mathbf{x} = \mathbf{f}(t) \tag{4.1}$$

where $\mathbf{M}$, $\mathbf{K}$ and $\mathbf{C}$ are the mass, stiffness and damping matrix of the structure, $\mathbf{x}$, $\dot{\mathbf{x}}$ and $\ddot{\mathbf{x}}$ are n-displacement, velocity and acceleration response vectors, $\mathbf{f}(t)$ is the n-dimensional excitation force vector.

Assuming that the initial state of the system is zero, the matrix equation with a complex s variable (Eq. (4.2)) can be obtained by the Laplace transformation on both sides of Eq. (4.1)

$$[\mathbf{M}s^2 + \mathbf{C}s + \mathbf{K}]\mathbf{X}(s) = \mathbf{F}(s) \tag{4.2}$$

The matrix in the formula is

$$\mathbf{Z}(s) = [\mathbf{M}s^2 + \mathbf{C}s + \mathbf{K}] \tag{4.3}$$

It reflects the dynamic characteristics of the system, which is the system dynamic matrix or impedance matrix. Its inverse matrix is

$$\mathbf{H}(s) = [\mathbf{M}s^2 + \mathbf{C}s + \mathbf{K}]^{-1} \tag{4.4}$$

$\mathbf{H}(s)$ is the admittance matrix, that is, transfer function matrix. According to Eq. (4.2)

$$\mathbf{X}(s) = \mathbf{H}(s)\mathbf{F}(s) \tag{4.5}$$

Set $s = j\omega$ in Eq. (4.5), the relationship between the output (response vector $\mathbf{X}(\omega)$) and input (excitation vector $\mathbf{F}(\omega)$) in the frequency domain can be obtained

$$\mathbf{X}(\omega) = \mathbf{H}(\omega)\mathbf{F}(\omega) \tag{4.6}$$

where $\mathbf{H}(\omega)$ is the frequency response function matrix. The elements in rows and columns of the matrix $\mathbf{H}(\omega)$ are

$$H_{ij}(\omega) = \frac{X_i(\omega)}{F_j(\omega)} \tag{4.7}$$

Set $s = j\omega$ in Eq. (4.3), the impedance matrix can be obtained

$$\mathbf{Z}(\omega) = (\mathbf{K} - \omega^2\mathbf{M}) + j\omega C \tag{4.8}$$

Using the weighted orthogonality of a real symmetric matrix, matrix equations are obtained

$$\mathbf{\Phi}^{\mathrm{T}}\mathbf{M}\mathbf{\Phi} = \begin{bmatrix} \ddots & & \\ & m_r & \\ & & \ddots \end{bmatrix} \qquad \mathbf{\Phi}^{\mathrm{T}}\mathbf{K}\mathbf{\Phi} = \begin{bmatrix} \ddots & & \\ & k_r & \\ & & \ddots \end{bmatrix} \tag{4.9}$$

The matrix $\mathbf{\Phi} = [\phi_1, \phi_2, \ldots, \phi_N]$ is the vibration mode matrix, and it is assumed that the damping matrix also satisfies the orthogonality of vibration modes

$$\mathbf{\Phi}^{\mathrm{T}}\mathbf{C}\mathbf{\Phi} = \begin{bmatrix} \ddots & & \\ & c_r & \\ & & \ddots \end{bmatrix} \tag{4.10}$$

Substitute equation (4.10) into equation (4.8), equation (4.11) is obtained

$$\mathbf{Z}(\omega) = \mathbf{\Phi}^{-\mathrm{T}} \begin{bmatrix} \ddots & & \\ & z_r & \\ & & \ddots \end{bmatrix} \mathbf{\Phi}^{-1} \tag{4.11}$$

where $z_r = (k_r - \omega^2 m_r) + j\omega c_r$

$$H_{ij}(\omega) = \sum_{r=1}^{N} \frac{\phi_{ri}\phi_{rj}}{m_r[(\omega_r^2 - \omega^2) + j2\xi_r\omega_r\omega]} \tag{4.12}$$

4.2. Modal test theory

The connection between the steel plate and the bolt is a continuous structural system, but in vibration modal tests and analysis, it can only be described as a finite degree of freedom system. In the frequency band of interest, such as (f_a, f_b), according to the complex mode theory, the frequency response function of the structure can be expressed as

$$H_{ij}(\omega) = \frac{1}{2}\sum_{k=k_a}^{k_0}\left[\frac{r_{ijk}\mathrm{e}^{\theta_{ijk}}}{(\omega_k - \omega) + i\sigma_k} - \frac{r_{ijk}\mathrm{e}^{-\theta_{ijk}}}{(\omega_k - \omega) - i\sigma_k}\right] + R_{ij} = R_{ij} + \sum_{k=k_a}^{k_0} h_{ijk}(\omega) \tag{4.13}$$

where $h_{ijk}(\omega)$ is the k-th order single-mode expression, R_{ij} stands for the residual term of the frequency band. k_0, k_a are the lowest and highest modal orders in the (f_a, f_b) frequency band. σ_k, ω_k, r_{ijk} and θ_{ijk} are the damping coefficient of the k-th mode, damped natural frequency and amplitude, and the amplitude of the vibration mode vector component generated at the point i when the excitation force is applied at the point j. Equation (4.13) shows that the measured frequency response is the superposition of various modes.

The coupling between the total vibration of the steel plate and bolt connection is weaker than that of the lower modes. Therefore, it can be considered that the measured frequency response function is only the contribution near the modal frequency, and the influence of the adjacent modes can be neglected. According to the assumption of the single freedom model, the frequency response function is reduced to the form

$$h_{ijk}(\omega) = \frac{r_{ijk}}{\Omega_k^2 - \omega^2 + 2i\xi_k\Omega_k\omega} \tag{4.14}$$

where $\xi_k = \sigma_k/\Omega_k$ is the damping ratio; $\Omega_k = \sqrt{\sigma_k^2 + \omega_k^2}$ is the undamped natural frequency.

In this test, if the pickup signal of the response is acceleration, then

$$h_{ijk}(\omega) = \frac{-\omega^2 r_{ijk}}{\Omega_k^2 - \omega^2 + 2i\xi_k\Omega_k\omega} \tag{4.15}$$

From frequency response function (4.15)

$$\begin{aligned}
\mathrm{Re}[h_{ijk}(\omega)] &= \frac{-\omega^2(\Omega_k^2 - \omega^2)r_{ijk}}{(\Omega_k^2 - \omega^2)^2 + (2i\xi_k\Omega_k\omega)^2} \\
\mathrm{Im}[h_{ijk}(\omega)] &= \frac{2i\xi_k\Omega_k\omega^3 r_{ijk}}{(\Omega_k^2 - \omega^2)^2 + (2i\xi_k\Omega_k\omega)^2} \\
|h_{ijk}(\omega)| &= \frac{\omega^2 r_{ijk}}{(\Omega_k^2 - \omega^2)^2 + (2i\xi_k\Omega_k\omega)^2}
\end{aligned} \tag{4.16}$$

After the measured frequency response function is obtained, the real frequency, imaginary frequency and amplitude frequency curves can be obtained at the same time. From Eq. $(4.16)_1$, when $\omega = \Omega_k$, $\mathrm{Re}[h_{ijk}(\omega)]$ takes the zero value. In $\omega = \Omega_k$, Eqs $(4.16)_2$ and $(4.16)_3$ is the mean value. It can be seen that after measuring the frequency response function curve, each order of the frequency is very easy to obtain.

$\mathrm{Re}[h_{ijk}(\omega)]$ calculates the derivative, and making it zero one obtains the two extreme point frequencies near the zero value frequency (modal frequency) on the real frequency curve ω_a, $\omega_b(\omega_a > \omega_b)$

$$\omega_a^2 = \frac{\Omega_k^2}{1 + 2\xi_k} \qquad \omega_b^2 = \frac{\Omega_k^2}{1 - 2\xi_k} \tag{4.17}$$

The above two equations are combined to find the damping ratio

$$\xi_k = \frac{(\omega_b/\omega_a)^2 - 1}{2[(\omega_b/\omega_a)^2 + 1]} \tag{4.18}$$

The vibration mode vector component of the k-th mode is obtained by the following equation

$$\phi_k = \{\mathrm{Im}[h_{ijk}(\omega)]\} \tag{4.19}$$

5. Modal numerical analysis

According to the above, the modal analysis of the bolted structure is completed, and the results are listed in Table 1. The corresponding vibration modes are shown in Figs. 8 and 9. We can get the natural frequency when the right end of formula (4.1) is 0.

Since deformation of vibration modes calculated by different models are similar, the mode of each order for 1B model are given as Figs. 8 and 9.

Table 1. The natural frequency of the bolted plate structure

Model	One end rigid fixed frequency [Hz]				Rigid fixed at both ends [Hz]			
	First	Second	Third	Fourth	First	Second	Third	Fourth
1A	27.14	172.10	212.26	494.49	171.72	569.35	956.20	965.80
1B	28.26	175.75	219.01	494.98	174.50	575.32	968.42	979.57
2A	28.20	173.37	213.18	494.62	173.64	569.80	960.59	976.59
2B	28.32	177.15	219.49	494.93	176.46	574.96	977.58	984.01
3A	28.35	177.81	219.84	494.89	177.21	574.98	979.34	986.85
3B	28.44	178.37	219.73	496.73	177.78	574.49	982.62	986.41
4A	28.25	174.56	205.64	494.66	174.88	564.25	966.80	979.57
4B	28.17	161.14	172.45	492.25	172.96	534.09	895.70	955.41
4C	28.14	172.09	203.09	494.54	171.75	559.27	956.13	969.09
5A	28.23	174.26	216.37	494.65	174.71	571.34	965.56	974.48
5B	28.23	173.78	189.03	494.52	174.46	541.12	961.27	981.99
5C	28.28	175.20	213.82	494.66	175.78	565.08	969.43	982.49

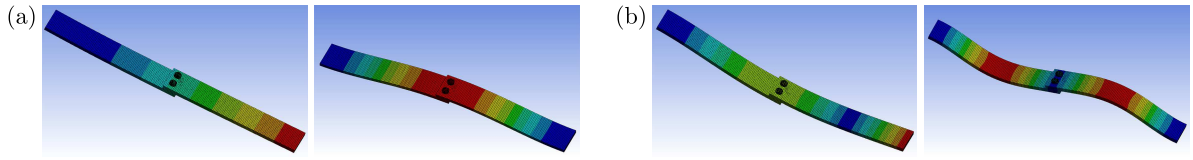

Fig. 8. (a) First order mode, (b) second order mode: left – one end fixed, right – two ends fixed

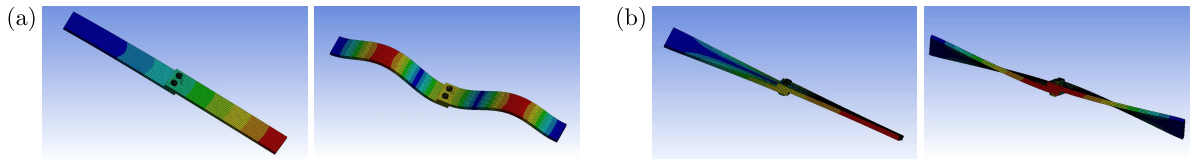

Fig. 9. (a) Third order mode, (b) fourth order mode: left – one end fixed, right – two ends fixed

The solid element can simulate more rich information. From the calculation results, it can be seen that the solid elements have little difference, so it can be inferred that the solid model adopted by the bolt is the closest model to the real structure. And the calculation results are the most accurate. However, the grid scale is much larger, especially when there are many bolts, the grid scale increases significantly, and the grid scale directly determines computational efficiency. When the grid scale is the same and there are many contacts, the computational efficiency is lower than that of node merging. When the elements and nodes are numerous, the bolt is recommended to be simplified by line or beam elements, and the bolt contact surface is set to stress surface, which can reduce the scale of the finite element model, improve calculation efficiency and high simulation accuracy. Using the simplified methods to simulate bolts can also ensure their quality and stiffness characteristics. Line or beam elements can simulate the quality and stiffness characteristics. From the natural frequency error calculated, we can see the error is small. For the bolt connection of two flat plates, the solid unthreaded element is adopted to analyse the impact of the parameters on dynamic characteristics.

The local structure of the bolted connection is free from structural deformation caused by external pressure in the deep-sea environment. Therefore, the main factors affecting vibration of bolted structures include friction, external pressure and temperature. Friction is reflected by different preloads. As depth of a deep sea varies, the external pressure and temperature on bolted structures vary with depth. This paper focuses on the influencing factors in 5.1-5.3. When

friction, pressure, temperature and bolt preload are loaded on the right end of formula (4.1), we can get results under different conditions.

5.1. The effect of the friction coefficient on vibration transmission

Based on model 1B, the influence of the friction coefficient on dynamic characteristics of the bolted plate structure is studied by two restraint methods:

Model F1: one end is rigidly fixed, the bolt is in contact with the upper and lower surfaces of the plate, and the upper and lower plates are in contact, the preload is 0;
Model F2: two ends are rigidly fixed, the bolt is in contact with the upper and lower surfaces of the plate, and the upper and lower plates are in contact, the preload is 0.

The change of natural frequencies of each order with the friction coefficient is calculated, which is listed in Table 2.

Table 2. Calculation results of models F1 and F2

Friction coefficient	F1 natural frequency [Hz]				F2 natural frequency [Hz]			
	First	Second	Third	Fourth	First	Second	Third	Fourth
0.02	27.70	160.65	194.20	483.99	162.78	559.09	880.94	963.95
0.10	27.92	165.66	197.72	486.60	165.80	560.52	905.38	964.16
0.20	27.95	166.34	199.81	487.56	166.25	561.62	909.23	964.26
0.90	28.00	167.60	208.29	490.93	165.35	564.00	902.18	964.41

Automatic adjustment of contact with structural deformation can be realized by the penalty function method. Through a change in the natural frequency with the friction coefficient, it can be seen that bolted plates become a fixed overall structure and the stiffness changes little with the friction coefficient. The natural frequency of each order increases with an increase of the friction coefficient.

5.2. The effect of bolt preload on vibration transmission

Based on model 1B, the friction coefficient is taken as 0.2 to study the influence of preload on the dynamic characteristics of the bolted plate structure:

Model P1: one end is rigidly fixed, the bolt is in contact with the upper and lower surfaces of the plate and the upper and lower plates are in contact. The friction coefficient is 0.2.

The law of natural frequencies of each order of the bolted structure with preload calculated are listed in Table 3.

Table 3. Calculation results of model P1

Preload	Natural frequency [Hz]			
	First	Second	Third	Fourth
2550 N	28.01	169.16	209.83	492.91
4200 N	28.02	169.17	209.83	492.94
6750 N	28.02	169.19	209.83	492.97
9000 N	28.03	169.21	209.86	493.04
13200 N	28.03	169.23	209.91	493.10
15500 N	28.04	169.27	209.95	493.14

The analysis shows that the two flat plates connected by bolts become a fixed overall structure. Its stiffness does not change much with the preload, and the natural frequency of each order increases with an increase of preload, but the change is not obvious.

5.3. The effect of temperature on vibration transmission

Based on model 1B, the influence of temperature on dynamic characteristics of bolted plates is studied, and the following two calculation models are established.

Model T1: one end is rigidly fixed, the bolt is in contact with the upper and lower surfaces of the plate, the upper and lower plates are in contact. The friction coefficient is 0.2 and the preload is 4200 N.

Model T2: two ends are rigidly fixed, the bolt is in contact with the upper and lower surfaces of the plate, the upper and lower plates are in contact. The friction coefficient is 0.2 and the preload is 4200 N.

According to calculations, the change of each order natural frequency with temperature is listed in Table 4.

Table 4. Calculation results of model T1 and T2

Temperature	T1 natural frequency [Hz]				T2 natural frequency [Hz]			
	First	Second	Third	Fourth	First	Second	Third	Fourth
100°C	27.88	167.20	207.83	492.03	69.42	468.10	839.41	955.32
22°C	28.03	169.25	209.94	493.10	169.54	566.76	939.27	964.93
10°C	28.04	169.50	210.34	493.43	178.34	578.20	943.49	966.13
0°C	28.05	169.71	210.97	493.78	185.18	587.03	945.75	967.10
−10°C	28.05	169.93	212.00	494.14	191.97	596.14	956.07	968.12
−20°C	28.06	170.11	212.63	494.35	198.57	605.07	964.00	969.16
−30°C	28.06	170.14	212.72	494.35	204.88	614.45	970.18	971.95
−50°C	28.07	170.19	213.82	494.92	217.45	632.18	972.32	992.06

The calculation results show that the influence of temperature on the frequency change is related to the connection form of the structure and boundary conditions. For the rigid fixed boundary condition at one end, it is equivalent to a cantilever beam. When temperature changes, its structure can expand or contract freely, and its internal stress (stiffness) changes little. Although the natural frequencies of each order decrease with an increase of temperature, the change is not obvious. For the rigid fixed boundary conditions at both ends, the connection form is equivalent to the rigid fixed beam. When temperature changes, the structure cannot expand freely. The temperature stress will be generated inside, which will affect the structural stiffness. The natural frequencies of each order decrease with an increase of temperature, and the change is obvious. When temperature drops from 22°C to −50°C, the first natural frequencies increase by about 5%-28%.

5.4. The effect of pressure on vibration transmission

Based on model 1B, the following is established:

Model N1: one end is rigidly fixed, the bolt is in contact with the upper and lower surfaces of the plate, the upper and lower plates are in contact. The friction coefficient is 0.2, preload 4200 N and temperature 22°C.

The change of natural frequencies of each order of the bolted structure with pressure is shown in Table 5.

The calculation results show that the two flat plates connected by bolts become a fixed overall structure, so stiffness changes little with pressure. The natural frequencies of each order increase with an increase of water depth, but the change is not obvious.

Table 5. Calculation results of model N1

Depth	Natural frequency [Hz]			
	First	Second	Third	Fourth
50 m	28.04	169.70	210.98	493.78
100 m	28.05	169.70	210.99	493.80
150 m	28.05	169.70	211.00	493.80
200 m	28.05	169.70	211.02	493.81
250 m	28.05	169.71	211.05	493.83
300 m	28.05	169.71	211.08	493.83

6. Comparison between calculations and tests

6.1. Test device

In order to study the influence of bolted plates on structural vibration transmission characteristics, the paper completes the modal test.

A cantilever beam is used to complete vibration modal analysis of bolted connection and fit. The experimental beam is made of steel. As shown in Fig. 10, the size of two steel plates is 200 mm×40 mm×5 mm, which are steel plates 1 and 2, respectively. The left side of steel plate 1 is rigidly fixed to restrict the translational and rotational degree of freedom. The overlap length between steel plates is 20 mm. The whole test piece is connected to the column and fixed on the large stiffness base by means of bolt connection. The test device and location of measuring points are shown in Fig. 10. The FEA testing tool is commercial. It is the special vibration testing tool of the Brüel&Kjær, named PULSE.

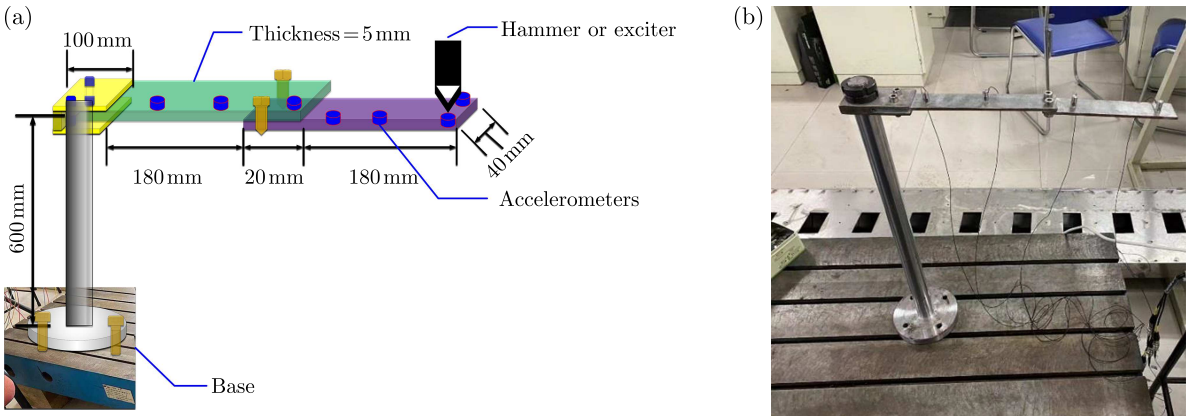

Fig. 10. Test device: (a) schematic diagram, (b) actual lab stand

The structural modal test of the cantilever beam is carried out through Jiangsu Dong Hua DH5922D data collector and Japan Riyin PV-91CH acceleration sensor. Because the length to width ratio of the cantilever beam is large, the test model is simplified to a beam element.

6.2. Comparison analysis

In the test, vertical first-order, vertical second-order and vertical third-order vibration modes appear, followed by a torsional first-order mode. The vibration modes are consistent with the numerical simulation results. The modal test results are as follows:

Through the change of bolt preload of the cantilever beam structure, the simulation results are compared with the experimental ones. Table 6 shows the test results of fit bolts under different preloads. The fit bolts in real connections are also preloaded.

Table 6. Comparison of frequency from simulations and tests

	Preload [N]	Natural frequency [Hz]			
		First	Second	Third	Fourth
Calculation	2550	28.01	169.16	209.83	492.91
	4200	28.02	169.17	209.83	492.94
	6750	28.02	169.19	209.83	492.97
Test	2550	24.414	140.365	180.624	362.305
	4200	24.414	141.602	181.439	379.883
	6750	24.414	141.602	182.001	380.654
Max difference [%]		14.7	20.5	16.2	36.0

Since the bolt preload has little effect on the natural frequency, the numerical calculation results for preload 2550 N are compared with the experimental results. The relative difference of the first-order natural frequency value is 14.7%, the second-order one 20.5%, third-order 16.2% and the fourth-order 36%. The first-order, second-order and third-order vertical mode appear firstly in the numerical simulation, followed by the first-order torsional mode, the same law as in experiment. And the change trend of the corresponding natural frequency value is roughly the same.

In the beam, the natural frequency is $\omega = \sqrt{k/m}$, where k is the stiffness coefficient and m is the structural mass. The experimental value is higher than that from numerical simulation, because when the boundary conditions are applied, the simulation can reach the stiffness of the cantilever beam, while the actual cantilever beam will not reach the ideal boundary conditions. In reality, the stiffness and natural frequency of the overall beam are reduced. The single mass of the acceleration sensor used in this experiment accounts for 0.46%. Four sensors are used, which makes the mass increase a little which, in turn, may reduce the natural frequency a little.

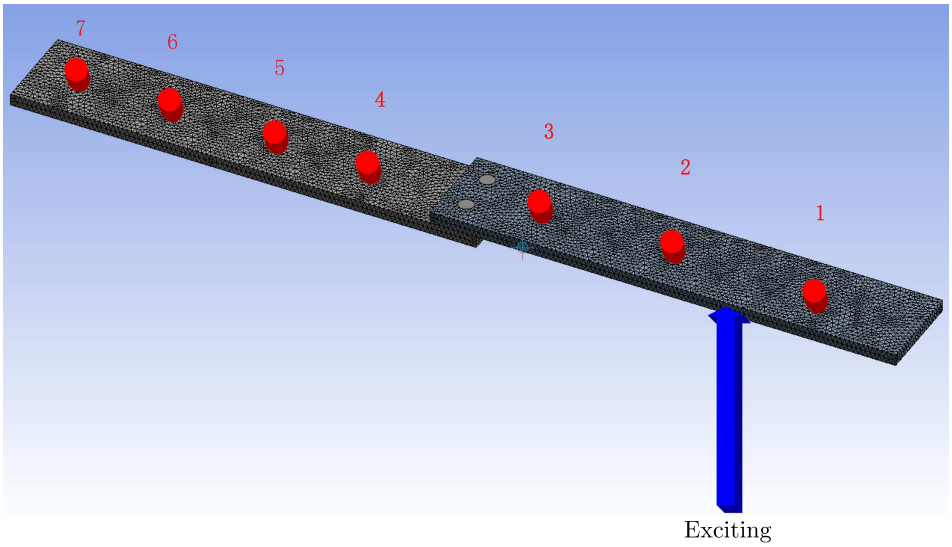

Fig. 11. Vibration response test points

The vibration response between simulation and test has been contrasted. In order to obtain more obvious vibration phenomena, the excitation with the same resonant frequency as the structure is used, so a force with a smaller excitation amplitude can also be used to obtain more obvious vibration phenomena. The response points are shown in Fig. 11. Applying a force with an amplitude of 1N at the exciting point and changing excitation frequencies, the vibration response at different points is obtained. Comparing the vibration response of point 3 and 4

under different preloads, the vibration change after transmission through the bolted connection is detrmined.

Through analysis, it is found that the bolted connection structure can be regarded as a whole structure under reaching the critical preload, and the stiffness of the bolted structure will not change greatly. This way, the effect of connection stiffness on vibration transmission is explained.

Table 7. Differences in the vibration response between simulations and tests

		Exciting frequency [Hz]			
		24.4	100	150	200
Preload	2550 N	0.0%	−3.3%	−1.4%	0.8%
	4200 N	0.0%	−2.4%	−1.4%	0.8%
	6750 N	0.0%	−3.3%	−1.4%	0.8%

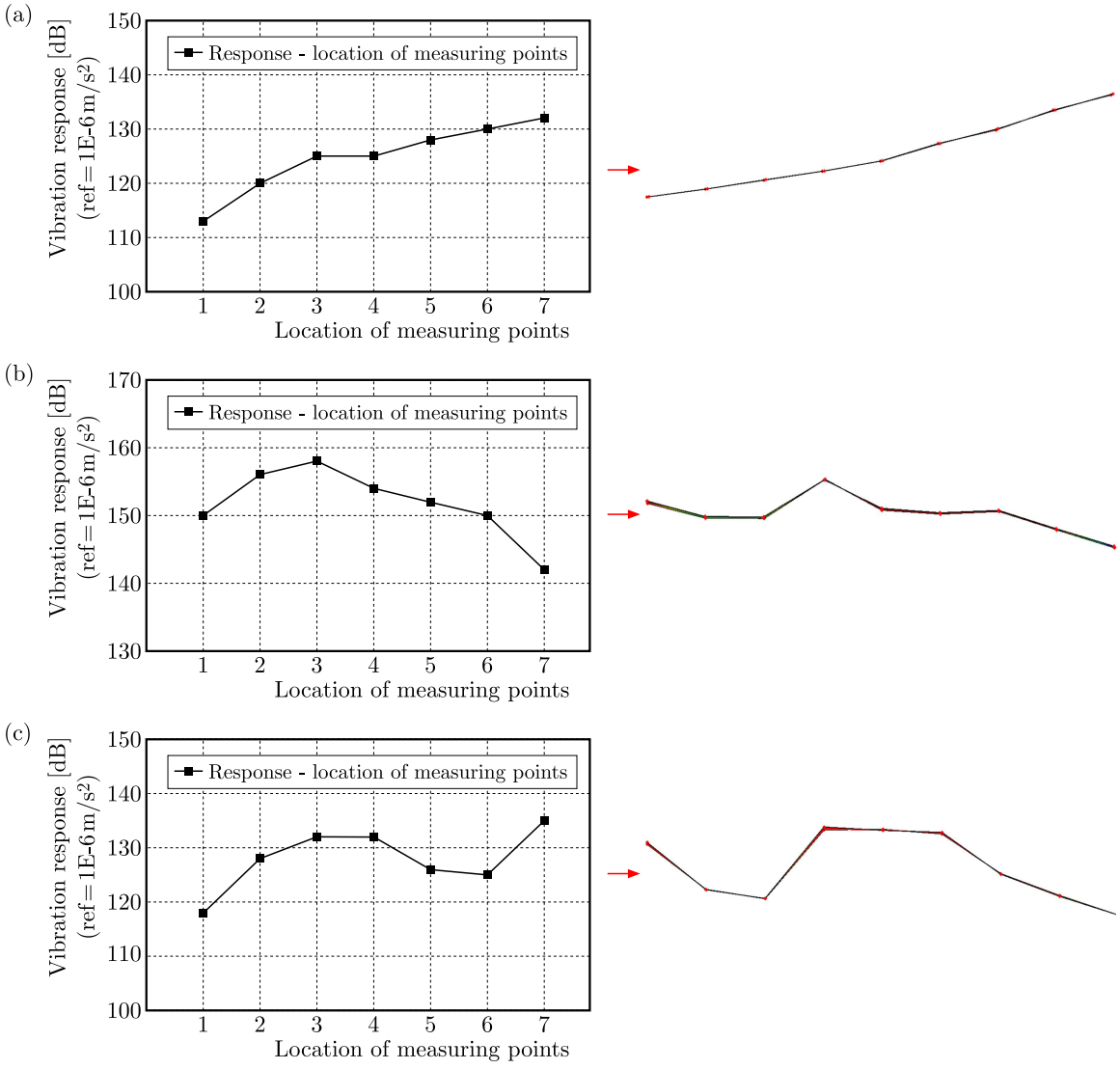

Fig. 12. The change trend of the response and mode (left: test vibration response; right: calculation mode): (a) first natural frequency, (b) second natural frequency, (c) third natural frequency

In order to verify validity of the calculation results, the trend of vibration response and vibration mode changes under the preload of 2550 N is compared. The natural frequency (1st-3rd) is as the exciting frequency. In Fig. 12, the displacement of modal nodes of natural frequencies

is consistent with the change trend of the forced vibration response at the same excitation frequency.

7. Conclusion

Two flat plates connected by bolts become a fixed overall structure, so their stiffness changes little with the friction coefficient, preload, temperature and internal pressure. The natural frequencies of each order increase with an increase of the friction coefficient, preload and pressure, and decrease with an increase of temperature, but the overall trend is not obvious (except for temperature). If the two flat plates connected by bolts cannot become a fixed overall structure, or the bolted structure fails, the stiffness of the structure will change.

At present, according to the calculation and test results, it can be seen that the connection stiffness is the main factor affecting the dynamic characteristics of the bolted connection structure. And various influencing factors studied in this paper will be examined further. An appropriate simulation method for the bolt connection based on the actual situation can be adopted.

In this paper, only two simple boundary conditions of bolted structures are studied. In the case of other boundary conditions, the effects of the friction coefficient, preload and temperature on the natural frequency of the structure need to be studied.

References

1. Du Z., Mi J., Yan W.F., 2018, Research on modeling method of dynamic contact stiffness of bolted joint, *Journal of Beijing Information Science and Technology University*, **33**, 2, 86-91
2. Hao Y., Wang J.L., Liu B., Sun H.C., Han Y.H. Chen F., 2021, Modal analysis theory and engineering application, *Journal of Hebei Institute of Architecture and Civil Engineering*, **3**, 4-47
3. Li J.F., Yang T., Du Y., Niu X.J., 2017, Composite laminates vibration theory and experimental modal analysis based on hammering method, *Aerospace Materials and Technology*, **47**, 1, 25-28+36
4. Rogers P.F., Boothroyd G., 1975, Damping at metallic interfaces subjected to oscillating tangential loads, *Journal of Engineering for Industry*, **97**, 3, 1087-1093
5. Shen P., Niu T.Y., Chen J.Y., 2020, A comparative study on modal analysis and testing technology of cantilever beam, *Journal of Xinxiang University*, **9**, 54-56
6. Tullini N., Laudiero F., 2008, Dynamic identification of beam axial loads using one flexural mode shape, *Journal of Sound and Vibration*, **318**, 1-2, 131-147

Manuscript received September 20, 2022; accepted for print April 8, 2023

JOURNAL OF THEORETICAL AND APPLIED MECHANICS
61, 3, pp. 613-624, Warsaw 2023
https://doi.org/10.15632/jtam-pl/168601

ON MITIGATION OF OSCILLATIONS OF A MECHANICAL SYSTEM WITH TWO DEGREES OF FREEDOM IN THE VICINITY OF EXTERNAL RESONANCES

Volodymyr Puzyrov, Nataliya Losyeva
Universidad de Barcelona, Spain, and
Nizhyn Mykola Gogol State University, Ukraine
e-mail: for.my.postbox@gmail.com; natalie.loseva@gmail.com

Nina Savchenko
National Aerospace University KhAI, Ukraine
e-mail: nina_savchenko@hotmail.com

In this article, we study dynamical behaviour of a 2-DOF mechanical system subjected to an external harmonic force. This system which consists of the Duffing oscillator considered as a bulk system and a linear dynamic vibration absorber (LDVA) attached to it. An analytical approach for optimal choice of the parameters of the LDVA is suggested with the aim to avoid the "superfluous" increase in the amplitude of forced oscillations of the main system. The analysis performed shows that when using a linear absorber, its proper tuning (choice of stiffness and damping coefficients) gives satisfactory results – the peak values of the frequency-amplitude curve (FAC) are decreasing comparatively with the case of the linear main oscillator.

Keywords: vibration absorber, averaging method, resonant frequency, peaks equalizing

1. Intoduction

Undesirable vibrations occur in many areas of human activity. They arise as a result of continuous operation of machines in industry, as a result of earthquakes that are transmitted to neighboring structural elements, due to motion of an object in a stream of a liquid or gas etc. Appearance of such vibrations generates serious problems which may lead to malfunction of equipment in many engineering areas including rotating machinery, aeronautics, seafaring, space-crafting and robotics. Eliminating or mitigation of vibrations is the main goal of various industrial and technical practices (Jangid, 2021; Kremer and Liu, 2017; Vakakis *et al.*, 2009; Lu *et al.*, 2018; Balaji *et al.*, 2021). One of the possible ways to counteract unwanted vibrations is the use of passive vibration absorbers. For the first time, such a device was patented by Frahm (1911), and later a mathematical model was presented and analyzed by Ormondroyd and Den Hartog (1928), Den Hartog (1934) and Brock (1946).

Initially, a vibration absorber was considered as a linear single degree of freedom (DOF) spring-mass system that abolishes or reduces excessive vibration of a harmonic-excited system. In the literature, several terms are used for such devices: dynamic vibration absorber (DVA), tuned mass damper (TMD) or inertial damper. Numerous types of non-linear absorbers are in use today (Ocak *et al.*, 2022). Among them are: pendulum-like absorbers, torsional absorbers, absorbers with quasi-zero or negative stiffness, vibro-impact dampers and many others.

Over the past two decades the efforts of many authors have been directed to the study of dynamics of a 2-DOF system with nonlinear coupling. The authors mainly used a combination of the analytical approach and numerical methods. The following analytical methods are commonly

used: multiple scale method (Jo and Yabuno, 2009; Ji and Zhang, 2010; Cirillo *et al.*, 2017; Liu *et al.*, 2022), averaging method (Gendelman and Starosvetsky, 2007; Zhu *et al.*, 2004; Yang *et al.*, 2014; Febbo and Machado, 2013) harmonic balance method (Habib *et al.*, 2015; Peng *et al.*, 2012) and some combined techniques (Luongo and Zulli, 2012).

Many different aspects of the problem have been investigated and numerous kinds of DVA design were suggested. In the paper by Yu and Luo (2019), analytical solutions were obtained for periodic steady-state characteristics in a nonlinear vibration absorber under harmonic excitation. The stability and bifurcations analysis of periodic responses were obtained through eigenvalue analysis. Zhou *et al.* (2019) considered a DVA with negative stiffness, and their parameter optimization was conducted according to two tuning methodologies: the fixed points theory and the stability maximization criterion. Li and Zhang (2020) studied a 2-DOF system composed of a linear main structure under harmonic excitation and a TMD mass block connected by nonlinear with viscous damping. Special formula for a frequency of a tuned mass damper was suggested. A similar system was studied by Awrejcewicz *et al.* (2020) with the assumption that the frequency and amplitude of the excitation are not known. The noteworthy results based on experimental study were obtained in papers by Gatti *et al.* (2010), Kremer and Liu (2017) and Bronkhorst *et al.* (2018). In the paper by Islam and Jangid (2022), the performance of the LDVA was studied using multiple objective functions of the damped SDOF structure. Namely, the impact of the absorber damping ratio, frequency ratio, inertance ratio and structural damping ratio on its performance were investigated. Tuning of the DVA for such a system subjected to stationary white-noise earthquake excitation was discussed in the paper by Prakash and Jangid (2022).

At the same time, in the case of uncertain parameters, the problem is complex and numerical study does not give a complete picture of dynamics of the system. From the theoretical point of view, the problem cannot be considered closed because different aspects may be taken into consideration, and some of them are more (or less) important depending on the situation. In other words, there is no universal formula for DVA characteristics.

In the present paper, we discuss dynamics of a 2-DOF system which consists of a Duffing oscillator subjected to simple harmonic excitation with a linear DVA attached and uncertain parameters (frequency and amplitude of external excitation). The main attention is paid to the development of an analytical technique for determining absorber parameters that contribute to the maximum reduction in the amplitude of oscillations of the main system in the vicinity of resonant frequencies. To simplify the mathematical model, the Krylov-Bogolyubov averaging method is used. Then analysis of state-response maximal amplitudes was performed. Relations for determining the characteristics of the absorber are presented. Finally, some numerical examples illustrate the results obtained.

2. Description of the model and preliminary simplifications

The mechanical system under study consists of the Duffing oscillator with a hardening spring (primary system) with an attached linear DVA (Fig. 1).

The equations of motion of this system may be written in the following form

$$\begin{aligned} &m_1\ddot{x}_1 + c_a(\dot{x}_1 - \dot{x}_a) + k_{lin}x_1 + k_{nl}x_1^3 + k_a(x_1 - x_a) = F_0\cos\omega t \\ &m_a\ddot{x}_a + c_a(\dot{x}_a - \dot{x}_1) + k_a(x_a - x_1) = 0 \end{aligned} \tag{2.1}$$

where $x_1(t)$ and $x_a(t)$ are the displacements of the harmonically forced primary system and the absorber. The Duffing oscillator has a hardening spring ($k_{nl} > 0$), the damping coefficient and stiffness of the absorber are c_a and k_a, respectively. Introducing a new variable $x_2 = x_a - x_1$, system (2.1) may be rewritten in the following form

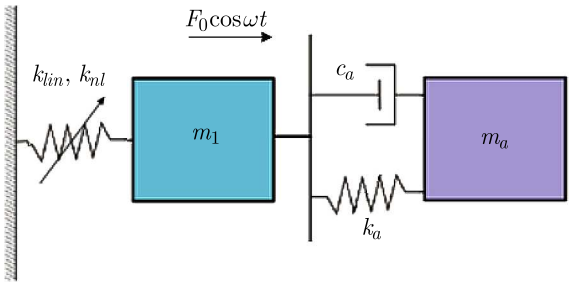

Fig. 1. Mechanical system

$$\begin{aligned}&(m_1+m_a)\ddot{x}_1+m_a\ddot{x}_2+k_{lin}x_1+k_{nl}x_1^3=F_0\cos\omega t\\&m_a\ddot{x}_1+m_a\ddot{x}_2+c_a\dot{x}_2+k_ax_2=0\end{aligned}\tag{2.2}$$

Let us introduce the dimensionless parameters and time by formulas

$$\begin{aligned}&\omega_1=\sqrt{\frac{k_{lin}}{m_1}}\qquad \omega_a=\sqrt{\frac{k_a}{m_a}}\qquad \mu=\sqrt{\frac{m_a}{m_1}}\qquad q=\Big(\frac{\omega}{\omega_1}\Big)^2\\&\gamma=\frac{\omega_a^2}{\omega_1^2}\qquad \widetilde{h}=\frac{c_a}{m_a\omega_1}\qquad \widetilde{\alpha}=\frac{k_{nl}F_0^2}{k_{lin}}\qquad \tau=\omega t\end{aligned}\tag{2.3}$$

Also, we introduce the dimensionless displacements by formulas

$$\widetilde{x}_1=\frac{x_1}{F_0}\qquad \widetilde{x}_2=\frac{\sqrt{\mu}}{F_0}x_2\tag{2.4}$$

and now the equations of motion are in the following form

$$\mathbf{M}\widetilde{\mathbf{x}}''+\mathbf{D}\widetilde{\mathbf{x}}'+\mathbf{K}\widetilde{\mathbf{x}}=\mathbf{\Phi}(\tau,\widetilde{x}_2)\tag{2.5}$$

where the matrices $\mathbf{M}$, $\mathbf{D}$, $\mathbf{K}$, $\mathbf{\Phi}$ are defined according to formulas

$$\begin{aligned}&\mathbf{M}=q\begin{bmatrix}1+\mu & \sqrt{\mu}\\ \sqrt{\mu} & 1\end{bmatrix}\qquad \mathbf{D}=\operatorname{diag}(0,h_\star)\qquad \mathbf{K}=\operatorname{diag}(1,\gamma)\\&h_\star=\widetilde{h}\sqrt{q}\qquad \mathbf{\Phi}=\begin{bmatrix}\cos\tau-\widetilde{\alpha}\widetilde{x}_1^3\\ 0\end{bmatrix}\qquad \widetilde{\mathbf{x}}=\begin{bmatrix}\widetilde{x}_1\\ \widetilde{x}_2\end{bmatrix}\end{aligned}\tag{2.6}$$

Here, the prime denotes the derivative with respect to time τ. For convenience, the superscript "$\sim$" over x_1, x_2 is subsequently discarded. After the transformation

$$x_j=u_j\cos\tau+v_j\sin\tau\qquad x_j'=-u_j\sin\tau+v_j\cos\tau\qquad j=1,2\tag{2.7}$$

equations (2.5) take the following form

$$\begin{aligned}&\cos\tau[\mathbf{M}\mathbf{v}'+(-\mathbf{M}+\mathbf{K})\mathbf{u}+\mathbf{D}\mathbf{v}]-\sin\tau[\mathbf{M}\mathbf{u}'+\mathbf{D}\mathbf{u}+(\mathbf{M}-\mathbf{K})\mathbf{v}]=\mathbf{\Phi}\\&\cos\tau(\mathbf{u}'+\mathbf{v})+\sin\tau(\mathbf{v}'-\mathbf{u})=-\sin\tau\mathbf{u}+\cos\tau\mathbf{v}\end{aligned}\tag{2.8}$$

Multiplying the previous system by the matrix

$$\begin{bmatrix}-\sin\tau & \cos\tau\\ \cos\tau & \sin\tau\end{bmatrix}\tag{2.9}$$

on the left throughout, we get the following equations

$$\begin{aligned}
&\mathbf{M}\mathbf{u}' + \frac{1}{2}[(1-c_2)\mathbf{D} + s_2(\mathbf{M}-\mathbf{K})]\mathbf{u} + \frac{1}{2}[-s_2\mathbf{D} + (1-c_2)(\mathbf{M}-\mathbf{K})]\mathbf{v} = \mathbf{\Phi}_1 \\
&\mathbf{M}\mathbf{v}' + \frac{1}{2}[-s_2\mathbf{D} + (1+c_2)(\mathbf{K}-\mathbf{M})]\mathbf{u} + \frac{1}{2}[(1+c_2)\mathbf{D} + s_2(\mathbf{K}-\mathbf{M})]\mathbf{v} = \mathbf{\Phi}_2
\end{aligned} \tag{2.10}$$

The expressions for the right-hand sides are described by formulas

$$\mathbf{\Phi}_1 = \frac{1}{8}\begin{bmatrix}\phi_1\\0\end{bmatrix} \qquad \mathbf{\Phi}_{=}\frac{1}{8}\begin{bmatrix}\phi_2\\0\end{bmatrix} \tag{2.11}$$

where

$$\begin{aligned}
&\phi_1 = -4s_2 + \widetilde{\alpha}[(2s_2+s_4)u_1^3 + 3(1-c_4)u_1^2v_1 + 3(2s_2-s_4)u_1v_1^2 + (3-4c_2+c_4)v_1^3] \\
&\phi_2 = 4(1+c_2) - \widetilde{\alpha}[(3+4c_2+c_4)u_1^3 + 3(2s_2+s_4)u_1^2v_1 + 3(1-c_4)u_1v_1^2 + (2s_2-s_4)v_1^3] \\
&s_2 = \sin 2\tau \qquad c_2 = \cos 2\tau \qquad s_4 = \sin 4\tau \qquad c_4 = \cos 4\tau
\end{aligned}$$

Now, we apply the Krylov-Bogolyubov averaging method. Assuming that u, v vary slowly with time τ, we obtain the averaged equations

$$\begin{aligned}
&\mathbf{M}\mathbf{u}' + \frac{1}{2}[\mathbf{D}\mathbf{u} + (\mathbf{M}-\mathbf{K})\mathbf{v}] = \frac{3}{8}\begin{bmatrix}\widetilde{\alpha}v_1(u_1^2+v_1^2)\\0\end{bmatrix} \\
&\mathbf{M}\mathbf{v}' + \frac{1}{2}[(\mathbf{K}-\mathbf{M})\mathbf{u} + \mathbf{D}\mathbf{v}] = \frac{1}{8}\begin{bmatrix}4-3\widetilde{\alpha}u_1(u_1^2+v_1^2)\\0\end{bmatrix}
\end{aligned} \tag{2.12}$$

Let us find the stationary points of system (2.12). Technically, it is easier to do this by introducing the complex variables $\mathbf{z} = \mathbf{u} + \mathrm{i}\mathbf{v}$. Then equations (2.12) take the following form

$$\mathbf{M}\mathbf{z}' + \frac{1}{2}(\mathbf{B}+\mathrm{i}\mathbf{D})z = \frac{1}{2}\mathrm{i}\begin{bmatrix}1-\alpha z_1^2\overline{z}_1\\0\end{bmatrix} \qquad \mathbf{M}\overline{z}' + \frac{1}{2}(\mathbf{B}+\mathrm{i}\mathbf{D})\overline{z} = \frac{1}{2}\mathrm{i}\begin{bmatrix}-1+\alpha z_1\overline{z}_1^2\\0\end{bmatrix} \tag{2.13}$$

Here, the following notions are introduced

$$\mathbf{K}-\mathbf{M} \triangleq \mathbf{B} = \begin{bmatrix}b_{11} & b_{12}\\ b_{12} & b_{22}\end{bmatrix} \tag{2.14}$$

where

$$b_{11} = 1 - q(1+\mu) \qquad b_{12} = -\mu q \qquad b_{22} = \gamma - q \qquad \alpha = \frac{3}{4}\widetilde{\alpha}$$

The condition $z' = 0$ leads to the following system of algebraic equations

$$\begin{aligned}
&b_{11}z_1 + b_{12}z_2 - 1 + \alpha z_1^2\overline{z}_1 = 0 \qquad b_{12}z_1 + (b_{22} - \mathrm{i}h)z_2 = 0 \\
&CC_1 = 0 \qquad CC_2 = 0
\end{aligned} \tag{2.15}$$

where CC_1, CC_2 are corresponding complex conjugates.

Expressing the variable z_2 from the second equation, we come to a pair of nonlinear equations with respect to z_1, $\overline{z}_1$

$$(b_{22} - \mathrm{i}\widetilde{h})z_1^2\overline{z}_1 + (b_{11}b_{22} - b_{12}^2 - \mathrm{i}\widetilde{h}b_{11})\overline{z}_1 - b_{22} + \mathrm{i}\widetilde{h} = 0 \qquad CC = 0 \tag{2.16}$$

Further, we rewrite equalities (2.16) in the form

$$\begin{aligned}
&[\alpha r(b_{22} - \mathrm{i}\widetilde{h}) + \det\mathbf{B} - \mathrm{i}\widetilde{h}b_{11}]z_1 = b_{22} - \mathrm{i}\widetilde{h} \\
&[\alpha r(b_{22} + \mathrm{i}\widetilde{h}) + \det\mathbf{B} + \mathrm{i}\widetilde{h}b_{11}]\overline{z}_1 = b_{22} + \mathrm{i}\widetilde{h} \qquad r = z_1\overline{z}_1
\end{aligned} \tag{2.17}$$

Now, multiplying separately the left- and right-hand sides of the two last equalities, we obtain the real-valued equation

$$\begin{aligned} &rq^4 - r[2\alpha r + 2(1+\mu)\gamma - h(1+\mu)^2 + 2]q^3 + \{\alpha^2 r^3 + 2\alpha[(2+\mu)\gamma - (1+\mu)h + 1]r^2 \\ &\quad + [(1+\mu)^2\gamma^2 + 2(2+\mu)\gamma - 2(1+\mu)h + 1]r - 1\}q^2 \\ &\quad - \{\alpha^2(2\gamma - h)r^3 + 2\alpha[(1+\mu)\gamma^2 + 2g - h]r^2 + [2(1+\mu)\gamma^2 + 2\gamma - h]r - 2\gamma + h\}q \\ &\quad + \gamma^2[r(\alpha r + 1)^2 - 1] = 0 \qquad h = \widetilde{h}^2 \end{aligned} \tag{2.18}$$

This equation determines the frequency-amplitude hyper-surface in six-dimensional space (related to equation (2.18)), where the square of amplitude of the primary mass $r = (u_1^2 + v_1^2)$ depends also on dimensionless parameters μ, α, h, γ. When the mechanical parameters of both masses are known, we have a traditional frequency-amplitude curve. Note that in the case $\alpha = 0$ (linear system), equation (2.18) is equivalent to the well-known classical form (Den Hartog, 1934).

Remark 1. We do not present here the conditions for stability of stationary points, as well as the conditions for the existence of three positive roots for r of polynomial (2.18). These conditions can be obtained in a similar manner, as it was done in the paper by Awrejcewicz *et al.* (2020).

3. Mitigation of the responses of the main mass

Assuming that the parameters m_1, k_{lin}, k_{nl} of the main system are given, as well as the mass of the absorber, we want to choose the damping coefficient and absorber stiffness in order to reduce the maximum level of possible oscillation amplitude in the vicinity of resonant frequencies (i.e., the peaks of the frequency-amplitude curve). With respect to dimensionless parameters, which means that μ and α are known, while the parameters h and γ should be determined.

The optimal case holds place when the ordinates of the peaks coincide, which geometrically means that at these points the tangents $r = r_1$, $r = r_2$ to the curve $r(q)$ coincide. In other words, the equation $f(r_0, q) = 0$ ($r_0 =$ const) has three or four different real roots if $r_0 < r_{max}$, and two multiple roots if $r_0 = r_{max}$ (Fig. 2). Here r_{max} corresponds to the maximum value of r.

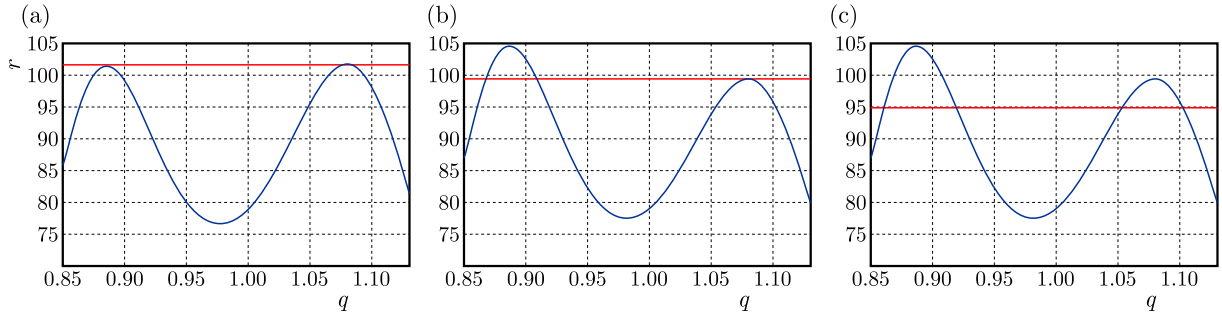

Fig. 2. Different number of solutions of equation $f(r_0, q) = 0$ depending on values of h and γ ($\mu = 0.02$, $\alpha = 0.002$): (a) $r_0 = r_{max}$, (b), (c) $r_0 < r_{max}$

The conditions for a fourth-degree polynomial

$$P(\xi) = a_4\xi^4 + a_3\xi^3 + a_2\xi^2 + a_1\xi + a_0 \qquad a_1 a_3 \neq 0 \tag{3.1}$$

to have two roots of multiplicity are

$$\psi_1 \triangleq a_0 a_3^2 - a_1^2 a_4 = 0 \qquad \psi_2 \triangleq a_3^3 - 4a_2 a_3 a_4 + 8a_1 a_4^2 = 0 \tag{3.2}$$

Substituting the corresponding expressions for the coefficients a_j, we have

$$\psi_1(r) = \sum_{j=0}^{3} \psi_{1j} r^j \qquad \psi_2(r) = \sum_{j=0}^{6} \psi_{2j} r^j \tag{3.3}$$

where

$$\begin{aligned}
&\psi_{10} = 4[2(1-\mu)\gamma + h(1-2\mu-\mu^2) + 2] \qquad \psi_{13} = 8\mu^2\alpha^2 h \\
&\psi_{11} = 4(1+\mu)^2\gamma^4 - 4h(1+\mu)^3\gamma^3 - [4 + 4\mu(1+\mu)h - (1+\mu)^4h^2]\gamma^2 + 8h\gamma - 2h^2 \\
&\psi_{12} = 4h(1+\mu)^3\gamma^3 - [(1+\mu)^4h^2 - 4\mu 1 + \mu)(1-\alpha)h + 8\alpha]\gamma^2 + 4h(1-4\alpha)\gamma - h^2(1-4\alpha) \\
&\psi_{20} = 4[-2(1-\mu)\gamma + h(1-2\mu-\mu^2) + 2 \\
&\psi_{21} = -4(1+\mu)^2\gamma^4 + 4h(1+\mu)^3\gamma^3 + [4 + 4\mu(1+\mu)h - (1+\mu)^4h^2]\gamma^2 - 8h\gamma + 2h^2 \\
&\psi_{22} = -4h(1+\mu)^3\gamma^3 + [(1+\mu)^4h^2 - 4\mu(1+\mu)(1-\alpha)h + 8\alpha]\gamma^2 \\
&\quad + 4h(1-4\alpha)\gamma - h^2(1-4\alpha) \\
&\psi_{23} = -2\alpha\{4h(1+\mu)^3\gamma^3 - [(1+\mu)^4h^2 - 6\mu(1+\mu)h + 2\alpha]\gamma^2 - 4h(2-\alpha)\gamma + h^2(2-\alpha)\} \\
&\psi_{24} = -\alpha^2 h\{4(1+\mu)^3\gamma^3 + (1+\mu)[12\mu - (1+\mu)^3 h]\gamma^2 - 24\gamma + 6h\} \\
&\psi_{25} = -4\alpha^3 h[\mu(1+\mu)\gamma^2 - 4\gamma + h] \qquad \psi_{26} = \alpha^4 h(4\gamma - h)r^6
\end{aligned} \tag{3.4}$$

Thus, we have two conditions $\psi_1 = 0$, $\psi_2 = 0$ connecting the function r and the optimization parameters h, γ. Considering $\psi_1 = 0$ as an implicit function of $r(h, \gamma)$ and $\psi_2 = 0$ as a constraint (or vice versa), we arrive at the problem of finding a conditional extremum. Compiling a linear combination $\psi(y, h, \gamma) = \psi_1 + \lambda\psi_2$ (λ is the Lagrange multiplier), we obtain a necessary condition for the existence of an extremum in the following form

$$\Delta(y, h, \gamma, \mu, \alpha) = \frac{\partial\psi_1}{\partial h}\frac{\partial\psi_2}{\partial\gamma} - \frac{\partial\psi_1}{\partial\gamma}\frac{\partial\psi_2}{\partial h} = 0 \tag{3.5}$$

Thus, for given values of the parameters μ and α, we have a system of three algebraic equations from which the corresponding values of the DVA parameters can be found numerically. Since the polynomials ψ_1, ψ_2, Δ have a very high degree, the direct solution of such a system of equations is computationally costly and may need an extra effort to avoid errors. Therefore, it makes sense to localize suitable ranges of values of γ and h firstly. It is convenient to do this geometrically, that is, to approximately determine the intersection point of the surfaces

$$\psi_1(\gamma, h, r) = 0 \qquad \psi_2(\gamma, h, r) = 0 \qquad \Delta(\gamma, h, r) = 0 \tag{3.6}$$

as shown in Fig. 3.

By choosing the values h_0, γ_0, r_0 found from Fig. 3 as an initial approximation, it is much easier to determine appropriate corrections. For example, substituting $h_1 = h_0 + \delta_h$, $\gamma_1 = \gamma_0 + \delta_\gamma$, $r_1 = r_0 + \delta_r$ into expressions ψ_1, ψ_2, Δ, and expanding the latter into the Taylor series in δ_h, δ_γ, δr, we can limit ourselves to a linear approximation while finding the refined approximation (with subsequent comparison of errors for thr left-hand sides of system (3.5) in both cases). In particular, for $\mu = 0.05$, $\alpha = 0.002$ we find $h \approx 0.07$, $\gamma \approx 0.973$, the corresponding FAC is shown in Fig. 4. The evolution of FAC with optimized DVA parameters depending on the value of α is presented in Fig. 5. With a growth of α, the value of γ slowly increases and the peaks go down.

Remark 2. Due to the fact that polynomials in system (3.5) are of extremely high degrees, it seems impossible to obtain explicit expressions for h, γ, r as functions of μ, α. These expressions can be approximately obtained in the form of asymptotic expansions. However,

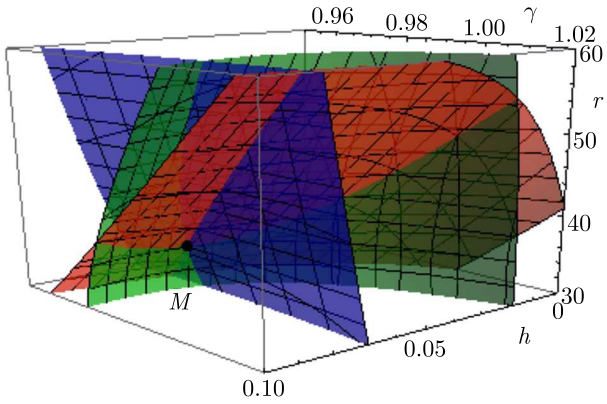

Fig. 3. Geometrical interpretation of system (3.5), where orange, green and blue surfaces correspond to $\psi_1 = 0$, $\psi_2 = 0$ and $\Delta = 0$, $\mu = 0.05$, $\alpha = 0.002$

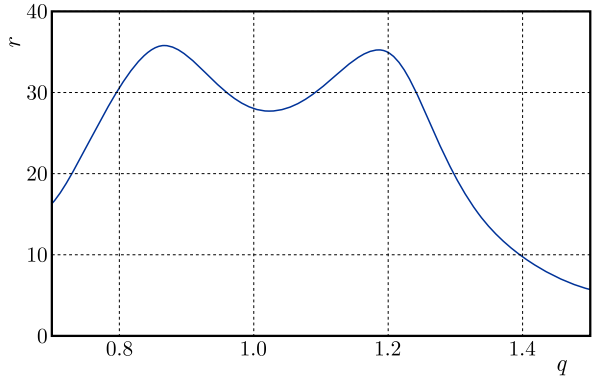

Fig. 4. The frequency-amplitude curve with optimized DVA parameters (based on Eq. (2.18), $\mu = 0.05$, $\alpha = 0.002$, $h = 0.07$, $\gamma = 0.973$

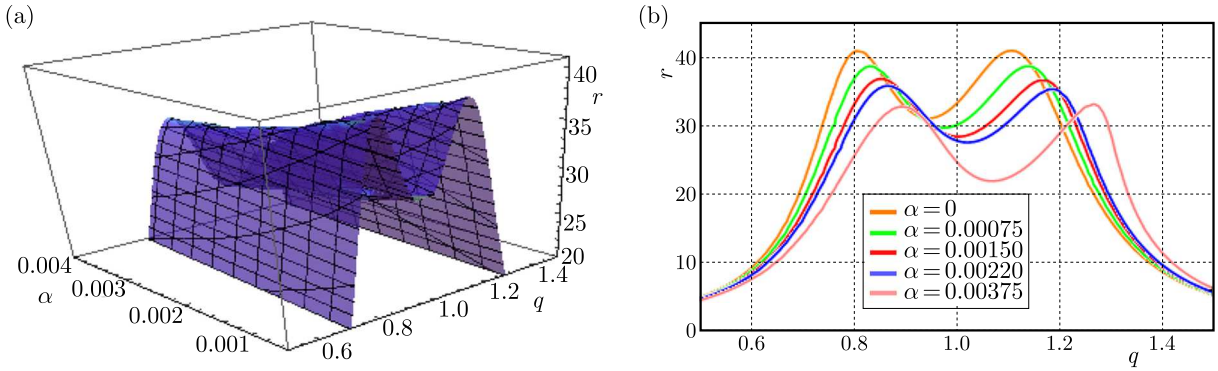

Fig. 5. Dependence of the responses of primary mass on the parameter α for $\mu = 0.05$

taking into account that the problem contains three small parameters (μ, F_0, k_{nl}), obtaining such expansions essentially depends on how these parameters relate to each other (for example, k_{nl} can be considered an independent small parameter, it can be considered proportional to μ or μ^2 etc.). The conscientious obtaining of such formulas is a subject of separate consideration.

4. Discussion and numerical validation

The procedure described above makes it possible to make an optimal choice of the absorber parameters, assuming that the parameter α is known. As can be seen from formulas (2.3), this parameter depends not only on the nonlinear stiffness k_{nl} of the main system, but also on the amplitude F_0 of the external force. If its exact value is unknown, then what corrections should be made? This issue was discussed, in particular, in (Habib *et al.*, 2015), where the authors proposed the use of a nonlinear absorber with "mirror" characteristics (proportional to characteristics of the main system). Such an approach seems to be logical, but the complexity of analysis significantly increases. For example, a cubic polynomial on r in formula (2.18) transforms into a polynomial of the ninth degree, and even the problem of determining the number of real roots is mathematically very difficult (and the numerical approach is not very reliable due to the large number of unknown parameters). Thus, the question arises: is it possible to use a linear absorber in conditions where the exact value of F_0 is vague, but the interval of possible values of the amplitude is known, i.e. $F_0 \in [F_1, F_2]$. If this interval is not too wide, say $F_2/F_1 \leqslant 2$, then taking into account that with a growth of α, the value of γ also increases (and to a lesser extent the value of h), as can be seen in Fig. 5, then we suggest that when choosing the value of γ we should take the maximum possible value of the amplitude of the external excitation F_2. This is illustrated in Figs. 6 and 7.

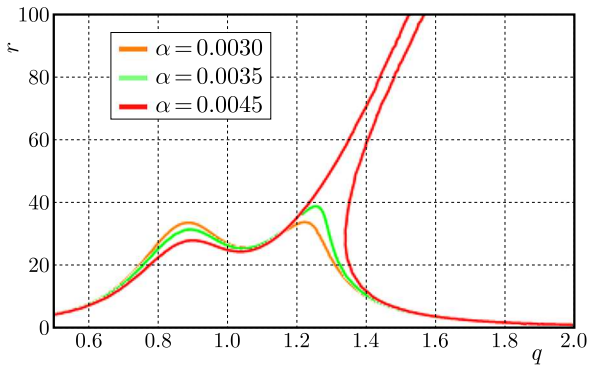

Fig. 6. Evolution of the responses as F_0 goes up for $h = 0.07$, $\gamma = 0.999$

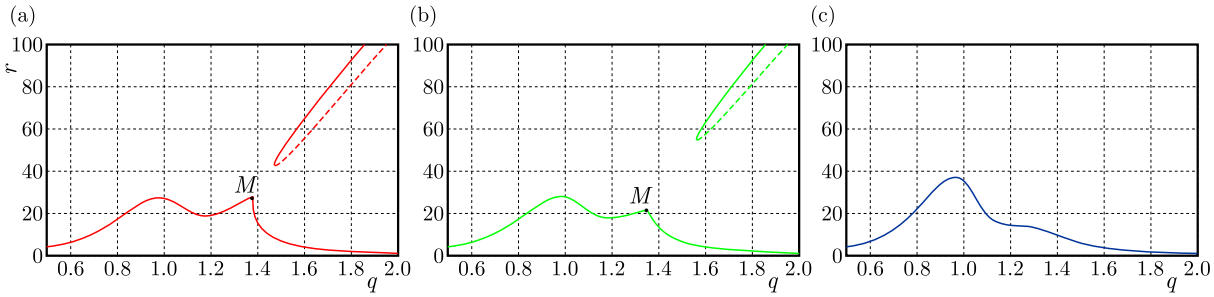

Fig. 7. Shape of the FAC when DVA parameters are chosen for α corresponding to $F_0 = F_2$ for $h = 0.071$: (a) $\alpha = 0.008$, $\gamma = 1.109$, (b) $\alpha = 0.008$, $\gamma = 1.12$, (c) $\alpha = 0.005$, $\gamma = 1.12$

Suppose that $\alpha \in [0.002, 0.008]$ and the "expected" value of α is equal to 0.003. Then calculated values for the absorber are: $\gamma \approx 0.999$, $h \approx 0.07$. The corresponding FAC is shown in Fig. 6. It has one branch and two equal peaks at $r \approx 34$. The allowable frequency range is wide enough. If the amplitude grows by 10%, the maximal amplitude increases up to 40 units, but the curve remains "robust" – no bifurcations, no blow-up, etc. However with a further growth by 10%, we get bifurcations and a significant increase in the amplitude of oscillations for primary

mass. From the other side, calculating the absorber parameters for the upper limit $\alpha = 0.008$, we get $\gamma \approx 1.09$, $h \approx 0.071$. The FAC for such values is presented in Fig. 7. It looks the same as in the case of the linear system, the value of r_{max} decreases down to ≈ 28, and there is some distance between the right peak and the upper branch, thus the "jump" from the lower branch to the upper one as a result of some occasional perturbations is not expected. Moreover, if we choose $\gamma = 1.12$, then r_{max} grows up to 30 units, but the point M now is far enough from the upper branch (Fig. 7).

In order to verify the obtained analytical results, we carried out numerical integration of averaged system (2.12) and equations (2.5). Also, in order to compare the efficiency of the absorber based on the proposed approach with other results, we took of the parameters $\mu = 0.05$, $\alpha = (3/4) \cdot 0.013$, as it was done in the article (Habib *et al.*, 2016) in Fig. 4a. Those authors considered a nonlinear absorber, however the values for h and γ were taken as optimal values for the linear system, namely $\gamma = 0.9524^2$, $h = (2 \cdot 0.134)^2\gamma$. The corresponding cubic component of stiffness of the absorber was taken $\beta = (4/3) \cdot 0.0851 \cdot \alpha$[1]. The maximum dimensionless response of main mass was between 5.5 and 6.0. At the same time, solving system (3.6) (or using its geometrical interpretation like it is shown in Fig. 3) for the LDVA we found: $h = 0.081$, $\gamma = 1.15$, $q = 1.39$. Substituting these values into system (2.15), we have $u_1 = -2.624$, $u_2 = -0.50619$, $v_1 = 2.70287$, $v_2 = -2.79266$ (two other solutions are complex with respect to $\mathbf{u}$, $\mathbf{v}$). After this, we integrate the averaged equations for both cases LDVA and NLDVA (with identical initial values), the results are shown in Fig. 8a. The distance from the origin to the attraction point is shorter with our choice of parameters of the absorber. Also, as one can see, trajectories with different initial values tend to the attraction point, and coordinates of this point correlate with the found values of u_1, v_1. The fact that the averaged equations describe well the behavior of the solutions of the original system is confirmed by integrating equations (2.5).

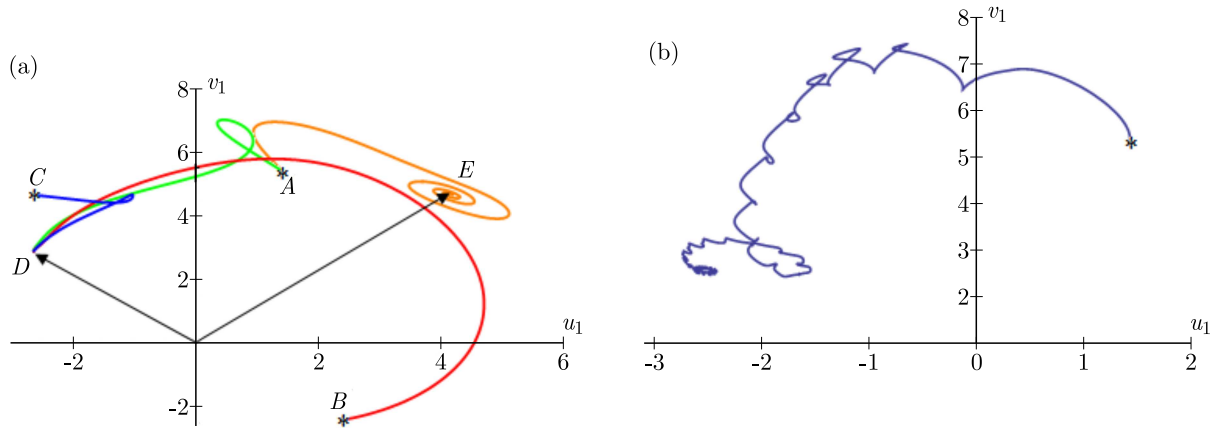

Fig. 8. (a) Phase trajectories for system (2.12) with different initial values (points A, B, C) and the stationary point D, $\mu = 0.05$, $\alpha = 0.00975$. The point E is the attraction point for NLDVA with cubic nonlinearity and parameters of the absorber taken according to (Habib *et al.*, 2016); (b) trajectory for non-averaged system (2.10) with the initial point A

As can be seen in Fig. 9a, the stationary point of system (2.12) corresponds to the limit cycle of system (2.5). The projection of the phase trajectory on the plane x_1, x_1' which corresponds to the NLDVA with values according to (Habib *et al.* 2016), see Fig. 4a, is shown in Fig. 9b, and a comparison of two time histories for the dimensionless response of main mass is presented in Fig. 9c.

[1]The averaged equations for such a case will differ from (2.5) by appearing the term $-\beta x_2^3$ in the second row of the matrix $\mathbf{\Phi}$.

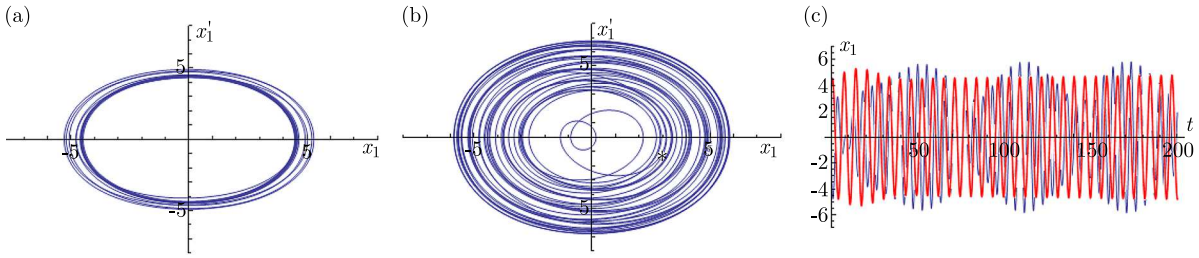

Fig. 9. (a) Projection of the phase trajectory on the plane $x_1 x_1'$ for dimensionless system (2.5) with the proposed LDVA parameters, the frequency ratio corresponds to the maximum response value $q = 1.39$; (b) trajectory corresponding to the NLDVA, $q = 1.25$; (c) comparison of two time histories for the LDVA and NLDVA

5. Conclusions

The article considers the problem of determining the parameters of a DVA connected to a Duffing's oscillator, which is under the influence of a periodic external excitation. The goal is to reduce the maximum possible oscillation amplitude of the main system under conditions of uncertainty (frequency ratio and external excitation amplitude) in the vicinity of resonant frequencies. We paid special attention to the development of an analytical procedure for selection the DVA parameters. It is shown that an appropriate choice of absorber stiffness depends significantly on the amplitude of the external action. In the case when this amplitude can take values from a certain range, it is advisable to focus on the upper limit of this range when choosing the absorber frequency.

The future work will be related to obtaining asymptotic formulas for the absorber parameters, more detailed comparison of the efficiency of using linear and non-linear absorbers and estimating the region of attraction.

Acknowledgement

The part of these results were presented at the 30th Conference "Vibrations in Physical Systems".

References

1. Awrejcewicz J., Cheaib A., Losyeva N., Puzyrov V., 2020, Responses of a two degrees-of-freedom system with uncertain parametrs in the vicinity of resonance 1:1, *Nonlinear Dynamics*, **101**, 1, 85-106

2. Balaji P.S., Karthik K., Kumar S., 2021, Applications of nonlinearity in passive vibration control: A review, *Journal of Vibration Engineering and Technologies*, **9**, 183-213

3. Brock J.E., 1946, A note on the damped vibration absorber, *Journal of Applied Mechanics*, **13**, 4, A284

4. Bronkhorst K.B., Febbo M., Lopes E.M.O., Bavastri C.A., 2018, Experimental implementation of an optimum viscoelastic vibration absorber for cubic nonlinear systems, *Engineering Structures*, **163**, 323-331

5. Cirillo G.I., Habib G., Kerschen G., Sepulchre R., 2017, Analysis and design of nonlinear resonances via singularity theory, *Journal of Sound and Vibration*, **392**, 295-306

6. Den Hartog J.P., 1934, *Mechanical Vibrations*, McGraw-Hill, New York

7. Febbo M., Machado S.P., 2013, Nonlinear dynamic vibration absorbers with a saturation, *Journal of Sound and Vibration*, **332**, 1465-1483

8. Frahm H., 1911, Device for damping vibrations of bodies, US Patent 989958
9. Gatti G., Brennan M.J., Kovacic I., 2010, On the interaction of the responses at the resonance frequencies of a nonlinear two degrees-of-freedom system, *Physica D*, **239**, 591-599
10. Gendelman O.V., Starosvetsky Y., 2007, Quasi-periodic response regimes of linear oscillator coupled to nonlinear energy sink under periodic forcing, *Journal of Applied Mechanics*, **74**, 325-331
11. Habib G., Detroux T., Viguié R., Kerschen G., 2015, Nonlinear generalization of Den Hartog's equal-peak method, *Mechanical Systems and Signal Processing*, **52**, 17-28
12. Habib G., Kerschen G., 2016, A principle of similarity for nonlinear vibration absorbers, *Physica D*, **332**, 1-8
13. Islam N.U., Jangid R. S., 2022, Optimum parameters of tuned inerter damper for damped structures, *Journal of Sound and Vibration*, **537**, 117218
14. Jangid R.S., 2021, Optimum tuned inerter damper for base-isolated structures, *Journal of Vibration Engineering and Technologies*, **9**, 1483-1497
15. Ji J.C., Zhang N., 2010, Suppression of the primary resonance vibrations of a forced nonlinear system using a dynamic vibration absorber, *Journal of Sound and Vibration*, **329**, 2044-2056
16. Jo H., Yabuno H., 2009, Amplitude reduction of primary resonance of nonlinear oscillator by a dynamic vibration absorber using nonlinear coupling, *Nonlinear Dynamics*, **55**, 67-78
17. Kremer D., Liu K., 2017, A nonlinear energy sink with an energy harvester: Harmonically forced responses, *Journal of Sound and Vibration*, **410**, 287-302
18. Li L.Y., Zhang T., 2020, Analytical analysis for the design of nonlinear tuned mass damper, *Journal of Vibration and Control*, **26**, 9-10, 646-658
19. Liu J., Yao J., Huang K., Zhang Q., Ze L., 2022, Analysis of a nonlinear tuned mass damper by using the multi-scale method, *Journal of Theoretical and Applied Mechanics*, **60**, 3, 463-477
20. Lu Z., Wang Z.X., Zhou Y., Lu X.L., 2018, Nonlinear dissipative devices in structural vibration control: A review, *Journal of Sound and Vibration*, **423**, 18-49
21. Luongo A., Zulli D., 2012, Dynamic analysis of externally excited NES-controlled systems via a mixed multiple scale/harmonic balance algorithm, *Nonlinear Dynamics*, **70**, 3, 2049-2061
22. Ocak A., Nigdeli S.M., Bekdaş G., 2022, Passive control via mass dampers: a review of state-of-the-art developments, [In:] *Optimization of Tuned Mass Dampers – Using Active and Passive Control*, G. Bekdaş, S.M. Nigdeli (Edit.), **432**, Springer, 15-40
23. Ormondroyd J., Den Hartog, J.P., 1928, Theory of the dynamic vibration absorber, *Transactions of the American society of Mechanical Engineers*, **50**, 9-22
24. Peng Z.K., Meng G., Lang Z.Q., Zhang W.M., Chu F.L., 2012, Study of the effects of cubic nonlinear damping on vibration isolations using harmonic balance method, *International Journal of Non-Linear Mechanics*, **47**, 1073-1080
25. Prakash Sh., Jangid R.S., 2022, Optimum parameters of tuned mass damper-inerter for damped structure under seismic excitation, *International Journal of Dynamics and Control*, **10**, 1322-1336
26. Vakakis A.F., Gendelman O., Bergman L.A., McFarland D.M., Kerschen G., Lee Y.S., 2009, *Nonlinear Targeted Energy Transfer in Mechanical and Structural System*, Springer, Berlin
27. Yang J., Xiong Y.P., Xing J.T., 2014, Power flow behaviour and dynamic performance of a nonlinear vibration absorber coupled to a nonlinear oscillator, *Nonlinear Dynamics*, **80**, 3, 1063-1079
28. Yu B., Luo A.C.J., 2019, Steady state performance of a nonlinear vibration absorber on vibration reduction of a harmonically forced oscillator, *European Physical Journal Special Topics*, **228**, 1823-1837

29. Zhou S., Jean-Mistral C., Chesne S., 2019, Closed-form solutions to optimal parameters of dynamic vibration absorbers with negative stiffness under harmonic and transient excitation, *International Journal of Mechanical Sciences*, **157-158**, 528-541

30. Zhu S.J., Zheng Y.F., Fu Y.M., 2004, Analysis of non-linear dynamics of a two-degree-of--freedom vibration system with non-linear damping and non-linear spring, *Journal of Sound and Vibration*, **271**, 15-24

Manuscript received December 13, 2022; accepted for print May 31, 2023

JOURNAL OF THEORETICAL AND APPLIED MECHANICS
61, 3, pp. 625-641, Warsaw 2023
https://doi.org/10.15632/jtam-pl/168989

STUDY ON STRESS CHARACTERISTICS OF HIGH-POROSITY COAL GANGUE SUBGRADE DURING FILLING PROCESS

Bing Hui
Shandong Transportation Research Institute, Jinan, China
Yingxin Hui
Ningxia Communications Construction Group Co., Ltd., Ningxia, China
e-mail: huiyx@seu.edu.cn
Xu Zhang, Wenjun Zhang
Shandong Transportation Research Institute, Jinan, China
Sheng Yan, Guangyu Men
Ningxia Communications Construction Group Co., Ltd., Ningxia, China

By analyzing geological conditions of a coal gangue filling roadbed, stress characteristics and settlement changes during the filling process of the coal gangue roadbed are simulated. The following conclusions are drawn: (1) As height of the coal gangue filling increases, the stress and settlement of each part will also increase. (2) During the filling process, the vertical stress acts as the first principal stress, and the stress and strain at the centerline of the roadbed are 10 times that of the roadbed. (3) The final stable value of uneven settlement of the coal gangue roadbed is 18.85 mm. (4) The monitoring results indicate that the settlement of the coal gangue roadbed is stable, and the settlement amount is small ensuring safety of the roadbed.

Keywords: coal gangue subgrade, subgrade stability, numerical analysis, stress characteristics

1. Introduction

As a subsidiary industrial waste in the process of coal mining, coal gangue belongs to historical materials. Due to the influence of various factors such as high ground stress, high temperature and humidity and crustal movement in underground engineering, it has its particularity, complexity and anisotropy. Spontaneous combustion, physical, chemical and biological changes occur in coal gangue stored in the natural air resulting in changes in particle characteristics of coal gangue. Especially for a coal gangue subgrade roller compaction under an external load, coal gangue subgrade particles exhibit significant changes, reflected in the porosity attenuation (Li and Wang, 2019). Finally, causing reconstruction of the coal gangue particle composition.

Li *et al.* (2020a) tested basic properties of coal gangue such as particle size distribution, loss on ignition, strength changes under water softening and compression performance. Based on this, a technology of using coal gangue as a railway roadbed filler was proposed. Through on-site tests, it has been shown that the coal gangue roadbed has excellent performance. Chen *et al.* (2020b) conducted a series of pressure plate tests on coal gangue fillers in the roadbed and analyzed variation patterns of model parameters. The research has shown that the compacted roadbed coal gangue filler has a double pore group structure, and its soil water characteristic curve (SWCC) exhibits a double step phenomenon. Fan *et al.* (2022) analyzed the dynamic evolution process, grading evolution law, and corresponding micromechanical properties of coal gangue particles during the crushing process under stress. The research has shown that the

interaction between lateral confinement and unidirectional compression of granular materials is mainly compression. Zhang *et al.* (2020) studied the effects of the substitution rate (r (SCGA)) and particle size distribution of coarse SCGA on mechanical properties of concrete. The results showed that coarse SCGA had a significant impact on the mechanical properties of concrete. When the SCGA substitution rate was 100%, the compressive strength, splitting tensile strength, and elastic modulus decreased by 19.4%, 36.1%, and 32.2%, respectively. Based on this, a prediction method for coarse SCGA concrete was proposed. Chen *et al.* (2020a) systematically studied the feasibility of using mineral waste as a roadbed filler. The optimal compaction parameters for waste residue were determined. The effects of different factors on the particle size distribution and mechanical properties of slag were evaluated and construction parameters of slag recommended. Chang *et al.* (2019) validated the use of solid waste such as sludge as raw materials for production of ecological cement, bricks, ceramic materials and lightweight aggregates through sintering processes. In addition, suggestions for future research were also proposed to strengthen high value-added application of sewage sludge. Zhang and Ling (2020) reviewed the effects of four main activation methods, namely thermal activation, mechanical activation, microwave activation and composite activation with a focus on discussing their interaction mechanisms with coal gangue. This provides valuable ideas and guidance for better understanding of the pricing of coal gangue, especially for its reuse in cement-based building materials. Li *et al.* (2020b) developed a new type of green concrete using large volume fly ash and coal gangue aggregates. The research results indicated that the fly ash coal gangue mixture had the advantages of acid resistance, waste recycling and lower carbon emissions, making it more effective than previous foundation improvement methods. Li *et al.* (2020c) simulated compression deformation of four different particle sizes of coal gangue filling materials using PFC3D. The compression deformation law, particle cluster distribution and changes in the shape of coal gangue blocks of coal gangue filling materials were analyzed. Based on the force chain distribution, the microscopic mechanism of compression deformation of coal gangue filling materials was studied. Li and Wang (2019) conducted a comprehensive literature review on the utilization of coal gangue in building material production, energy production, soil improvement and other high value-added applications. The research results have opened up a new door for further application of coal gangue, hoping to inspire future related research and guide decision-making. Long *et al.* (2019) studied mechanical properties and durability of a new type of cement-soil mixture reinforced by locally discarded coal gangue aggregates. The results indicated that the addition of coal gangue significantly improved strength, stiffness and corrosion resistance of the cement-soil mixture. Chen *et al.* (2019) systematically analyzed mechanical properties and microscopic mechanisms of red mud treated loess with a small amount of cement additive (RMCL). The results showed that the content of red mud C-R had a significant impact on the unconfined compressive strength (UCS) of RMCL. An appropriate amount of red mud waste can effectively improve mechanical properties of loess roadbed fillers. Ashfaq *et al.* (2020b) conducted a carbon footprint analysis of coal gangue to evaluate its CO_2 emissions when used as an embankment material. The study confirmed the fact that the utilization of coal gangue could significantly reduce generation of carbon footprint, thereby having a positive impact on the environment. Ashfaq *et al.* (2020b) showed through leaching research that there were trace elements in coal gangue, However, it was found that their concentration levels were far below the allowable limits.

Based on characterization studies, it can be inferred that coal gangue is a potential substitute for existing traditional geotechnical materials such as soil and other recycled materials. Leistner *et al.* (2017) studied the use of an artificial binary model particle system with magnetite as the target mineral and quartz as the gangue mineral to minimize problems related to ultrafine gangue particles. The results showed that hen gangue particles were small, ultrafine magnetite could also be recovered like fine magnetite. Ashfaq *et al.* (2022) conducted a comprehensive assessment on physical, chemical, mineralogy, geotechnical engineering and environmental (trace

metal mobilization and life cycle assessment) characteristics of coal gangue to assess its potential in promoting sustainable development.

The above studies have carried out a lot of analysis on the mechanical properties of mixtures of coal gangue and different materials, put forward the experimental methods of various properties of coal gangue and introduced the application of coal gangue to subgrade engineering. However, there are few studies on the high-porosity coal gangue subgrade. Based on the above investigations, the corresponding studies are carried out.

2. Engineering overview

The section of Beijing-Shanghai Expressway from Laiwu to Linyi (Rusujie) (hereinafter referred to as "Beijing-Shanghai Expressway") is located in Shandong Province. The starting point of the main line of the project is located in the southeast of Malonggu Village, Fengcheng Street Office, Laiwu City. It ends at the Rusujie of Beijing-Shanghai Expressway and connects to the Jiangsu section of Beijing-Shanghai Expressway. The main line is 232.191 km long. The main line of the project is based on the technical standards of a two-way eight-lane highway. The design speed from the starting point to Bianjiaquan section (K477+442.25-K508+000) is 100 km/h, and the design speed from Bianjiaquan to the end section (K508+000-K710+000) is 120 km/h. The integral subgrade is widened to 42 m, and width of the new single separated subgrade is 20.75 m. The field coal gangue yard has been fully spontaneously combusted in the air for nearly 30 years, and the porosity of coal gangue particles is 51.4% (Fig. 1).

Fig. 1. Coal gangue yard

According to the geotechnical engineering investigation report, the engineering geological conditions in this region are mainly divided into plain fill, silty clay and gravel soil. The stratigraphic distribution is shown in Table 1, and the groundwater level is within the range of 20 m underground.

Table 1. Stratigraphic distribution

Soil type	Average thickness [m]	Minimum thickness [m]	Maximum thickness [m]	Groundwater level [m]
Plain fill	0.4	0.2	0.6	–
Silty clay	2.0	1.0	3.0	–
Stone	13.0	11	17.5	–

3. Construction of the elastic-plastic model of s porous media coal gangue subgrade

The coal gangue subgrade has characteristics of high porosity and particle break-age. The remodeling will occur under the effect of subgrade rolling, resulting in the evolution of the coal gangue subgrade into porous media as shown by the physical and mechanical model in Fig. 2.

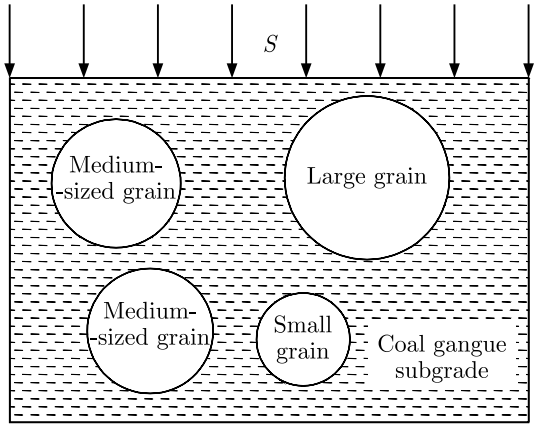

Fig. 2. Loading diagram of s porous medium of the coal gangue subgrade

3.1. Mathematical model

The coal gangue subgrade has characteristics of material heterogeneity and porous distribution. The coal gangue subgrade and foundation soil are both regarded as elastic-plastic materials, and Drucker-Prager (Jiang, 2021) ideal elastic-plastic constitutive model is adopted for the constitutive relation.

The following assumptions are used in the finite element analysis of the coal gangue subgrade:

- Each material is homogeneous, continuous and isotropic, an ideal elastic-plastic body, and the constitutive relation of soil satisfies the D-P yield criterion;
- The consolidation deformation and compression deformation of the foundation under the action of its own weight have been completed, and the embankment deformation is caused by the self-weight of the filler, without considering the influence of traffic load and climate factors on it;
- The coal gangue subgrade and foundation are unsaturated soil, without considering the consolidation of the embankment filler and foundation soil, and the influence of pore water pressure and embankment gravity load is applied once.

According to the effective stress principle of classical soil mechanics

$$\sigma = (1-n)\sigma^e + n\mu \tag{3.1}$$

where n is porosity, μ is pore water pressure, σ^e is effective stress and σ is total stress. The coal gangue subgrade is in a dry state, $\mu = 0$, therefore

$$\sigma = (1-n)\sigma^e \tag{3.2}$$

The composite D-P criterion with the strength limit is the failure criterion of the model.

According to the D-P failure criterion $f(\tau, \sigma) = 0$. From point A to point B on the graph, the failure envelope $f^s = 0$ is defined by the shear failure criterion

$$f^s = \tau + q_\emptyset \sigma - k_\emptyset \tag{3.3}$$

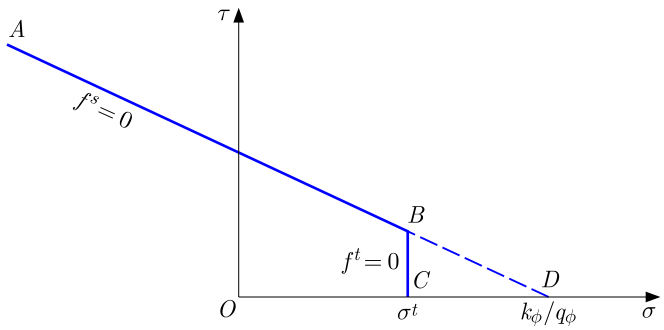

Fig. 3. Failure criterion of the D-P model

From point B to point C, by tensile failure criterion $f^t = 0$

$$f^t = \sigma - \sigma^t \tag{3.4}$$

In the formula, $q_\emptyset$ is the friction force of the D-P model, $k_\emptyset$ is the cohesive force, σ^t is the tensile strength. For the material $q_\emptyset$ is not equal to zero, the ultimate tensile strength is

$$\sigma^t_{max} = \frac{k_\emptyset}{q_\emptyset} \tag{3.5}$$

The potential function $\sigma(\tau, \sigma) = \text{ const}$, consisting of g^s and g^t, is used to describe shear and tensile plastic flow, respectively. The function g^s generally corresponds to an unrelated law in the form of

$$g^s = \tau + q_\varphi \sigma \tag{3.6}$$

When the flow rule is applicable, q_φ is a constant, which is numerically equal to $q_\emptyset$. The function g^t corresponds to a relevant flow rule given below

$$g^t = \sigma \tag{3.7}$$

when the D-P failure criterion follows shear failure characteristics. First of all, considering the shear failure, from Eq. (3.4) the partial differentials are

$$\frac{\partial g^s}{\partial \tau} = 1 \qquad \frac{\partial g^s}{\partial \sigma} = q_\varphi \tag{3.8}$$

Using $f = f^s$, Eq. (3.1), we get

$$\tau^N = \tau^I - \lambda^s G \qquad \sigma^N = \sigma^I - \lambda^s K q_\varphi \qquad \lambda^s = \frac{f^s(\tau^I, \sigma^I)}{G + K q_\emptyset q_\varphi} \tag{3.9}$$

The stress tensor component can be expressed as a generalized stress by the transformation equation. In form, Eq. (3.7) can be written as

$$\tau^N = \mu \tau^I \tag{3.10}$$

where μ is the known proportional factor $\tau^N = \mu \tau^I$, where

$$\mu = 1 - \lambda^s \frac{G}{\tau^I} \tag{3.11}$$

Using the tensor component S_{ij} to represent τ, we get

$$S^N_{ij} = \mu S^I_{ij} \tag{3.12}$$

Eliminating μ from the last two expressions, we get

$$S_{ij}^N = S_{ij}^I \frac{\tau^N}{\tau^I} \tag{3.13}$$

Finally, using this definition, new stress components can be calculated by Eq. (3.8), and

$$\sigma_{ij}^N = S_{ij}^N + \sigma^N \delta_{ij} \tag{3.14}$$

Equation (3.12) is modified as follows

$$(1-n)\sigma_{ij}^N = S_{ij}^N + (1-n)\sigma'^N \delta_{ij} \tag{3.15}$$

The boundary conditions: all directions of the foundation bottom are completely constrained, and the foundation is horizontally constrained along the cross direction of the road foundation.

3.2. Calculation model

In order to eliminate the boundary effect and stress influence range, the calculation size of the model is 100 m×10 m×50 m, in which the subgrade calculation area size is 60 m×10 m×22 m, the subgrade slope is 1:0.75, and the geometric model is shown in Fig. 4.

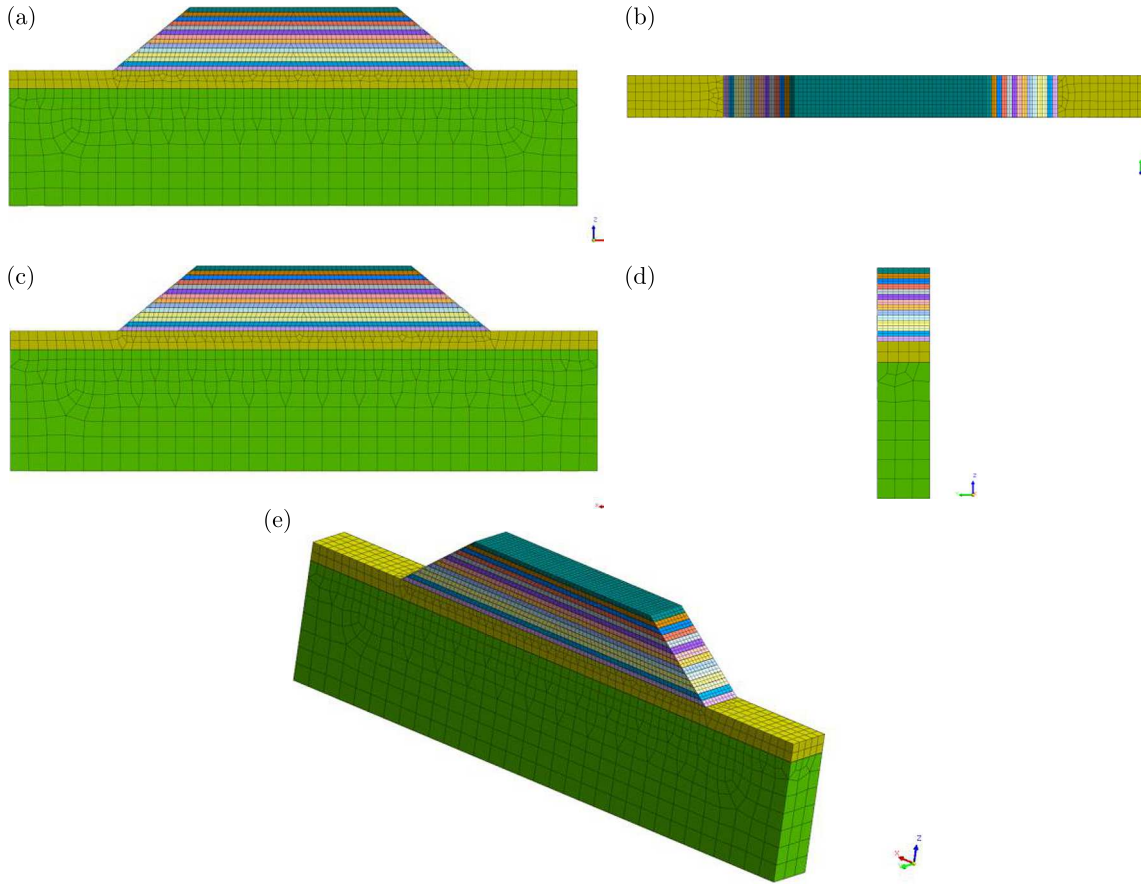

Fig. 4. Geometric model: (a) front view, (b) vertical view, (c) rear view, (d) side view, (e) graphic model

The model is generated by a hybrid grid, with the grid size transiting from 0.5 m to 2 m. The coal gangue subgrade is divided into fine grids and coarse foundations with a total of 15615 units including 9284 units for the coal gangue subgrade. The bottom of the model adopts fixed boundaries with the X-direction displacement limited on the left and right sides, and Y-direction displacement limited on the front and rear sides.

3.3. Physical and mechanical parameters

According to the laboratory test analysis, the physical and mechanical parameters of coal gangue and stratum in the calculation model are shown in Table 2. The porosity is set to 0.5.

Table 2. Material parameters of subgrade soil

Soil type	Thickness [m]	Elastic modulus [GPa]	Modulus of deformation [MPa]	Gravity [kN/m^3]	Poisson's ratio	Force of cohesion [kPa]	Angle of internal friction [°]
Coal gangue	7.0	1.1	–	18.5	0.3	75	45
Silty clay	2.0	–	15	18	0.35	15	23
Stone	13.0	–	60	22.5	0.35	40	30

3.4. Boundary conditions

The boundary conditions of the model are as follows: the fixed boundary is used at the bottom of the model, and the displacement in the X-direction is limited on both sides, and the displacement in the Y-direction is limited on both sides. The model boundary conditions are shown in Fig. 5.

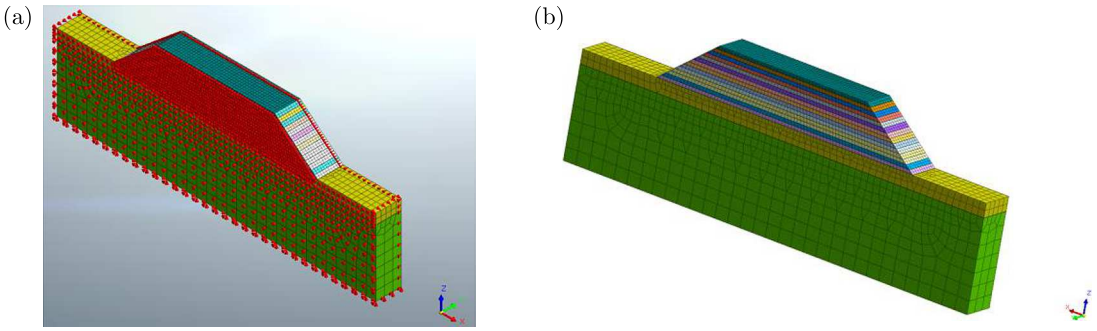

Fig. 5. Model boundary conditions: (a) boundary division, (b) mesh subdivision

3.5. Calculation model scheme

In order to better study the stress characteristics of the high-porosity coal gangue subgrade filling process, the calculation condition of coal gangue layered filling is 0.5 m, and the specific calculation model scheme is shown in Table 3.

Table 3. Calculation model scheme

Model calculation conditions	Calculation contents
Condition 1	Initial stress equilibrium
Condition 2	Filling to 0.5 m
Condition 3	Filling to 7.0 m

4. Mechanical characteristics analysis of the high-porosity coal gangue subgrade during construction

4.1. Initial stress balance

When the numerical calculation model starts to calculate the first step, the initial stress balance is needed, that is, to eliminate deformation caused by the self-weight stress. As shown in Fig. 6, when $Z = 0$, the gravity stress is zero. When $Z = 15\,\text{m}$, the gravity stress is $3.17 \cdot 10^2\,\text{kN/m}^2$. It can be seen from Fig. 5.b that when the silty clay $Z = 0$ on the surface and the gravel layer $Z = 10\,\text{m}$ at the bottom of the stratum, the deformation is zero.

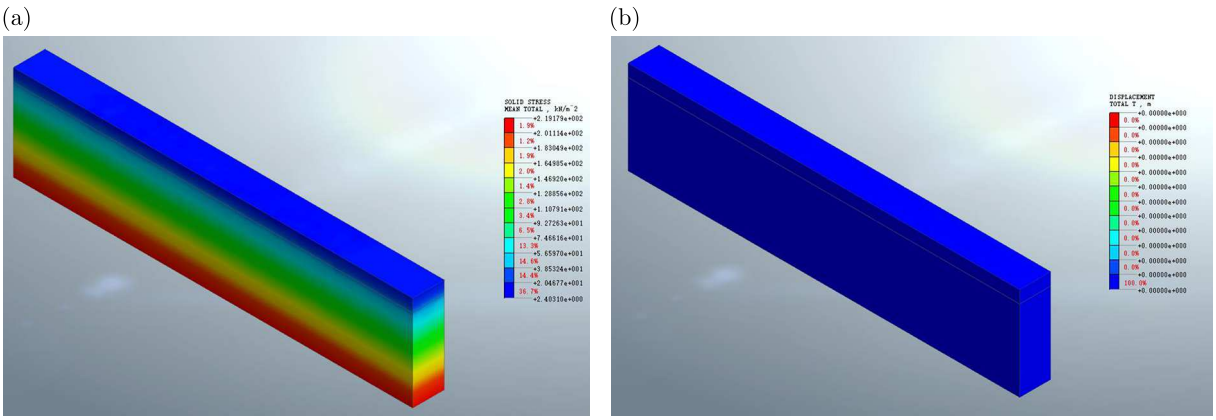

Fig. 6. Initial cloud images of the model: (a) stress cloud, (b) deforming cloud

4.2. Coal gangue subgrade first layer (0.5 m) filling

4.2.1. Stress nephogram

According to the numerical calculation results, the stress and deformation nephogram of the first layer of coal gangue filling are extracted. The center position at the bottom of the subgrade and the slope foot position at the bottom of the subgrade are mainly analyzed.

From Figs. 7a to 7c, it can be seen that when the layered filling height of coal gangue is 0.5 m, the total stress at the center of the subgrade bottom is 2.08 kPa, the horizontal (S-XX direction) stress is 1.37 kPa, and the vertical (S-ZZ direction) stress is 3.02 kPa. The total stress at the bottom slope foot of subgrade is 2.06 kPa, the horizontal (S-XX direction) stress is 1.58 kPa, and the vertical (S-ZZ direction) stress is 3.37 kPa.

Analysis of Figs. 7d-7f shows that when the height of coal gangue layered filling is 0.5 m, the total displacement of the center of the subgrade bottom is 1.64 mm, the horizontal (TX direction) displacement is $8.37{\cdot}10^{-4}$ mm, and the vertical (TZ direction) displacement is 1.63 mm. The total displacement at the bottom slope foot of the subgrade is 0.41 mm, the horizontal (TX direction) displacement is $5.87 \cdot 10^{-2}$ mm, and the vertical (TZ direction) displacement is 0.32 mm.

4.2.2. Differential settlement

Analysis of Fig. 8 shows that when the height of coal gangue layered filling is 0.5 m, the line at the bottom of the subgrade is extracted as the research object. The maximum settlement at the center of the subgrade bottom is 1.54 mm, and the maximum settlement at the foot of the subgrade bottom is 0.585 mm. It can be seen that an uneven settlement occurs between the bottom slope toe of the subgrade and the center of the subgrade bottom, and the differential settlement is 0.955 m.

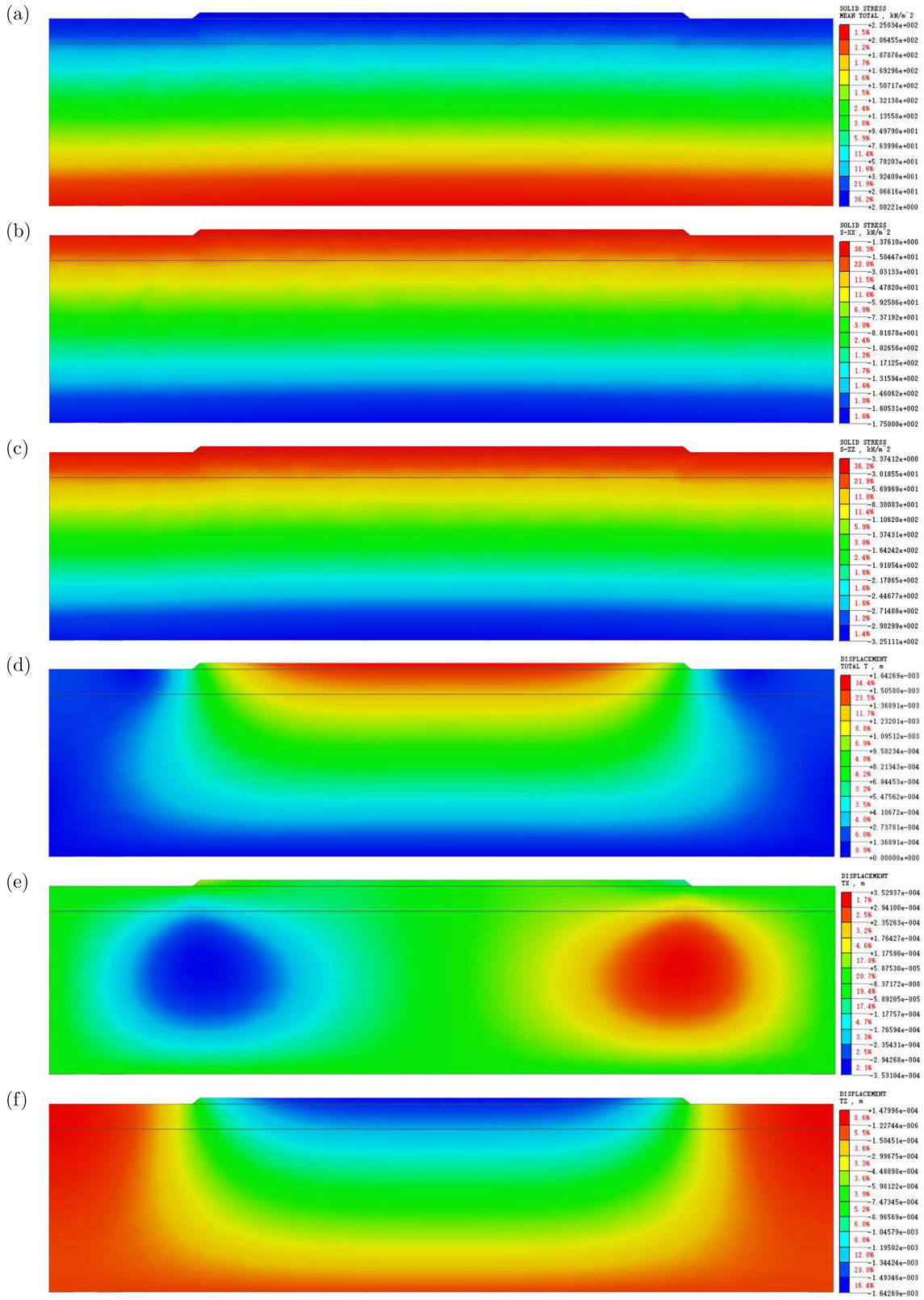

Fig. 7. Stress and deformation nephogram of the coal gangue filling first floor: (a) total stress, (b) horizontal (S-XX direction) stress, (c) vertical (S-ZZ direction) stress, (d) total displacement (T), (e) horizontal (TX direction) displacement, (f) vertical (TZ direction) displacement

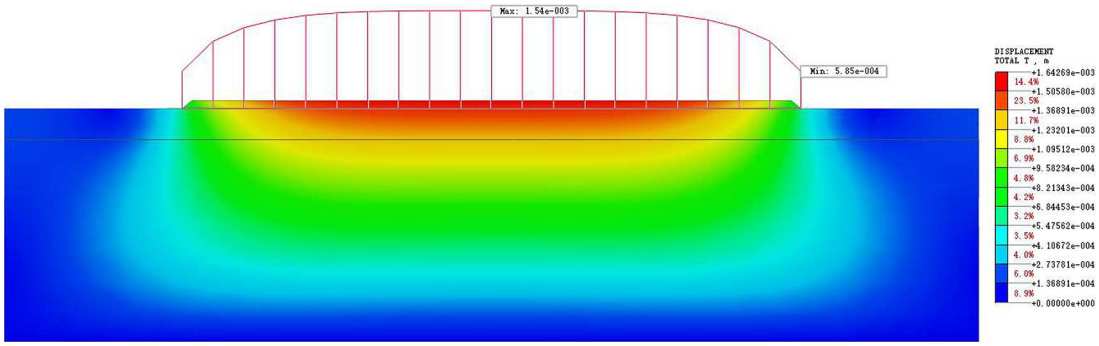

Fig. 8. Settlement curve between the slope toe and subgrade center

4.3. Filling of a 14th floor (7.0 m) of coal gangue subgrade

4.3.1. Stress nephogram

According to the numerical results, the stress and deformation nephogram of the fourteenth layer of coal gangue filling are extracted. The center position at the bottom of the subgrade and the slope foot position at the bottom are mainly analyzed.

From Figs. 9a to 9c, it can be seen that when the layered filling height of coal gangue is 7.0 m, the total stress at the center of the subgrade bottom is 74.90 kPa, the horizontal (S-XX direction) stress is 48.20 kPa, and the vertical (S-ZZ direction) stress is 125.00 kPa. The total stress at the bottom slope foot is 11.20 kPa, the horizontal (S-XX direction) stress is 12.20 kPa, and the vertical (S-ZZ direction) one is 12.60 kPa.

Analysis of Figs. 9d-9f shows that when height of the coal gangue layered filling is 7.0 m, the total displacement at the center of the bottom of the subgrade is the largest, which is 21.90 mm, and the maximum horizontal (TX direction) displacement is 3.17 mm, which appears on both sides of the subgrade center, and the maximum vertical (TZ direction) displacement is 21.90 mm. The total displacement at the bottom slope foot is 3.71 mm, the horizontal (TX direction) displacement is 2.48 mm, and the vertical (TZ direction) displacement is 3.05 mm.

4.3.2. Differential settlement

Analysis of Fig. 10 shows that when height of the coal gangue layered filling is 7.0 m, the line at the bottom of the subgrade is extracted as the research object. The maximum settlement at the center of the subgrade bottom is 21.90 mm, and the maximum settlement at the foot of the subgrade bottom is 3.05 mm. It can be seen that uneven settlement occurs between the bottom slope toe and the center of the bottom, and the differential settlement is 18.85 mm.

5. Study on the evolution of stress characteristics of the coal gangue filled subgrade construction process

With an increase of coal gangue filling height, the stress at the bottom of the subgrade, the slope foot and the middle line will increase, as shown in Fig. 11. The change curves of total stress, S-XX and S-ZZ in the process of coal gangue filling are extracted. The results show that the vertical stress (S-ZZ) of the middle line of the subgrade occupies the dominant position of the stress change. As the main control factor of stress growth, it is the first principal stress in the stress redistribution and particle incarceration of the subgrade. The stress of the coal gangue subgrade increases linearly from 0 m to 7 m, and the vertical stress (S-ZZ) reaches 125 kPa. The change of the vertical stress (S-ZZ) at the slope toe of the subgrade is the smallest, and it grows slowly in the process of coal gangue filling. The third principal stress plays a role in the stress redistribution and particle embedding of the subgrade. During the filling process of the

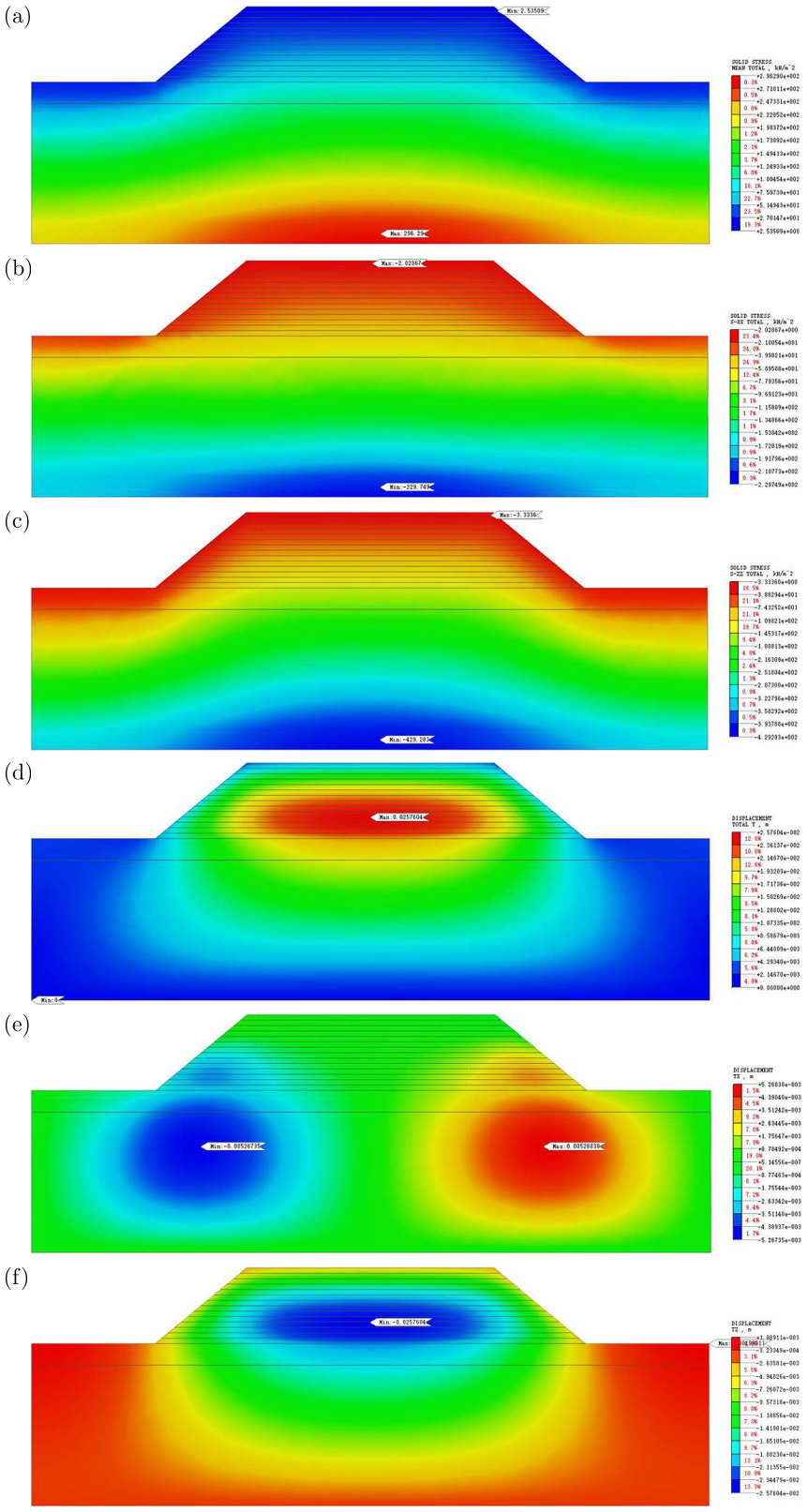

Fig. 9. Stress and deformation nephogram of coal gangue filling of the 14th floor: (a) total stress, (b) horizontal (S-XX direction) stress, (c) vertical (S-ZZ direction) stress, (d) total displacement (T), (e) horizontal (TX direction) displacement, (f) vertical (TZ direction) displacement

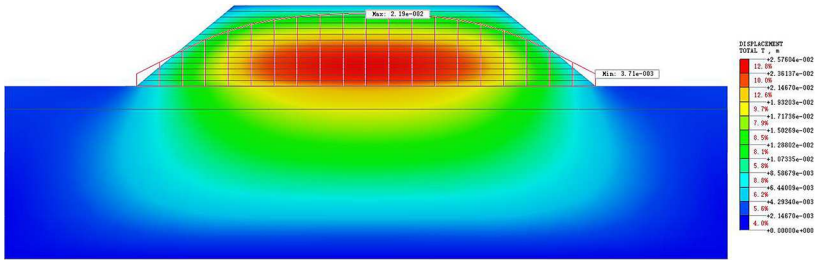

Fig. 10. Settlement curve between the slope toe and subgrade center

coal gangue subgrade from 0 m to 7 m, the stress shows a linear growth trend, and the vertical stress (S-ZZ) of subgrade slope toe reaches 12.2 kPa. The vertical stress change of the middle line of the subgrade is 10 times that of the slope toe, and the stress change directly affects the rigidity of the coal gangue subgrade, which varies the distribution of stress.

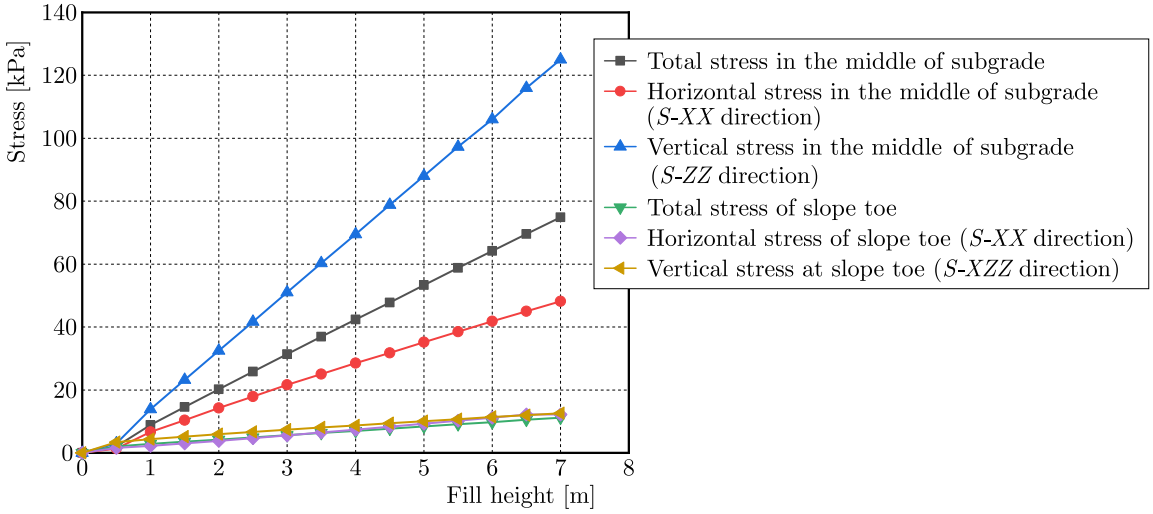

Fig. 11. Curve of stress variation with filling height

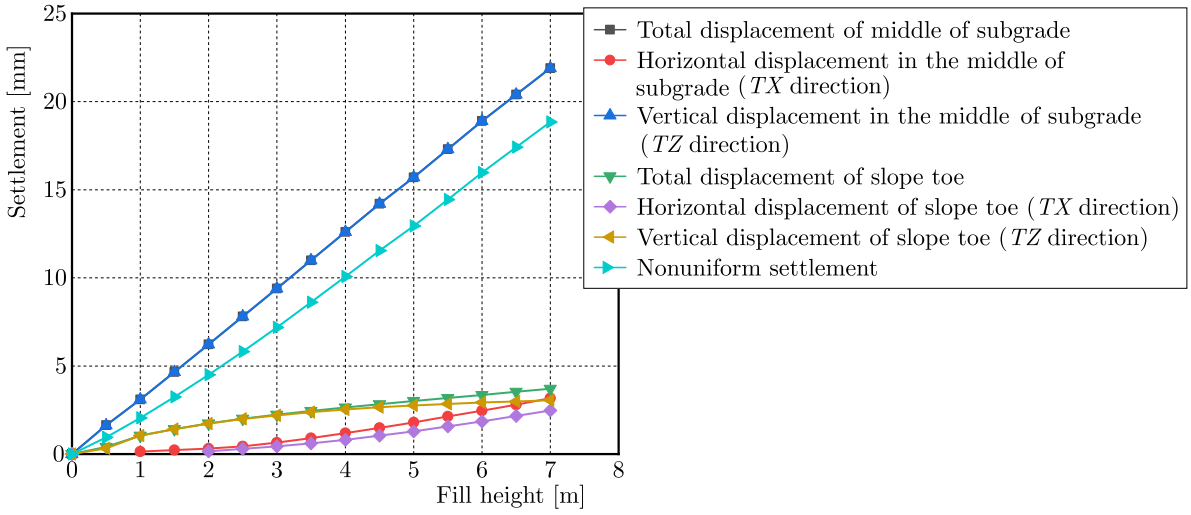

Fig. 12. Curve of settlement variation with filling height

With an increase of coal gangue filling height, the displacement at the bottom of the subgrade, the slope foot and the middle line will increase, as shown in Fig. 12. The change curves of total

displacement, TX and TZ during the coal gangue filling process are extracted. The results show that the vertical displacement TZ of the subgrade midline occupies the dominant position of deformation, which plays an important role in the uneven deformation of the subgrade as the main control factor of deformation growth. The displacement of the coal gangue subgrade increases linearly from 0 m to 7 m, and the vertical displacement TZ reaches 21.9 mm. The horizontal displacement of the subgrade slope toe TX changes minimum, and it grows slowly in the process of coal gangue filling. The displacement of the coal gangue subgrade increases linearly from 0 m to 7 m, and the slope TX reaches 2.48 mm. The vertical displacement of the middle line is 10 times of the horizontal displacement of the slope toe. The change of displacement directly affects the overall safety and stability of the coal gangue subgrade, and it is easy to achieve variable settlement, which results in cracking defects of the subgrade.

With an increase of coal gangue filling height, the uneven settlement of the bottom slope foot and the bottom center of the subgrade will increase, as shown in Fig. 13. The variation curves of the total displacement and the total displacement of the bottom slope foot and the center of the bottom during the filling process of coal gangue are extracted. The results show that the variation of uneven settlement shows a linear growth trend. In the range of 5 m of coal gangue filling, the variation rate of uneven settlement is fast. When the height reaches 7 m, the settlement tends to be stable, and the stable value is 18.85 mm.

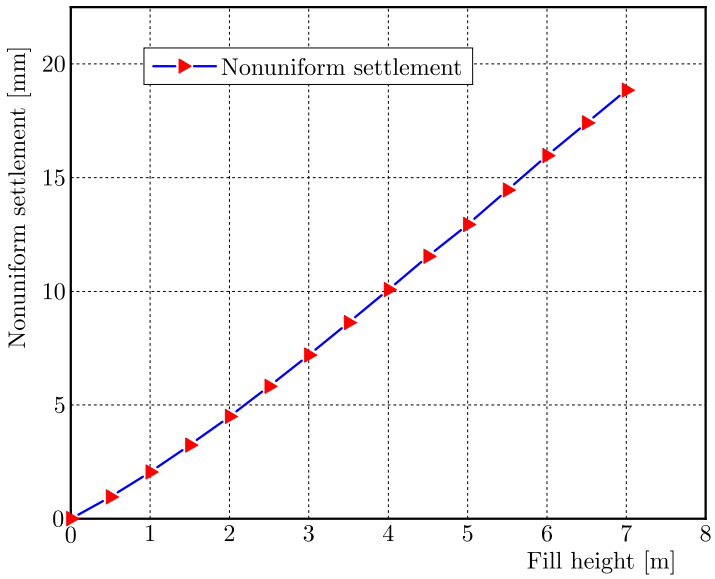

Fig. 13. Variation curve of differential settlement

6. Field stress and deformation monitoring

6.1. Field monitoring

In order to detect the state of coal gangue subgrade, it is necessary to control the coal gangue subgrade. According to the existing norms and standards, the settlement variation, elastic modulus and deflection value of coal gangue can be detected. However, the above is only the traditional detection method. In order to directly reflect the filling quality of coal gangue, the authors propose to use a set of key technologies for quality detection of coal gangue.

During the filling of the coal gangue subgrade, there are three test components, namely, earth pressure box, pore water pressure gauge and fixed inclinometer probe. The on-site coal gangue monitoring and sampling adopts a solar panel wireless transmission automatic monitoring

system. After installation, the flow card is used to realize computer receiving data at any position, as shown in Fig. 14a.

Through data collection and analysis of the above test elements, it is concluded that the coal gangue subgrade structure is stable and there is no quality problem, as shown in Fig. 14b.

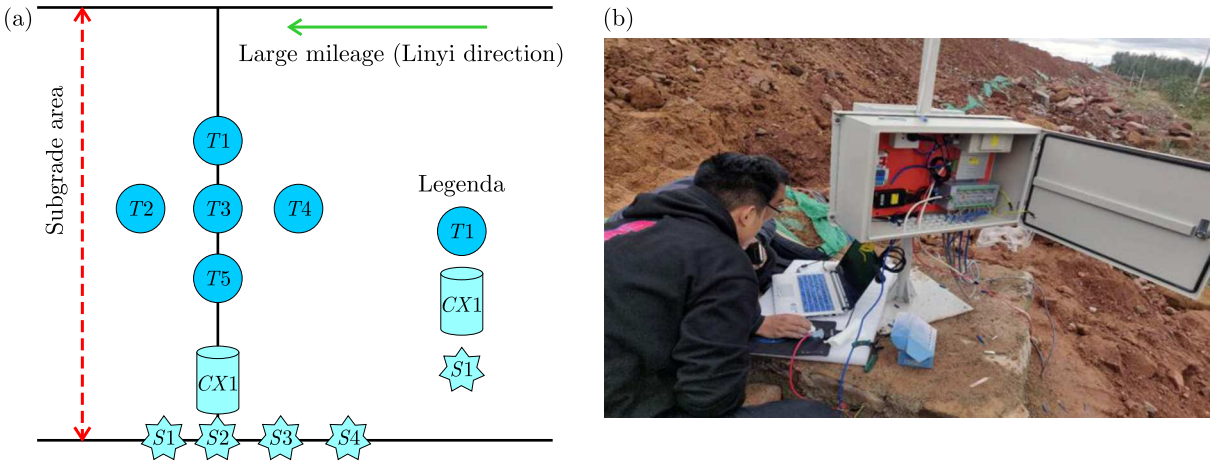

Fig. 14. (a) Setting diagram of test elements at each section, (b) data collection

6.2. Monitoring data analysis

Analysis of Fig. 15 shows that after nearly a year of monitoring data it turns out that the coal gangue subgrade does not occur groundwater infiltration and better guarantee its stability and safety.

Analysis of Fig. 16 shows that during the construction of the coal gangue subgrade the soil pressure increased sharply, after 100 days it stabilized, and the stable value is 185 kPa-207 kPa.

Figure 17 shows that the deformation of coal gangue subgrade is mainly reflected in the horizontal displacement and settlement change. The horizontal displacement and settlement change rate are faster in the early stage of subgrade construction. After completion of subgrade construction, the settlement reaches a stable state, with a horizontal deformation of 4.83 mm and settlement of 15.66 mm. And with construction of the base and surface layer, the load of the subgrade increases, which directly continues the deformation of the subgrade to increase. When the frequency of coal gangue subgrade monitoring is 400 d, the horizontal displacement and settlement reach a stable state. The horizontal displacement is maintained at 8.4 mm, and the settlement at 17.5 mm. The monitoring results show that the settlement of coal gangue subgrade is stable and the settlement is small, which ensures safety of the subgrade.

7. Conclusions

By analyzing geological conditions of the coal gangue filling subgrade, a three-dimensional geological mechanical model of coal gangue is established. Based on the Mohr-Coulomb failure criterion, stress characteristics and settlement changes during the filling process of the coal gangue roadbed are simulated. By extracting the stress and deformation cloud images of each layer of coal gangue filling, the stress and deformation curves of the center position at the bottom of the subgrade and the slope toe position at the bottom of the subgrade are analyzed. The following conclusions are drawn:

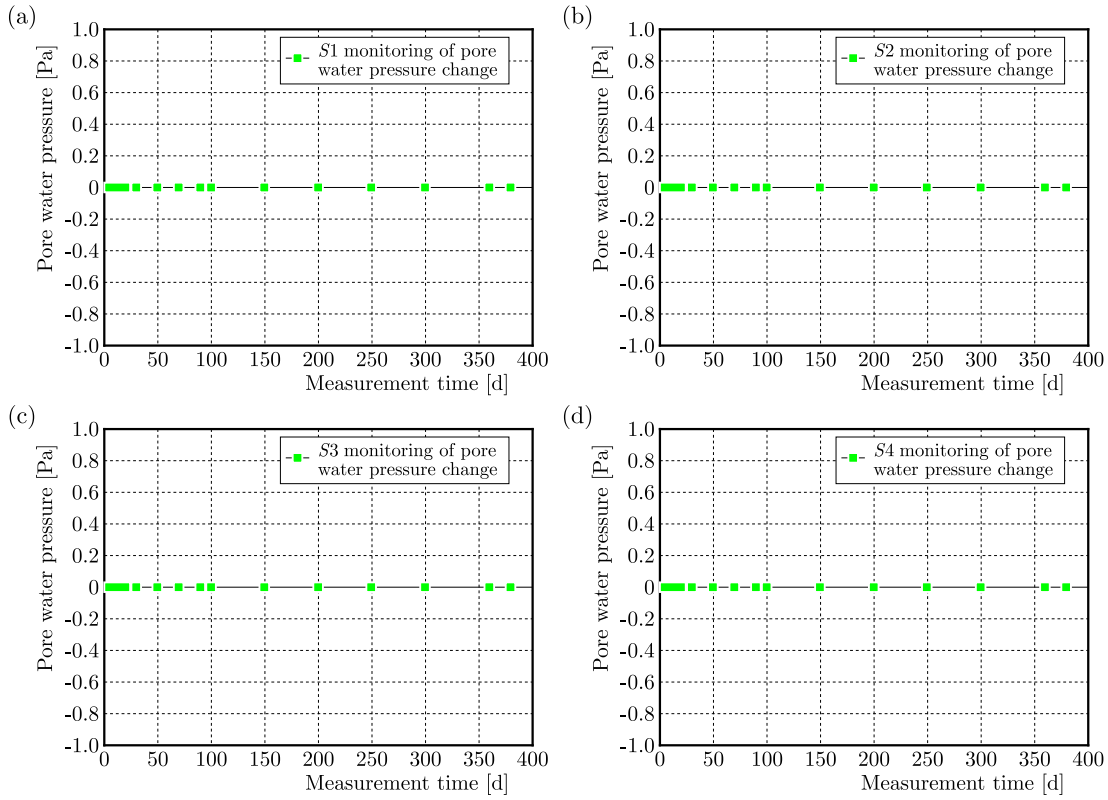

Fig. 15. Monitoring of pore water pressure variation of the coal gangue subgrade: (a) $S1$ pore water pressure, (b) $S2$ pore water pressure, (c) $S3$ pore water pressure, (d) $S4$ pore water pressure

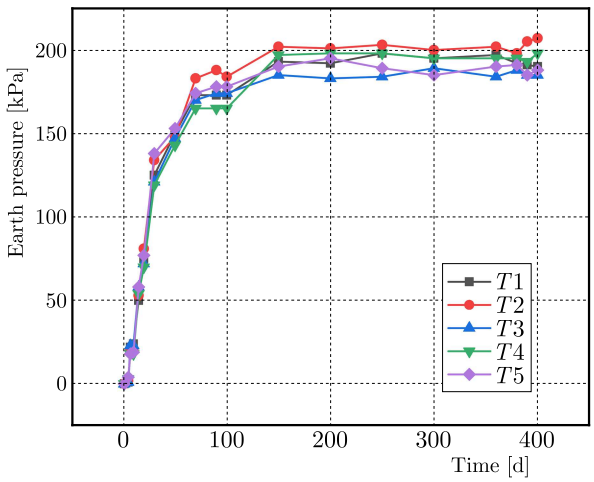

Fig. 16. Monitoring of earth pressure variation of the coal gangue subgrade

- As height of the coal gangue filling increases, the stress at the base of the road, the foot of the roadbed slope, and the center line of the roadbed will increase, and the settlement will also increase accordingly.
- During the filling process, the vertical stress (S-ZZ) plays a primary role in the stress redistribution and particle squeezing of the roadbed. The vertical stress change in the centerline of the roadbed is 10 times that of the vertical stress change at the foot of the roadbed slope, and the vertical displacement change in the centerline of the roadbed is 10 times that of the horizontal displacement change at the foot of the roadbed slope.

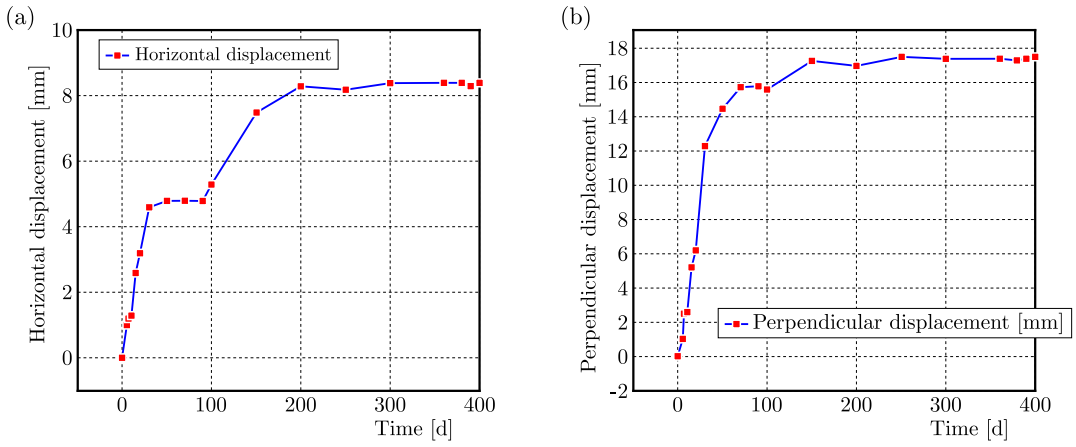

Fig. 17. (a) Monitoring of horizontal displacement change of the coal gangue subgrade, (b) monitoring of settlement change of the coal gangue subgrade

- As height of the coal gangue filling increases, the uneven settlement between the foot of the road base slope and the center of the road base will increase. The uneven settlement during the filling process shows a linear growth trend, and within the 5 m range of the coal gangue filling, the uneven settlement change rate is faster. When reaching a height of 7 m, the settlement tends to stabilize, and the stable value is 18.85 mm.
- The deformation of the coal gangue roadbed is mainly reflected in horizontal deformation and settlement changes. After completion of the roadbed construction, the horizontal deformation is 4.83 mm, and the settlement is 15.66 mm. With construction of the base and surface layers, the horizontal deformation increased to 8.4 mm and the settlement remained at 17.5 mm. The monitoring results indicate that the settlement of the coal gangue roadbed is stable and the settlement amount is small, ensuring safety of the roadbed.

Acknowledgment

This work was supported by the Science and Technology Planning Project of Transportation Department in Shandong Province (2019B24).

References

1. Ashfaq M., Heeralal M., Moghal A.A.B., 2020a, Characterization studies on coal gangue for sustainable geotechnics, *Innovative Infrastructure Solutions*, **5**, 1
2. Ashfaq M., Lal M.H., Moghal A.A.B., Murthy V.R., 2020b, Carbon footprint analysis of coal gangue in geotechnical engineering applications, *Indian Geotechnical Journal*, **50**, 4, 646-654
3. Ashfaq M., Moghal A.A.B., Basha B.M., 2022, The sustainable utilization of coal gangue in geotechnical and geoenvironmental applications, *Journal of Hazardous Toxic and Radioactive Waste*, **26**, 3
4. Chang Z.Y., Long G.C., Zhou J.L., Ma C., 2020, Valorization of sewage sludge in the fabrication of construction and building materials: A review, *Resources Conservation and Recycling*, **154**, 104606
5. Chen M., Wen P.H., Wang C.H., Chai Z., Gao Z.W., 2020a, Evaluation of particle size distribution and mechanical properties of mineral waste slag as filling material, *Construction and Building Materials*, **253**, 119183
6. Chen R.F., Cai G.J., Dong X.Q., Mi D.Y., Puppala A.J., Duan W., 2019, Mechanical properties and micro-mechanism of loess roadbed filling using by-product red mud as a partial alternative, *Construction and Building Materials*, **216**, 188-201

7. Chen R.P., Wang P.F., Liu P., Cheng W., Kang X., Yang W., 2020b, Experimental study on soil-water characteristic curves of subgrade coal gangue filler, *Rock and Soil Mechanics*, **41**, 2, 372-378
8. Fan X.X., Hui B., Ma S.J., Fu J.C., Zhang W.J., Meng L.X., Sun Z., 2022, Study on characteristics of three-dimensional granular meso-reconstruction of coal gangue roadbed, *Journal of Theoretical and Applied Mechanics*, **60**, 3, 361-374
9. Jiang J., 2021, *Modification and Engineering Application Research Based on the Drucker-Prager Strength Criterion of Releasable Strain Energy*, Guizhou University
10. Leistner T., Peuker U.A., Rudolph M., 2017, How gangue particle size can affect the recovery of ultrafine and fine particles during froth flotation, *Minerals Engineering*, **109**, 1-9
11. Li J.Y., Wang J.M., 2019, Comprehensive utilization and environmental risks of coal gangue: A review, *Journal of Cleaner Production*, **239**, 117946
12. Li L.H., Long G.C., Bai C.N., Ma K.L., Wang M., Zhang S., 2020b, Utilization of coal gangue aggregate for railway roadbed construction in practice, *Sustainability*, **12**, 11
13. Li L.H., Long G.C., Ma K.L., Ma H.W., Wang W.B., Zhang C., Xie Y.J., 2020, Preparation of green low strength mixture for foundation reinforcement treatment by using fly ash and waste coal gangue, *Materials*, **13**, 3
14. Li M., Li A.L., Zhang J.X., Huang Y.L., Li J.M., 2020, Effects of particle sizes on compressive deformation and particle breakage of gangue used for coal mine goaf backfill, *Powder Technology*, **360**, 493-502
15. Long G.C., Li L.H., Li W.G., Ma K.L., Dong W.K., Bai C.N., Zhou J.L., 2019, Enhanced mechanical properties and durability of coal gangue reinforced cement-soil mixture for foundation treatments, *Journal of Cleaner Production*, **231**, 468-482
16. Zhang Y.L., Ling T.C., 2020, Reactivity activation of waste coal gangue and its impact on the properties of cement-based materials – A review, *Construction and Building Materials*, **234**, 117424
17. Zhang Y.Z., Wang Q.H., Zhou M., Fang Y.F., Zhang Z.K., 2020, Mechanical properties of concrete with coarse spontaneous combustion gangue aggregate (SCGA): Experimental investigation and prediction methodology, *Construction and Building Materials*, **255**, 119337

Manuscript received March 1, 2023; accepted for print May 23, 2023

INFORMATION FOR AUTHORS

Journal of Theoretical and Applied Mechanics (***JTAM***) is devoted to all aspects of solid mechanics, fluid mechanics, thermodynamics and applied problems of structural mechanics, mechatronics, biomechanics and robotics. Both theoretical and experimental papers as well as survey papers can be proposed.

JTAM accepts full-text articles (max. 12 pages) as well as the short communications with all the requirements concerning standard publications, except a volume that is limited to 4 pages.

We accept articles in English only. The text of JTAM paper should not exceed 12 pages of standard format A4 (11-point type size, standard margins – 2.5 cm, single line spacing) including abstract, figures, tables and references.

The material for publication should be sent to the Editorial Office via electronic journal system: http://www.editorialsystem.com/jtam

Papers are accepted for publication after the review process. Blind review model is applied, which means that the reviewers' names are kept confidential to the authors. Reviewer(s) declare that there is no interpersonal relation with the author(s) that would affect the opinion and recommendation of the article for publication in JTAM. The final decision on paper acceptance belongs to the Editorial Board.

Starting from January 1, 2020, the Publisher of *Journal of Theoretical and Applied Mechanics* introduces a fee for published articles.

This applies only to papers submitted after this date and accepted by the Editorial Board for publication.

A payment of 500 EUR will be a condition for commencing the editorial procedure for upcoming articles.

After qualifying your paper for publication we will require LaTeX or TeX or Word document file and figures.

The best preferred form of figures are files obtained by making use of editorial environments employing vector graphics.

Requirements for paper preparation

Contents of the manuscripts should appear in the following order:

- Title of the paper.
- Authors' full name, affiliation and e-mail.
- Short abstract (maximum 100 words) and 3-5 key words (1 line).
- Article text (equations should be numbered separately in each section; each reference should be cited in the text by the last name(s) of the author(s) and the publication year).
- References (maximum 25) in alphabetical order.
- Titles of references originally published not in English, should be translated into English.

All the data should be reported in SI units.

Cena 40,00 zł (VAT 8%)

Contents